

Mechanical modeling of microstructures in elasto-plastically deformed crystalline solids

Dennis Kochmann



**Mechanical Modeling of
Microstructures in Elasto-Plastically Deformed
Crystalline Solids**

Dissertation

zur

Erlangung des Grades

Doktor-Ingenieur

der

Fakultät für Maschinenbau
der Ruhr-Universität Bochum

von

Dennis Michael Kochmann
aus Bottrop

Bochum 2009

Dissertation eingereicht am: 29. April 2009

Tag der mündlichen Prüfung: 29. Juni 2009

Erster Referent: Prof. Dr. rer. nat Klaus Hackl

Zweiter Referent: Prof. Dr. rer. nat. Khanh Chau Le

Vorsitzender: Prof. Dr. rer. nat. Alexander Hartmaier

*Die Neigung der Menschen, kleine Dinge für wichtig zu halten,
hat sehr viel Großes hervorgebracht.*

Georg Christoph Lichtenberg

Herausgeber:

Institut für Mechanik

— Schriftenreihe —

Ruhr-Universität Bochum

D-44780 Bochum

Summary

This thesis reports research progress on several fields of modeling microstructures in crystalline solids under elasto-plastic deformations. Based on thermodynamic minimum principles, the origin and subsequent evolution of microstructures is analyzed and computational techniques for their determination are presented. The present work decomposes into two major parts which emphasize different modeling aspects in this context.

In the first part, microstructures as minimizers of non-convex energy potentials in finite plasticity are investigated, following the thermodynamic principles of minimum potential energy and of minimum dissipation potential. The relaxation of these potentials by application of a rank-one-convex approximation of the quasiconvex hull allows for the description of the evolving microstructural parameters involved. A novel incremental solution formulation is derived for the simulation of laminate microstructures and applied to problems of single- and double-slip single-crystal plasticity. In contrast to many literature approaches which were based on a condensed energy, the present incremental method accounts for the existing microstructure at the beginning of each time step. Numerical results from the present variational formulation comprise the evolution of all microstructural laminate characteristics upon deformation, and they indicate a considerable reduction of the energy during the course of loading as compared to previous models.

The second part deals with the description of dislocation structures by means of a continuum dislocation theory. The free energy is modified to account for the energy of lattice defects, so that dislocation characteristics may enter the constitutive equations as an integral part. The particular choice of this defect energy entails a saturation behavior: the local maximum dislocation concentration is bounded. Based on this approach, closed-form analytical solutions for the pile-up of dislocations at the boundaries of bicrystals subject to a mixed deformation of shear and extension are presented. Interestingly, results indicate a size-dependence of the yield stress and of the hardening behavior. A variational formulation allows for the numerical treatment of fundamental two-dimensional problems with one active slip system. Numerical results comprise the formation of dislocation sub-structures within single-crystal grains as well as an underlying size effect through all results, which is typical to problems of crystal plasticity. Finally, the continuum dislocation approach is applied to deformation twinning. The twinning mechanism is decomposed into a plastic shear and a rigid plastic rotation. The present continuum dislocation approach successfully represents the influence of dislocations in the twin model: the pile-up of dislocations within the parent and twin phases gives rise to the appearance of some of the specific characteristics of TWIP alloys in the present model.

Kurzfassung

Die vorliegende Arbeit thematisiert verschiedene Aspekte der Modellierung von Mikrostrukturen in elasto-plastisch deformierten, kristallinen Werkstoffen. Auf der Grundlage thermodynamischer Minimumprinzipien werden die Ursachen von Mikrostrukturen analysiert sowie numerische Methoden zu deren Bestimmung präsentiert. Diese Arbeit lässt sich inhaltlich in zwei Hauptteile gliedern, die unterschiedliche Modellierungsgesichtspunkte in diesem Kontext hervorheben. Im ersten Teil der Arbeit werden Mikrostrukturen als Minimierer nicht-konvexer Energiepotentiale vorgestellt. Eine neuartige inkrementelle Lösungsstrategie zur Simulation solcher Mikrostrukturen wird präsentiert und angewandt. Im zweiten Teil der Arbeit folgt eine Zusammenfassung der Möglichkeiten, Versetzungsmikrostrukturen mit Hilfe einer Kontinuumsversetzungstheorie zu beschreiben und vorherzusagen.

Der tatsächliche Verformungszustand eines belasteten Körpers resultiert aus den thermodynamischen Prinzipien des minimalen Energiepotentials sowie des minimalen Dissipationsfunktionals, die im Falle nicht-konvexer Energiedichten zur Ausbildung von feinskaligen Strukturen führen. Die Relaxierung der freien Energie durch eine Approximation der rank-1-konvexen Hülle ermöglicht die Lösung eines korrekt gestellten Minimierungsproblems. Im ersten Teil der Arbeit wird eine analytische Relaxierung der Energie eines inkompressiblen Neo-Hooke-Materials mit einem oder zwei aktiven Gleitsystemen präsentiert. Die relaxierte Energie wird zusammen mit einer inkrementellen Formulierung verwendet, um die Evolution aller mikrostrukturellen Charakteristika eines Laminates erster Ordnung (d.h. die plastische Gleitung in allen Laminatphasen, die zugehörigen Volumenanteile und die Verfestigungsparameter) zu modellieren. Im Gegensatz zu vielen früheren Ansätzen, die auf der Minimierung eines kondensierten Energiefunktionals beruhen, ermöglicht die hier vorgestellte Methode die Berücksichtigung der bereits vorhandenen Mikrostruktur am Anfang jedes inkrementellen Zeitschritts. Darüber hinaus wird ein Verfahren zur Abbildung der tatsächlichen Veränderungen der Mikrostruktur während eines Zeitschritts im inkrementellen Modell vorgestellt. Die Ergebnisse zeigen deutliche Vorteile gegenüber der Benutzung des kondensierten Energiefunktionals für einen einzigen Zeitschritt.

Der zweite Teil der Arbeit stellt die Beschreibung von Versetzungsstrukturen mit Hilfe der Kontinuumsversetzungstheorie in den Mittelpunkt. Die freie Energie wird um einen zusätzlichen Term erweitert, der die Defektenergie der Versetzungen berücksichtigt. Die hier getroffene Wahl der speziellen Form dieser Defektenergie birgt einen Sättigungseffekt: Die Versetzungsdichte kann lokal nicht beliebig ansteigen, sondern ist durch einen Materialparameter begrenzt. Auf der Grundlage dieses Ansatzes werden zunächst analytische Lösungen für den Aufstau von Versetzungen an den Korngrenzen eines Bikristalls, der einer kombinierten Scher- und Zugbelastung ausgesetzt ist, hergeleitet. Eine variationelle Formulierung erlaubt die Erweiterung des Modells zur numerischen Lösung beliebiger zweidimensionaler Randwertprobleme mit einem aktiven Gleitsystem. Die Ergebnisse dieses Verfahrens umfassen die Ausbildung von Versetzungssubstrukturen im Innern der einkristallinen Körner eines Polykristalls sowie einen durch alle Ergebnisse sichtbaren Skaleneffekt, der typisch für Probleme in der Kristallplastizität ist. Schließlich wird der Kontinuumsversetzungsansatz auf die Modellierung von Deformationszwillingen angewendet. Hierbei spielt der Aufstau von Versetzungen an den Zwillingsgrenzen im verzwilligten Material eine entscheidende Rolle, welcher im Modell berücksichtigt werden kann. Dies resultiert in der qualitativ korrekten Repräsentation vieler Charakteristika von TWIP-Legierungen im Modell.

Acknowledgements

Looking back on my time at the Institute of Mechanics at Ruhr-University Bochum, I would like to express my sincere gratitude to all of those who have supported me and have thereby contributed – in one or the other way – to the accomplishments reported in this thesis. This work certainly would not have been possible without the help from very many persons, the most important of whom I would like to mention here.

First of all, I would like to express my utmost gratitude to my advisors who have made this dissertation possible. Let me thank Prof. Khanh Chau Le for actually bringing me back to Bochum for my doctoral research on micro-mechanical dislocation models. Since then, he has always been a great teacher and an excellent advisor, whose ideas and approaches have laid the basis for parts of this thesis. His kind and open-minded but always focussed way has been a valuable incentive for successful research over the last few years.

Equally important, let me thank Prof. Klaus Hackl for a variety of reasons. He introduced me to the fields of microstructures and relaxation theory. Not only has he been an always patient and imaginative research advisor but also the best possible supervisor. His liberal style of leadership provided me with the freedom in research that has helped me pursue many research ideas and projects beyond the scope of this thesis. In this context I would also like to thank Prof. Walter J. Drugan who has not advised any of my thesis research but our ongoing joined research has often been a very welcome change whenever I was stuck in the tempting numerics of microstructure simulations.

Research of the present work was carried out within the framework of two research communities which I am particularly thankful for: Ruhr-University Research School funded by Germany's Excellence Initiative (DFG GSC 98/1), and Forschergruppe Microplast (DFG FOR 797). Not only the financial support is gratefully acknowledged but also the fruitful interactions made possible in an interdisciplinary environment.

Finally, I would like to thank all those who have gone a long way towards the completion of this thesis. I am especially thankful for my family and my friends for always supporting me and for bearing with me even when I worked late or weekends to eventually submit this thesis. Furthermore, I would like to thank all of my colleagues at the Institute of Mechanics and in particular at the Lehrstuhl für Allgemeine Mechanik. There are so many former and current colleagues whose ideas and comments have been a crucial help for my research and – maybe even more importantly – whose friendship has been an enduring inspiration: our pleasant atmosphere and research conditions have predominantly been their merit. Let me express my gratitude also to a number of student assistants I could advise during the last few years and who have been an enormous support in doing some of the cumbersome computational tasks of this research.

Table of Contents

Nomenclature	xiii
1 Introduction	1
1.1 Structures and Patterns	1
1.2 Experimental Evidence of Microstructures in Solids	2
1.3 Modeling Plasticity and Microstructures: Motivation and State of the Art . .	5
1.3.1 Description of Microstructures Based on Energy Relaxation in Fi- nite Elasto-Plasticity	5
1.3.2 Continuum Dislocation Description of Dislocation Pile-Ups and Dis- location Substructures	7
1.3.3 An Energy-Based Continuum Dislocation Approach to Deformation Twinning	9
1.4 Scope of this Thesis	10
2 Mathematical and Mechanical Fundamentals	11
2.1 Vector and Tensor Analysis	11
2.1.1 Vector Calculus	11
2.1.2 Tensor Calculus	12
2.1.3 Basic Vector and Tensor Transformations	15
2.1.4 Vector and Tensor Analysis	17
2.2 Notions of Convexity and Minimum Criteria	20
2.3 Fundamentals of Continuum Mechanics	24
2.3.1 Elastic Deformation	24
2.3.2 Plastic Deformation	28
2.3.3 Stresses and Equilibrium	29
2.3.4 Constitutive Laws	33
2.3.5 Variational Formulation for Linear Elasticity	36
2.4 Continuum Theories of Plasticity and Dislocations	40
2.4.1 Bridging the Scales in Elasto-Plasticity	40
2.4.2 The Crystal Lattice, Elastic and Plastic Deformation	41
2.4.3 Lattice Defects	42
2.4.4 Properties of Dislocations	44
2.4.5 Dislocation Interactions and Sources	49
2.4.6 Continuum Theory of Plasticity	52
2.4.7 Continuum Theory of Dislocations	55
2.5 Thermodynamic Principles and the Origin of Microstructure	60
2.5.1 Thermo-Mechanical Principles	60
2.5.2 Energy Minimizers, Minimizing Sequences and Microstructure . .	66
2.5.3 Material Microstructures	70
3 Time-Continuous Evolution of Inelastic Microstructures in Finite Plasticity	73
3.1 Introduction	73
3.2 Application of Relaxation Theory to Inelastic Microstructures	75

3.2.1	Minimum Principles and Young Measures	75
3.2.2	Approximation via Lamination	77
3.3	Incompressible Neo-Hooke Material in Single-Slip Plasticity	79
3.3.1	Constitutive Framework for a Single Active Slip System	79
3.3.2	Time-Continuous Evolution for a Single Active Slip System	83
3.3.3	Numerical Scheme for a Single Active Slip System	86
3.4	Generalization to Multiple Active Slip Systems	86
3.4.1	Constitutive Framework for Multiple Active Slip Systems	86
3.4.2	Numerical Scheme for Double-Slip	88
3.5	Results	90
3.5.1	Relaxed and Condensed Energy	90
3.5.2	Single-Slip Plasticity for a First-Order Laminate	93
3.5.3	Double-Slip Plasticity for a First-Order Laminate	104
3.6	Discussion and Conclusions	104
4	Modeling Microstructures via Continuum Dislocation Theory	107
4.1	Introduction to Continuum Dislocation Theory	107
4.1.1	Motivation	107
4.1.2	Continuum Dislocation Theory	108
4.1.3	Energy of Dislocations and Constitutive Framework	109
4.2	Plastic Deformation of Bicrystals: Boundary Value Problem	113
4.3	Energetic Threshold for Dislocation Nucleation	116
4.4	Plane-Constrained Shear of Single-Slip Bicrystals	120
4.4.1	Plane-Constrained Shear at Zero Dissipation	120
4.4.2	Plane-Constrained Shear at Non-Zero Dissipation	122
4.4.3	Numerical Solution for Plane-Constrained Shear with Non-Symmetric Active Slip Systems	126
4.5	Plane-Strain Uniaxial Extension of Single-Slip Bicrystals	132
4.5.1	Plane-Strain Uniaxial Extension at Zero Dissipation	132
4.5.2	Plane-Strain Uniaxial Extension at Non-Zero Dissipation	134
4.5.3	Numerical Solution for Uniaxial Extension for Non-Symmetric Active Slip Systems and for Arbitrary Crystal Heights	137
4.6	Combined Shear and Extension of Single-Slip Bicrystals	139
4.6.1	Combined Shear and Extension at Non-Zero Dissipation	139
4.6.2	Combined Shear and Extension at Zero Dissipation	142
4.7	Size Effects of the Bicrystal Problem	144
4.8	Variational Formulation	146
4.8.1	Finite Element Formulation at Zero Dissipation	146
4.8.2	Finite Element Formulation at Non-Zero Dissipation	157
4.9	Numerical Examples	162
4.10	Discussion and Conclusions	169
5	A Continuum Model for the Initiation and Evolution of Deformation Twins	175
5.1	Introduction	175
5.2	Plane-Constrained Shear of Twins	176
5.3	Energy Minimizers and the Initiation of Slip and Twinning	181
5.3.1	Deformation of the Crystal at Zero Dissipation	181
5.3.2	Onset of Twinning and Number of Twins	184
5.3.3	Stress-Strain Behavior at Zero Dissipation	188
5.4	Plastic Deformation at Non-Zero Dissipation	188

5.4.1	Evolution of Plastic Distortion and Volume Fractions	188
5.4.2	Stress-Strain Behavior	192
5.5	Discussion and Conclusions	193
6	Conclusions and Outlook	199
	References	203
	Reference to Pre-Publications	214
	Curriculum Vitae	215

Nomenclature

This thesis makes use of the following notation conventions: scalar variables are denoted by lower case characters, vector and tensor quantities by bold lower and upper case characters, respectively. Einstein's summation convention is implied.

Use of the mathematical symbols is explained in detail in Section 2 and not repeated here for conciseness. The following list gives a brief overview of those characters and symbols with a specific physical meaning and the abbreviations used:

Latin notations

a, A	deformed and undeformed area
\mathbf{a}_i	amplitudes of laminate deformation gradients
\mathcal{A}	assembly operator for FE matrices
b	Burgers' vector
\mathbf{b}	laminate orientation unit vector, Finger tensor
$\hat{\mathbf{b}}$	vector of nodal plastic distortion values
\mathbf{B}	gradient matrix for FE computations
\mathcal{C}	elasticity tensor
\mathbf{C}	right Cauchy-Green tensor
d	problem dimension
\mathcal{D}	dissipation
D	dissipation distance
\mathbf{e}_i	Cartesian unit vectors
E	Young's modulus, dimensionless energy
\mathbf{E}	elastic modulus tensor for FE computations Almansi-Hamel tensor
\mathcal{E}	tensor of the defect energy constants,
\mathbf{F}	deformation gradient tensor
$\mathbf{F}_e, \mathbf{F}_p$	elastic and plastic deformation gradient tensors
\mathbf{f}	body or surface force vector
$\mathbf{f}_{\text{int}}, \mathbf{f}_{\text{ext}}$	vector of internal and external forces
h	height of the bicrystal or grain
$H = hb\rho_s$	dimensionless height of the bicrystal or twin
\mathcal{I}	total free energy
$j = \det \mathbf{F}$	determinant of the deformation gradient tensor
\mathbf{J}	Jacobian
J	determinant of the Jacobian
k	material parameter (scaling factor of the defect energy)
K	elastic bulk modulus
\mathbf{K}	stiffness matrix

ℓ	linear functional (power of the external forces)
\mathbf{L}	velocity gradient tensor
\mathcal{L}	Lagrange functional
\mathbf{m}	unit vector normal to the active glide plane
\mathbf{n}	are unit normal vector
N_i, \tilde{N}_i	shape functions
$\mathbf{N}, \tilde{\mathbf{N}}$	shape function matrices
p, p_i	hardening history variables
P	power
q	driving force on the volume fractions
\mathbf{Q}	FE auxiliary matrix for the plastic strains
Q	heat
\mathbf{R}	rotation tensor
r	material parameter (critical resolved shear stress)
s	volume fraction of the twin phase
S	entropy
\mathbf{s}	slip direction unit vector
sign	sign function
sig	sigmoid function (approximated sign function)
$\text{sym}(\cdot) = \frac{1}{2}(\cdot + \cdot^T)$	symmetric part of a tensor
$t, \Delta t$	time and time increment
t	thickness of a plane body
\mathbf{t}	traction vector
T	temperature
\mathbf{T}	tangent stiffness matrix
\mathbf{u}, \mathbf{v}	displacement field components in x - and y -direction
$\hat{\mathbf{U}}$	solution vector containing displacements and plastic distortion
\mathbf{U}, \mathbf{V}	right and left stretch tensor
\mathbf{v}	velocity vector
W_i	Gauß weight factors
\mathbf{x}, \mathbf{X}	coordinates in the deformed and in the reference configuration
x, y, z	Cartesian coordinates

Abbreviations

cond.	condensed (energy)
EBSD	electron backscatter diffraction
GB	grain boundary
GND	geometrically necessary dislocation
NH	Neo-Hooke
rel.	relaxed (energy)
red.	reduced (energy)
SEM	scanning electron microscopy
SSD	statistically stored dislocations
TEM	transmission electron microscopy

Greek notations and other symbols

α	(scalar) normalized dislocation density
$\boldsymbol{\alpha}$	Nye's dislocation density tensor
β, β_1	plastic distortion and normalized plastic distortion
β_a, β_s	symmetric and antisymmetric part of the plastic distortion
$\boldsymbol{\beta}$	plastic distortion tensor
χ	parameter of the logarithmic energy approximation
δ	variation, Dirac-Delta distribution function
δ, δ_{cr}	load parameter (extension and shear), critical load
$\delta_r = \delta - \delta_{cr}$	(positive) deviation of the load from the critical value
$\delta_l = \delta + \delta_{cr}$	(negative) deviation of the load from the critical value
δ_{ij}	Kronecker delta
Δ, Δ^*	dissipation potentials
γ	plastic slip or distortion
γ, γ_{cr}	load parameter (shear), critical load
γ_{en}	energetic threshold for the shear strain
γ_r, γ_l	shear strains, see δ_r, δ_l
Γ	boundary surface energy
Γ_u, Γ_t	boundary subsets with prescribed displacements or forces, resp.
$\mathbf{\Gamma}$	inverse Jacobian for FE mapping
ε	load parameter (extension), strain
$\varepsilon_r, \varepsilon_l$	extension strains, see δ_r, δ_l
ε_{en}	energetic threshold for the extension strain
$\boldsymbol{\varepsilon}$	linear strain tensor
$\boldsymbol{\varepsilon}_p, \boldsymbol{\varepsilon}_e$	linear plastic and elastic strain tensors
$\tilde{\boldsymbol{\varepsilon}}$	strain vector in Voigt notation
ϵ_{ijk}	permutation symbol
$\boldsymbol{\phi}$	deformation field
φ	angle of the slip direction \boldsymbol{s} with the x -axis
φ_l, φ_u	slip system orientation in lower and upper bicrystal part
η	dimensionless parameter in Section 4
κ	hardening modulus
$\bar{\kappa} = \mu/(\lambda + 2\mu)$	dimensionless modulus ratio
λ, μ	elastic Lamé moduli
λ_i	volume fractions of the laminate phases
Λ	Lagrange parameter
ν	Possion's ratio
Π	energy potential
ϑ	load orientation
ρ, ρ_s	scalar dislocation density and saturated dislocation density
ρ_i	Lagrange parameters
$\boldsymbol{\sigma}$	Cauchy stress tensor
$\tilde{\boldsymbol{\sigma}}$	stress vector in Voigt notation
$\boldsymbol{\Sigma}^I, \boldsymbol{\Sigma}^{II}$	first and second Piola-Kirchhoff stress tensors
τ_{ij}	shear stresses
τ_{cr}	critical resolved shear stress

$\tau_\varepsilon, \tau_\gamma$	critical resolved stresses (extension and shear)
$\omega = \lambda/\mu$	dimensionless modulus ratio
$\boldsymbol{\omega}$	skew-symmetric rotation tensor
Ω	body volume
$\xi = yb\rho_s$	dimensionless coordinate
ξ, η	dimensionless coordinates for FE mapping
Ψ	Helmholtz free energy density
$\Psi^{\text{rel}}, \Psi^{\text{cond}}$	relaxed and condensed energy
$C\Psi, P\Psi, Q\Psi, R\Psi$	convex, polyconvex, quasiconvex and rank-one-convex hull
∂	(partial) derivative
∇	Nabla operator
$\langle \cdot \rangle = \frac{1}{h} \int_h \cdot \, dy$	average quantity
$[[\cdot]]$	jump of the quantity in brackets

1 Introduction

1.1 Structures and Patterns

A close look at the constituents of nature reveals underlying structures in very many natural aspects at various length scales. What appears macroscopically uniform and homogeneous turns out to be composed of a large number of structural members on smaller scales. The detailed inspection of a snowflake (see Figure 1.1) unveils the highly ordered branching structure of what appears as a homogeneous, soft, white something to the naked eye. Many biological, chemical or physical systems exhibit a more or less regular structure on a smaller scale, and such structures are based on the very same of nature's fundamental principles of thermodynamics, which are commonly dictated by energies. These thermodynamic laws govern the formation of structures and patterns on all scales. Therefore, it is not surprising that very similar structures to those of the ice crystal appear e.g. during dendritic solidification of metals from the melt.

Despite the huge variety of different structures and patterns in nature, these naturally appearing small-scale structures have another crucial aspect in common (besides the same underlying causal principles): the aggregate of all structural characteristics on the small scale fulfills a functional purpose on a superior scale or, in other words, the macroscopic appearance and behavior considerably depends on the microstructure. Let us outline a few more examples.

Figure 1.2 illustrates three examples of natural structures on a small scale, which give rise to a specific effect or property on some larger scale. The skin of a shark resembles a rough sandpaper to the touch. As can be seen from the first micrograph, this property stems from a very distinct small-scale composition of the shark skin, which is not a uniform surface tissue. Instead, the skin is covered by millions of dermal teeth and their arrangement provides the shark with hydrodynamic advantages (reducing turbulence while swimming) and additional protection from damage and parasites. The middle image illustrates the inner structure of human trabecular bone. In contrast to the white compact bone tissue surrounding the outer layer of bones and providing them with their smooth and white appearance, the inner structure (the trabecular bone) is less dense and consists of the shown network structure. This special structure helps to reduce weight and provide space for blood vessels and marrow, and to generally provide bones with their important viscoelastic properties. The third image displays the surface of a lotus leaf which is well-known for the eponymous lotus effect. Due to the specific micro- and nanoscopic architecture of the surface, these leaves exhibit a maximum water repellency and a minimum adhesion (predominantly for self-cleaning purposes), which has successfully been imitated in technical applications. Despite the differences between these three examples they all demonstrate how the (more or less random) arrangement of structural members on a smaller scale gives rise to specific macroscopic properties. Therefore, these examples stress the crucial importance to gain insight into the causal mechanisms of the formation of such microstructures, into the behavior of these microstructures and the resulting macroscopic characteristics.



Figure 1.1: Optical micrographs of ice crystals, courtesy of Kenneth Libbrecht (2009). Reprinted by permission.

Components in engineering applications are predominantly composed of metals. These crystalline solids admit a similar decomposition into structures on smaller scales. Their composition spans several length scales and, on each of these scales, is more or less regularly ordered: from the periodic atomic lattice (which determines the elastic properties) to the microstructure of all lattice defects to mesostructures of the grain assembly (the latter two considerably determine the plastic properties) to composite morphologies. The enormous influence of these microstructural characteristics credits special importance to the investigation of the microstructure's origin and evolution in the modeling of crystalline solids.

1.2 Experimental Evidence of Microstructures in Solids

Modern microscopic techniques allow for a detailed characterization of the microstructure of crystalline solids, which comprises all characteristics and defects on the microscale with

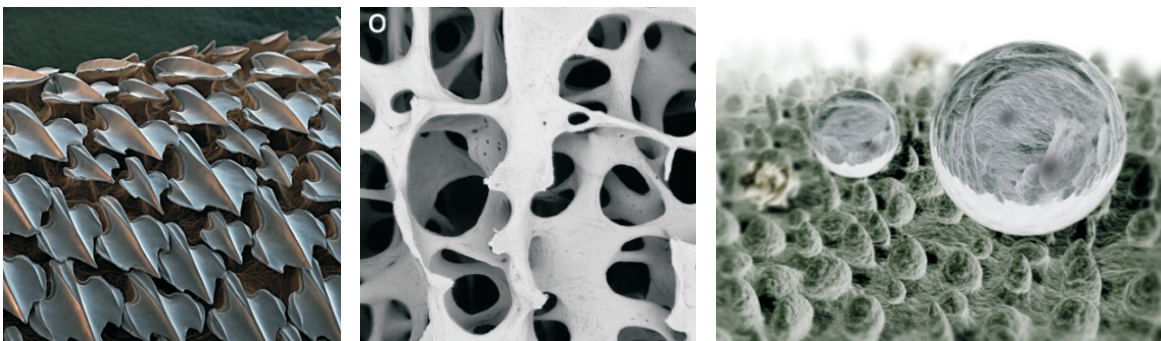


Figure 1.2: Natural structures and patterns: micrograph of a shark's skin, © eye of science; scanning electron micrograph of the inner structure of bone (Boyde, 2003); computer graphic of the surface of a lotus leaf with water drops, courtesy of William Thielicke. All images reprinted by permission.

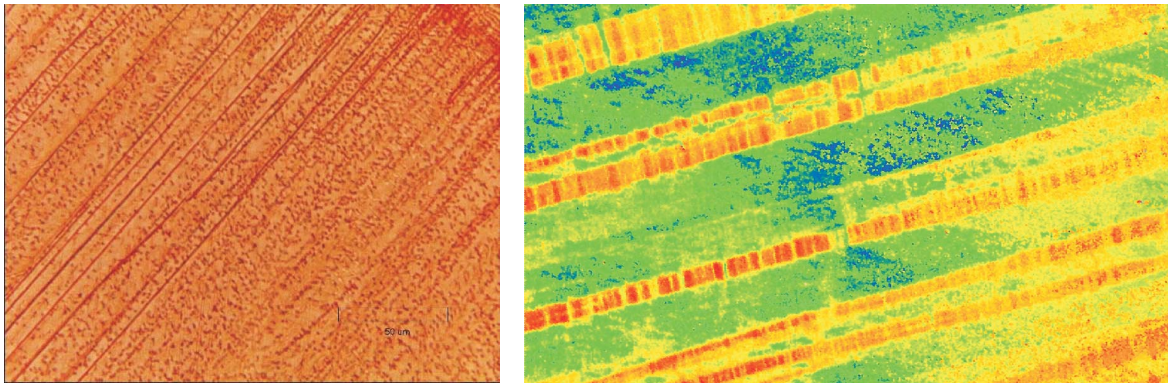


Figure 1.3: Transmitted-light micrograph of lattice dislocation structure in an olivine single crystal, courtesy of Read F. Cooper; EBSD map of a shear-deformed copper single crystal with several microbands of different relative crystallographic orientation (Dmitrieva et al., 2009). Images reprinted by permission.

typical length scales of a few micrometers. Similarly to those structures presented above, microstructures in solids play a crucial role in the design, manufacturing and application of engineering materials, as the microstructure of a material significantly affects its macroscopic mechanical properties.

The mechanical properties of solids have been characterized by a large number of material parameters which all depend – in some sense – on the material’s structure on smaller scales (Reed-Hill, 1973). The average grain size and the dislocation density of metals have a significant effect on the material’s strength, its hardness, and its fracture properties. Pre-existing textures give rise to anisotropy. Dislocation mobility (highly dependent on the crystalline structure and the presence of foreign atoms) affects the hardening rate, the yield stress, or the ductility of the material. All of these examples confirm the tight connection between the microstructure and a specific mechanical behavior. Therefore, it is of great importance to understand the origin and the subsequent evolution of microstructural characteristics in order not only to comprehend but even more to design materials according to engineering demands.

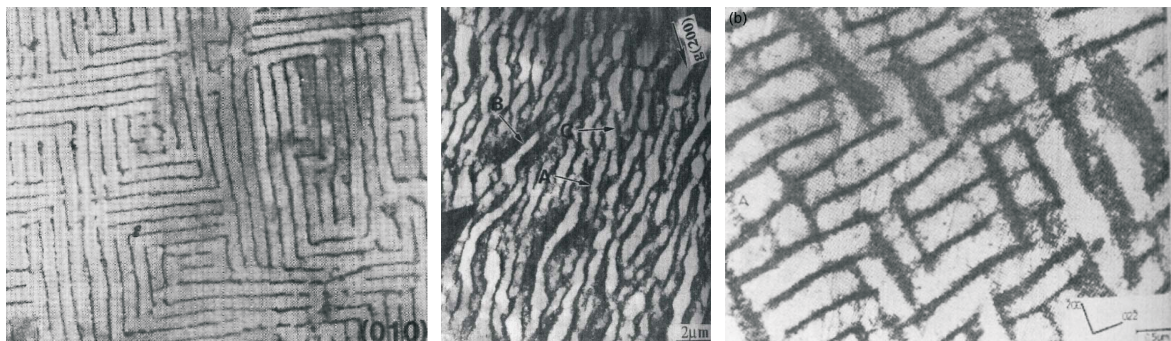


Figure 1.4: Labyrinth wall structures in a fatigued copper single crystal (Jin and Winter, 1984), wall structures in fatigued polycrystalline copper (Yumen, 1989) and a polycrystalline CuNi alloy (Charsley, 1981). All images reprinted by permission.

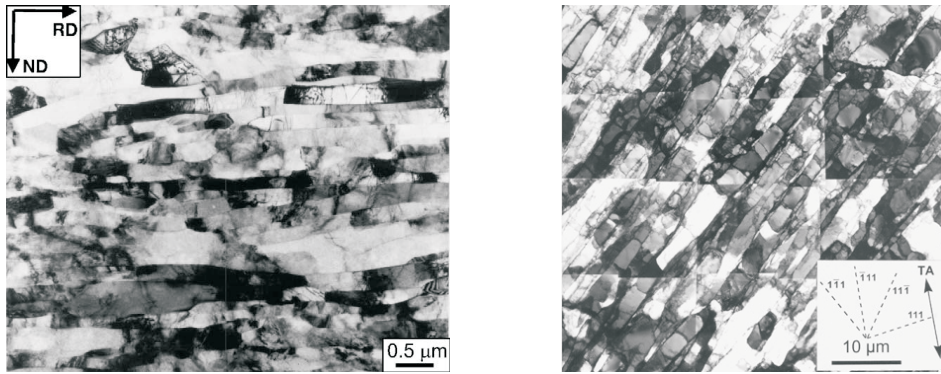


Figure 1.5: Transmission electron micrographs of polycrystalline pure aluminum: dislocation wall structures deformed in tension (Hansen et al., 2001) and after cold rolling (Liu et al., 2002). Images reprinted by permission.

Figures 1.3 to 1.6 give a brief (and of course very limited) overview of some of the frequently observed microstructures in metals. Common to all of these micrographs, the observed microstructure hardly ever appears to be completely random but rather arranges dislocations and other lattice defects to specific ordered segments or sub-structures or, at least, along preferred orientations. Figures 1.3 illustrate one of the geometrically simplest structures commonly observed in deformed solids (here, in olivine and copper). The material forms a lamellar structure with alternating micro-bands of differing states of deformation with dislocation concentrations at the separating walls. Figures 1.4 show dislocations arranging to cell structures of labyrinth- and other types in fatigued copper single crystals. Of course, the orientation of such dislocation walls is commonly not random but accommodates specific lattice directions as will be discussed.

Figures 1.5 illustrate another type of dislocation arrangement which can be observed during severe plastic deformation: dislocations accommodate wall structures within existing grains. Such dislocation walls form within grains of a polycrystal and thus constitute sub-structures and conglomerates of dislocation cells, which, upon further straining, can transform into smaller grains, resulting in collective grain refinement (Hansen et al., 2008). Small grains in the nanometer range are of particular interest for many engineering applications as they give rise to considerably higher strength.

Figures 1.6 show transmission electron micrographs (TEM) of dislocation microstructures in a high manganese steel. Graphics illustrate the arrangement of network dislocations in more or less regular arrays. Besides, this type of steel tends to form deformation twins (Christian and Mahajan, 1995). Deformation twins are lamellar structures with alternating parent and twin phases with different (but symmetric) crystal lattice orientations. The twin lattice is generated either by a rotation of the original crystal lattice or by reflection. Twin structures give rise to higher yield strength and hardening rates. Practical applications make use of this effect in so-called TWIP (*twinning-induced plasticity*) alloys.

As all of these microstructural characteristics show a direct impact on the macroscopic mechanical behavior, a fundamental understanding of the origin and evolution of such microstructures is of great importance. Therefore, any thorough plasticity theory aiming at describing those effects observed experimentally must account for the thermo-mechanical processes on the microscale. This thesis summarizes progress in research on three particular microstructural aspects: firstly, the formation of laminate microstructures as minimizers in

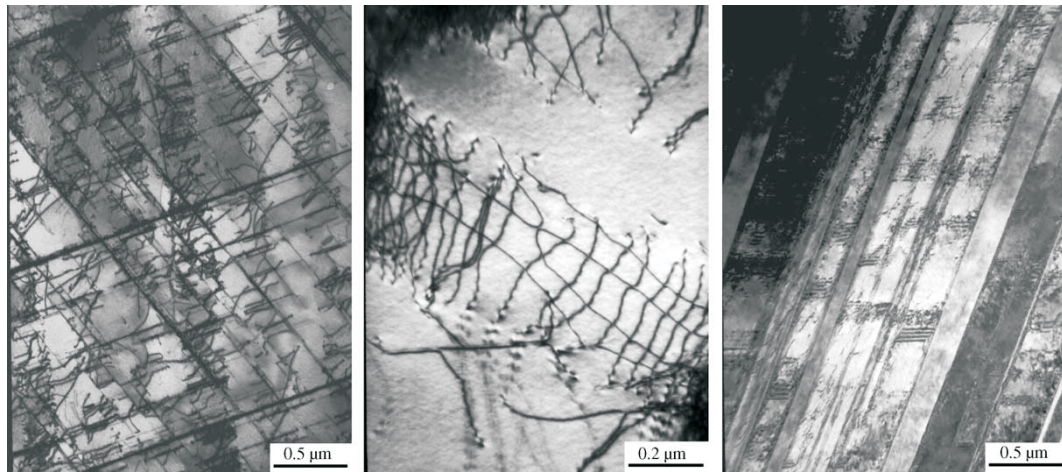


Figure 1.6: TEM records of 32Mn–7Cr–1Mo–0.3N steel after impact testing: network dislocations, planar dislocation array, interaction between dislocation slip band and stacking fault (Fu et al., 2005). Reprinted by permission.

finite elasto-plasticity; secondly, the arrangement and pile-up of dislocations in single and polycrystals and the resulting dislocation structures; and thirdly, the interaction of dislocation pile-ups and deformation twins in single crystals.

1.3 Modeling Plasticity and Microstructures: Motivation and State of the Art

There has been a long history of plasticity models to describe elasto-plastic material behavior and the related origin and evolution of microstructures in crystals. These models are as various as the length scales involved, from macroscopic continuum approaches to multiscale models to molecular dynamics simulations. Here, we stay within the framework of continuum plasticity and continuum dislocation theory and we present progress on the following fields of research.

1.3.1 Description of Microstructures Based on Energy Relaxation in Finite Elasto-Plasticity

Inelastic microstructures in finite elasto-plasticity can be described by non-convex variational problems. The non-existence of energy minimizers in these problems gives rise to small-scale fluctuations, i.e. fine-scale minimizing sequences, which may be interpreted as microstructures. The formation of such microstructures as a consequence of non-convex potentials was shown first for elastic crystals undergoing phase transformations, in particular the austenite-martensite transformation, see e.g. (Ball and James, 1987, 1992; Chu and James, 1995; Bhattacharya, 2003).

The boundary value problem in finite elasto-plasticity can be formulated as a variational

minimization problem, where the deformation field $\phi : \Omega \rightarrow \mathcal{R}^3$ results from

$$\phi = \arg \min \left\{ \mathcal{I}(\phi, \mathbf{K}) = \int_{\Omega} \Psi(\nabla \phi, \mathbf{K}) \, dv - \ell(\phi) \mid \phi = \phi_0 \text{ on } \partial\Omega \right\}, \quad (1.1)$$

where Ψ is the elastic energy storage function, \mathbf{K} is a set of internal variables capturing the microstructural characteristics within volume Ω , and $\ell(\phi)$ is a linear functional. In contrast to non-linear elasticity, the plasticity model requires an additional variational formulation for the evolution of the internal variables \mathbf{K} . The fundamental idea of a general incremental variational formulation goes back to Ortiz and Repetto (1999) and Ortiz et al. (2000) and was later enhanced by Carstensen et al. (2002), Miehe (2002), Miehe et al. (2002). For generalized standard media the variational formulation of inelasticity is thereby governed by the aforementioned energy storage function Ψ and a dissipation functional Δ . This type of material model is useful for a broad range of constitutive models in viscoelasticity and -plasticity, and it can be related to those of Biot (1965); Ziegler and Wehrli (1987); Germain (1973); Nguyen (2000). For this class of materials the minimum principle of the dissipation functional governs the evolution of the internal variables by

$$\dot{\mathbf{K}} = \arg \min \left\{ \frac{d}{dt} \Psi(\nabla \phi, \mathbf{K}) + \Delta(\mathbf{K}, \dot{\mathbf{K}}) \mid \dot{\mathbf{K}} \right\}, \quad (1.2)$$

which is evaluated locally and for discrete time steps. The variational problem given by (1.1) and (1.2) can be employed to determine inelastic microstructures and also analyze the stability of the incremental inelastic response, see e.g. Dacorogna (1989); Marsden and Hughes (1994); Šilhavý (1997); Gürses (2007). For rate-independent materials (1.2) can account for instantaneous change of the value of \mathbf{K} , since it can be integrated to finally yield a condensed energy

$$\Psi_{\mathbf{K}_n}^{\text{cond}}(\mathbf{F}) = \inf \left\{ \Psi(\mathbf{F}, \mathbf{K}) + D(\mathbf{K}_n, \mathbf{K}) \mid \mathbf{K} \right\}, \quad (1.3)$$

with a so-called dissipation distance D (Mielke, 2002).

The existence of solutions to the minimum principle in (1.1) requires the quasiconvexity (Morrey, 1952) of the energy storage function Ψ (Ball, 1977). In many problems of finite elasto-plasticity, however, Ψ is not quasiconvex such that the lack of solutions of the non-convex variational problem must be treated by the mathematical theory of relaxation (Dacorogna, 1989). The non-quasiconvex energy storage function is replaced by its quasiconvex envelope

$$\Psi_Q(\nabla \phi) = \inf \left\{ \frac{1}{|\omega|} \int_{\omega} \Psi(\mathbf{F} + \nabla \varphi) \, dv \mid \varphi : \varphi = \mathbf{0} \text{ on } \partial\omega \right\}, \quad (1.4)$$

such that the relaxed functional \mathcal{I}_Q (with Ψ replaced by Ψ_Q) is well-posed, and a minimizer exists. Unfortunately, the condition of quasiconvexity is non-local and so far no general approach for determining the quasiconvex hull has been found, except for some particular cases where it could be derived analytically, see e.g. (Kohn, 1991) or (DeSimone and Dolzmann, 2000). However, the quasiconvex hull can be approximated by upper and lower bounds given in terms of the rank-one-convex envelope and the polyconvex envelope, respectively, which can be utilized to develop numerical schemes for the computation of approximate hulls; examples can be found e.g. in (Dolzmann, 2003; Bartels et al., 2004). The rank-one-convex hull has been of particular interest since it describes laminate-type microstructures (Pedregal, 1993) which can be observed experimentally. Accordingly, one can

determine an approximation $R_1\Psi$ of the rank-one-convex hull $R\Psi$ for a first-order laminate microstructure:

$$R_1\Psi(\mathbf{F}) = \inf \left\{ \lambda_1\Psi(\mathbf{F}_1) + \lambda_2\Psi(\mathbf{F}_2) \mid \lambda_i, \mathbf{F}_i; \sum_{i=1}^n \lambda_i = 1, 0 \leq \lambda_i \leq 1, \right. \\ \left. \sum_{i=1}^n \lambda_i \mathbf{F}_i = \mathbf{F}, \text{rank}(\mathbf{F}_1 - \mathbf{F}_2) \leq 1 \right\}, \quad (1.5)$$

where λ_i are the volume fractions and \mathbf{F}_i the (rank-one-connected) deformation gradients (the so-called atoms) in the laminate phases.

During the last decade, relaxation theory has been applied to a number of problems in crystal plasticity, beginning with the seminal works by Ortiz and Repetto (1999) and Ortiz et al. (2000), who developed a relaxation algorithm based on a rank-one-convexification and sequential lamination for modeling dislocation microstructures in single crystals. Their approach was limited by certain assumptions concerning the form and type of the laminate microstructures considered. In particular, the evolution of the phase volume fractions was not determined. These and many of the following approaches made use of the condensed energy functional (1.3) to analyze the development of microstructures in multiplicative plasticity (Ortiz and Repetto, 1999; Lambrecht et al., 2003; Bartels et al., 2004; Mielke, 2004; Conti and Theil, 2005). This approach is well-suited for the determination of an originating microstructure; however, it is not suitable to describe the evolution of microstructures, as for each time step the internal variables already exhibit a microstructure at the beginning of the time increment as a result of a relaxation process in the preceding time-increment (Hackl and Kochmann, 2008). The present approach attacks this problem by taking into account not only the microstructure at the beginning of each time step but also the actual amount of dissipation required to incrementally alter all microstructural variables (i.e., plastic slips, volume fractions, hardening variables).

1.3.2 Continuum Dislocation Description of Dislocation Pile-Ups and Dislocation Substructures

From the micro-mechanical point of view, plastic deformation is accommodated by the nucleation and motion of dislocations, i.e. crystallographic defects or irregularities within the periodic crystal lattice. The arrangement of the dislocation network is predominantly dictated by the crystal's energy. Plastic flow breaks up into moving dislocations which in turn dissipate energy. Dislocation mechanisms on the microscale can hence be treated by the very same aforementioned thermodynamic principles involving the energy and the dissipation potential. Although well-suited for the description of plastic strains, classical plasticity theory, unfortunately, does not allow for a direct treatment of dislocations in the deformed crystal, and hence their influence cannot explicitly be accounted for in the constitutive equations.

Many continuum descriptions of elasticity or elasto-plasticity have been developed to account for the influence of microstructure on the mechanical material response, beginning with the early works by Cosserat and Cosserat (1909). Multi-polar and higher gradient elasticity theories were established among others by Truesdell and Toupin (1960), Green and Rivlin (1964) and Eringen (1972), followed by early strain gradient plasticity descriptions as by Fox (1968), Teodosiu (1969), Lardner (1969) or Dillon and Perzyna (1972). Although

the fundamentals of continuum dislocation theory were laid down around the same time by Kondo (1952), Nye (1953), Bilby et al. (1955a), Kröner (1958), and Berdichevsky and Sedov (1967), among others, the applicability of the theory became feasible only in recent years (Ortiz and Repetto, 1999; Ortiz et al., 2000; Groma et al., 2003; Berdichevsky, 2006b), thanks to the progress in statistical mechanics and thermodynamics of the dislocation network (Berdichevsky, 2005, 2006b). In addition, higher order strain gradient models have been developed to numerically capture the underlying size effects (Shu and Fleck, 1999; Evers et al., 2002), to characterize deformation bands (Aifantis, 1987) or to describe the nucleation of dislocations.

Various dislocation-based plasticity theories followed, see e.g. (Gao et al., 1999; Acharya and Bassani, 2001; Huang et al., 2000, 2004; Han et al., 2005a,b; Aifantis and Willis, 2005; Aifantis et al., 2006). Most dislocation-based plasticity theories make use of the concept of geometrically necessary dislocations (GNDs) based on Nye's tensorial description (1953). All strain gradient-based plasticity theories have as a common feature the incorporation of higher order strain gradients into the formulation of the free energy,

$$\Psi(\mathbf{F}_e, \boldsymbol{\alpha}) = \Psi_0(\mathbf{F}_e) + \Psi_\rho(\boldsymbol{\alpha}), \quad \boldsymbol{\alpha} = \text{curl } \mathbf{F}_p, \quad (1.6)$$

where $\boldsymbol{\alpha}$ denotes Nye's dislocation density tensor. Ψ_0 is the classical elastic energy storage function whereas Ψ_ρ captures the energy of the microstructure, often termed the defect energy. A crucial question to all theories is how to formulate the contribution of the microstructural dislocation network to the free energy in a physically-reasoned way rather than for reasons of mathematical regularization. Gurtin and co-workers (Gurtin, 2003; Gurtin and Anand, 2005; Gurtin et al., 2007) e.g. used second powers of strain gradients in their works. Other approaches have been developed, e.g. by Volokh and Trapper (2007), based on the idea that the effective plastic strain depends on the defect density. In this thesis we adopt the free energy formulation proposed by Berdichevsky (2006a,b), in which the energy of the microstructure involves a logarithmic dependency on the dislocation density:

$$\Psi_\rho(\rho) = k\mu \ln \frac{1}{1 - \rho/\rho_s}. \quad (1.7)$$

k is a material constant, ρ the scalar dislocation density, and ρ_s represents a saturation dislocation density. Superior to many higher order plasticity theories, this approach is physically suitable as the energy of the microstructure rises linearly at small dislocation densities (where the interaction energy is negligible (Hirth and Lothe, 1982)) but increases to infinity as the dislocation density reaches some saturation density (Berdichevsky, 2006b).

Now, one can combine the minimum principle (1.1) with a Biot-type evolution equation for the internal variables,

$$\frac{\delta \Psi}{\delta \mathbf{K}} + \frac{\partial \Delta}{\partial \dot{\mathbf{K}}} = 0, \quad (1.8)$$

to solve the boundary value problem. Berdichevsky and Le (2007) used this energy formulation to model the pile-up of dislocations in a single crystal. Le and Sembriring (2008a,b) generalized the previous study to single- and double-slip in thin, infinitely extended single crystal strips. Here, we investigate the plastic deformation of bicrystals first and then generalize the model to arbitrary two-dimensional boundary value problems. A variational formulation analogous to (1.2) has been reported for related problems, see e.g. (Dimitrijevic and Hackl, 2008), but has not been applied to dislocation-based plasticity. Based on this formulation, the arrangement of dislocations in confined volumes (e.g. within grains of a polycrystal, at boundaries of single crystals and bicrystals, or at twin boundaries) can be studied, giving rise to typical effects of crystal plasticity.

1.3.3 An Energy-Based Continuum Dislocation Approach to Deformation Twinning

Besides plastic slip by dislocations there is another important mode of plastic deformation in many crystalline solids, known as deformation twinning. Experimental evidence of deformation twins was found long time ago and described in terms of dislocations e.g. in the early works by Frenkel (1926), Cahn (1954), and Hall (1954). A newer comprehensive state-of-the-art survey of deformation twinning from a rather materials science perspective was presented by Christian and Mahajan (1995). A very recent experimental study of the competing mechanisms of slip and twin in Zr and Mg alloys was presented in a series of papers by Kaschner et al. (2006, 2007) and Proust et al. (2009). Twinning becomes particularly important in metals with only a limited number of slip systems, as it can operate to provide the five slip systems required to satisfy the criterion for a general slip deformation. Deformation twinning basically divides the originally uniform single crystal into two volumetric parts – a parent phase (with unaltered crystal lattice) and a twin phase (with a different, symmetric crystal lattice orientation). Both phases normally occur in the form of lamellar structures, where a bicrystal consisting of neighboring parent and twin phase is commonly referred to as a twin.

The formation of deformation twins has a significant impact on the macroscopic stress-strain response. The evolution of twins provides TWIP alloys with excellent hardening behavior (Allain et al., 2004), allowing for higher stresses and larger strains than in common f.c.c. or b.c.c. metals. As a special characteristic, the onset of twinning, i.e. the rapid nucleation of deformation twins, often gives rise to a load drop in the stress-strain behavior (Christian and Mahajan, 1995). The increase of strength and work hardening during microstructure refinement by twinning in manganese steels or other TWIP alloys remains until now not quite well understood. Perhaps the dislocation pile-up near the twin boundaries (raising the boundary energy) and the related size effects play an important role in this context. Several dislocation-based mechanisms have been proposed (Cohen and Weertman, 1963; Venables, 1964; Hirth and Lothe, 1982; Narita and Takamura, 1992) to explain twin nucleation in f.c.c. materials. Most of these models are based on phenomenological observations rather than physically reasoned on the microscale. The influence of temperature, strain-rate or microstructural characteristics such as grain size or stacking fault energy on the onset of twinning were investigated e.g. by Meyers et al. (1995).

Based on the continuum dislocation approach outlined in Section 1.3.2, it is possible to describe the dislocation activity related to deformation twinning by introducing a so-called twinning shear produced by the existing dislocations in the already active slip system, which plays a similar role as Bain's strain in the theory of martensitic phase transformations, see e.g. (Bhattacharya, 2003). This twinning shear followed by a rotation enables the initially homogeneous crystal to form the twin phase from the parent phase. The underlying mechanism of twin formation is closely related to that of Bullough (1957), who employed a decomposition of the deformation into shear and rotation. The introduction of the twinning shear into the energy of the twin renders the energy multi-welled and non-convex, which gives rise to the formation of microstructures.

1.4 Scope of this Thesis

Following this introduction, **Chapter 2** gives a broad overview of the mathematical and mechanical fundamentals which lay the basis of the micro-mechanical models in this thesis. First, a mathematical introduction summarizes basic vector and tensor calculus and analysis, followed by a survey of the notions of convexity. An introduction to continuum mechanics at finite strains for elasticity and elasto-plasticity follows. A major part of the second half of the Chapter deals with properties and mechanisms of dislocations as a motivation for the subsequent introduction to continuum dislocation theory. Finally, Chapter 2 is completed by a summary of the underlying thermodynamic principles and the energetic reasons for the formation of microstructures.

Chapter 3 begins with a brief outline of the variational framework in finite elasto-plasticity for those inelastic materials treated here. We then derive a partially relaxed energy functional for single and multi-slip plasticity in single crystals. Furthermore, we introduce an incremental setting by which the time-continuous evolution of laminate microstructures can be modeled by solving the stationarity conditions rather than minimizing a condensed energy functional. Our results comprise several examples for microstructure evolution in single and double-slip plasticity, both for monotonic and for cyclic loading.

In **Chapter 4** we outline a plasticity model based on a continuum dislocation theory at small strains. We apply the aforementioned energetic approach to derive closed-form analytical solutions for the nucleation and pile-up of dislocations in single-slip bicrystals with symmetric slip systems and outline a numerical procedure for arbitrary slip system orientation. Our results comprise an energetic threshold for the dislocation nucleation, the typical effects of work hardening and hysteresis, the Bauschinger effect and, especially, size effects typical of crystal plasticity. Then follows a variational approach to determine equilibrium dislocation substructures within grains and in polycrystals, for which we show various computational examples.

The continuum dislocation approach outlined in Chapter 4 can then, in **Chapter 5**, be applied to the problem of deformation twinning. We derive energetic thresholds both for the onset of plastic flow and for deformation twinning in a single-slip single crystal and compute the evolution of volume fractions, plastic slips and the spatial distribution of dislocations in partially analytical form for a plane-constrained shear problem. Our results comprise the stress-strain hysteresis as well as the evolution of all internal variables involved.

Chapter 6 finally discusses and summarizes the results presented in the preceding Chapters and hints at possible future generalization and applications of the presented models.

2 Mathematical and Mechanical Fundamentals

2.1 Vector and Tensor Analysis

2.1.1 Vector Calculus

Before introducing the fundamental concepts of continuum mechanics, let us review basic notation conventions and mathematical operations on vector and tensor quantities, as given e.g. by Flügge (1972) and Betten (1987). The following summary is, of course, far away from being complete but sufficient to lay the basis for subsequent Sections.

In order to describe mechanical and physical phenomena in space, it is necessary to define a frame of reference. The physical space \mathcal{R}^3 has three dimensions ($d = 3$), and it hence takes three coordinates to locate a point in space. The orthonormal basis (also known as the Cartesian or rectangular coordinate basis) in the three-dimensional Euclidean vector space, which we assume to be time-invariant, be denoted by

$$\mathcal{B} = \{\mathbf{e}_1, \mathbf{e}_2, \mathbf{e}_3\} \quad (2.1)$$

such that each vector with components u_i ($i = 1 \dots 3$) in the Euclidean vector space can be expressed in its basic representation

$$\mathbf{u} = \sum_{i=1}^3 u_i \mathbf{e}_i \quad (2.2)$$

or, using Einstein's summation convention,

$$\mathbf{u} = u_i \mathbf{e}_i \quad (2.3)$$

where summation over repeated indices is implied. We denote vector and tensor quantities by bold symbols, vectors being assigned lower case and tensors upper case characters; scalar quantities are assigned lower case symbols. In the following, let us introduce the basic vector operations needed for subsequent analyses. According to the requirements of later Sections, we limit our review here to vector and tensor analysis in Cartesian coordinates only.

The scalar product of two vectors, also termed the inner product, be defined by

$$\mathbf{u} \cdot \mathbf{v} = \mathbf{u}^T \mathbf{v} = u_i v_j \mathbf{e}_i \cdot \mathbf{e}_j = u_i v_j \delta_{ij} = u_i v_i, \quad (2.4)$$

with the Kronecker delta

$$\delta_{ij} = \mathbf{e}_i \cdot \mathbf{e}_j = \begin{cases} 1, & \text{if } i = j, \\ 0, & \text{if } i \neq j. \end{cases} \quad (2.5)$$

The length of a vector (i.e. the norm of a vector) in the Euclidean space be defined by

$$\|\mathbf{u}\| = \sqrt{\mathbf{u} \cdot \mathbf{u}} = \sqrt{u_i u_i}. \quad (2.6)$$

A unit vector \mathbf{e} is characterized by unit length, i.e. $\|\mathbf{e}\| = \mathbf{e} \cdot \mathbf{e} = 1$. Denoting the angle between vectors \mathbf{u} and \mathbf{v} as φ , a geometric interpretation of the scalar product becomes apparent from

$$\mathbf{u} \cdot \mathbf{v} = \cos \varphi \|\mathbf{u}\| \|\mathbf{v}\|. \quad (2.7)$$

As a consequence, the scalar product of orthogonal vectors vanishes:

$$\mathbf{u} \perp \mathbf{v} \Leftrightarrow \mathbf{u} \cdot \mathbf{v} = 0. \quad (2.8)$$

Let us introduce the cross product of two vectors,

$$\mathbf{u} \times \mathbf{v} = u_i v_j \mathbf{e}_i \times \mathbf{e}_j = u_i v_j \epsilon_{ijk} \mathbf{e}_k, \quad (2.9)$$

with the permutation symbol ϵ_{ijk} defined by

$$\epsilon_{ijk} = \begin{cases} 1, & \text{if } i, j, k \text{ is a cyclic sequence,} \\ -1, & \text{if } i, j, k \text{ is an anticyclic sequence,} \\ 0, & \text{if } i, j, k \text{ is an acyclic sequence.} \end{cases} \quad (2.10)$$

The absolute value of the cross product $\|\mathbf{u} \times \mathbf{v}\|$ can be interpreted geometrically as the area of the parallelogram spanned by \mathbf{u} and \mathbf{v} . The absolute value of the triple product $\|\mathbf{u} \cdot (\mathbf{v} \times \mathbf{w})\|$ equals the volume of the parallelepiped spanned by \mathbf{u} , \mathbf{v} and \mathbf{w} .

Following the above definitions, the following useful identities hold true (m and n denote scalar quantities, \mathbf{u} , \mathbf{v} and \mathbf{w} are vectors):

$$\begin{aligned} \mathbf{u} + \mathbf{v} &= \mathbf{v} + \mathbf{u} && \text{(commutative law for addition)} \\ \mathbf{u} + (\mathbf{v} + \mathbf{w}) &= (\mathbf{u} + \mathbf{v}) + \mathbf{w} && \text{(associative law for addition)} \\ m(n\mathbf{u}) &= (mn)\mathbf{u} && \text{(associative law for multiplication)} \\ (m+n)\mathbf{u} &= m\mathbf{u} + n\mathbf{u} && \text{(distributive law)} \\ m(\mathbf{u} + \mathbf{v}) &= m\mathbf{u} + m\mathbf{v} && \text{(distributive law)} \end{aligned}$$

$$\begin{aligned} \mathbf{u} \cdot \mathbf{v} &= \mathbf{v} \cdot \mathbf{u} && \text{(commutative law for scalar multiplication)} \\ (\mathbf{u} + \mathbf{v}) \cdot \mathbf{w} &= \mathbf{u} \cdot \mathbf{w} + \mathbf{v} \cdot \mathbf{w} && \text{(distributive law for scalar multiplication)} \\ m(\mathbf{u} \cdot \mathbf{v}) &= (m\mathbf{u}) \cdot \mathbf{v} = \mathbf{u} \cdot (m\mathbf{v}) && \text{(associative law for scalar multiplication)} \end{aligned}$$

$$\begin{aligned} \mathbf{u} \times \mathbf{v} &= -\mathbf{v} \times \mathbf{u} && \text{(cross product not commutative)} \\ (\mathbf{u} + \mathbf{v}) \times \mathbf{w} &= \mathbf{u} \times \mathbf{w} + \mathbf{v} \times \mathbf{w} && \text{(distributive law for cross product)} \\ m(\mathbf{u} \times \mathbf{v}) &= (m\mathbf{u}) \times \mathbf{v} = \mathbf{u} \times (m\mathbf{v}) && \text{(associative law for cross product)} \end{aligned}$$

2.1.2 Tensor Calculus

A tensor quantity \mathbf{T} of second-order (commonly referred to as tensor) may result from the outer product (often termed the tensor product or dyadic product) of two vectors \mathbf{u} and \mathbf{v} , which is defined by

$$\mathbf{T} = \mathbf{u} \otimes \mathbf{v} = u_i v_j \mathbf{e}_i \otimes \mathbf{e}_j = T_{ij} \mathbf{e}_i \otimes \mathbf{e}_j, \quad T_{ij} = u_i v_j \quad (2.11)$$

with the special characteristic

$$(\mathbf{u} \otimes \mathbf{v}) \cdot \mathbf{w} = \mathbf{u} \otimes (\mathbf{v} \cdot \mathbf{w}). \quad (2.12)$$

Note that in the \otimes -sign is generally not omitted to ensure differentiation from the inner product. The components of a dyad \mathbf{T} in the three-dimensional Cartesian coordinate space can for conciseness be arranged in a square matrix

$$(T_{ij}) = \begin{pmatrix} T_{11} & T_{12} & T_{13} \\ T_{21} & T_{22} & T_{23} \\ T_{31} & T_{32} & T_{33} \end{pmatrix}. \quad (2.13)$$

Having introduced the concept of dyads and tensors, we can extend the definition of the dot product by the linear mapping between tensors and vectors, i.e.

$$\mathbf{T} \cdot \mathbf{u} = u_j T_{ij} \mathbf{e}_i. \quad (2.14)$$

where the following relations apply:

$$\mathbf{T} \cdot (\mathbf{u} + \mathbf{v}) = \mathbf{T} \cdot \mathbf{u} + \mathbf{T} \cdot \mathbf{v} \quad (\text{distributive law})$$

$$\mathbf{T} \cdot (m \mathbf{u}) = m (\mathbf{T} \cdot \mathbf{u}) \quad (\text{associative law})$$

$$(m \mathbf{T}) \cdot \mathbf{u} = m (\mathbf{T} \cdot \mathbf{u}) \quad (\text{associative law})$$

$$\mathbf{0} \cdot \mathbf{u} = \mathbf{0} \quad (\text{zero element of linear mapping})$$

The scalar product of two tensors of second order yields

$$\mathbf{S} \cdot \mathbf{T} = S_{ij} T_{jk} \mathbf{e}_i \otimes \mathbf{e}_k. \quad (2.15)$$

Furthermore, we mention the following helpful laws:

$$(\mathbf{T} \cdot \mathbf{S}) \cdot \mathbf{u} = \mathbf{T} \cdot (\mathbf{S} \cdot \mathbf{u}) \quad (\text{associative law})$$

$$(\mathbf{S} + \mathbf{T}) \cdot \mathbf{u} = \mathbf{S} \cdot \mathbf{u} + \mathbf{T} \cdot \mathbf{u} \quad (\text{distributive law})$$

Note that by an integer power of a tensor we simply denote

$$\mathbf{T}^n = \mathbf{T} \cdot \mathbf{T} \cdot \mathbf{T} \cdot \dots \cdot \mathbf{T} \quad (n \text{ factors}). \quad (2.16)$$

Sums and products of tensors also obey the common algebraic manipulation rules such as associative or distributive laws, except that the scalar product of two tensors, in general, is not commutative.

$$\mathbf{T} + \mathbf{S} = \mathbf{S} + \mathbf{T} \quad (\text{commutative law}),$$

$$\mathbf{T} \cdot (\mathbf{S} + \mathbf{V}) = \mathbf{T} \cdot \mathbf{S} + \mathbf{T} \cdot \mathbf{V} \quad (\text{distributive law})$$

$$\mathbf{T} \cdot (\mathbf{S} \cdot \mathbf{V}) = (\mathbf{T} \cdot \mathbf{S}) \cdot \mathbf{V} \quad (\text{associative law})$$

$$\mathbf{T} \cdot \mathbf{S} \neq \mathbf{S} \cdot \mathbf{T}$$

A specific component T_{ij} of a tensor \mathbf{T} in the Cartesian coordinate space can be obtained from

$$T_{ij} = \mathbf{e}_i \cdot \mathbf{T} \cdot \mathbf{e}_j. \quad (2.17)$$

Since the dot product of a dyad with a vector is not in general commutative it makes sense to introduce the transpose \mathbf{T}^T of a tensor such that

$$\mathbf{T}^T \cdot \mathbf{u} = \mathbf{u} \cdot \mathbf{T} \quad (2.18)$$

and thus the transpose of a dyad follows as

$$(\mathbf{u} \otimes \mathbf{v})^T = \mathbf{v} \otimes \mathbf{u}. \quad (2.19)$$

The transpose of tensor quantities obeys the following rules:

$$(\mathbf{T} + \mathbf{S})^T = \mathbf{T}^T + \mathbf{S}^T \quad (\text{transpose of a sum})$$

$$(\mathbf{T} \cdot \mathbf{S})^T = \mathbf{S}^T \cdot \mathbf{T}^T \quad (\text{transpose of a product})$$

$$(\mathbf{T}^T)^T = \mathbf{T} \quad (\text{double transpose})$$

We call a tensor symmetric if $\mathbf{T}^T = \mathbf{T}$, and antisymmetric if $\mathbf{T}^T = -\mathbf{T}$.

Analogously to the length of a vector, we define the norm of a tensor quantity \mathbf{T} (the Hilbert-Schmidt norm) by

$$\|\mathbf{T}\| = \sqrt{T_{ij}T_{ij}}. \quad (2.20)$$

A special symmetric tensor is the identity tensor, i.e. the identity element of linear mapping defined by

$$\mathbf{I} = \delta_{ij} \mathbf{e}_i \otimes \mathbf{e}_j, \quad \mathbf{I} \cdot \mathbf{u} = \mathbf{u}, \quad (2.21)$$

with the special properties $\mathbf{T} \cdot \mathbf{I} = \mathbf{I} \cdot \mathbf{T} = \mathbf{T}$, $\mathbf{I} = \mathbf{I}^T = \mathbf{I}^{-1}$ and $\mathbf{T}^0 = \mathbf{I}$.

Beside the scalar product of tensors, we introduce the double contraction operator

$$(\mathbf{u} \otimes \mathbf{v}) : (\mathbf{w} \otimes \mathbf{x}) = (\mathbf{u} \cdot \mathbf{w})(\mathbf{v} \cdot \mathbf{x}), \quad (2.22)$$

$$\mathbf{T} : \mathbf{S} = T_{ij}S_{ij}. \quad (2.23)$$

For inverting the linear mapping as well as when solving sets of linear equations, it is essential to introduce the inverse \mathbf{T}^{-1} of a tensor \mathbf{T} , which is defined via

$$\mathbf{T} \cdot \mathbf{T}^{-1} = \mathbf{I}. \quad (2.24)$$

Note that for conciseness we write $\mathbf{T}^{-T} = (\mathbf{T}^T)^{-1} = (\mathbf{T}^{-1})^T$. For inverse tensors, the following identities hold:

$$(\mathbf{T}\mathbf{S})^{-1} = \mathbf{S}^{-1}\mathbf{T}^{-1} \quad (\text{inverse of the scalar product})$$

$$(\mathbf{u} \otimes \mathbf{v})^{-1} = -\mathbf{u} \otimes \mathbf{v} \quad (\text{inverse of the dyadic product})$$

Unfortunately, there does not exist a comparably simple identity for the inverse of a sum of tensors.

In addition, let us introduce the cofactor of a tensor \mathbf{T} (and its transpose, the adjoint), which is defined (if \mathbf{T}^{-1} exists) by

$$\text{cof } \mathbf{T} = \mathbf{T}^{-T} \det \mathbf{T}, \quad (\text{cof } \mathbf{T})^T = \text{adj } \mathbf{T}. \quad (2.25)$$

The cofactor matrix is obtained by replacing each entry with the determinant of the corresponding matrix minor.

Following the above theorems, we can now define two important scalar characteristics of second-order tensor quantities, the first being the determinant of a tensor $\mathbf{T} = T_{ij}\mathbf{e}_i \otimes \mathbf{e}_j$,

$$\det \mathbf{T} = \epsilon_{ijk} T_{1i} T_{2j} T_{3k}. \quad (2.26)$$

When dealing with determinants, the following relations may be useful:

$$\det (\mathbf{T} \cdot \mathbf{S}) = \det \mathbf{T} \cdot \det \mathbf{S}, \quad (2.27)$$

$$\det \mathbf{T}^T = \det \mathbf{T}, \quad (2.28)$$

$$\det \mathbf{T}^{-1} = (\det \mathbf{T})^{-1} \quad (2.29)$$

$$\det (\mathbf{u} \otimes \mathbf{v}) = 0 \quad (2.30)$$

$$\det (\mathbf{I} + \mathbf{u} \otimes \mathbf{v}) = 1 + \mathbf{u} \cdot \mathbf{v}. \quad (2.31)$$

Beside the determinant, another important scalar property of a tensor is its trace, which is defined by

$$\text{tr} \mathbf{T} = \mathbf{T} : \mathbf{I} = T_{ii}, \quad (2.32)$$

i.e. the sum of all diagonal elements; in particular, $\text{tr} \mathbf{I} = 3$. Here, we mention the following useful identities:

$$\text{tr} (\mathbf{u} \otimes \mathbf{v}) = \mathbf{u} \cdot \mathbf{v}, \quad (2.33)$$

$$\text{tr} \mathbf{T} = \text{tr} \mathbf{T}^T. \quad (2.34)$$

All tensors introduced so far were of zero order (scalars), first order (vectors) or second order (commonly referred to as tensors in the preceding). In general, one can define tensors of arbitrary order by combining tensor quantities via the dyadic product. The elasticity tensor \mathcal{C} e.g. is a tensor of fourth order and it is defined by

$$\mathcal{C} = C_{ijkl} \mathbf{e}_i \otimes \mathbf{e}_j \otimes \mathbf{e}_k \otimes \mathbf{e}_l. \quad (2.35)$$

2.1.3 Basic Vector and Tensor Transformations

Although we limit our review of the basic vector and tensor relations in this Section to Cartesian coordinate systems for conciseness, we briefly review some of the basic vector and tensor transformation rules as needed for subsequent Sections. The necessity to transform vectors and tensors arises from situations where more than one Cartesian coordinate system is used, since all vector or tensor quantities may be transformed from one coordinate system to another. Having defined two independent Cartesian coordinate systems with unit vectors \mathbf{e}_i and \mathbf{e}'_i ($i = 1, 2, 3$), respectively, we can represent a position vector \mathbf{u} with respect to both coordinate systems by its components in each coordinate system, namely

$$\mathbf{u} = u_i \mathbf{e}_i = u'_i \mathbf{e}'_i. \quad (2.36)$$

A coordinate transformation is available in the form

$$\mathbf{u}' = \mathbf{Q} \cdot \mathbf{u} \quad (2.37)$$

where the transformation matrix \mathbf{Q} is defined by

$$\mathbf{Q} = \mathbf{e}' \otimes \mathbf{e} \quad (2.38)$$

with the special properties $\mathbf{Q} \cdot \mathbf{Q}^T = \mathbf{I}$, $\mathbf{Q}^{-1} = \mathbf{Q}^T$ and $\det \mathbf{Q} = 1$. \mathbf{Q} is often termed a rotation matrix as it maps the original coordinate system in space by a rotation onto the new coordinate system. Analogously, we can transform a tensor \mathbf{T} in the aforementioned manner between independent coordinate systems, where the coordinate transformation rule for second-order tensors now reads

$$\mathbf{T}' = \mathbf{Q} \cdot \mathbf{T} \cdot \mathbf{Q}^T \quad (2.39)$$

with \mathbf{Q} from (2.38), obeying the same relations as above. For any second-order tensor \mathbf{T} , there exist three specific transformation dyads \mathbf{Q} such that \mathbf{T}' is diagonal (these three choices of \mathbf{Q} are not independent but represent different permutations of the three column vectors). These diagonal entries are the so-called eigenvalues of a matrix \mathbf{T} . (Note that changing the ordering of the column vectors in \mathbf{Q} simply changes the order of the eigenvalues on the diagonal of \mathbf{T} but not their values.) The eigenvalues of a matrix can also be interpreted as follows: If we understand a second-order tensor \mathbf{T} as a linear mapping of a vector \mathbf{x} by

$$f(\mathbf{x}) = \mathbf{T} \cdot \mathbf{x}, \quad (2.40)$$

then there will be special vectors \mathbf{x}_i that fulfill the relation

$$\mathbf{T} \cdot \mathbf{x}_i = \lambda_i \mathbf{x}_i. \quad (2.41)$$

These vectors \mathbf{x}_i are termed the eigenvectors of \mathbf{T} , and λ_i are the corresponding eigenvalues. λ_i and \mathbf{x}_i are independent of the choice of the Cartesian coordinate system. Re-arranging (2.41), we arrive at the sufficient condition (the characteristic equation) to determine the eigenvalues λ_i of a tensor \mathbf{T} ,

$$\det(\mathbf{T} - \lambda_i \mathbf{I}) = 0. \quad (2.42)$$

Expansion of the determinant in (2.42) yields

$$\det(\mathbf{T} - \lambda_i \mathbf{I}) = -\lambda_i^3 + J_1 \lambda_i^2 - J_2 \lambda_i + J_3, \quad (2.43)$$

with

$$\begin{aligned} J_1 &= \lambda_1 + \lambda_2 + \lambda_3, \\ J_2 &= \lambda_1 \lambda_2 + \lambda_2 \lambda_3 + \lambda_1 \lambda_3, \\ J_3 &= \lambda_1 \lambda_2 \lambda_3. \end{aligned}$$

As the determinant is invariant with respect to coordinate transformations so are the so-called tensor invariants J_1 , J_2 and J_3 . To come back to our original introduction of the eigenvalues of a tensor, note that, having determined all three eigenvalues λ_i and the corresponding three eigenvectors \mathbf{x}_i of a second-order tensor \mathbf{T} , we can write \mathbf{T} in its diagonal form

$$\mathbf{T} = \begin{bmatrix} \lambda_1 & 0 & 0 \\ 0 & \lambda_2 & 0 \\ 0 & 0 & \lambda_3 \end{bmatrix}, \quad (2.44)$$

and the rotation matrix \mathbf{Q} to obtain this diagonal form (i.e., the basis of \mathbf{T}) is given by the normalized eigenvectors $\bar{\mathbf{x}}_i = \mathbf{x}_i / \|\mathbf{x}_i\|$ as

$$\mathbf{Q} = (\bar{\mathbf{x}}_1, \bar{\mathbf{x}}_2, \bar{\mathbf{x}}_3), \quad (2.45)$$

i.e. the normalized eigenvectors form the basis of the coordinate system in which \mathbf{T} has the form (2.44).

With this definition of eigenvalues and -vectors, we can introduce special tensor operations commonly needed in the context of continuum mechanics. Let us first introduce the square root of a second-order tensor $\sqrt{\mathbf{T}}$ by

$$\sqrt{\mathbf{T}} = \begin{bmatrix} \sqrt{\lambda_1} & 0 & 0 \\ 0 & \sqrt{\lambda_2} & 0 \\ 0 & 0 & \sqrt{\lambda_3} \end{bmatrix}, \quad (2.46)$$

where λ_i are the eigenvalues of \mathbf{T} and the rectangular bracket denotes a tensor with respect to its eigenbasis \mathbf{Q} . Analogously, one can also define other tensor operations such as e.g. the logarithm:

$$\ln \mathbf{T} = \begin{bmatrix} \ln \lambda_1 & 0 & 0 \\ 0 & \ln \lambda_2 & 0 \\ 0 & 0 & \ln \lambda_3 \end{bmatrix}. \quad (2.47)$$

Finally, let us mention for completeness specific tensor properties which can directly be related to the concept of eigenvalues and -vectors. A second-order tensor \mathbf{T} is called positive-definite, if

$$\mathbf{x} \cdot \mathbf{T} \cdot \mathbf{x} > 0 \quad \forall \mathbf{x} \in \mathcal{R}^3, \mathbf{x} \neq 0. \quad (2.48)$$

For a positive-definite tensor \mathbf{T} all eigenvalues λ_i are real and positive. Analogously, we can define a positive-semi-definite tensor \mathbf{T} which satisfies $\mathbf{x} \cdot \mathbf{T} \cdot \mathbf{x} \geq 0 \quad \forall \mathbf{x} \in \mathcal{R}^3, \mathbf{x} \neq 0$ (all eigenvalues of \mathbf{T} are real and non-negative), a negative-definite tensor by $\mathbf{x} \cdot \mathbf{T} \cdot \mathbf{x} < 0 \quad \forall \mathbf{x} \in \mathcal{R}^3, \mathbf{x} \neq 0$ (all eigenvalues of \mathbf{T} are negative), and a negative-semi-definite tensor by $\mathbf{x} \cdot \mathbf{T} \cdot \mathbf{x} \leq 0 \quad \forall \mathbf{x} \in \mathcal{R}^3, \mathbf{x} \neq 0$ (all eigenvalues of \mathbf{T} are real and non-positive). A fourth-order tensor \mathbf{T} is called elliptic if

$$(\mathbf{u} \otimes \mathbf{v}) : \mathbf{T} : (\mathbf{u} \otimes \mathbf{v}) \geq 0 \quad \forall \mathbf{u}, \mathbf{v} \in \mathcal{R}^3, \mathbf{u}, \mathbf{v} \neq 0, \quad (2.49)$$

and strongly elliptic if the inequality is fulfilled strongly.

2.1.4 Vector and Tensor Analysis

In continuous systems, the physical variables are distributed through space. A function of space is commonly known as a field. If to each position \mathbf{x} of a region $\Omega \in \mathcal{R}^3$ in space there corresponds a scalar $\phi(\mathbf{x})$, then $\phi : \Omega \rightarrow \mathcal{R}$ is called a scalar function. If to each position \mathbf{x} of a region $\Omega \in \mathcal{R}^3$ in space there corresponds a vector $\mathbf{u}(\mathbf{x})$ then $\mathbf{u} : \Omega \rightarrow \mathcal{R}^3$ is called a vector function. Analogously, we may define a tensor function $\mathbf{T}(\mathbf{x})$ with $\mathbf{T} : \Omega \rightarrow \mathcal{R}^3 \times \mathcal{R}^3$. Let us extend the common definition of partial derivatives to vector derivatives in the Cartesian coordinate space by

$$\frac{\partial}{\partial x_i} \mathbf{u}(\mathbf{x}) = \lim_{\Delta x_i \rightarrow 0} \frac{\mathbf{u}(\mathbf{x} + \Delta x_i \mathbf{e}_i) - \mathbf{u}(\mathbf{x})}{\Delta x_i} \quad (2.50)$$

and introduce the abbreviation

$$\mathbf{u}_{,i} = \partial_i \mathbf{u} = \frac{\partial \mathbf{u}}{\partial x_i}. \quad (2.51)$$

The vector differential operator ∇ be defined by

$$\nabla \circ \mathcal{F} = \partial_i \mathcal{F} \circ \mathbf{e}_i, \quad (2.52)$$

so that the gradient of a scalar field $\phi(\mathbf{x})$ and of a vector field $\mathbf{u}(\mathbf{x})$ can be written as

$$\text{grad } \phi(\mathbf{x}) = \nabla \phi(\mathbf{x}) = \frac{\partial \phi(\mathbf{x})}{\partial x_i} \mathbf{e}_i, \quad (2.53)$$

$$\text{grad } \mathbf{u}(\mathbf{x}) = \nabla \mathbf{u}(\mathbf{x}) = \frac{\partial u_i(\mathbf{x})}{\partial x_j} \mathbf{e}_i \otimes \mathbf{e}_j. \quad (2.54)$$

In a similar manner, the divergence of a vector field $\mathbf{u}(\mathbf{x})$ and of a tensor field $\mathbf{T}(\mathbf{x})$ be defined by

$$\text{div } \mathbf{u}(\mathbf{x}) = \frac{\partial u_i(\mathbf{x})}{\partial x_i} = u_{i,i}(\mathbf{x}), \quad (2.55)$$

$$\text{div } \mathbf{T}(\mathbf{x}) = \frac{\partial T_{ij}(\mathbf{x})}{\partial x_j} \mathbf{e}_i = T_{ij,j}(\mathbf{x}) \mathbf{e}_i. \quad (2.56)$$

Note that by $\nabla \mathbf{u}$ we mean $\nabla \mathbf{u} = \nabla \otimes \mathbf{u}$. We complete the above definitions by introducing the curl of a vector field \mathbf{u} as

$$\text{curl } \mathbf{u}(\mathbf{x}) = \epsilon_{ijk} u_{k,j}(\mathbf{x}) \mathbf{e}_i. \quad (2.57)$$

Note the following useful identities (where \mathbf{u} is a vector field and ϕ is a scalar field)

$$\text{grad } (\phi \mathbf{u}) = \mathbf{u} \otimes \text{grad } \phi + \phi \text{grad } \mathbf{u} \quad (2.58)$$

$$\text{div } (\text{grad } \mathbf{u})^T = \text{grad } (\text{div } \mathbf{u}) \quad (2.59)$$

$$\text{curl } (\text{curl } \mathbf{u}) = \text{grad } (\text{div } \mathbf{u}) - \text{grad } (\text{grad } \mathbf{u}) \mathbf{I} \quad (2.60)$$

$$\text{div } (\text{curl } \mathbf{u}) = 0 \quad (2.61)$$

$$\text{curl } (\text{grad } \phi) = 0 \quad (2.62)$$

$$\text{curl } (\text{grad } \mathbf{u}) = 0 \quad (2.63)$$

$$\text{div } (\phi \mathbf{u}) = \mathbf{u} \text{grad } \phi + \phi \text{grad } \mathbf{u}. \quad (2.64)$$

Furthermore, let us introduce the Laplace operator,

$$\Delta = \nabla \cdot \nabla = \sum_{i=1}^3 \frac{\partial^2}{\partial x_i^2} \mathbf{e}_i \quad (2.65)$$

with

$$\Delta \phi = \text{div } (\text{grad } \phi), \quad (2.66)$$

$$\Delta \mathbf{u} = \text{grad } (\text{div } \mathbf{u}) - \text{curl } (\text{curl } \mathbf{u}) = \text{grad } (\text{grad } \mathbf{u}) \mathbf{I}. \quad (2.67)$$

For the treatment of mechanical problems in the three-dimensional Euclidean space, we will evaluate volume and surface integrals, using the abbreviation for the integral over a volume Ω as

$$\int_{\Omega} \phi \, dv = \int \int \int \phi(\mathbf{x}) \, dx_1 \, dx_2 \, dx_3, \quad (2.68)$$

where the order of integration in the latter form is arbitrary. When integrating over a volume Ω , we assume in subsequent analyses, that Ω is non-empty, open and bounded. Analogously, we can define a surface integral over the surface $\partial\Omega$ parametrized by a system of curvilinear coordinates $\mathbf{x}(s, t)$. Then, the surface integral is given by

$$\int_{\partial\Omega} \phi \, ds = \int_{\partial\Omega} \phi(\mathbf{x}(s, t)) \left| \frac{\partial \mathbf{x}}{\partial s} \times \frac{\partial \mathbf{x}}{\partial t} \right| \, ds \, dt. \quad (2.69)$$

In problems of continuum mechanics, it is often beneficial to transform volume integrals into surface integrals and vice-versa. This can be accomplished by employing Gauß' theorem, which states that

$$\int_{\Omega} \nabla \cdot \mathbf{u} \, dv = \oint_{\partial\Omega} \mathbf{u} \cdot d\mathbf{s} = \oint_{\partial\Omega} \mathbf{u} \cdot \mathbf{n} \, ds, \quad (2.70)$$

where \mathbf{n} is the unit outward normal vector on the surface $\partial\Omega$.

So far, we have introduced only scalar derivatives of vector and tensor quantities. Dealing with elastic potentials, the need arises for taking derivatives with respect to vectors and tensors. Therefore, let us first introduce the (Frechet) derivative of a scalar function ϕ with respect to a vector \mathbf{x} by

$$\frac{d\phi}{d\mathbf{x}} = \frac{\partial \phi}{\partial x_i} \mathbf{e}_i = \partial_{\mathbf{x}} \phi. \quad (2.71)$$

The derivative of a vector-valued function \mathbf{v} or a tensor-valued function \mathbf{T} with respect to a vector \mathbf{x} can be defined, respectively, by

$$\frac{d\mathbf{v}}{d\mathbf{x}} = \frac{\partial v_i}{\partial x_j} \mathbf{e}_i \otimes \mathbf{e}_j = \partial_{\mathbf{x}} \mathbf{v}, \quad (2.72)$$

$$\frac{d\mathbf{T}}{d\mathbf{x}} = \frac{\partial T_{ij}}{\partial x_k} \mathbf{e}_i \otimes \mathbf{e}_j \otimes \mathbf{e}_k = \partial_{\mathbf{x}} \mathbf{T}. \quad (2.73)$$

Note that the resulting quantities obtained from these derivatives are tensors of higher order than the original field; more accurate, the resulting quantity is of the same order as the sum of the orders of the two original quantities involved (function and variable).

Rules for scalar derivatives also apply to vector and tensor derivatives in a somewhat modified manner. The derivative of a product of two scalar fields $\phi(\mathbf{x})$ and $\psi(\mathbf{x})$ e.g. follows from the well-known rule of product differentiation

$$\frac{d}{d\mathbf{x}}(\phi\psi) = \frac{d\phi}{d\mathbf{x}}\psi + \frac{d\psi}{d\mathbf{x}}\phi. \quad (2.74)$$

Care must be taken when applying product and chain rules since the multiplication symbol between partial differentiation factors is no longer unique as for scalar variables and needs adjustment, e.g.

$$\frac{d\phi(\mathbf{u}(\mathbf{x}))}{d\mathbf{x}} = \frac{\partial \phi}{\partial \mathbf{u}} \cdot \frac{\partial \mathbf{u}}{\partial \mathbf{x}}, \quad (2.75)$$

$$\frac{d\mathbf{T}(\mathbf{u}(\mathbf{x}))}{d\mathbf{x}} = \frac{\partial \mathbf{T}}{\partial \mathbf{u}} : \frac{\partial \mathbf{u}}{\partial \mathbf{x}}. \quad (2.76)$$

The following list gives an overview of special tensor derivatives commonly needed (e.g. for deriving stress tensors from elastic potentials), which will be useful in subsequent Sections:

$$\begin{aligned}
\partial_{\mathbf{T}} \mathbf{T} &= \mathcal{I} = \delta_{ik} \delta_{jl} \mathbf{e}_i \otimes \mathbf{e}_j \otimes \mathbf{e}_k \otimes \mathbf{e}_l && \text{(fourth-order identity tensor),} \\
\partial_{\mathbf{T}} \operatorname{tr} \mathbf{T} &= \mathbf{I} = \delta_{ij} \mathbf{e}_i \otimes \mathbf{e}_j && \text{(second-order identity tensor),} \\
\partial_{\mathbf{S}} \operatorname{tr}(\mathbf{T}^T \cdot \mathbf{S}) &= \mathbf{T}^T, \\
\partial_{\mathbf{T}} \operatorname{tr}(\mathbf{T}^T \cdot \mathbf{S}) &= \mathbf{S}^T, \\
\partial_{\mathbf{T}} \operatorname{tr}(\mathbf{T}^T \cdot \mathbf{T}) &= 2\mathbf{T}^T, \\
\partial_{\mathbf{T}} \det \mathbf{T} &= \mathbf{T}^{-1} \det \mathbf{T}, \\
\partial_{\mathbf{T}} (\mathbf{u} \cdot \mathbf{T}^T \cdot \mathbf{T} \cdot \mathbf{v}) &= \mathbf{T} \cdot (\mathbf{u} \otimes \mathbf{v} + \mathbf{v} \otimes \mathbf{u}).
\end{aligned}$$

2.2 Notions of Convexity and Minimum Criteria

Before we introduce the framework of continuum mechanics, let us review a crucial mathematical concept for finding solutions of mechanical problems and introduce the different notions of convexity as well as minimum criteria. As we will see in subsequent Sections, microstructures commonly arise as energy minimizers whenever a non-uniform, microstructured deformation field exhibits lower energy than a uniform homogeneous deformation state. In order to investigate these energy minima, it is important to investigate the conditions for the existence of such minimizers.

Let $\phi : \mathcal{R}^3 \rightarrow \mathcal{R}^3$ be a vector-valued function called the displacement field, and $\mathcal{I} : \mathcal{R}^3 \rightarrow \mathcal{R}$ an energy potential commonly defined by

$$\mathcal{I}(\phi) = \int_{\Omega} \Psi(\nabla \phi) \, dv - \ell(\phi), \quad (2.77)$$

where $\Psi : \mathcal{R}^3 \times \mathcal{R}^3 \rightarrow \mathcal{R}$ denotes an energy density and $\ell(\phi)$ is a linear functional of ϕ (resulting from body forces or surface tractions in the context of continuum mechanics), for a given set of boundary conditions, e.g. $\phi = \mathbf{0}$ on some part $\partial\Omega_u$ of the boundary of the bounded domain $\Omega \in \mathcal{R}^3$. (In this case the linear term $\ell(\phi)$ drops and the energy potential reduces to one which only depends on $\mathbf{F} = \nabla \phi$.) Following the principle of minimum potential energy (see Section 2.5.1), the actual displacement field ϕ is obtained from the minimum principle

$$\inf \{ \mathcal{I}(\phi) \mid \phi, \phi = \phi_0 \text{ on } \partial\Omega \} \quad (2.78)$$

Without going into detail about the physical meaning, let us investigate in which cases there exists a solution to the variational problem (2.78). It has been shown (see e.g. Dacorogna (1989) and the references therein) that there exists at least one minimum of $\mathcal{I}(\mathbf{F})$ if functional \mathcal{I} is

- bounded, i.e. there exist some $a, b \in \mathcal{R}$ with $a > 0$ and $b \geq 1$ such that

$$|\mathcal{I}(\mathbf{F})| \leq a (1 + \|\mathbf{F}\|^b) \quad \forall \mathbf{F}, \quad (2.79)$$

- coercive, i.e. there exist some $a, b, c \in \mathcal{R}$ with $a > 0$ and $b > 1$ such that

$$|\mathcal{I}(\mathbf{F})| \geq c + a \|\mathbf{F}\|^b \quad \forall \mathbf{F}, \quad (2.80)$$

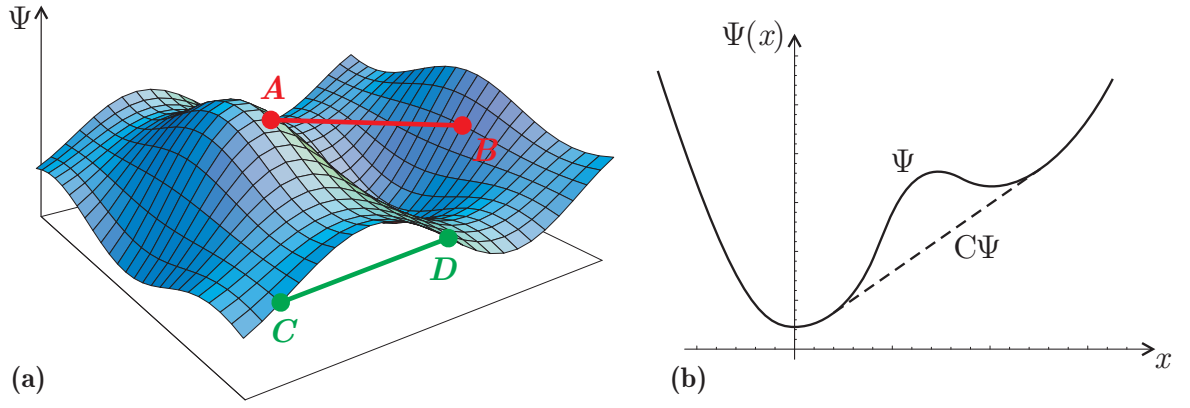


Figure 2.1: (a) A non-convex surface Ψ : The line connecting points C and D does not lie above the surface. (b) The one-dimensional function Ψ is not convex. The dashed line represents the convex hull.

- weakly lower semi-continuous, i.e.

$$\lim_{n \rightarrow \infty} \inf \mathcal{I}(\varphi_n) \geq \mathcal{I}(\varphi), \quad (2.81)$$

for all weakly converging sequences $\varphi_n \rightharpoonup \varphi$.

These conditions are the sufficient general conditions for the existence of a minimum of \mathcal{I} . Note that in general the minimum is not unique. The first two conditions provide upper and lower bounds on \mathcal{I} to prohibit minima at infinity as well as too strong a discontinuous rise or jump of \mathcal{I} . Softening or exponential growth of the energy potential are also prohibited.

Ball (1977) showed that the above three conditions can be recast into conditions applied directly to the energy density function Ψ : There exists at least one minimum of \mathcal{I} if

- Ψ is coercive,
- Ψ is bounded,
- Ψ is quasiconvex.

Indeed, the condition of weakly lower semi-continuity is rather complicated and, in common practice, often replaced by the condition of quasiconvexity of the potential $\Psi(\mathbf{F})$. A potential $\Psi(\mathbf{F})$ is called *quasiconvex* (Morrey, 1952) if for every domain ω and every perturbation field $\varphi : \mathcal{R}^3 \rightarrow \mathcal{R}^3$ of the displacement field it holds that

$$\Psi(\mathbf{F}) \leq \frac{1}{\omega} \int_{\omega} \Psi(\mathbf{F} + \nabla \varphi) \, dv \quad \text{with } \varphi = \mathbf{0} \text{ on } \partial\omega. \quad (2.82)$$

It becomes apparent (Dacorogna, 1989) that it is sufficient to ensure that (2.82) holds for an arbitrary domain ω to prove quasiconvexity in any domain ω . Therefore, one can replace the integral in (2.82) with one over the unit volume which we abbreviate to $(0, 1)^d$. Unfortunately, quasiconvexity is a non-local condition which is hence hard to prove. Therefore, it is convenient to replace quasiconvexity with related approximate local conditions. Therefore, let us complete our review by introducing the different notions of convexity:

A potential $\Psi(\mathbf{F})$ is *convex* (Rockafellar, 1970) if for all $\mathbf{F}_1, \mathbf{F}_2 \in \mathcal{R}^{d \times d}$, and $\lambda \in [0, 1]$

$$\Psi(\lambda \mathbf{F}_1 + (1 - \lambda) \mathbf{F}_2) \leq \lambda \Psi(\mathbf{F}_1) + (1 - \lambda) \Psi(\mathbf{F}_2), \quad (2.83)$$

which is equivalent to

$$\Psi(\mathbf{F}) \leq \lambda \Psi(\mathbf{F} + (1 - \lambda)\mathbf{F}_1) + (1 - \lambda)\Psi(\mathbf{F} - \lambda\mathbf{F}_1). \quad (2.84)$$

A geometrical interpretation reveals that a surface defined by a function Ψ is convex if the connecting line between any two points on the surface lies above the surface everywhere, see Figure 2.1.

A potential $\Psi(\mathbf{F})$ is called *polyconvex* (Ball, 1977) if there exists a convex function $f : \mathcal{R}^{d \times d} \rightarrow \mathcal{R}$ such that

$$\Psi(\mathbf{F}) = f(\mathbf{F}, \text{cof } \mathbf{F}, \det \mathbf{F}). \quad (2.85)$$

In Section 2.3 we will see that the quantities \mathbf{F} , $\text{cof } \mathbf{F}$ and $\det \mathbf{F}$ have a physical meaning; they describe the change of a line, area and volume segment of a deformed body, respectively.

A potential Ψ is *rank-one-convex* if function $\Psi(\mathbf{F})$ satisfies (2.83) with the constraint

$$\text{rank}(\mathbf{F}_1 - \mathbf{F}_2) \leq 1 \quad \text{or} \quad \mathbf{F}_1 - \mathbf{F}_2 = \mathbf{m} \otimes \mathbf{n} \text{ for } \mathbf{m}, \mathbf{n} \in \mathcal{R}^3. \quad (2.86)$$

It follows that if Ψ is quasiconvex, Ψ is also rank-one-convex. So, quasiconvexity is a sufficient condition for rank-one-convexity which, in turn, is a necessary condition for quasiconvexity. One can show that a potential Ψ is rank-one-convex if function

$$f(\xi) = \Psi(\mathbf{F} + \xi \mathbf{m} \otimes \mathbf{n}) \quad \text{is convex} \quad \forall \mathbf{m}, \mathbf{n} \in \mathcal{R}^3. \quad (2.87)$$

Also, following a Taylor expansion, rank-one-convexity ensures that

$$\Psi(\mathbf{F} + \mathbf{m} \otimes \mathbf{n}) \geq \Psi(\mathbf{F}) + \partial_{\mathbf{F}} \Psi : (\mathbf{m} \otimes \mathbf{n}) \quad \forall \mathbf{m}, \mathbf{n} \in \mathcal{R}^3 \quad (2.88)$$

and furthermore

$$(\mathbf{m} \otimes \mathbf{n}) : \partial_{\mathbf{F}\mathbf{F}}^2 \Psi : (\mathbf{m} \otimes \mathbf{n}) \geq 0 \quad \forall \mathbf{m}, \mathbf{n} \in \mathcal{R}^3. \quad (2.89)$$

The latter condition is equivalent to that of Hadamard (1903) for strong ellipticity, see e.g. (Marsden and Hughes, 1994). This condition can also be recast by introducing the acoustic tensor

$$\mathbf{T}_{\mathbf{n}} = \mathbf{n} \cdot \partial_{\mathbf{F}\mathbf{F}}^2 \Psi \cdot \mathbf{n}, \quad (2.90)$$

which must be positive-definite to ensure rank-one-convexity of Ψ . Following Morrey's (1952) conjecture, it had been a long time belief that quasiconvexity and rank-one-convexity are equivalent until Šverák (1992) presented a counterexample. Now we know that the following relations hold among the various notions of convexity: Among the aforementioned conditions, convexity is the strongest, which automatically implies polyconvexity, quasiconvexity and rank-one-convexity. Convexity is a sufficient condition for polyconvexity which, in turn, is a sufficient condition for quasi-convexity which then implies rank-one-convexity. Accordingly, rank-one-convexity is the weakest of all four conditions, it is a necessary condition for quasi-convexity, which, in turn, is a necessary condition for polyconvexity. Poly-convexity then is a necessary condition for convexity. The relations among all four definitions are summarized in Figure 2.2. In one-dimensional problems all four notions of convexity coincide, see Figure 2.1.

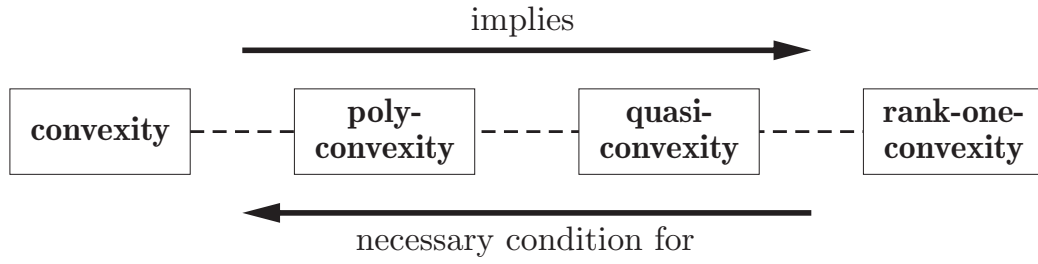


Figure 2.2: Relations among the conditions of convexity.

In many physical problems as those discussed in Chapter 3, the energy density is not quasiconvex such that there exists no solution to the minimization problem in the classical sense. Instead, the energy minimum is accommodated by minimizers in the sense of Ball (1977), forming fine-scale microstructures whose characteristics can be determined by employing *energy hulls* also known as *envelopes*.

We make use of the abbreviation $f \leq g \Leftrightarrow f(x) \leq g(x) \forall x$. Then, let us define the convex hull $C\Psi$, the polyconvex hull $P\Psi$, the quasiconvex hull $Q\Psi$ and the rank-one-convex hull $R\Psi$ of Ψ in the following manner:

$$C\Psi = \sup \{ \Phi \mid \Phi \text{ convex}; \Phi \leq \Psi \}, \quad (2.91)$$

$$P\Psi = \sup \{ \Phi \mid \Phi \text{ polyconvex}; \Phi \leq \Psi \}, \quad (2.92)$$

$$Q\Psi = \sup \{ \Phi \mid \Phi \text{ quasiconvex}; \Phi \leq \Psi \}, \quad (2.93)$$

$$R\Psi = \sup \{ \Phi \mid \Phi \text{ rank-one-convex}; \Phi \leq \Psi \}. \quad (2.94)$$

$$(2.95)$$

We can find the alternative definition of the *convex hull*

$$C\Psi(\mathbf{F}) = \inf \left\{ \sum_{i=1}^n \lambda_i \Psi(\mathbf{F}_i) \mid \lambda_i, \mathbf{F}_i; \sum_{i=1}^n \lambda_i = 1, 0 \leq \lambda_i \leq 1, \sum_{i=1}^n \lambda_i \mathbf{F}_i = \mathbf{F} \right\}, \quad (2.96)$$

where the \mathbf{F}_i are often called the atoms. For finding the convex envelope in d dimensions, $d^2 + 1$ atoms are necessary. The *polyconvex hull* can be defined by

$$P\Psi(\mathbf{F}) = \inf \left\{ \sum_{i=1}^n \lambda_i \Psi(\mathbf{F}_i) \mid \lambda_i, \mathbf{F}_i; \sum_{i=1}^n \lambda_i = 1, 0 \leq \lambda_i \leq 1, \sum_{i=1}^n \lambda_i \mathbf{F}_i = \mathbf{F}, \right. \\ \left. \sum_{i=1}^n \lambda_i \text{cof } \mathbf{F}_i = \text{cof } \mathbf{F}, \sum_{i=1}^n \lambda_i \det \mathbf{F}_i = \det \mathbf{F} \right\} \quad (2.97)$$

and it requires 10 atoms in 2-D and 20 atoms in 3-D. The *quasiconvex hull* can be defined analogously, following the definition of quasiconvexity:

$$Q\Psi(\mathbf{F}) = \inf \left\{ \frac{1}{\omega} \int_{\omega} \Psi(\mathbf{F} + \nabla \varphi) \, dv \mid \varphi; \varphi = \mathbf{0} \text{ on } \partial\omega \right\}. \quad (2.98)$$

Finally, the most important hull for practical applications is the *rank-one-convex envelope*

$R\Psi$ which can be approximated by

$$R_1\Psi(\mathbf{F}) = \inf \left\{ \lambda_1\Psi(\mathbf{F}_1) + \lambda_2\Psi(\mathbf{F}_2) \mid \lambda_i, \mathbf{F}_i; \sum_{i=1}^n \lambda_i = 1, 0 \leq \lambda_i \leq 1, \right. \\ \left. \sum_{i=1}^n \lambda_i \mathbf{F}_i = \mathbf{F}, \text{rank}(\mathbf{F}_1 - \mathbf{F}_2) \leq 1 \right\}. \quad (2.99)$$

$R_1\Psi$ approximates the rank-one-convex hull by assuming a particular pattern of microstructures: a first-order laminate. A better agreement with the rank-one-convex hull can be achieved by recursively repeating the above construction to obtain higher-order phase mixtures with $R_2\Psi = R_1(R_1\Psi) = R_1^2\Psi$, and higher order laminates with increasing number of recursions:

$$R_k\Psi = R_1^k\Psi. \quad (2.100)$$

The rank-one-convex hull of Ψ can now be defined as

$$R\Psi = \lim_{k \rightarrow \infty} R_k\Psi. \quad (2.101)$$

In the context of continuum mechanics it would be most convenient to construct the quasiconvex hull. Since quasiconvexity is a non-local condition, however, the construction of quasiconvex hulls in an analytical fashion turns out not to be feasible in many cases. Therefore, the quasiconvex hull is approximated by other convex hulls (note that all other notions of convexity involve purely local conditions). Following Figure 2.2 the relations among the different hulls are:

$$C\Psi \leq P\Psi \leq Q\Psi \leq R\Psi \leq R_k\Psi \leq R_1\Psi \leq \Psi. \quad (2.102)$$

One possibility to determine the quasiconvex hull is now to derive an upper and a lower bound on the quasiconvex hull; e.g. authors have determined the polyconvex and the rank-one-convex hulls of the energy under consideration. In those cases where these two hulls (which bound the quasiconvex envelope from above and from below) coincide, they also coincide with the quasiconvex hull which has thus been found. In those cases where the upper and lower bounds do not coincide, it is at least possible to approximate the quasiconvex hull by e.g. the rank-one-convex hull (or one of its approximations $R_k\Psi$).

2.3 Fundamentals of Continuum Mechanics

2.3.1 Elastic Deformation

The description of the mechanical behavior of material bodies requires a mathematical model to represent the physical reality in a simplified and mathematically sound setting. Physically, any material consists of enumerable particles, molecules and atoms and is hence discrete in nature. If the dimensions of the material body under consideration, however, are much larger than those of atoms or molecules, the discrete nature can be neglected and the material body may be treated as a continuum consisting of particles continuously distributed in space. For this reason, we limit our analyses in this work to be within the framework of classical continuum theory (Truesdell and Noll, 1965), which is based on the assumption

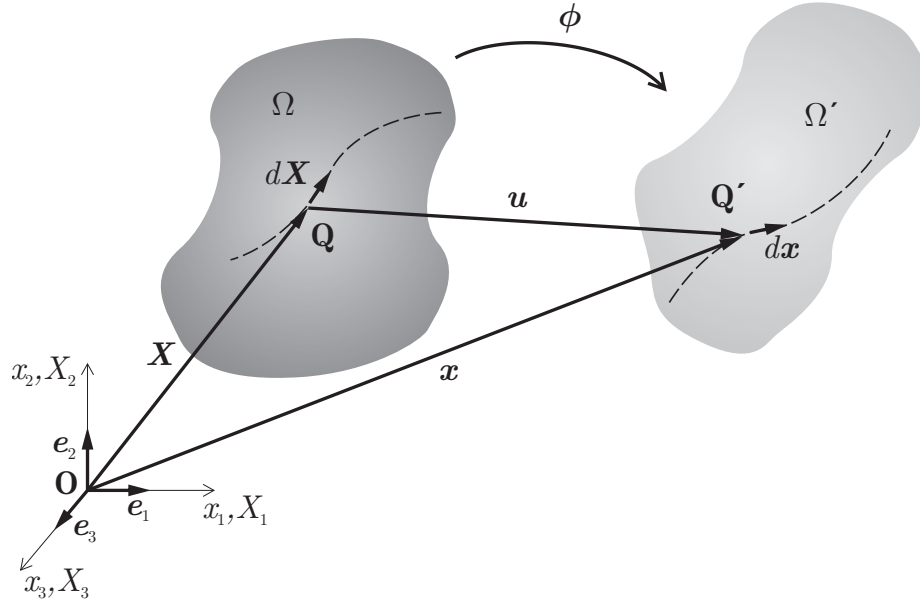


Figure 2.3: Reference and deformed configuration of a material body in the Cartesian reference coordinate system.

of a continuous distribution of a body's physical properties such as its density or its elastic properties, but also of the mechanical field variables under consideration, e.g. displacement, stress or temperature. Hence, we describe every material body as a compact, continuous infinite set of material points in space, whose total entity forms a material body $\Omega \subset \mathcal{R}^3$ with surface $\partial\Omega = \Gamma$. To describe the position of each material point in space, we introduce a time-invariant Cartesian coordinate system which is defined by the unit vectors e_i with respect to a fixed reference point, the origin O (see Figure 2.3).

As a consequence, the position of a point in space can be specified in terms of its coordinates or its position vector, where we have to differentiate between the undeformed (reference) configuration Ω and the deformed (current) configuration Ω' of a body. Hence, we write for each point in the undeformed configuration the position vector

$$\mathbf{X} = X_i \mathbf{e}_i, \quad \mathbf{X} \in \Omega \subset \mathcal{R}^3, \quad (2.103)$$

and for the same material point in the deformed configuration

$$\mathbf{x} = x_i \mathbf{e}_i, \quad \mathbf{x} \in \Omega' \subset \mathcal{R}^3. \quad (2.104)$$

The deformation of a body can be regarded as a mapping $\phi : \Omega(\mathcal{R}^3) \rightarrow \Omega'(\mathcal{R}^3)$ of a domain Ω (i.e. of every material point contained in Ω) onto a domain Ω' . The change of position of each material point can be described by its new position

$$\mathbf{x} = \phi(\mathbf{X}), \quad (2.105)$$

or by introducing a displacement field \mathbf{u} that relates \mathbf{x} to \mathbf{X} by

$$\mathbf{u} = \mathbf{x} - \mathbf{X} = \phi(\mathbf{X}) - \mathbf{X}. \quad (2.106)$$

Note that in general the displacement vector \mathbf{u} can be given in terms of the original coordinates as $\mathbf{u}(\mathbf{X}) = \mathbf{x}(\mathbf{X}) - \mathbf{X}$ or in terms of the coordinates in the deformed configuration

as $\mathbf{u}(\mathbf{x}) = \mathbf{x} - \mathbf{X}(\mathbf{x})$. In the following, we will neglect the latter formulation and use the reference coordinate system only unless explicitly stated otherwise.

Not only material points but also line segments in Ω are mapped onto the deformed configuration Ω' . An infinitesimal line segment $d\mathbf{X}$ is transformed into $d\mathbf{x}$ by

$$d\mathbf{x} = \frac{\partial \mathbf{x}}{\partial \mathbf{X}} \cdot d\mathbf{X} = \mathbf{F} \cdot d\mathbf{X}. \quad (2.107)$$

$\mathbf{F} = \nabla \phi$ is called the deformation gradient tensor with components

$$F_{ij} = \delta_{ij} + u_{i,j} = \phi_{i,j}. \quad (2.108)$$

As a consequence, area segments $d\mathbf{A} = \mathbf{N} dA$ (with \mathbf{N} being the unit outward normal vector on the surface of area dA) and volume segments dV of the reference configuration Ω are deformed in Ω' and given as

$$d\mathbf{a} = \mathbf{n} da = (\det \mathbf{F}) \mathbf{F}^{-T} \cdot d\mathbf{A} = (\text{cof } \mathbf{F}) d\mathbf{A}, \quad (2.109)$$

$$dv = \det \mathbf{F} dV. \quad (2.110)$$

For incompressible (i.e. volume-preserving) materials the deformation gradient tensor must hence obey the requirement $\det \mathbf{F} = 1$. Note that for physically reasonable deformations the requirement

$$\det \mathbf{F} > 0 \quad (2.111)$$

must hold. Analyzing the change of the length of a line segment ds in Ω , which can be calculated as

$$||ds||^2 = d\mathbf{X} \cdot \mathbf{F}^T \mathbf{F} \cdot d\mathbf{X}, \quad (2.112)$$

Cauchy and Green introduced the following tensors to describe finite deformations:

$$\mathbf{C} = \mathbf{F}^T \mathbf{F}, \quad \mathbf{b} = \mathbf{F} \mathbf{F}^T, \quad (2.113)$$

where \mathbf{C} and \mathbf{b} are the so-called right and left Cauchy-Green tensors; the inverse of \mathbf{b} is often referred to as the finger tensor $\mathbf{c} = \mathbf{b}^{-1}$. These tensors are commonly used to describe finite deformation. For some applications, it is useful to employ the following representation of the deformation gradient tensor, which follows Cauchy's polar decomposition theorem and states that any deformation gradient (or any tensor, in general) can be decomposed into the symmetric, positive-definite right and left Cauchy tensors \mathbf{U} and \mathbf{V} , respectively, and a rotation tensor \mathbf{R} by

$$\mathbf{F} = \mathbf{R} \cdot \mathbf{U} = \mathbf{V} \cdot \mathbf{R}, \quad (2.114)$$

from which it follows that

$$\mathbf{b} = \mathbf{V}^2, \quad \mathbf{C} = \mathbf{U}^2. \quad (2.115)$$

Note that transformation rules discussed in Section 2.1.3 apply, so that the deformation gradient tensor can also be written in terms of the principal stretches λ_i , i.e.

$$\mathbf{F} = \begin{bmatrix} \lambda_1 & 0 & 0 \\ 0 & \lambda_2 & 0 \\ 0 & 0 & \lambda_3 \end{bmatrix}. \quad (2.116)$$

The three invariants of the deformation gradient tensor follow as

$$\begin{aligned} I_1 &= \text{tr } \mathbf{F} = F_{ii} = \lambda_1 + \lambda_2 + \lambda_3, \\ I_2 &= \frac{1}{2}(\mathbf{F} : \mathbf{F} - (\text{tr } \mathbf{F})^2) = \frac{1}{2}(F_{ij}F_{ij} - F_{ii}F_{jj}) = \lambda_1\lambda_2 + \lambda_2\lambda_3 + \lambda_1\lambda_3, \\ I_3 &= \det \mathbf{F} = \lambda_1\lambda_2\lambda_3. \end{aligned} \quad (2.117)$$

A special case of deformation is that of rigid body motion during which the original body Ω only translates and/or rotates in space without changing its shape. For translational motion, the displacement vector for each point in Ω is independent of its location \mathbf{X} and hence $\mathbf{F} = \mathbf{I}$ and $\mathbf{C} = \mathbf{F}^T \mathbf{F} = \mathbf{I}$. For pure rotation, \mathbf{F} is a rotation tensor and e.g. for a two-dimensional in-plane rotation about the \mathbf{e}_3 -axis by an arbitrary angle φ specified by

$$\mathbf{F} = \begin{pmatrix} \cos \varphi & -\sin \varphi & 0 \\ \sin \varphi & \cos \varphi & 0 \\ 0 & 0 & 1 \end{pmatrix} \quad (2.118)$$

such that again $\mathbf{C} = \mathbf{F}^T \mathbf{F} = \mathbf{I}$. So, for rigid body motion we have $\mathbf{C} = \mathbf{I}$ (and thus $\mathbf{b} = \mathbf{I}$). Normally, any deformation measure is expected to yield a zero tensor for rigid body motion. This leads to the introduction of the Almansi-Hamel strain tensor

$$\mathbf{E} = \frac{1}{2}(\mathbf{C} - \mathbf{I}), \quad (2.119)$$

which can also be written in terms of the displacement vector \mathbf{u} so that its components read

$$E_{ij} = \frac{1}{2}(u_{i,j} + u_{j,i} + u_{k,i}u_{k,j}). \quad (2.120)$$

It can easily be verified that for rigid body motion $\mathbf{E} = \mathbf{0}$.

To keep the mathematical analysis as simple as possible, it is often useful to resort to the most important simplification in the analysis of deformation, viz. the assumption of infinitesimal deformation, which is valid in the presence of small elastic but also small elasto-plastic displacements; i.e. we assume infinitesimal strains if the displacements are negligible compared to the geometric extensions of the body under investigation. Since $\|u_{i,j}\| \ll 1$ in this case, Eq. (2.120) reduces to the infinitesimal strain tensor ε with components

$$\varepsilon_{ij} = \frac{1}{2}(u_{i,j} + u_{j,i}). \quad (2.121)$$

When the material body Ω deforms in space, each point in Ω travels through space with a velocity vector $\mathbf{v}(t)$, which is a function of time and position and can be expressed mathematically as

$$\mathbf{v}(\mathbf{x}, t) = \lim_{\Delta t \rightarrow 0} \frac{\mathbf{u}(\mathbf{x}, t + \Delta t) - \mathbf{u}(\mathbf{x}, t)}{\Delta t} = \left. \frac{\partial \mathbf{u}}{\partial t} \right|_{\mathbf{x}} \quad (2.122)$$

where the subscript \mathbf{x} denotes keeping \mathbf{x} constant while taking the partial derivative with respect to time. For subsequent Sections, it is beneficial to introduce a new quantity which describes the change of the velocity field $\mathbf{v}(\mathbf{x}, t)$ for a fixed time t but with varying spatial coordinates \mathbf{x} . Therefore, let us calculate the velocity increment $d\mathbf{v}$ due to an infinitesimal variation $d\mathbf{x}$,

$$d\mathbf{v} = \mathbf{v}_{,x} \cdot d\mathbf{x} = \mathbf{L} \cdot d\mathbf{x}, \quad (2.123)$$

where \mathbf{L} is the gradient of \mathbf{v} with respect to the spatial coordinates \mathbf{x} . Applying the chain rule and rearranging tensors, we obtain the following identities of practical use:

$$\mathbf{L} = \dot{\mathbf{F}} \mathbf{F}^{-1}, \quad \mathbf{F} = \mathbf{L} \mathbf{F}, \quad \dot{\mathbf{F}}^{-1} = -\mathbf{F}^{-1} \cdot \mathbf{L}. \quad (2.124)$$

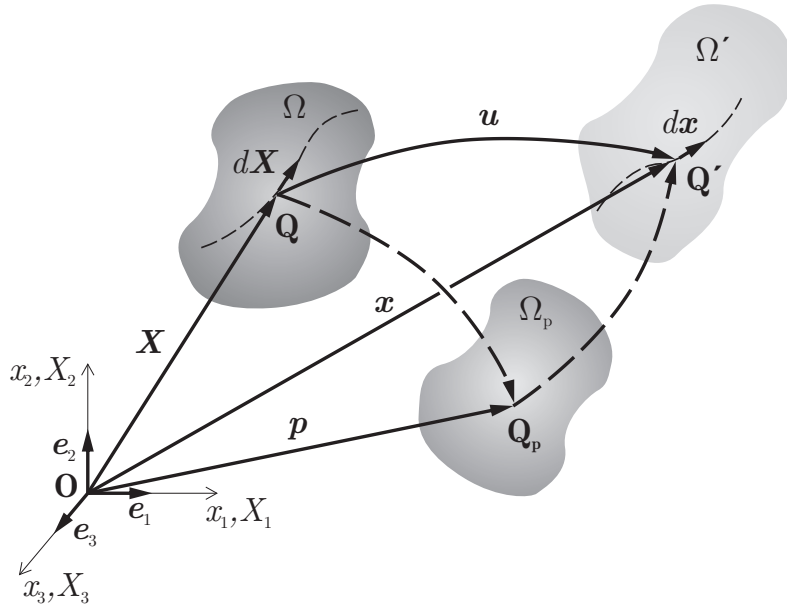


Figure 2.4: Reference, intermediate and final deformed configuration of the material body.

2.3.2 Plastic Deformation

In the previous Section we introduced the fundamental deformation measures and their relations, regardless of their physical origin and nature. In reality, however, we must differentiate between two types of deformations. On the one hand, deformation can occur as a reversible process which is naturally recovered and vanishes upon removing all externally applied loads. This type of deformation is termed *elastic*. In contrast, *plastic* deformation denotes a permanent mapping into a deformed configuration, i.e. this type of deformation is irreversible – the material body remains in a strained configuration upon releasing all external loads. These effects can be translated into the following mathematical concept illustrated in Fig. 2.4. As before, the reference configuration Ω is mapped onto the deformed configuration Ω' and any infinitesimal line segment $d\mathbf{X}$ deforms into $d\mathbf{x} = \mathbf{F} \cdot \mathbf{X}$ with \mathbf{F} being the deformation gradient tensor. Let us now introduce an intermediate configuration described by a coordinate \mathbf{p} , as sketched in Fig. 2.4. This intermediate configurations Ω_p is assumed to be obtained from the deformed configuration Ω' by unloading the continuum to a zero stress state, or from the reference configuration Ω by pure plastic deformation. Therefore, the current configuration and its line segment $d\mathbf{x}$ can be obtained by first deforming $d\mathbf{X}$ purely plastically via $d\mathbf{p} = \mathbf{F}_p \cdot d\mathbf{X}$, where \mathbf{F}_p is the plastic deformation tensor, and further deformation into $d\mathbf{x}$ by an elastic deformation via $d\mathbf{x} = \mathbf{F}_e \cdot d\mathbf{p}$, where \mathbf{F}_e is the elastic deformation tensor. Combining these two steps, we arrive at the well-known multiplicative decomposition of the deformation gradient originally introduced by Lee and Lin (1967):

$$\mathbf{F} = \mathbf{F}_e \cdot \mathbf{F}_p. \quad (2.125)$$

Note that for any plastic deformation

$$\det \mathbf{F}_p = 1, \quad (2.126)$$

i.e. plastic deformation is volume-preserving. From Eq. (2.119), the Almansi-Hamel strain tensor can now be written as

$$\mathbf{E} = \frac{1}{2}(\mathbf{F}^T \mathbf{F} - \mathbf{I}) = \mathbf{F}_p^T \mathbf{E}_e \mathbf{F}_p + \mathbf{E}_p \quad (2.127)$$

with

$$\mathbf{E}_e = \frac{1}{2}(\mathbf{V}_e^2 - \mathbf{I}), \quad \mathbf{E}_p = \frac{1}{2}(\mathbf{F}_p^T \mathbf{F}_p - \mathbf{I}). \quad (2.128)$$

If the total deformation gradient is infinitesimal (i.e. elastic, plastic and total strains are infinitesimal), then Eq. (2.127) reduces to

$$\mathbf{E} = \boldsymbol{\varepsilon} = \boldsymbol{\varepsilon}_e + \boldsymbol{\varepsilon}_p, \quad (2.129)$$

which is the well-known additive decomposition of the strain tensor for infinitesimal deformations. Use of this additive decomposition requires caution: In many physical problems the elastic strain is very small compared to the plastic deformation and hence negligible. This allows for the assumption that $\|\boldsymbol{\varepsilon}_e\| \ll 1$, which in turn, however, does not automatically imply the validity of Eq. (2.129). This can only be applied if also the plastic deformation is infinitesimal. For most problems, one has to employ Eq. (2.125) which is generally applicable. Note that the formulation $\mathbf{E} = \mathbf{E}_e + \mathbf{E}_p$ is not universally true and depends on the definition of \mathbf{E}_e and \mathbf{E}_p . In particular, only \mathbf{E} is kinematically expressible in terms of the deformation gradient. For a detailed discussion see e.g. (Khan and Huang, 1995). In general, we will obtain the strain tensor \mathbf{E} from the overall deformation, define \mathbf{E}_p by a constitutive relation, and then obtain \mathbf{E}_e from

$$\mathbf{E}_e = \mathbf{E} - \mathbf{E}_p, \quad (2.130)$$

which can be applied for both finite and infinitesimal deformations (for the latter in the analogous form $\boldsymbol{\varepsilon}_e = \boldsymbol{\varepsilon} - \boldsymbol{\varepsilon}_p$).

2.3.3 Stresses and Equilibrium

Following the mathematical description of the purely geometrical behavior of a material body in terms of its deformation measures in the previous Sections, we will now focus on the characterization of tractions and forces applied to a material body and the resultant internal stresses within the material body. In general, we can divide the applied forces into external forces (comprising body and surface forces) and internal forces (stresses within the material body, following the Euler-Cauchy stress principle (Scipio, 1967)). The external forces can further be subdivided into body forces

$$\mathbf{f}_v(\mathbf{x}) = f_{v_i}(\mathbf{x})\mathbf{e}_i, \quad \mathbf{x} \in \Omega, \quad (2.131)$$

which are continuously distributed throughout the volume of a body Ω (e.g. gravitational forces), and surface forces (depending on the surface normal orientation \mathbf{n})

$$\mathbf{f}_t(\mathbf{x}, \mathbf{n}) = f_{t_i}(\mathbf{x})\mathbf{e}_i, \quad \mathbf{x} \in \Gamma_t, \quad (2.132)$$

which act on a part of the body's surface and commonly result from contact of two bodies. Therefore, we have divided the body's surface $\Gamma = \partial\Omega = \Gamma_t \cup \Gamma_u$ into two parts, Γ_t denoting that part of Γ , on which the applied surface forces act, and Γ_u being that part of Γ , on which displacements \mathbf{u}_0 are prescribed.

Externally applied forces result in internal forces, which are commonly characterized by a second-order stress tensor. The internal traction at a material point in a direction \mathbf{n} is defined

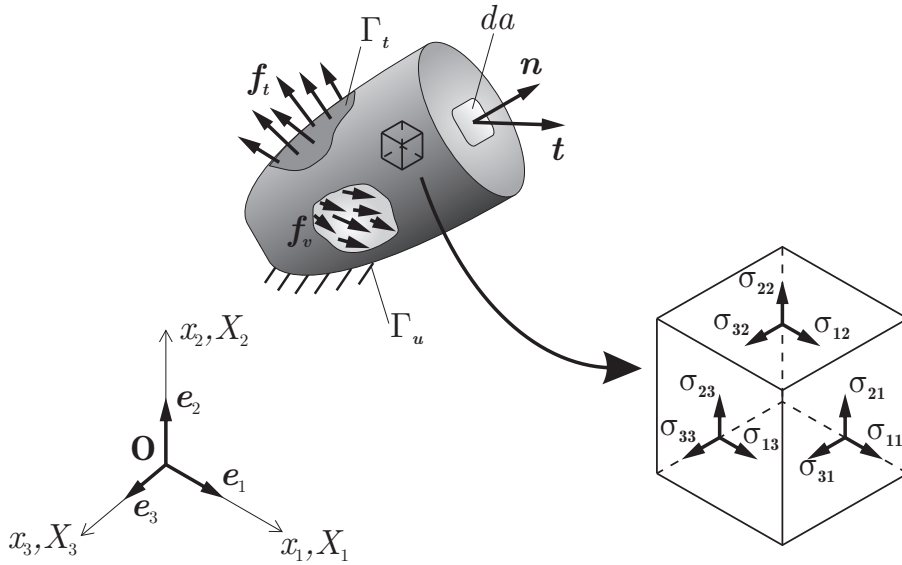


Figure 2.5: Stress, force and traction definitions.

as that force $\mathbf{t} = t_i \mathbf{e}_i$ which acts on an infinitesimal area element Δa with normal \mathbf{n} after cutting the material body into two parts, as illustrated in Figure 2.5:

$$\mathbf{t} = \lim_{\Delta a \rightarrow 0} \frac{\Delta \mathbf{p}}{\Delta a}. \quad (2.133)$$

Note that the shape of the area Δa does not affect the traction \mathbf{t} . To uniquely describe the complete stress state in any material point in Ω , it is sufficient to determine the traction vector \mathbf{t} on three mutually orthogonal surfaces at that point. For example, we can cut from the material body an infinitesimal cube volume element around the material point whose surfaces point into the directions of the three Cartesian coordinate axes, so that we obtain a vector $\mathbf{t}_i = (\sigma_{1i}, \sigma_{2i}, \sigma_{3i})$ on each surface of the cube, as sketched in Figure 2.5. We can arrange all three surface traction vectors in a tensor, the stress tensor $\boldsymbol{\sigma} = \sigma_{ij} \mathbf{e}_i \otimes \mathbf{e}_j$, which uniquely defines the complete stress state at a material point and whose components may be arranged in a square matrix,

$$(\sigma_{ij}) = \begin{pmatrix} \sigma_{11} & \sigma_{12} & \sigma_{13} \\ \sigma_{21} & \sigma_{22} & \sigma_{23} \\ \sigma_{31} & \sigma_{32} & \sigma_{33} \end{pmatrix}. \quad (2.134)$$

By definition, the first index of σ_{ij} then indicates the direction in which the stress component is acting and the second index indicates the direction of the surface normal vector \mathbf{n} of the plane in which the stress is defined. In general, σ_{ij} is the stress on the j -plane in the i -direction. The diagonal entries σ_{ii} hence act normal to the surface on which they are defined and are therefore called the normal stresses. All entries on secondary diagonals $\sigma_{ij} (i \neq j)$ act parallel to the surface on which they are defined and are referred to as shear stresses. As transformation rules for tensors apply, the traction vector at a material point in any arbitrary surface with unit normal vector \mathbf{n} can be obtained from the stress tensor as

$$\mathbf{t} = \boldsymbol{\sigma} \cdot \mathbf{n}. \quad (2.135)$$

Therefore, every component of $\boldsymbol{\sigma}$ can be obtained from

$$\sigma_{ij} = \mathbf{e}_i \cdot \boldsymbol{\sigma} \cdot \mathbf{e}_j. \quad (2.136)$$

The stress tensor defined in the aforementioned way (i.e. in the deformed configuration) is commonly named the Cauchy stress tensor.

Although components of the stress tensor vary with orientation in the material body, there are three invariants to transformations (cf. Eq. (2.117)), which are commonly defined by

$$\begin{aligned} J_1 &= \text{tr } \boldsymbol{\sigma} = \sigma_{ii}, \\ J_2 &= \frac{1}{2} (\sigma_{ij}\sigma_{ji} - \sigma_{ii}\sigma_{jj}), \\ J_3 &= \det \boldsymbol{\sigma} = \frac{1}{3} \sigma_{ij}\sigma_{jk}\sigma_{ki}. \end{aligned} \quad (2.137)$$

When we cut the cube from the material body, we observe that the traction components acting on its surfaces are not all independent but must be chosen in such way that the cube is in a state of equilibrium, which means that the resultant force and momentum vectors on the cube must vanish under the assumption of static deformation. Enforcing equilibrium on an infinitesimal cube as in Figure 2.5, we derive from the (static) force balance equations the equilibrium conditions

$$\text{div } \boldsymbol{\sigma} + \mathbf{f}_v = \mathbf{0} \quad \text{in } \Omega, \quad (2.138)$$

where \mathbf{f}_v is the vector of body forces. Analogously, the momentum balance equations yield the equilibrium conditions in the absence of continuously distributed body moments

$$\boldsymbol{\sigma} = \boldsymbol{\sigma}^T \quad \text{in } \Omega. \quad (2.139)$$

At the free surfaces of the material body, we must satisfy the condition

$$\boldsymbol{\sigma} \cdot \mathbf{n} = \mathbf{f}_t \quad \text{on } \Gamma_t. \quad (2.140)$$

When dealing with infinitesimal deformations and hence the infinitesimal stress tensor, the definition of the stress tensor is unique and the above description is sufficient. Especially for the description of elasto-plastic or hyperelastic material behavior, the assumption of infinitesimal deformation is often not appropriate. In the context of finite deformation analysis the stress tensor is no longer uniquely defined but we must specify the configuration in which the tensor is defined. The Cauchy stress tensor is defined in the deformed configuration Ω' . It varies with coordinate \mathbf{x} and it is the true stress in a deformed body. In general elasticity theory, there are two independent configurations, so that we can specify the stress tensor with respect to \mathbf{X} and \mathbf{x} , and we can map the stresses between these configurations by application of \mathbf{F} (see Figures 2.3). In elasto-plasticity there are even three distinct configurations (see Figure 2.4) so that, when determining a stress tensor, it becomes even more important to specify the configuration in which it is defined.

The first Piola-Kirchhoff stress tensor $\boldsymbol{\Sigma}^I$ (often abbreviated as first PK stress tensor) is introduced to give the actual force or traction ΔP on the deformed area Δa in the deformed configuration Ω' , but it refers to the area ΔA in the reference configuration. It is therefore linked to the Cauchy stress tensor $\boldsymbol{\sigma}$ via

$$\boldsymbol{\sigma} = \boldsymbol{\Sigma}^I \cdot \mathbf{F}^T (\det \mathbf{F})^{-1}. \quad (2.141)$$

This stress measure is often termed the nominal stress because its component Σ_{ij}^I represents the stress component in the x_i -direction of the force per unit area in the reference configuration on a surface that is normal to the X_j -axis in that configuration. Note that, because $\boldsymbol{\sigma}$

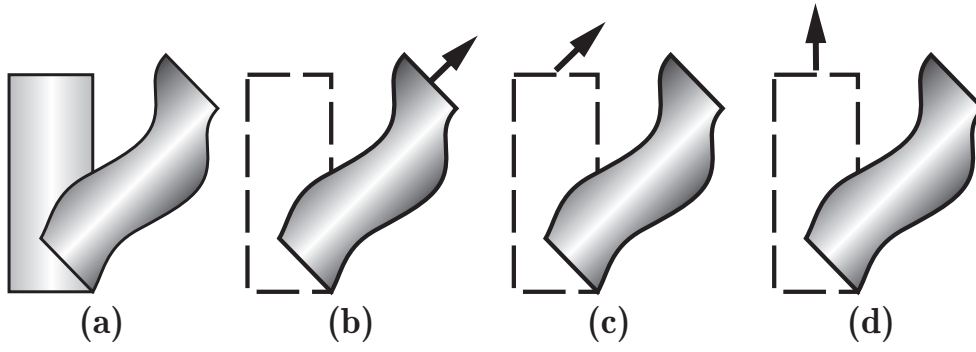


Figure 2.6: Physical comparison between the stress tensors: (a) reference and deformed configuration, (b) Cauchy stress (force in deformed configuration on deformed area), (c) 1st PK stress (force in deformed configuration on undeformed area), (d) 2nd PK stress (force mapped to undeformed configuration on undeformed area).

is symmetric and \mathbf{F} is generally not, the first Piola-Kirchhoff stress tensor is not symmetric. Therefore, the second Piola-Kirchhoff stress tensor Σ^{II} was introduced, which gives the stress mapped to the reference area and measured on the undeformed area dA . It relates to the Cauchy stress σ as

$$\sigma = \mathbf{F} \cdot \Sigma^{II} \cdot \mathbf{F}^T (\det \mathbf{F})^{-1} \quad (2.142)$$

All three stress tensor definitions and the corresponding reference frames are compared in Fig. 2.6. Comparing Eqs. (2.141) and (2.142), we finally conclude

$$\Sigma^I = \mathbf{F} \cdot \Sigma^{II}. \quad (2.143)$$

Note that in problems of elasto-plasticity, $\mathbf{F} \neq \mathbf{F}_e$ such that extra caution is required, see Section 2.3.4.

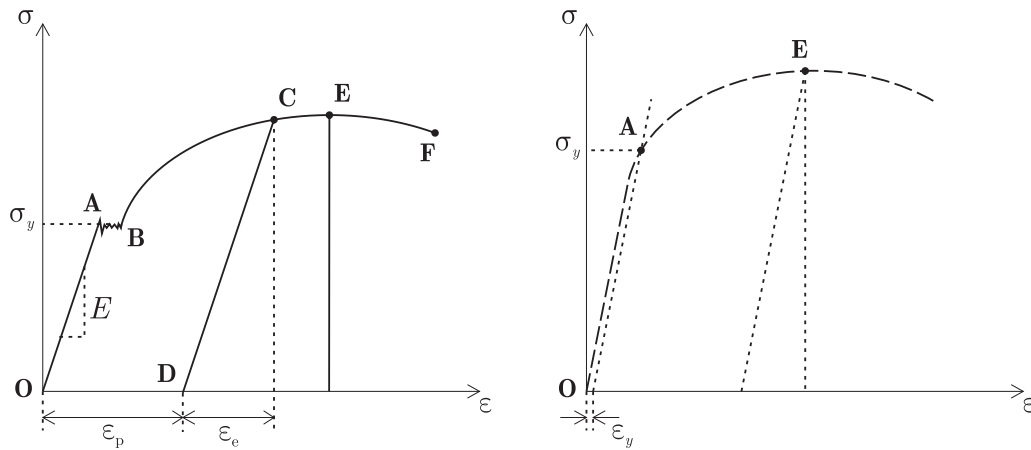


Figure 2.7: Stress-strain curve example for uniaxial loading.

2.3.4 Constitutive Laws

So far, we have described the concept of the strain tensor to describe the deformation state of a material body, and the different formulations of the stress tensor to define the internal forces acting within a material body subject to external forces. The goal of every mechanical model is a description of the physical behavior of a material body by means of constitutive laws which relate the strain tensor to the stress tensor. A *constitutive law* in our context is hence nothing else but a mathematical equation relating stresses to strains, and its concept was introduced among others by Noll (1954). In solid mechanics these constitutive laws commonly do not follow directly from physical law but are rather a result of experimental observation and very often of phenomenological nature.

An exemplary stress-strain relation for a simple uniaxial tension test e.g. for a mild steel (a) and for aluminum (b) is illustrated in Figure 2.7. These curves depict results from displacement-controlled experiments, i.e. the hard test device prescribes displacements (and hence the overall strain ε) while the stress σ is measured and recorded as a function of strain. Analogously, experiments can also be load-controlled, i.e. the external forces (or stresses) are prescribed and the displacement is recorded. In technical reality the latter type of experiment is the only one which can ideally be realized, since load-controlled testing can simply be accomplished by means of dead loads, but a perfectly rigid hard device to rigidly enforce displacements is a technical impossibility.

Let us discuss the exemplary stress-strain curves for a uniaxial tension test of a slender bar, shown in Figure 2.7, to introduce some common definitions. In both curves we can clearly identify an initial section **OA**, where the stress-strain behavior is linear with the proportionality factor E (Young's modulus). This initial section of a stress-strain curve therefore describes a purely elastic loading of the material. Elastic loading is completely reversible and the initial (stress- and strain-free) state is recovered as all external loads are removed (i.e. when we load the body up to a point below **A** and then unload the body, we will return to point **O**). At point **A** this linear relationship breaks down and the material begins to yield; the material exhibits plastic flow. Consequently, **A** is called the yield point and, accordingly, the stress at point **A** is termed the *yield stress* σ_y .

Upon further loading, the stress-strain curve commonly exhibits a decreasing slope depending on the type of material. The stress-strain curve during plastic yielding sometimes shows an almost horizontal line, known as perfectly plastic behavior, or it exhibits a further increase of the stress but with a lower slope than during elastic loading. Often both appearances occur in a combined fashion, as depicted in Figure 2.7a. The zig-zag curve between points **A** and **B** is commonly referred to as a Lüdersband and usually arises due to stick-slip mechanisms on the microscale, which involve dislocations whose motion is temporarily impeded. After point **B**, the material exhibits plastic flow and it hardens until point **E**. From point **E** on the material softens and finally undergoes damage leading to material failure due to fracture at point **F**. In the elastic region between points **O** and **A** the deformation is reversible, and the material body recovers upon unloading, going back to point **O**. If we unload the body after plastic, i.e. irreversible, deformation e.g. at point **C**, the stress-strain curve follows the line **CD** which is parallel to **OA** (elastic unloading). State **D** is characterized by zero stresses. The strain, however, is non-zero: the irreversible plastic strain ε_p remains. So, only the elastic strain ε_e is recovered, whereas the plastic strain ε_p remains as permanent deformation. While in Figure 2.7a the onset of plastic flow is sharp and clearly visible, the stress-strain curve for aluminum in Figure 2.7b does not allow for such a clear identification

of σ_y . For such materials, one commonly defines the yield point by means of a maximum deviation from the proportional behavior, i.e. one introduces a critical overall strain ε_y (often 2%) at which the yield point is defined.

As discussed in Section 2.3.1 and as shown in Figure 2.7, the total strain can be decomposed into elastic and plastic strain, $\varepsilon = \varepsilon_e + \varepsilon_p$ for infinitesimal strains, and $\mathbf{F} = \mathbf{F}_e \mathbf{F}_p$ for finite strains. This decomposition of the total strain calls for constitutive laws for both ε_e and ε_p or \mathbf{F}_e and \mathbf{F}_p , respectively. During elastic loading (section **OA**) only ε_e or \mathbf{F}_e may evolve; during general elasto-plastic deformation (section **AF**) both ε_e and ε_p or \mathbf{F}_e and \mathbf{F}_p evolve. The constitutive law for the elastic strain (the proportionality in the above example) will be discussed first. The constitutive law for the plastic strain, which is also known as the *flow rule*, is subject of Section 2.4, where it can be linked to microscale mechanisms.

In elasticity theory, a constitutive law can be given directly, e.g. in the form of Hooke's law for linear elasticity

$$\boldsymbol{\sigma} = \mathcal{C} : \boldsymbol{\varepsilon}_e, \quad (2.144)$$

or indirectly by defining an elastic energy potential, which we will discuss in a moment. In general, the elasticity tensor $\mathcal{C} = C_{ijkl} \mathbf{e}_i \otimes \mathbf{e}_j \otimes \mathbf{e}_k \otimes \mathbf{e}_l$ of fourth-order has 81 components which link the strain tensor to the stress tensor. Very often, it is not necessary to consider all 81 components independent but due to symmetry of the stress and strain tensor and due to isotropic material behavior (i.e. no directional dependence of the elastic properties), one can reduce the relationship between stresses and strains to only two independent material properties. One possible formulation is given in terms of the Lamé elastic moduli μ and λ , i.e.

$$C_{ijkl} = \lambda \delta_{ij} \delta_{kl} + \mu (\delta_{ik} \delta_{jl} + \delta_{il} \delta_{jk}). \quad (2.145)$$

The constitutive law for linear elasticity now reads

$$\boldsymbol{\sigma} = \lambda (\text{tr } \boldsymbol{\varepsilon}_e) \mathbf{I} + 2\mu \boldsymbol{\varepsilon}_e. \quad (2.146)$$

Other typical engineering formulations of the elastic properties employ Young's modulus E , Poisson's ratio ν and the bulk modulus K , which can be related to the Lamé moduli via

$$E = \mu \frac{3\lambda + 2\mu}{\lambda + \mu}, \quad \nu = \frac{\lambda}{2(\lambda + \mu)}, \quad K = \lambda + \frac{2}{3}\mu. \quad (2.147)$$

Note that in all formulations the stress state depends only on the elastic strain tensor (or the elastic deformation gradient, as applicable). This agrees with the observation that the introduced intermediate configuration Ω_p is stress-free.

As already mentioned, a constitutive law can also be given indirectly and obtained from an elastic energy potential, which for the above example of linear elasticity reads

$$\Psi(\boldsymbol{\varepsilon}_e) = \frac{1}{2} \boldsymbol{\varepsilon}_e^T : \mathcal{C} : \boldsymbol{\varepsilon}_e. \quad (2.148)$$

Such an energy potential Ψ , also termed the *Helmholtz free energy*, describes the stored elastic energy at a given point of the material body, and it can be obtained from experimental results, molecular dynamics simulations or other phenomenological approaches. For more details on the possible choices of the energy potential Ψ see Section 2.5.1. In the theory of infinitesimal elasticity, the stress tensor in Eq. (2.144) follows from the elastic potential via

$$\boldsymbol{\sigma} = \frac{\partial \Psi}{\partial \boldsymbol{\varepsilon}_e} = \mathcal{C} : \boldsymbol{\varepsilon}_e. \quad (2.149)$$

In finite elasticity, the constitutive law is most often given via an elastic energy potential, which can be defined in many ways depending on the type of material to be described. The well-known St. Venant-Kirchhoff potential is analogous to that of a Hookean material in linear elasticity, i.e.

$$\Psi_K(\mathbf{C}_e) = \frac{1}{2} \mathbf{E}_e^T : \mathcal{C} : \mathbf{E}_e = \frac{1}{8} (\mathbf{C}_e - \mathbf{I})^T : \mathcal{C} : (\mathbf{C}_e - \mathbf{I}). \quad (2.150)$$

Another important because widely used material model follows the so-called Neo-Hookean constitutive law, which may be formulated e.g. as

$$\Psi_{NH}(\mathbf{C}_e) = \frac{\mu}{2} (\text{tr } \mathbf{C}_e - 3) + \frac{K}{4} \left[\det \mathbf{C}_e - \frac{K + 2\mu}{K} \ln (\det \mathbf{C}_e) - 1 \right]. \quad (2.151)$$

One important characteristic of this Neo-Hookean material model is the logarithmic term, which penalizes the reduction of the body to zero volume since $\det \mathbf{C}_e = 2 \det \mathbf{F}_e = 2 \det \mathbf{F}$ captures the relative change of volume, cf. Eq. (2.110). For some materials (in particular, for rubbers and also for some metals) it is convenient to assume incompressibility ($\det \mathbf{F} = 1$), which reduces the elastic potential to

$$\Psi_{NH}(\mathbf{C}_e) = \frac{\mu}{2} (\text{tr } \mathbf{C}_e - 3), \quad (2.152)$$

Finally, let us mention a common model for the description of incompressible hyperelastic materials, which was introduced independently by Mooney (1952) and Rivlin (1952):

$$\Psi_{MR}(\mathbf{C}_e) = \frac{\mu}{2} \text{tr } \mathbf{C}_e + \frac{\bar{\mu}}{2} \text{tr } \mathbf{C}_e^{-1} + c_0. \quad (2.153)$$

The choice of the elastic potential in an engineering application should be made by the type of material to be modeled (and, unfortunately, very often by the amount of computational complexity allowed).

As we have seen before, several stress tensor definitions exist in finite elasticity. As before, the stress-strain relation is obtained from the elastic potential Ψ via differentiation, but we must differentiate between the three stress tensors defined above. The first and second Piola Kirchhoff tensors Σ^I and Σ^{II} , respectively, are obtained from the elastic potential Ψ in general by

$$\Sigma^I = \frac{\partial \Psi}{\partial \mathbf{F}} = \frac{\partial \Psi}{\partial \mathbf{F}_e} \cdot \mathbf{F}_p^{-T}, \quad (2.154)$$

$$\Sigma^{II} = \frac{\partial \Psi}{\partial \mathbf{E}} = 2 \frac{\partial \Psi}{\partial \mathbf{C}}. \quad (2.155)$$

The Cauchy stress tensor cannot directly be obtained by differentiation of the elastic potential (there is no conjugate strain measure corresponding to the Cauchy stress), instead the Cauchy stress can be obtained from the Piola-Kirchhoff stresses by mapping from the intermediate plastic configuration to the deformed configuration by use of \mathbf{F}_e , e.g.

$$\boldsymbol{\sigma} = \mathbf{F} \cdot \Sigma^{II} \cdot \mathbf{F}^T (\det \mathbf{F})^{-1}. \quad (2.156)$$

Note that very often it is more convenient (or even the only possible way) to define the constitutive relation for infinitesimal changes of stress $d\boldsymbol{\sigma}$ and strain $d\boldsymbol{\varepsilon}$, which for linear elasticity coincides with the infinitesimal formulation:

$$d\boldsymbol{\sigma} = \mathcal{C} : d\boldsymbol{\varepsilon}. \quad (2.157)$$

So far, we have only dealt with constitutive laws that link stresses to the elastic strain measures. In elasto-plasticity, we also need constitutive laws to control the evolution of plastic internal variables and the plastic strain tensor. These constitutive laws are often termed *flow rules* since they specify the way in which plastic flow occurs. Explicit examples for flow rules within the context of continuum plasticity and continuum dislocation theory will be discussed in Sections 2.4 and 2.5.

2.3.5 Variational Formulation for Linear Elasticity

In previous Sections we have outlined the concepts of stresses and strains in a deformed material body, and we have investigated the relationship between these tensor quantities by means of constitutive equations. In problems of solid mechanics, a material body is subject to external surface forces \mathbf{f}_t on some part of its surface, Γ_t , and volume forces \mathbf{f}_v , and it is constrained by given displacements \mathbf{u}_0 on the remaining part of its surface, Γ_u . These given external sources of influences give rise to internal stresses $\boldsymbol{\sigma}$ and strains $\boldsymbol{\varepsilon}$ (or \mathbf{F}) and result in a deformation of the material body Ω , given in terms of the displacement vector \mathbf{u} . As required in the sequel, we limit our consideration in this Section to the geometrically linear theory only. The problem is then to determine $\boldsymbol{\sigma}$, $\boldsymbol{\varepsilon}$ and \mathbf{u} which satisfy the constitutive laws and the boundary conditions

$$\mathbf{u} = \mathbf{u}_0 \quad \text{on } \Gamma_u, \quad (2.158)$$

$$\boldsymbol{\sigma} \cdot \mathbf{n} = \mathbf{f}_t \quad \text{on } \Gamma_t, \quad (2.159)$$

where \mathbf{n} is the outward unit normal vector. This leads to the boundary value problem, whose formulation within the scope of linear elasticity can be given by

$$\left. \begin{aligned} \operatorname{div} \boldsymbol{\sigma} + \mathbf{f}_v &= \mathbf{0} \\ \boldsymbol{\sigma}^T &= \boldsymbol{\sigma} \\ \boldsymbol{\sigma} &= \mathcal{C} : \boldsymbol{\varepsilon} \\ \boldsymbol{\varepsilon} &= \frac{1}{2}(\nabla \mathbf{u} + \nabla \mathbf{u}^T) \end{aligned} \right\} \quad \text{in } \Omega, \quad (2.160)$$

subject to the boundary conditions

$$\begin{aligned} \mathbf{u} &= \mathbf{u}_0 \quad \text{on } \Gamma_u, \\ \boldsymbol{\sigma} \cdot \mathbf{n} &= \mathbf{f}_t \quad \text{on } \Gamma_t. \end{aligned} \quad (2.161)$$

This formulation of the problem in terms of differential equations is the so-called strong form of the boundary value problem.

Unfortunately, an analytical solution does not appear feasible for many physical applications, which leads to the idea of deriving a numerical setting to obtain an approximate solution to the problem. Following the principle of minimum potential energy (see Section 2.5 for details), we will now introduce a variational formulation for the above boundary value problem, which allows for a numerical treatment by means of the finite element method (Hughes, 1987). This Section follows mainly the concepts and notation introduced by Cook et al. (2002). Note that we will briefly review the well-known concept of the finite element analysis for isothermal, purely elastic infinitesimal deformations only, as described by Hughes (1987) and Cook et al. (2002). If plastic flow occurs and hence dissipation

due to changes of the internal microstructure is no longer negligible, the problem becomes more complex and cannot be treated in this simple fashion. It requires adjustment to the appropriate form, which we will be discussed in Section 4.8.

According to the principle of minimum potential (see Section 2.5), the equilibrium state of a deformed body in space is characterized by a minimum of the body's total potential energy (as we neglect sources of dissipation here). Thus, the above boundary value problem can be transformed into a minimization problem which can then be solved numerically. Consider a material body of linear elastic material, which is subject to conservative loads – in particular, surface tractions \mathbf{f}_t , body forces \mathbf{f}_v – and surface constraints \mathbf{u}_0 . Furthermore, initial stresses $\boldsymbol{\sigma}_0$ and initial strains $\boldsymbol{\varepsilon}_0$ may be present. Then, the total elastic strain energy, Π_{int} , i.e. the inner energy of the body, and the work done by external forces, Π_{ext} , are given for infinitesimal strains and for quasi-static processes by

$$\Pi_{int}(\boldsymbol{\varepsilon}) = \int_{\Omega} \left[\frac{1}{2} (\boldsymbol{\varepsilon}^T : \mathcal{C} : \boldsymbol{\varepsilon}) - \boldsymbol{\varepsilon}^T : \mathcal{C} : \boldsymbol{\varepsilon}_0 + \boldsymbol{\varepsilon}^T \cdot \boldsymbol{\sigma}_0 \right] dv \quad (2.162)$$

$$\Pi_{ext}(\mathbf{u}) = - \int_{\Omega} \mathbf{u} \cdot \mathbf{f}_v dv - \int_{\Gamma_t} \mathbf{f}_t \cdot \mathbf{u} ds - \int_{\Gamma_u} \mathbf{t} \cdot (\mathbf{u} - \mathbf{u}_0) ds. \quad (2.163)$$

The total potential of a strained body is then given by

$$\Pi_{tot} = \Pi_{int} + \Pi_{ext}. \quad (2.164)$$

Note that here we only account for the stored elastic energy so that the Helmholtz free energy equals the elastic strain energy potential. As strains $\boldsymbol{\varepsilon} = \boldsymbol{\varepsilon}(\mathbf{u})$ directly follow from the displacement field \mathbf{u} , we can formulate the strain energy and the external work in terms of \mathbf{u} only. Let us furthermore neglect initial stresses and strains so that (with \mathbf{t} being the traction)

$$\Pi_{tot}(\mathbf{u}) = \frac{1}{2} \int_{\Omega} \boldsymbol{\varepsilon}^T(\mathbf{u}) : \mathcal{C} : \boldsymbol{\varepsilon}(\mathbf{u}) dv - \int_{\Omega} \mathbf{u} \cdot \mathbf{f}_v dv - \int_{\Gamma_t} \mathbf{u} \cdot \mathbf{f}_t ds - \int_{\Gamma_u} \mathbf{t} \cdot (\mathbf{u} - \mathbf{u}_0) ds. \quad (2.165)$$

Now, we can write the minimization problem as

$$\mathbf{u} = \operatorname{argmin} \{ \Pi_{tot}(\mathbf{u}) \mid \mathbf{u} = \mathbf{u}_0 \text{ on } \Gamma_u \}, \quad (2.166)$$

which leads to the variational equation

$$\delta \Pi_{tot}(\mathbf{u}) = 0. \quad (2.167)$$

Applying (2.165) to (2.167), we obtain

$$\int_{\Omega} \boldsymbol{\varepsilon}^T(\mathbf{u}) : \mathcal{C} : \boldsymbol{\varepsilon}(\delta \mathbf{u}) dv - \int_{\Omega} \delta \mathbf{u} \cdot \mathbf{f}_v dv - \int_{\Gamma_t} \delta \mathbf{u} \cdot \mathbf{f}_t ds - \int_{\Gamma_u} \delta \mathbf{t} \cdot (\mathbf{u} - \mathbf{u}_0) ds = 0. \quad (2.168)$$

We have arrived at the so-called weak form of the boundary value problem. If we now limit our analysis to finding approximate solutions only to the boundary value problem defined in (2.160) and (2.161), and hence consider a class of variations $\delta \mathbf{u}$ with $\mathbf{u} = \mathbf{u}_0$ on Γ_u , then the solution obtained from (2.168) will always exactly satisfy the boundary condition (2.158) as well as the strain-displacement relation (2.121) and the constitutive law (2.144), whereas the equilibrium conditions (2.138) and the boundary condition (2.159) hold true in an integral sense only. Keeping in mind these numerical deviations from the differential

problem, we can solve the variational problem (2.168) instead of the differential problem (2.160), (2.161).

The finite element method is based on the discretization of the geometry as well as all scalar and field variables involved and thereby provides approximate solutions to the given variational problem. In order to treat Eq. (2.168) numerically, let us first introduce the advantageous Voigt notation for stresses and strains, which arranges these quantities as vectors instead of tensors, i.e.

$$\tilde{\sigma} = (\sigma_{11}, \sigma_{22}, \sigma_{33}, \sigma_{12}, \sigma_{23}, \sigma_{31})^T, \quad (2.169)$$

$$\tilde{\varepsilon} = (\varepsilon_{11}, \varepsilon_{22}, \varepsilon_{33}, \gamma_{12}, \gamma_{23}, \gamma_{31})^T. \quad (2.170)$$

Following these definitions, the constitutive equation of linear elasticity reduces to

$$\tilde{\sigma} = \mathbf{E} \cdot \tilde{\varepsilon}, \quad (2.171)$$

where the elasticity matrix \mathbf{E} is given by

$$\mathbf{E} = \frac{E}{(1+\nu)(1-2\nu)} \begin{pmatrix} 1-\nu & \nu & \nu & 0 & 0 & 0 \\ \nu & 1-\nu & \nu & 0 & 0 & 0 \\ \nu & \nu & 1-\nu & 0 & 0 & 0 \\ 0 & 0 & 0 & \frac{1-2\nu}{2} & 0 & 0 \\ 0 & 0 & 0 & 0 & \frac{1-2\nu}{2} & 0 \\ 0 & 0 & 0 & 0 & 0 & \frac{1-2\nu}{2} \end{pmatrix} \quad (2.172)$$

for a general three-dimensional deformation of an isotropic linear-elastic material with Young's modulus E and Poisson's ratio ν . In many engineering applications this general formulation is not necessary and one can reduce the complexity of the mathematical problem by applying one of the two assumptions of plane strain or plane stress. If the body under investigation is very thick compared to its other geometric extension, one can neglect strain and deformation in direction of the thick extension so that the deformation and strain field can be approximated as being completely in-plane ($\varepsilon_{3i} = 0$), and the body is in a state of plane strain. If, in contrast, the body is very thin compared to the other geometric extensions, we can assume that the stresses in the thickness direction vanish ($\sigma_{3i} = 0$) and assume a state of plane stress. Applying one of these two assumptions can reduce the above problem's complexity. For plane stress, we have

$$\mathbf{E}_{\text{plane stress}} = \frac{E}{1-\nu^2} \begin{pmatrix} 1 & \nu & 0 \\ \nu & 1 & 0 \\ 0 & 0 & 1-\nu \end{pmatrix}, \quad (2.173)$$

and for plane strain

$$\mathbf{E}_{\text{plane strain}} = \frac{E}{(1+\nu)(1-2\nu)} \begin{pmatrix} 1-\nu & \nu & 0 \\ \nu & 1-\nu & 0 \\ 0 & 0 & 1-2\nu \end{pmatrix}, \quad (2.174)$$

with, in both cases,

$$\tilde{\varepsilon} = (\varepsilon_{11}, \varepsilon_{22}, \varepsilon_{12})^T, \quad \tilde{\sigma} = (\sigma_{11}, \sigma_{22}, \sigma_{12})^T. \quad (2.175)$$

In case of plane strain, the missing non-zero stress component in thickness direction follows as $\sigma_{33} = -\nu(\sigma_{11} + \sigma_{22})$. Analogously, in case of plane stress the missing non-zero strain component is obtained from $\varepsilon_{33} = -\nu(\sigma_{11} + \sigma_{22})/E$.

As the only numerical problems treated in this thesis are based on the assumption of plane strain, we will proceed by using Eq. (2.174) only. Then, let us introduce the differential operator matrix

$$\mathbf{B} = \begin{pmatrix} \frac{\partial}{\partial x_1} & 0 \\ 0 & \frac{\partial}{\partial x_2} \\ \frac{\partial}{\partial x_1} & \frac{\partial}{\partial x_2} \end{pmatrix} \quad (2.176)$$

in order to write the strain-deformation relation as

$$\tilde{\boldsymbol{\varepsilon}} = \mathbf{B} \cdot \tilde{\mathbf{u}}, \quad (2.177)$$

where for plane deformation states we use

$$\tilde{\mathbf{u}} = (u, v)^T. \quad (2.178)$$

As a consequence, the total strain energy takes the form

$$\Pi(\mathbf{u}) = \frac{1}{2} \int_{\Omega} \mathbf{u} \cdot \mathbf{B} \mathbf{E} \mathbf{B} \cdot \mathbf{u} \, dv - \int_{\Omega} \mathbf{u} \cdot \mathbf{f}_v \, dv - \int_{\Gamma_t} \mathbf{u} \cdot \mathbf{f}_t \, ds - \int_{\Gamma_u} \mathbf{t} \cdot (\mathbf{u} - \mathbf{u}_0) \, ds. \quad (2.179)$$

This formulation allows for the variational principle to be written as

$$\int_{\Omega} \mathbf{u} \cdot \mathbf{B} \mathbf{E} \mathbf{B} \cdot \delta \mathbf{u} \, dv - \int_{\Omega} \delta \mathbf{u} \cdot \mathbf{f}_v \, dv - \int_{\Gamma_t} \delta \mathbf{u} \cdot \mathbf{f}_t \, ds - \int_{\Gamma_u} \delta \mathbf{t} \cdot (\mathbf{u} - \mathbf{u}_0) \, ds = 0. \quad (2.180)$$

This variational formulation will be used in the following as the basis for finite element approximations of the given boundary value problem. After specifying a class of variations (i.e. a class of possible approximations for \mathbf{u}), the solution is obtained from solving the variational problem (2.180).

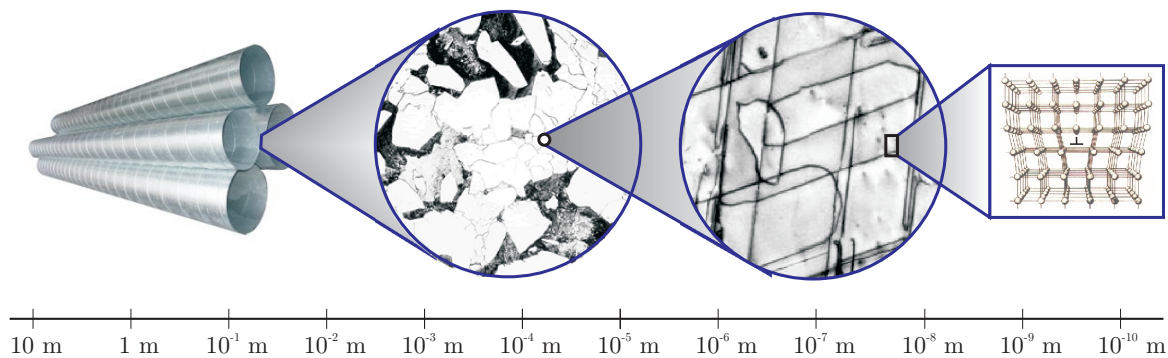


Figure 2.8: Different length scales involved in plasticity: from the macroscopic body to the grain level to the sub-grain dislocation network to an atomistic view.

2.4 Continuum Theories of Plasticity and Dislocations

2.4.1 Bridging the Scales in Elasto-Plasticity

One of the major difficulties when modeling the elasto-plastic behavior of engineering materials lies in the number of length scales involved. Elastic and in particular plastic deformation is not only the macroscopic behavior one can observe with the naked eye, but it involves many mechanisms on length scales far below the body's dimensions, which have only been made visible thanks to the progress in modern microscopic techniques over the last few decades. Figure 2.8 sketches the most important length scales involved.

The structure of a modeled body usually defines the *macroscopic* level, which can range from a few millimeters to kilometers depending on the body's extensions. This is the scale we can commonly observe without technical equipment and where we are interested in the mechanical behavior of the entire body or structure. A light microscope reveals characteristics on the first length scale invisible to the naked eye, often called the *mesoscale*. On the mesoscale, one notices that the seemingly homogeneous body consists of a large number of grains with different crystal orientations, whose usual diameters lie on the order of magnitude of $5 - 200 \mu\text{m}$. These grains form the polycrystal. In most of the investigations in this thesis, we limit our considerations to single crystals which consist of only one homogeneous grain. With the aid of transmission electron microscopy (TEM) one can reach the next length scale, often referred to as the *microscale* (with typical dimensions of $0.1 - 3 \mu\text{m}$). On this scale, large configurations of atomic lattice disorders (so-called dislocations) become visible, forming the dislocation sub-structures. Together with other crystal defects these appearances form the so-called microstructure. The dislocations, as discussed in subsequent Sections, are crucial to accommodate the plastic deformation of a crystalline solid. Finally, the lowest of all levels, the *atomic scale*, displays the atomic structure of the body with typical lengths of a few Å (10^{-10}m).

An ideal modeling approach for elasto-plasticity of solids would involve modeling the respective mechanisms on all length scales and combine these to finally determine the mechanical behavior. Common continuum mechanics approaches can attack the macroscopic problem effectively but usually lack influence from the underlying levels. On the other hand, molecular dynamics simulations can treat problems on the atomic level but are highly restrictive in time and space by the enormous computational effort. Modern approaches are

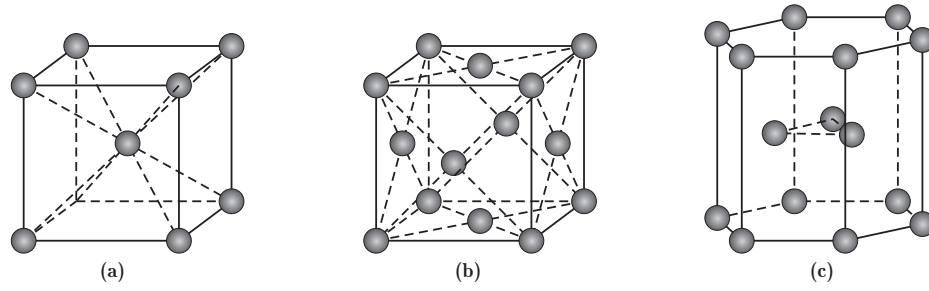


Figure 2.9: Unit cells of (a) bcc, (b) fcc and (c) hcp crystal structures.

capable of combining the effects on more than one length scale in a continuum sense; they are therefore called *multiscale methods* (Ilic, 2008; Bartel, 2009). In this thesis, we predominantly adopt a different approach which places the model on the macroscopic or mesoscopic scale but accounts for microstructural effects (such as dislocation mechanics) in a continuum way. In this Section we will give a brief outline of those mechanisms on the microscale which need to be represented in such models.

2.4.2 The Crystal Lattice, Elastic and Plastic Deformation

On a very small scale, every material consists of the very same fundamental components of nature, atoms and molecules. In contrast to many other materials metals arrange these atoms or molecules in a particular order, lining up the atomic cores in a three-dimensional regular periodic array and leaving the electrons move freely within their orbitals (sometimes referred to as the electron gas) around these core positions. In this configuration, every atom of the unstrained body is in a stable equilibrium position. For simplicity, we will no further consider this specific distribution of atomic cores and electrons but imagine only the far heavier cores to be lined up following a regular pattern, which results in a periodic crystal lattice. The repetitive structure of such a crystal lattice makes it sufficient to know only the structure of one unit cell, as the entire crystal lattice can be obtained from that unit cell via translational invariance. Depending on the arrangement of atoms in this unit cell, the crystal lattice structure is called *cubic face-centered* (fcc), *body-centered cubic* (bcc) or *hexagonal close-packed* (hcp), which constitute the most common configurations in metals.

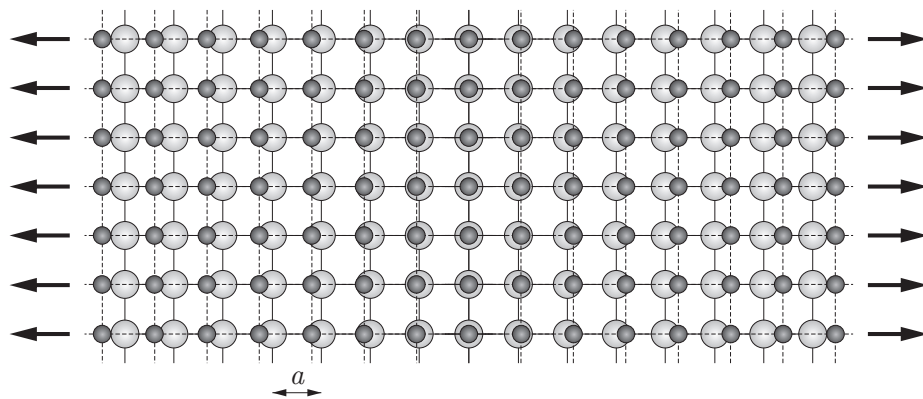


Figure 2.10: The crystal lattice accommodates elastic deformation.

The unit cells of all three configurations are illustrated in Figure 2.9. Of course, we will limit our analyses in this thesis to such scales where the discrete lattice structure can be neglected and the body hence treated by continuum theories. However, it is important to understand the underlying mechanisms and have a basic background of those phenomena accompanying elastic and plastic deformation of metals. Therefore, this Section will give a brief introduction into the basic deformation modes and mechanisms in metals.

Metals undergo elastic and plastic deformations, which are sometimes very hard to differentiate on the macroscale (remember the difficulty in finding the yield point in Figure 2.7b) but which are traced back to completely different mechanisms on the microscale. Elastic deformation results from collective straining of the crystal atoms about their equilibrium positions as sketched in Figure 2.10. This deformation is reversible and, upon unloading the crystal, all atoms will return to their equilibrium positions. (The elastic behavior can easily be imagined as a cluster of point masses connected by non-linear springs, which upon unloading return to their original state of minimum energy. Molecular dynamics simulations are, roughly speaking, based on this approach but with the spring-like interactions commonly characterized by Lennard-Jones potentials.) The elastic properties of a material are hence a macroscopic result of the crystal lattice properties (such as the average atomic spacing a and the resulting attractive and repulsive forces of regular lattice atoms), which allows for an atomistic determination of the elastic constants from energetic considerations.

Plastic deformation, in contrast, is irreversible, it does not collectively strain the crystal lattice, and its characteristics are far more complex and difficult to determine from the microscale than are the elastic constants. Ewing and Rosenhain (1899) were among the first to propose that plastic deformation is realized by a glide process on certain glide planes within the crystal, which was confirmed experimentally later. Crystallographic gliding is one of the most important microstructural mechanisms to accommodate plastic deformation, during which parts of the strained crystal irreversibly travel along a certain *glide plane* into a given *slip direction*, see Figure 2.11a. This often gives rise to steps at the free crystal surfaces. Plane and direction of slip determine the so-called *slip system*. The basic process of plastic gliding is depicted in Figure 2.11b,c. First assumptions that the upper part of the shown crystal would simply collectively glide on the lower part of the crystal were proved invalid because this would predict too high a critical strength of the crystal (Frenkel, 1926). The stress required to move a complete part of the crystal along another part at once would simply be too high. Instead, plastic slip normally results from motion and interaction of microstructural lattice defects of all kinds, the most important ones forming the large group of dislocations.

2.4.3 Lattice Defects

The crystal lattice depicted in Figure 2.10 is a perfect lattice. However, experimental observations have revealed that crystal lattice configurations in actual materials are hardly ever perfect. Indeed, one finds that there are probably even more defects than perfectly arranged lattice regions in a standard engineering metal. When talking about defects of crystal lattices, we differentiate several kinds of defects, which can roughly be grouped by their dimensions (see Figure 2.12b): Zero-dimensional defects or *point defects* comprise solute foreign atoms at lattice positions (1) (e.g. manganese atoms in high-manganese steels), displaced lattice atoms (2), interstitially solute foreign atoms (3) (e.g. nitrogen or hydrogen atoms in steels), or vacancies (i.e. missing lattice atoms) (4). These defects are closely re-

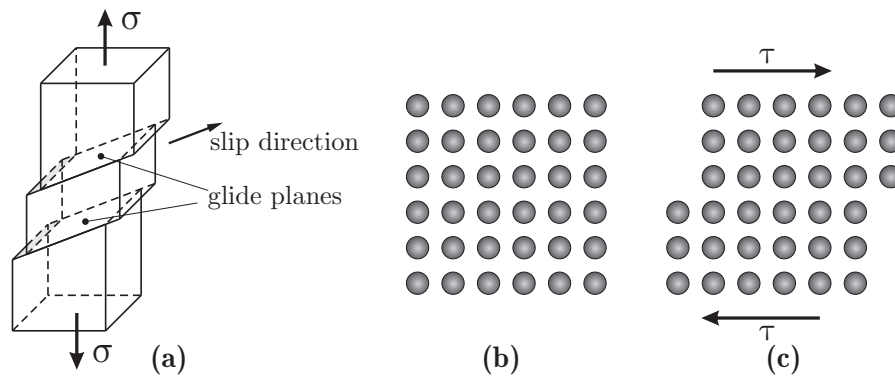


Figure 2.11: (a) Example of plastic slip in a uniaxial tension test, (b) microstructural sketch of the perfect lattice and (c) of the sliding of a glide plane.

lated to the well-known *Schottky defects*, where a lattice atom has wandered to the surface leaving a vacancy in the crystal lattice, and *Frenkel defects*, where a vacancy arises from a lattice atom misplaced at an interstitial position. One-dimensional linear lattice defects are, roughly speaking, irregularities in the periodic crystal lattice and very often extra or missing half-planes of atoms in the regular lattice, see e.g. Figure 2.12c. Since in all of these latter configurations groups of atoms are „dislocated“ from their regular equilibrium positions, we call these defects *dislocations*. Two- and three-dimensional defects finally comprise such lattice distortions as due to particulate inclusions, phase boundaries or grain boundaries, to mention only a few.

All of these crystal lattice defects influence their neighborhood through long-range stress fields. For example, the larger foreign atom (1) distorts the crystal lattice, resulting in a compressive stress in its neighborhood, which aims at expanding the crystal lattice locally, whereas a vacancy (4) in the lattice gives rise to tensile stresses in its neighborhood, attracting other defects and aiming at shrinking the lattice crystal locally. Finally, the small interstitials (3) e.g. impede motion of the neighboring crystal atoms.

All such crystal characteristics appear on the material's microscale. Therefore, they comprise the material's *microstructure*. As we have seen, the properties of the regular lattice (e.g. average atomic spacing, attractive and repulsive forces of regular lattice atoms) influence the elastic properties of a macroscopic material body. The crystal defects have some

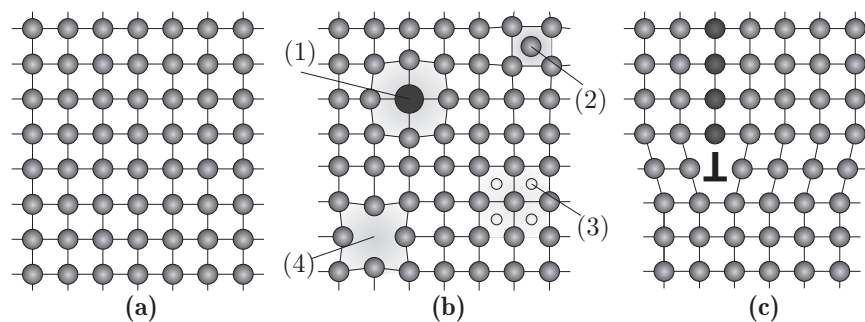


Figure 2.12: Lattice defects in crystalline solids: (a) perfect lattice; (b) disturbed lattice with substitute foreign atom, interstitially solute foreign atoms and a vacancy; (c) edge dislocation.

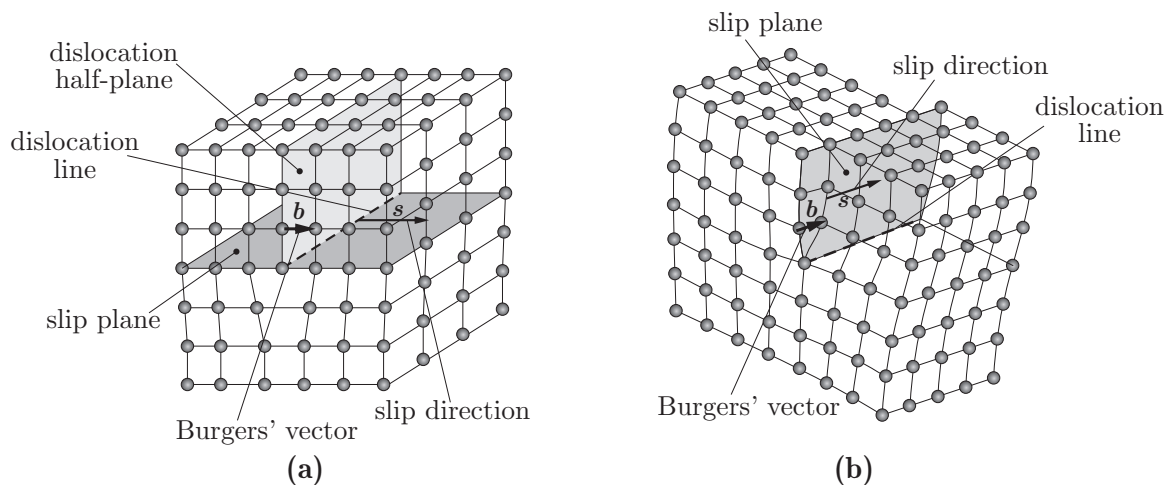


Figure 2.13: Edge and screw dislocation.

influence on the elastic properties (e.g. by changing the atomic spacing through foreign atoms or interstitials) but, most important, they affect the ability of the atomic lattice to undergo irreversible rearrangements and are hence responsible for the plastic behavior of a material. Of the aforementioned defects, the most important ones for plastic deformation of metals are the dislocations, which will be discussed in somewhat more detail in the next Section. For a more detailed investigation see (Hirth and Lothe, 1982).

2.4.4 Properties of Dislocations

The theory of dislocations was originally developed by Volterra (1905) at the beginning of the 20th century and has been enhanced and extended ever since. The foundation for the modern theory of slip due to dislocations goes back to Orowan (1934), Polanyi (1934) and Taylor (1934). Dislocations are irregularities in the periodic crystal lattice and there are two primary types of dislocations, the *edge dislocation* and the *screw dislocation*. Both types of dislocations are sketched in Figure 2.13. An edge dislocation results from an extra half-plane (or a missing half-plane) in the otherwise perfectly arranged crystal, as seen in Figure 2.13a. Therefore, an edge dislocation is often represented by a T-symbol as shown already in Figure 2.12c. For an edge dislocation, the dislocation line lies within the glide plane, the dislocation moves through the crystal perpendicularly to the dislocation line, i.e. in the direction of the shown slip vector s . Therefore, the *Burgers' vector* b (i.e. the resultant vector needed to close the unit circuit around the dislocation core) is perpendicular to the dislocation line. If the Burgers' vector equals a lattice vector, we speak of a *complete dislocation*, otherwise the dislocation is *incomplete*. The Burgers' vector is of the same order of magnitude as the lattice spacings and results from the lattice characteristics and the active slip system. A screw dislocation (symbol \odot) is regarded more difficult to understand as it usually results from a lattice irregularity that does not involve extra or missing elements but simply a disorder of the otherwise perfectly arranged lattice, as shown in Figure 2.13b. The dislocation line again lies within the glide plane, but now the dislocation moves parallel to the dislocation line, and so is the Burgers' vector, i.e. $s \parallel b$. Dislocations in actual materials are usually more complex and involve combinations of both types of dislocations, called *mixed dislocations*.

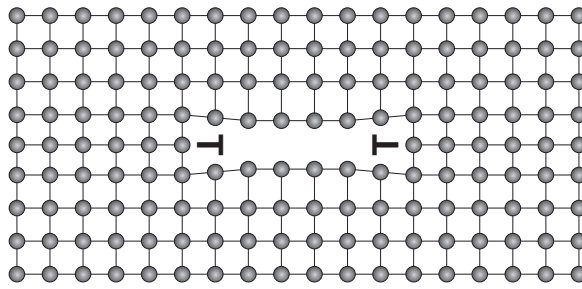


Figure 2.14: Prismatic dislocation loop.

In general, dislocation lines are not straight but may be curved in the crystal's interior, they can end at free surfaces (and only there) or they can close to form dislocation loops which comprise parts of both edge and screw dislocation character. A special case among these loops are the so-called *prismatic dislocation loops* which form around conglomerates of vacancies or around obstacles, see Figure 2.14.

The choice of glide planes and Burgers' vectors is, of course, not arbitrary but limited in terms of the given crystal structure. In fcc and bcc metals, glide planes are commonly close-packed planes in the lattice with the slip direction being in a close-packed direction. Examples for glide planes in bcc and fcc metals are illustrated in Figure 2.9. For an fcc metal e.g. glide planes commonly are of type $\{111\}$, and the slip direction is of type $\langle 110 \rangle$. In bcc metals, we commonly observe glide planes of type $\{110\}$ and slip directions of type $\langle 111 \rangle$. Planes and directions are characterized using standard Miller indices, see e.g. (Hirth and Lothe, 1982). Typical slip planes for bcc and fcc metals are sketched in Figure 2.16. In hcp materials, the choice of the slip direction is more limited than in fcc or bcc metals because only a few slip systems exist.

Dislocations are important to realize plastic deformation as they can easily travel through the crystal lattice. As already mentioned, early analyses revealed that metals do not deform plastically by collective motion of entire blocks of atoms by one another but they accommodate plastic deformation by dislocation motion. Figure 2.15 illustrates how a moving edge dislocation can accommodate the plastic deformation already depicted in Figure 2.11. The stress required to move the edge dislocation step-by-step through the crystal is essentially less than that required to move the upper part of the crystal as one, because – instead of

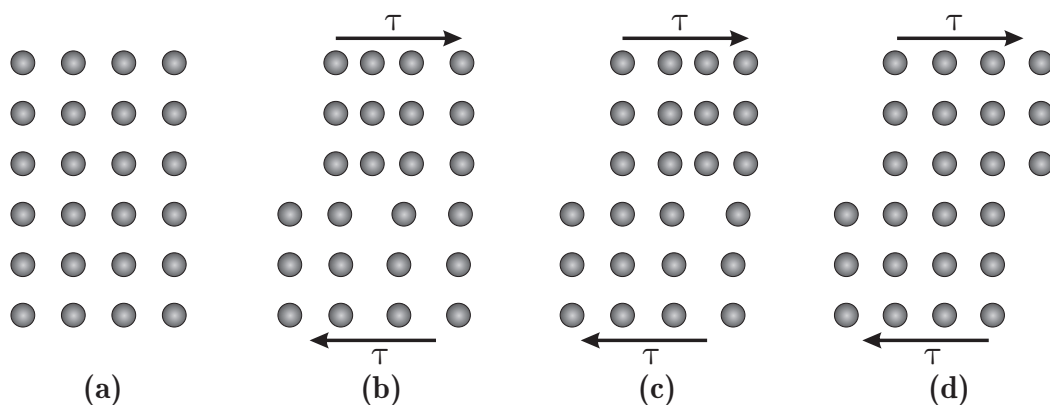


Figure 2.15: Basic mechanism of plastic slip through a propagating dislocation.

moving complete lattice regions one by another – it is sufficient to locally re-arrange the lattice around the dislocation only to plastically deform the crystal. Figure 2.17 exemplarily shows a moving edge dislocation traveling step-by-step through the crystal.

In metals dislocations have a variety of possible choices for active slip systems. In general, plastic slip will prefer predominantly those slip systems where the highest internal shear stresses act. If we apply an external tensile stress σ as in Figure 2.11a, this stress will result in a shear stress on each glide plane, the so-called *resolved shear stress*, which depends on the orientation of the slip system. The resolved shear stress τ_{res} resulting from an externally applied tensile stress σ takes the form

$$\tau_{\text{res}} = \sigma \cos \varphi \cos \theta, \quad (2.181)$$

where φ denotes the angle between the glide direction and the direction of the applied tensile stress, and θ represents the angle between the glide plane normal and the direction of the applied stress. A material's resistance to dislocation motion can now be characterized by a critical resolved shear stress $\tau_{\text{crit.}}$, which is a material property dependent on the slip system.

As this thesis is mainly concerned with edge dislocations to form microstructural patterns, we will limit some of the sequel to pure edge dislocations only. One can easily imagine that inserting an extra half-plane into an otherwise perfect crystal will give rise to an elastic distortion of the lattice and hence to a stress field around the dislocation, which is illustrated in Figure 2.18a: In the upper part of the crystal the extra half-plane will result in compressive stresses trying to relax the crystal lattice by expansion; in the lower part of the crystal the distorted lattice atoms below the dislocation core give rise to tensile stresses aiming at bringing the atoms closer together. The highest stresses occur in the neighborhood of the dislocation core. The stress field is of long-range nature and can influence neighboring atoms as well as other lattice defects, as will be discussed later. When treating the atomic body as an elastic quasi-continuum, the stress field around the core of a screw dislocation can be derived in a simple form using cylindrical coordinates (r, θ, z) , as the only non-zero component is the shear stress

$$\tau_{rz}(r) = \frac{\mu b}{2\pi r}. \quad (2.182)$$

For an edge dislocation, the picture is somewhat more complicated (see Figure 2.18a): The

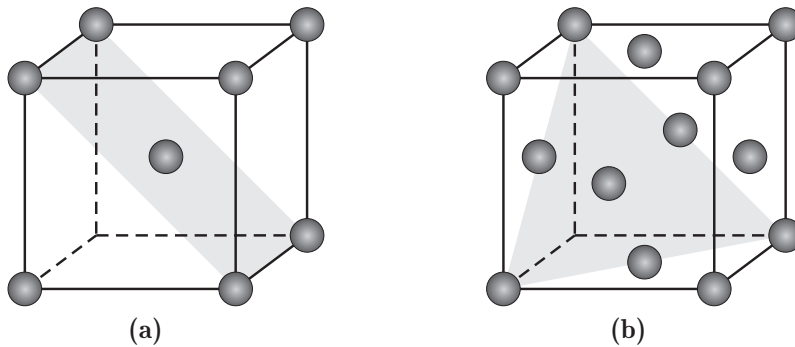


Figure 2.16: Typical slip planes in bcc and fcc unit cells (slip planes are closed-packed planes).

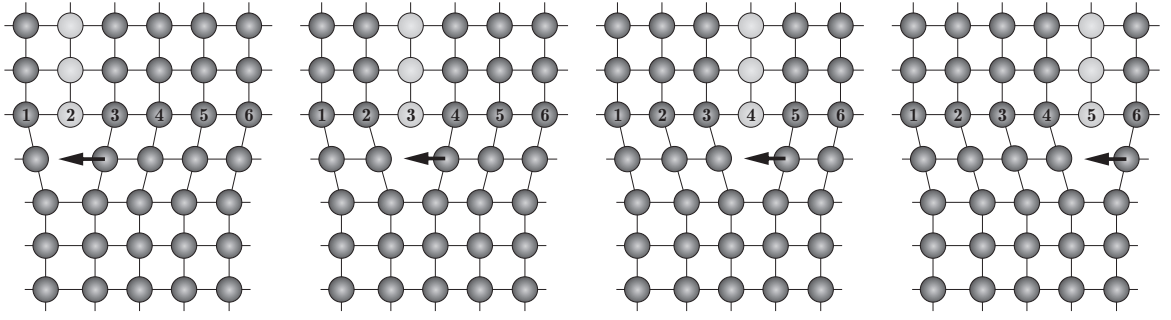


Figure 2.17: Edge dislocation traveling through the crystal lattice (numbering is for clearness only).

stress field in cylindrical coordinates is characterized by the non-zero components

$$\begin{aligned}\sigma_{rr} = \sigma_{\theta\theta} &= -\frac{\mu b \sin \theta}{2\pi(1-\nu)r}, \\ \sigma_{r\theta} &= \frac{\mu b \cos \theta}{2\pi(1-\nu)r}, \quad \sigma_{zz} = -\frac{\mu b \nu \sin \theta}{\pi(1-\nu)r}.\end{aligned}\quad (2.183)$$

For details on the derivation see e.g. (Hirth and Lothe, 1982). From these results it becomes obvious that the stress fields are long-range but decay rapidly with increasing distance r from the dislocation core.

Now, imagine an externally applied homogeneous stress field acting on an existing dislocation. Let the dislocation be straight with Burgers' vector \mathbf{b} but of mixed type such that the dislocation line with orientation vector $\boldsymbol{\xi}$ is not necessarily parallel to \mathbf{b} . Denoting the external stress field (without self-stresses) by $\boldsymbol{\sigma}$, the force on the dislocation per unit length equals (Peach and Köhler, 1950)

$$\mathbf{f} = (\mathbf{b} \cdot \boldsymbol{\sigma}) \times \boldsymbol{\xi}. \quad (2.184)$$

It can be shown that the force acting on the dislocation decomposes into a so-called glide component and a climb component:

$$\mathbf{f}_{\text{glide}} = \frac{[(\mathbf{b} \cdot \boldsymbol{\sigma}) \times \boldsymbol{\xi}] \cdot [\boldsymbol{\xi} \times (\mathbf{b} \times \boldsymbol{\xi})]}{|\mathbf{b} \times \boldsymbol{\xi}|}, \quad \mathbf{f}_{\text{climb}} = \frac{[(\mathbf{b} \cdot \boldsymbol{\sigma}) \times \boldsymbol{\xi}] \cdot (\mathbf{b} \times \boldsymbol{\xi})}{|\mathbf{b} \times \boldsymbol{\xi}|}. \quad (2.185)$$

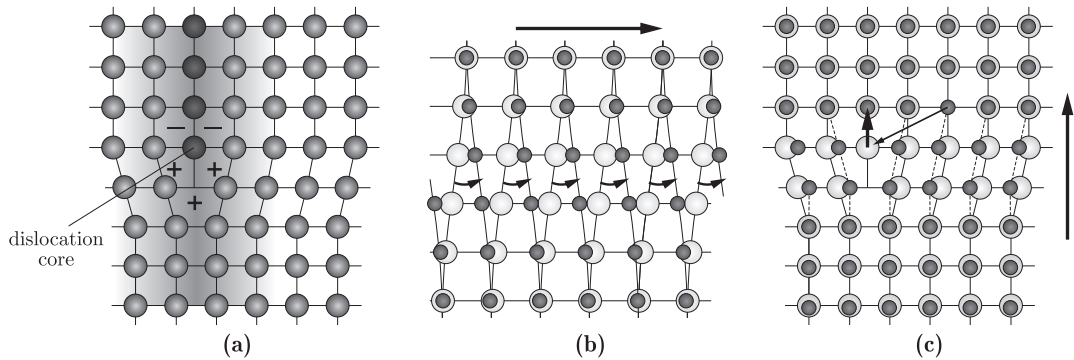


Figure 2.18: (a) Stress field around an edge dislocation; edge dislocation traveling through the crystal lattice (b) by sliding, (c) by climbing.

These forces can most easily be interpreted for a pure edge dislocation with $\mathbf{b} = (b, 0, 0)^T$ and the dislocation line direction $\mathbf{l} = (0, 1, 0)^T$, where the force per unit length reduces to the neat form

$$\mathbf{f}_{\text{edge}} = (-\sigma_{xz}b, 0, \sigma_{xx}b)^T. \quad (2.186)$$

The first entry aims at moving the dislocation in its principal slip direction in the active glide plane, it hence provides the driving force for dislocation gliding and is therefore called *glide force*. The last entry tends to move the dislocation perpendicular to the glide plane, i.e. the dislocation is driven to leave its glide plane by climbing upwards or downwards. Therefore, this component is often termed the *climb force*. The force per unit length \mathbf{f} is known as the Peach-Köhler force (Peach and Köhler, 1950).

Note that the above shown climb force of an edge dislocation is only correct for conservative dislocation climbing, as pointed out by Weertman (1965) who proposed a modification of the above formulation. Weertman (1965) argued that, in general, climbing of an edge dislocation is linked to motion or nucleation of vacancies in the crystal lattice, which, in turn, requires a chemical driving force. Hence the actual climb force is obtained by considering only the deviatoric stress tensor in (2.184) and taking into account a chemical driving force which depends on the vacancy concentration in the crystal.

Analogously for a pure screw dislocation ($\mathbf{b} = (b, 0, 0)^T$ and $\mathbf{l} = (1, 0, 0)^T$), we obtain the Peach-Köhler force

$$\mathbf{f}_{\text{screw}} = (0, -\sigma_{xz}b, -\sigma_{yz}b)^T. \quad (2.187)$$

So, the Peach-Köhler force for a screw dislocation acts equally in y - and z -direction perpendicular to the dislocation line. There is no unique slip direction, and a screw dislocation cannot climb like an edge dislocation.

Resulting from the glide and climb forces, there are two independent modes by means of which an edge dislocation can move through the crystal. These modes are shown in Figure 2.18. Figure 2.18b illustrates the same type of dislocation motion as already sketched in Figure 2.17 (light atoms illustrate the original position, dark atoms the current position after the dislocation has traveled through the plane). This mode of dislocation motion is known as *dislocation slip* or *dislocation gliding*, since a half-plane glides through the crystal on a certain glide plane. Figure 2.18c displays the other mode of dislocation motion, commonly referred to as *dislocation climbing*: Driven by its stress field, the dislocation leaves its glide plane and moves perpendicular to the Burgers' vector. As dislocation climbing requires the diffusion of a vacancy to the dislocation core (which, in turn, can only be thermally activated at higher temperatures due an Arrhenius-type law), dislocation climbing only occurs when thermally activated, e.g. at temperatures higher than half the holonomous temperature.

Now, it becomes apparent why plastic deformation accommodated by dislocation motion is irreversible: There is no difference or preference of the new and the original atom positions in Figure 2.18. It takes an external stress to move the dislocation from one position to another (which dissipates energy). The dislocation will not move back as the external stress is released, but it remains at its new position. Plastic deformation due to dislocation motion hence is permanent, i.e. irreversible, and it consumes energy.

The existence of a dislocation results in a distorted crystal lattice which, in turn, gives rise to elastic pre-strains and pre-stresses in the crystal, see Eqs. (2.182) and (2.183). Therefore,

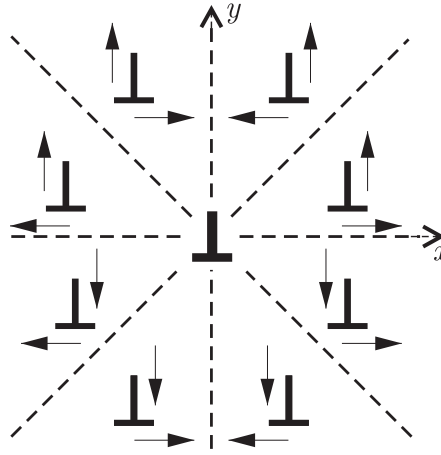


Figure 2.19: Glide and climb forces between two interacting parallel edge dislocations (the dislocation at the center is assumed fixed, the other dislocation mobile). Arrows show forces acting on the mobile dislocation due to the fixed dislocations.

the dislocation stores elastic energy in the crystal:

$$E_{\text{disl}} = \int_{\Omega} \boldsymbol{\sigma} : \boldsymbol{\varepsilon} \, dv \quad (2.188)$$

One can show (Hirth and Lothe, 1982) that the stored energy arising from a single dislocation, the so-called *self-energy* of the dislocation, is of the type

$$E_{\text{disl}} = \alpha \mu b^2, \quad \text{with } \alpha = 0.5 \dots 1.5, \quad (2.189)$$

and that

$$E_{\text{edge}} = 1.5 E_{\text{screw}}. \quad (2.190)$$

This comparably high energy of dislocations indicates that dislocations are (other than e.g. vacancies) non-equilibrium defects, i.e. it takes an externally applied force to create a dislocation. They do not arise from thermodynamic principles out of a homogeneous material body in equilibrium.

2.4.5 Dislocation Interactions and Sources

The stress field around a dislocation affects the interaction with other dislocations and defects as well. For example, two parallel edge dislocations will attract or repel each other depending on their arrangement as depicted in Figure 2.19 which illustrates the forces acting on a second edge dislocation depending on its position relative to the first edge dislocation in the center. Let us place the coordinate system's origin at the dislocation core of the central dislocation with the z -axis coming out of the plane (as illustrated). Now, the interaction force per unit length between the two edge dislocations with parallel Burgers' vectors \mathbf{b}_1 and \mathbf{b}_2 , the second being at position $(x, y, 0)$, yields

$$\mathbf{f}_{\text{inter}} = \frac{\mu \mathbf{b}_1 \cdot \mathbf{b}_2}{2\pi(1-\nu)} \frac{1}{r^4} \begin{pmatrix} x(x^2 - y^2) \\ y(3x^2 + y^2) \\ 0 \end{pmatrix}, \quad (2.191)$$

where $r = \sqrt{x^2 + y^2}$ is the distance between the dislocations. According to their orientation parallel and perpendicular to the glide plane, the first component represents a glide force, the second component a climb force. Figure 2.19 illustrates the interaction forces between two parallel edge dislocations of equal signs. Parallel edge dislocations with equal signs under angles between -45° and $+45^\circ$ hence repel each other. Under angles between $45^\circ < \varphi < 135^\circ$ and $-45^\circ > \varphi > 135^\circ$ parallel edge dislocations try to arrange above or below each other ($\varphi = 90^\circ$) since this configuration is stable. This is e.g. the reason for the formation of low-angle grain boundaries during recrystallization, see also Figure 2.22. The interaction forces for arbitrary dislocation geometries can be found in (Hirth and Lothe, 1982).

As a result of these interaction stresses and forces we can also introduce an *interaction energy* which results from the elastically distorted crystal lattice. For two parallel straight edge dislocations with common Burgers' vector the interaction energy scales as

$$E_{\text{inter}} \propto \frac{\mu b^2}{2\pi} \ln R, \quad (2.192)$$

where R is the distance between the dislocations. It becomes apparent that the energy tends to infinity as the dislocations move together. The total energy of all dislocations in a crystal equals the sum of the dislocation self-energies and the interaction energies. If only a few dislocations are present in the crystal (with consequently large distances between them), then the interaction energies are negligible and the dislocation self-energies dominate. With increasing number of dislocations, however, the interaction energy gains more importance as the dislocations move closer together. Examples for interaction energies are given in (Hirth and Lothe, 1982).

Dislocations do not only interact with other dislocations but also with other sorts of microstructural defects, some further examples of dislocation interactions are shown in Figure 2.20: Two parallel edge dislocations of opposite sign (a) attract and annihilate each other, forming an again perfect crystal. Dislocations are attracted by free surfaces (b) where the dislocation may leave the crystal. (Once having left the crystal, the dislocation does no longer distort the crystal. However, each dislocation at the free surface creates a step of the surface and thereby either additional surface energy.) Very often, dislocations are surrounded by other defects which restrict the dislocation motion. Interstitials e.g. can impede dislocation motion by forming clouds of interstitial atoms around the dislocation (c), so-called *Cottrell clouds*. The dislocation is *pinned*. Other dislocation-pinning obstacles are foreign atoms (d) but also grain or phase boundaries at which dislocations can pile-up. To move a pinned dislocation it takes higher stresses such that often stick-slip mechanisms are observed, where the dislocation is pinned until the increasing stress is high enough to move the dislocation until it is pinned again etc.

Of course, interacting dislocations are not always parallel and straight and there's hardly ever only one active slip system, but very often dislocations on different slip systems interact, and the presence of other slip systems can influence the behavior of an existing dislocations. Sometimes it is more convenient for a dislocation to leave its current slip system and to travel further on another glide plane; this process is known as *cross-slip*. However, the motion of dislocations in cross-slip is more complicated and requires higher activation stresses such that dislocations exhibiting cross-slip are more difficult to move. A similar behavior can be observed from dislocations having so-called *kinks* and *jogs* which form if not the entire dislocation climbs but only part of the dislocation line climbs to the new glide plane and the remaining slip line remains in the original glide plane. Kinks and jogs have a similar aggravating impact on dislocation motion.

As mentioned in the previous Section, dislocations are non-equilibrium defects and only form under applied external stresses. However, dislocations commonly do not originate out of a perfect crystal but they form heterogeneously at obstacles, crystal boundaries or other dislocation sources. For example, grain or phase boundaries can emit dislocations into the crystal. Dislocations can also originate at other obstacles where dislocations are pinned. The most well-known such source is the *Frank-Read source*, named after its pioneering inventors Frank and Read (1950). If a dislocation is pinned at both ends, as shown in Figure 2.21, an external stress will result in a force on the dislocation line (and perpendicular to the dislocation line) which makes the dislocation bow in the illustrated manner. As the external stress increases, the dislocation line bows out more until the dislocation forms a half-circle, which then becomes unstable and grows even without external stresses to finally form a new complete dislocation loop growing into the crystal. Therefore, a Frank-Reed source can emit dislocation loops into the crystal under external stresses.

As seen before, parallel edge dislocations of the same sign on neighboring planes in an infinite crystal would try to separate from each other as far as possible due to the interaction stresses to reduce the crystal's energy. In a similar manner, the stress fields of all microstructural defects interact and yield attractive and repulsive forces between defects. In a confined region, however, there is only limited space for those defects due to grain boundaries or other obstacles, so that nucleated dislocations pile-up between these obstacles according to certain energetic principles and yielding a specific structure, the so-called *dislocation network*. This will be discussed in somewhat more detail in Section 2.4.7.

The arrangement of dislocations to a dislocation network will be discussed in subsequent Sections. In general, dislocations are not disruptive defects but necessary ingredients to accommodate material microstructures. For example, the boundary between two neighboring grains with different crystal orientation can be accommodated by edge dislocations as illustrated in Figure 2.22. Here, dislocations at the boundary accommodate the local change of otherwise possibly incompatible crystal orientations. Dislocations which form (in particular at boundaries or obstacles) in order to accommodate a change of the crystal lattice or to accommodate kinematically necessary lattice distortions are called *geometrically necessary dislocations* (GNDs), whereas dislocations that appear stochastically at arbitrary positions within grains during deformation are known as *statistical dislocations*. (Often, an analogous differentiation is made into immobile and mobile dislocations.) The most important of these two types of dislocations in our models are the GNDs, since dislocations in the sequel are assumed to accommodate plastic distortions in the continuum body (Fox, 1968).

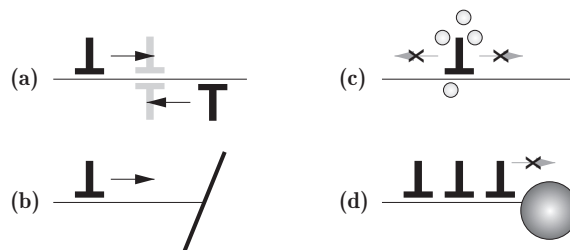


Figure 2.20: Cartoon of dislocation Interactions: (a) Attraction and annihilation of opposing dislocations, (b) attraction of dislocations to free surfaces, (c) pinning of a dislocation by foreign atoms, (d) pinning of dislocations and pile-up at large foreign atoms, grain boundaries etc.

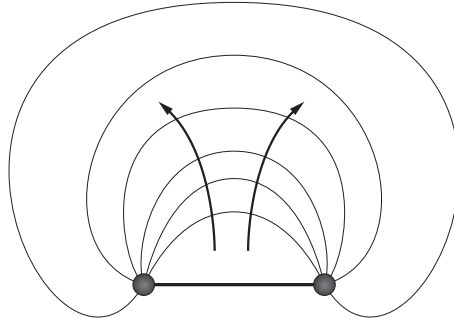


Figure 2.21: Frank-Read source of dislocation loops: Pinned dislocation between two obstacles bows under applied stress.

2.4.6 Continuum Theory of Plasticity

One can now – at least in principle – model the plastic deformation of crystalline solids by simulating the crystal as an ensemble of a large number of atoms which can constitute dislocations and other crystal defects to accommodate plastic flow. However, as pointed out in previous Sections, such molecular dynamics simulations are highly limited in time and space for reasons of computational effort. Instead, it is convenient to employ methods of continuum mechanics which allow for the simulation of macroscopic bodies while accounting for the underlying microscopic defect mechanisms described above.

In the context of continuum mechanics, the general state of deformation of a macroscopic body is described by

$$\mathbf{F} = \mathbf{F}_e \cdot \mathbf{F}_p, \quad \text{or} \quad \boldsymbol{\varepsilon} = \boldsymbol{\varepsilon}_e + \boldsymbol{\varepsilon}_p, \quad (2.193)$$

for finite deformations and the geometrically linear theory, respectively. In both cases, the elastic deformation results from the above decompositions as

$$\mathbf{F}_e = \mathbf{F} \cdot \mathbf{F}_p^{-1} \quad \text{or} \quad \boldsymbol{\varepsilon}_e = \boldsymbol{\varepsilon} - \boldsymbol{\varepsilon}_p. \quad (2.194)$$

It is now, at least in principle, possible to differentiate all variables involved into two types: On the one hand, there are elastic variables (here, the elastic strains) which change without dissipating energy. On the other hand, there are plastic variables (here, e.g. the plastic strains) which may be summarized in a vector \mathbf{K} . Any change of the plastic variables (i.e. a change of the plastic deformation) is accommodated by dislocation motion which, in turn, dissipates energy. Therefore, the free energy Ψ (and hence the stresses) depends on the

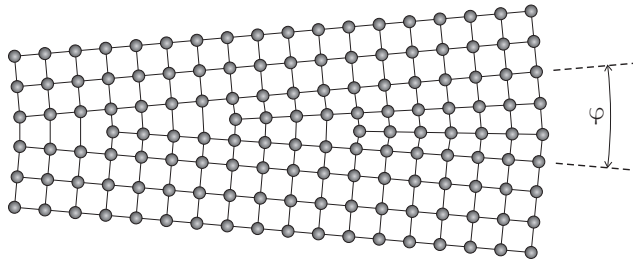


Figure 2.22: Low-angle grain boundary consisting of edge dislocations.

elastic variables only, the dissipation, however, is a function of the set of internal (plastic) variables,

$$\Psi = \Psi(\mathbf{F}_e), \quad \mathcal{D} = \mathcal{D}(\mathbf{K}). \quad (2.195)$$

The free energy and the dissipation functional determine the constitutive relations of the material. To complete the continuum description of elasto-plasticity, we need to specify the plastic deformation gradient \mathbf{F}_p or the plastic strains $\boldsymbol{\varepsilon}_p$, respectively, as well as the dissipation \mathcal{D} and link these quantities to dislocation dynamics.

The impact of each dislocation on the crystal lattice can be characterized by the tensor of plastic distortion, $\boldsymbol{\beta}$, which is defined as follows: Imagine a perfect crystal is distorted by inserting a single dislocation, e.g. an edge dislocation, i.e. an extra half-plane in the crystal lattice. Comparing the perfect and the distorted (deformed) crystal, we can write for the Burgers' vector \mathbf{b} , characterizing the jump of the displacements on the slip surface Σ ,

$$\mathbf{b} = [[\mathbf{u}]] = \mathbf{u}^+ - \mathbf{u}^-, \quad (2.196)$$

where the superscripts denote the limiting values of the displacements on both sides of the slip surface. Then, it follows that (Berdichevsky, 2006b)

$$\boldsymbol{\beta} = \mathbf{b} \otimes \mathbf{m} \delta(\Sigma), \quad (2.197)$$

with \mathbf{m} being the unit normal vector on the slip plane (directing from Σ^- to Σ^+), and δ denoting the delta function of the surface Σ , i.e.

$$\delta(\Sigma) = \int_{\Sigma} \delta(\mathbf{x} - \mathbf{x}_{\Sigma}) \, da, \quad (2.198)$$

where δ is the common three-dimensional Dirac delta function (Kunin, 1983).

The number of dislocations in deformed metals is quite high. In macroscopic problems, where the problem dimensions are much larger than the dislocation characteristics, we regard the crystalline solid as a continuous medium. Therefore, we neglect the fact that possible choices of \mathbf{b} are realized by the step-wise motion of dislocations, are hence limited in terms of the lattice spacings, and formulate the plastic distortion as a continuous function.

Let us assume a large number of dislocations on infinitesimally close planes of the same slip system. Denoting the slip direction by \mathbf{s} , we write for the plastic distortion

$$\boldsymbol{\beta} = \gamma \mathbf{s} \otimes \mathbf{m}, \quad (2.199)$$

where $\gamma = \gamma(\mathbf{x})$ is a continuous function, called *plastic slip* or *plastic distortion*. In order not to confuse notations in finite-strain and infinitesimal plasticity, we will use $\gamma(\mathbf{x})$ as the plastic slip for finite deformations and denote the plastic distortion for small strains by $\boldsymbol{\beta}(\mathbf{x})$. If several slip systems are active to accommodate plastic deformation (with slip directions \mathbf{s}_i and slip surface normals \mathbf{m}_i), dislocation slip can occur on any of the n active slip systems, such that the total plastic distortion results as

$$\boldsymbol{\beta} = \sum_i^n \gamma_i \mathbf{s}_i \otimes \mathbf{m}_i. \quad (2.200)$$

Now, we link the plastic distortion to the plastic deformation gradient and the plastic strains. This connection can also be interpreted as follows: As we saw in Figure 2.11, plastic deformation can be regarded as a collective gliding of parts of the crystal along certain slip

systems. Therefore, we should be able to formulate the overall plastic strain resulting from gliding of dislocations as a simple shear deformation. In the theory of finite plasticity, this results in the flow rule

$$\dot{\mathbf{F}}_p \mathbf{F}_p^{-1} = \dot{\boldsymbol{\beta}} = \sum_i^n \dot{\gamma}_i \mathbf{s}_i \otimes \mathbf{m}_i, \quad (2.201)$$

where – as before – \mathbf{s}_i denotes the slip direction and \mathbf{m}_i represents the normal unit vector on the glide plane of slip system i , with a total of n slip systems. If all slip systems under consideration have parallel unit normal vectors $\mathbf{m}_i = \mathbf{m}$, we can easily integrate (2.201) by assuming as an initial condition $\mathbf{F}_p = \mathbf{I}$ so that we arrive at (Carstensen et al., 2002)

$$\mathbf{F}_p = \mathbf{I} + \boldsymbol{\beta} = \mathbf{I} + \sum_i^n \gamma_i \mathbf{s}_i \otimes \mathbf{m}. \quad (2.202)$$

If the unit normal vectors of the slip systems are not parallel, such a neat form for \mathbf{F}_p is unfortunately not available (Hackl et al., 2003a). A derivation for an iterative solution can be found e.g. in (Miehe et al., 2004).

For the geometrically linear theory we can apply (2.202) for a single slip system to $\boldsymbol{\varepsilon}_p = \mathbf{E}_p = \frac{1}{2}(\mathbf{F}_p^T \mathbf{F}_p - \mathbf{I})$ and neglect the quadratic term in $\gamma = \beta$ (for infinitesimal strains we have $|\beta| \ll 1$) so that we arrive at the neat form

$$\boldsymbol{\varepsilon}_p = \frac{1}{2}\beta(\mathbf{s} \otimes \mathbf{m} + \mathbf{m} \otimes \mathbf{s}) = \frac{1}{2}(\boldsymbol{\beta} + \boldsymbol{\beta}^T). \quad (2.203)$$

For multiple slip systems of arbitrary orientation the relations in the linear theory are less complex than for finite strains, and the corresponding plastic strain tensor follows as

$$\boldsymbol{\varepsilon}_p = \frac{1}{2} \sum_i^n \beta_i (\mathbf{s}_i \otimes \mathbf{m}_i + \mathbf{m}_i \otimes \mathbf{s}_i) = \frac{1}{2} \sum_i^n (\boldsymbol{\beta}_i + \boldsymbol{\beta}_i^T). \quad (2.204)$$

With these representations at hand, we can compute the elastic strains required for the constitutive relations involving the free energy density. When dealing with plastic deformation of metals, we must also consider the dissipation due to dislocation motion. As we have seen, dislocation motion (and hence plastic deformation) is irreversible, i.e. dislocation motion dissipates energy. This is sometimes pictured by figuring dislocations not to ideally glide on the slip plane but to encounter some friction on that plane which consumes energy (this is, of course, only an instructive visualization). Therefore, any change of the plastic (internal) variables comes along with a certain amount of dissipation. This loss of energy should be related to the amount of plastic slip. The dissipation for rate-independent plasticity theory is often assumed of the form

$$\mathcal{D}(\dot{\gamma}_i) = \Delta(\dot{\gamma}_i) = \tau_{\text{crit},i} |\dot{\gamma}_i| = \tau_{\text{crit},i} |\dot{\beta}_i|, \quad (2.205)$$

where $\tau_{\text{crit},i}$ is a material constant, the critical resolved shear stress of slip system i . A more detailed description of the flow rules in finite and infinitesimal formulations will be given in Sections 3 and 4 where required. With this constitutive framework at hand we can describe the plastic deformation of crystalline solids.

2.4.7 Continuum Theory of Dislocations

The continuous quantities of plastic slip or distortion, introduced in the previous Section, allow for a clear characterization of the plastic deformation state of a material body. Unfortunately, they do not provide any direct information about the actual dislocation network nor does the dislocation network influence the free energy and, as a consequence, does not affect the constitutive relations. In order to describe the amount of dislocations stored in a crystal by a scalar quantity, the *dislocation density* ρ was introduced, which is defined as the total length of all dislocation lines in a unit volume or the total number of all dislocation lines cutting a unit area. The number of dislocations in deformed metals can be quite high. Un-deformed metals considered as almost „defect-free“ already exhibit dislocation densities of the order of magnitude of 10^8 m^{-2} . Heavily strained metals can exhibit dislocation densities as high as 10^{15} m^{-2} . Lining up all dislocation lines within a cube of a moderately strained steel with 1cm side length results in a dislocation line of about 500 – 1000km. Due to these large numbers it would be cumbersome and inefficient to account for every single dislocation and its interactions with all other dislocations independently. Therefore, the continuum theory of dislocations was developed, analogously to the continuum theory of plasticity, discussed in the previous Section. Although the fundamentals of continuum dislocation theory were laid down long time ago by Kondo (1952), Nye (1953), Bilby et al. (1955a), Kröner (1958), and Berdichevsky and Sedov (1967), among others, the applicability of the theory has become feasible only in recent years (Ortiz and Repetto, 1999; Ortiz et al., 2000; Berdichevsky, 2006b; Groma et al., 2003) thanks to the progress in statistical mechanics and thermodynamics of the dislocation network (Berdichevsky, 2005, 2006a).

The continuum theory of dislocations aims at describing the behavior of the ensembles of huge numbers of dislocations by the common methods of continuum mechanics. In contrast to the classical theory of plasticity (see Section 2.4.6), the free energy function Ψ is a function of the dislocation density which hence enters the constitutive relations. As another major difference it can include plastic rotations in the set of the dislocation network kinematic parameters in addition to plastic strains. The importance of these plastic rotations may be seen from Figure 2.23: Imagine an unstrained square body as depicted in Figure 2.23a. Now, let edge dislocations with their Burgers' vector in the x_1 -direction pass the square, resulting in a homogeneous plastic shear deformation, as shown in Figure 2.23b. Another set of edge dislocations passes the crystal in the x_2 -direction so that the square takes the form of Figure

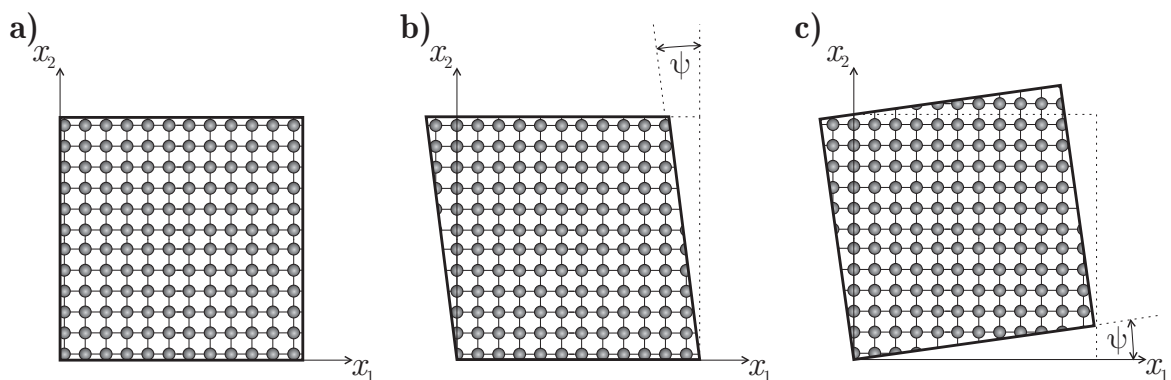


Figure 2.23: Schematic illustrating the rigid rotation resulting from edge dislocation flow (for small angle ψ).

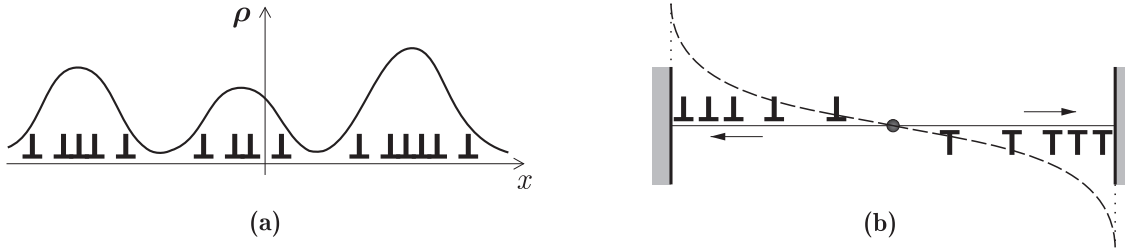


Figure 2.24: (a) Continuous approximation of the dislocation distribution, (b) pile-up of dislocations from a single source between two obstacles.

re 2.23c. If the shear angle ψ is small and the crystal isotropic, then the bodies sketched in Figure 2.23a and Figure 2.23c differ by only a rigid rotation; the plastic deformation obtained from Figure 2.23a to Figure 2.23c vanishes. If we only account for plastic strains \mathbf{F}_p or $\boldsymbol{\varepsilon}_p$, there is no difference between states a) and c), and hence the passing dislocations are unnoticeable, i.e. they would not affect any relation of the classical plasticity theory. However, the initial and final plastic states are different in reality, as the passing dislocations dissipate energy and thereby heat the crystal (Berdichevsky, 2006b). We see from Figure 2.23 that the passing dislocations do not change the orientation of the crystal lattice in space (denoted by the Cartesian coordinate system). However, they do change the material coordinate system which rotates as a consequence. Therefore, those tensors characterizing the crystal anisotropy rotate with respect to the material frame due to plastic flow. As a consequence, the free energy density should be an explicit function of the plastic distortion.

Let us introduce an important function, the scalar dislocation density distribution function $\rho(\mathbf{x})$. Figure 2.24a sketches a simple one-dimensional example where the finite number of dislocations in a crystal is approximated by a continuous function, $\rho(\mathbf{x})$. This function defines the dislocation density in every material point and satisfies the conditions of a density distribution function,

$$\rho(\mathbf{x}) \geq 0, \quad \rho = \frac{1}{|\Omega|} \int_{\Omega} \rho(\mathbf{x}) \, dv, \quad (2.206)$$

where ρ is the total dislocation density stored in the crystal of volume Ω . Now, we can deal with large numbers of dislocations without accounting for every single dislocation but by dealing with function $\rho(\mathbf{x})$ instead which carries all necessary information. A classical example which was analyzed by Eshelby et al. (1951) and Leibfried (1951) is illustrated in Figure 2.24b: Dislocations are emitted from a single source and pile up at opposite grain boundaries. For this problem the dislocation density function $\rho(\mathbf{x})$ can uniquely be derived. As all edge dislocations piling up at each of the obstacles repel each other, the obstacle encounters a considerable stress concentration with an increasing number of dislocations.

For general applications, the one-dimensional picture illustrated in Figure 2.24b is far too simplistic since dislocations may originate and interact on any admissible slip system in the crystal in three dimensions. Therefore, Nye (1953) introduced the concept of the dislocation density tensor $\boldsymbol{\alpha}$ which takes into account all geometrically necessary dislocations, later propagated by Ashby's seminal paper (Ashby, 1970). The dislocation density tensor $\boldsymbol{\alpha}$ has, as the stress or strain tensors, the advantage that it gives not only the number of dislocations cutting a single oriented area but it determines the dislocation density in any arbitrarily oriented area of the crystal. Nye's dislocation density tensor $\boldsymbol{\alpha}$ can be obtained from the

plastic distortion β by

$$\alpha = \text{curl } \beta = \text{curl } \mathbf{F}_p. \quad (2.207)$$

The dislocation density tensor has the following physical meaning: For an arbitrary infinitesimal surface da with the unit normal \mathbf{n} , $\alpha \cdot \mathbf{n} da$ gives the resultant Burgers' vector of all dislocations whose dislocation lines cut the surface da . The scalar dislocation density function $\rho(\mathbf{x})$ can then be obtained from α (Berdichevsky, 2006b) depending on the problem (see Section 4 for examples).

The first problem was then to find the stress field produced by a given set of dislocations. An elegant solution of this problem was found by Kröner (1958). As a next step the general kinematic framework of continuum dislocation theory was provided by Kondo (1952) and Bilby et al. (1955a). In their works the natural state of a crystal is considered as a manifold equipped with an affine connection. Bilby et al. (1955a) argued that for crystal lattices the curvature tensor obtained from this connection must vanish; consequently the metric tensor (the plastic strain) and the torsion tensor (the dislocation density tensor) remain the only characteristics of dislocations. The inverse statement also holds true: The plastic distortion can be determined if the plastic strain and the dislocation density tensor are known (Le and Stumpf, 1996a).

Another important ingredient to the continuum theory of dislocations is the energy of the dislocation network. As mentioned before, the dislocation density should enter the free energy density, which may therefore be written for isothermal processes as

$$\Psi(\mathbf{F}_e, \alpha) = \Psi_0(\mathbf{F}_e) + \Psi_\rho(\alpha), \quad (2.208)$$

where Ψ_0 is the elastic stored energy density and Ψ_ρ is the energy density of the dislocation network (which also accounts for plastic rotations). In general, the energy of all dislocations in a crystal could be computed as the sum of all self-energies and all interaction energies. Due to the large numbers of dislocations in deformed metals, this approach appears to be not applicable for large representative volume elements and large dislocation densities. Instead, we will make use of the introduced scalar dislocation density function $\rho(\mathbf{x})$ and introduce a free energy density of the microstructure $\Psi_\rho(\rho) = \Psi_{\text{self}} + \Psi_{\text{inter}}$. The *energy of the dislocation network* in a material body Ω is then given by

$$\mathcal{I}_\rho = \int_{\Omega} \Psi_\rho(\rho(\mathbf{x})) dv. \quad (2.209)$$

As it does not follow from any physical law, it is essential to make a correct choice for the type of Ψ_ρ , (i.e. a choice agreeing as well as possible with experimental observations and with thermodynamic principles). Until the end of the twentieth century all contributors to the continuum dislocation theory assumed the dislocation energy density in the form, see e.g. (Gurtin, 1972),

$$\Psi_\rho(\alpha) = \frac{1}{2} \alpha : \mathcal{E} : \alpha \quad (2.210)$$

with \mathcal{E}_{ijkl} being material constants.

The relevance of this quadratic dependence of the energy of the microstructure on the dislocation density to describe the behavior of dislocations remained questionable for a long time. The major concern was the smallness of the second term in (2.208). Constants \mathcal{E}_{ijkl}

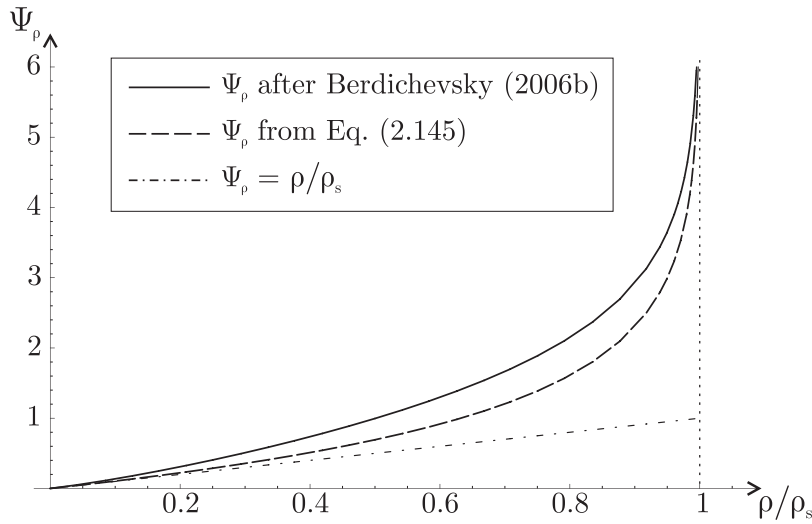


Figure 2.25: Comparison of dislocation energy functions.

must have the dimension of the shear modulus μ times length squared. It was shown by Berdichevsky (2006b) that, if the characteristic length is of the same order as the interatomic distance b (or the average distance between dislocations), then the second term in (2.208) is negligible compared to the first term for a body of macroscopic size. The problems dealing with bodies of meso- and microscopic sizes were not seen at that time and the theory was not pursued further. The aforementioned difficulty seems to have been overcome, at least partially, by a proposition about the microstructure energy made in (Ortiz and Repetto, 1999; Ortiz et al., 2000). Thanks to the progress in statistical mechanics and thermodynamics of the dislocation network (Le and Berdichevsky, 2001; Groma et al., 2003, 2007; Berdichevsky, 2005, 2006a), new understanding of the microstructure energy was gained. Berdichevsky (2006a) showed that the microstructure energy which includes the interaction energy between dislocations and the self-energy of dislocations is, in fact, a function of local characteristics of dislocations only, despite the long-range character of the dislocation interactions. For a single crystal deforming in single slip, Berdichevsky (2006a,b) proposed the energy of the microstructure in the form

$$\Psi_\rho = k \mu \left(\ln \frac{1}{1 - \sqrt{\rho/\rho_s}} - \sqrt{\frac{\rho}{\rho_s}} \right), \quad (2.211)$$

where k is a material constant and ρ_s is the saturated dislocation density. This form of Ψ_ρ identically satisfies Voce's law (Berdichevsky, 2006b) of phenomenological plasticity. As a good approximation we will often use the less complex form

$$\Psi_\rho = k \mu \ln \frac{1}{1 - \rho/\rho_s}. \quad (2.212)$$

The logarithmic energy stems from two facts: Firstly, the energy of the dislocation network for small dislocation densities is the sum of the energies of non-interacting dislocations (as the interaction energies are negligible) such that the energy must rise linearly for only few dislocations present in the crystal. Secondly, there exists a saturated dislocation density which characterizes the closest packing of dislocations admissible in the discrete crystal lattice in a bounded domain. The logarithmic term ensures a linear increase of the energy for

small dislocation density, as can easily be seen from a Taylor expansion,

$$\ln \frac{1}{1 - \rho/\rho_s} = \frac{\rho}{\rho_s} + \frac{1}{2} \left(\frac{\rho}{\rho_s} \right)^2 + O \left[\left(\frac{\rho}{\rho_s} \right)^3 \right], \quad (2.213)$$

and tends to infinity as ρ approaches the saturated dislocation density ρ_s . Due to the minimum principle of potential energy, the energy hence asymptotically penalizes any dislocation density approaching ρ_s . The saturated dislocation density can be observed experimentally and lies for common metals in the range $10^{14} - 10^{17} m^{-2}$. Of course, in a continuum approach we intend to neglect the discrete nature of the crystal lattice and treat the mechanical body as a continuum. If, however, we consider specimens at small scales where the size effects of plasticity become apparent, as will be the subject of Section 4, we will very soon reach those high dislocation densities and hence must account for the effect of saturation. A comparison of the dislocation energy densities from Eqs. (2.211) and (2.212) is shown in Figure 2.25, where the linear rise for small dislocation densities and the ultimate increase of energy with the dislocation density approaching the saturation point become apparent.

Berdichevsky (2006b) also made a suggestion how to differentiate between moving and stored dislocations such that the theory can account for discontinuities (which are prohibited by the above form). Here and in the following, we investigate the continuous plastic deformation of crystals and the dislocation pile-ups at boundaries, where the above formulation (2.212) is appropriate.

2.5 Thermodynamic Principles and the Origin of Microstructure

2.5.1 Thermo-Mechanical Principles

Before we can investigate the evolution of plastic microstructures in engineering materials, we will review the fundamental concepts leading to the formation of microstructures which are generally dictated by the body's free energy. Therefore, in this Section we will focus on the underlying thermodynamic principles, leading to the origin of microstructures.

The state of a general inelastic material is defined by external variables such as the temperature T or the deformation gradient $\mathbf{F} = \nabla \phi$ and by internal variables which are introduced to capture the microstructural characteristics and the history information concerning plastic deformations (e.g. plastic slip γ , dislocation density ρ , volume fractions λ_i for a multi-phase material, chemical composition etc.) In the following, we denote the collection of internal variables by \mathbf{K} . Of course, we will have to make a difference between formulations in finite and infinitesimal deformations. To render the summary in this Section most concise, we will generally describe the state of deformation by $\mathbf{F} = \nabla \phi$, which can be interpreted in both formulations.

Let us introduce an energy storage function Ψ with the following properties. Firstly, Ψ must be objective with respect to rigid rotations (while assuming that \mathbf{K} remains unaffected by the rotation), i.e.

$$\Psi(\mathbf{R}\mathbf{F}, \mathbf{K}) = \Psi(\mathbf{F}, \mathbf{K}), \quad \forall \mathbf{R} \in SO(3). \quad (2.214)$$

Secondly, we require an initial condition of zero stored energy and zero stresses, i.e.

$$\Psi(\mathbf{I}, \mathbf{K}_0) = 0, \quad \left. \frac{\partial \Psi(\mathbf{F}, \mathbf{K}_0)}{\partial \mathbf{F}} \right|_{\mathbf{F}=\mathbf{I}} = 0. \quad (2.215)$$

For problems of solid mechanics, we use the *Helmholtz free energy density* $\Psi(\mathbf{X}, t) = \Psi(\nabla \phi(\mathbf{X}, t), \mathbf{K}(\mathbf{X}, t))$ as the above introduced storage function, which represents the isothermal stored energy per volume at a material point \mathbf{X} at time t . When dealing with plasticity in finite deformation, one possible choice is a Neo-Hookean energy density of the type

$$\Psi_{\text{NH}}(\mathbf{F}_e, p) = \frac{\mu}{2} \text{tr} \mathbf{C}_e + \frac{K}{4} \left[\det \mathbf{C}_e - \frac{K + 2\mu}{K} \ln(\det \mathbf{C}_e) - 1 \right] + \kappa p^\alpha, \quad (2.216)$$

where p is a real, scalar-valued internal history variable introduced to account for material hardening, and α is commonly chosen to equal 2 (linear hardening) or higher even numbers. The total potential energy of a strained body with volume Ω can then be given in terms of the *total free energy* which reads

$$\mathcal{I}(t, \phi, \mathbf{K}) = \int_{\Omega} \Psi(\nabla \phi, \mathbf{K}) \, dv - \ell(t, \phi), \quad (2.217)$$

where $\ell(t, \phi)$ represents the linear potential of externally applied forces. As we are interested in isothermal processes of homogeneous solids only, we do not consider any dependence on temperature or chemical decomposition.

With the total potential energy \mathcal{I} at hand, let us introduce a first important thermodynamic principle. Well-known, the first law of thermodynamics requires that the total energy of an

isolated system remains constant for all times, i.e.

$$E_{\text{tot}} = \text{const.} \quad (2.218)$$

For example, a swinging ideal pendulum in the absence of friction or other dissipative effects will periodically exchange kinetic against potential energy but never come to rest and hence conserve its total energy. The second law of thermodynamics states that every isolated system aims at maximizing its total entropy S , which is a thermodynamic measure of the system's state of disorder; i.e. naturally driven processes must obey

$$dS \geq 0 \quad (2.219)$$

so that the equilibrium state is reached at the maximum total entropy where $dS = 0$.

We can decompose any change of the total energy of an isolated system into

$$\delta E_{\text{tot}} = \delta \Pi_{\text{tot}} + \delta Q, \quad (2.220)$$

where Π_{tot} denotes the stored potential energy (in our context $\Pi_{\text{tot}} = \mathcal{I}$) and Q represents the thermal energy, i.e. the heat stored in the isolated system. Furthermore, the change of the heat of an isolated system is linked to its entropy for a reversible process via

$$dQ = T dS. \quad (2.221)$$

Let us perform a gedanken experiment by considering an isolated system which aims to achieve an equilibrium state. As the system maximizes its entropy, the potential energy decreases due to the conservation of the total energy. As a consequence, maximizing the entropy of an isolated system is equivalent to minimizing its total potential energy. Therefore, we can conclude the first important principle, known as the *principle of minimum total potential energy* (Truesdell and Noll, 1965), which may be written in our context as

$$\phi = \arg \min \{ \mathcal{I}(t, \phi, \mathbf{K}) \mid \phi = \phi_0 \text{ on } \Gamma_u \}. \quad (2.222)$$

i.e. in an equilibrium state, the displacement field minimizes the free energy of the material body subject to given boundary conditions.

For inelastic materials a change of the placement field ϕ (or of any elastic variables, in general) does not entail dissipation. Any change of the internal (plastic) variables, however, commonly dissipates energy. For example, a change of plastic slip or the dislocation density involves nucleation and motion of dislocations, which dissipates energy. If the internal variables change without dissipating energy, the equilibrium state can be determined from

$$(\phi, \mathbf{K}) = \arg \min \{ \mathcal{I}(t, \phi, \mathbf{K}) \mid \phi = \phi_0 \text{ on } \Gamma_u, \mathbf{K} = \mathbf{K}_0 \text{ on } \Gamma_K \}. \quad (2.223)$$

The first law of thermodynamics can be recast into

$$\dot{E}_{\text{tot}} = \dot{\Pi}_{\text{int}} + P = 0, \quad (2.224)$$

where $\dot{\Pi}_{\text{int}}$ denotes the rate of the total stored energy, and P is the work done by externally applied forces, i.e.

$$\dot{\Pi}_{\text{int}} = \frac{d}{dt} \int_{\Omega} \Psi(\mathbf{F}, \mathbf{K}, S) dv, \quad P = \int_{\partial\Omega} \mathbf{n} \cdot \mathbf{P} \cdot \dot{\mathbf{u}} da, \quad (2.225)$$

where S denotes the entropy of the body Ω , \mathbf{n} is the outward normal vector on the boundary $\partial\Omega$, \mathbf{P} is a stress tensor and $\dot{\mathbf{u}}$ any prescribed boundary velocity. Computing the derivative of Π_{int} and applying Gauß' theorem to P , we obtain (in the absence of body forces)

$$\dot{\Pi}_{\text{int}} = \int_{\Omega} \left(\frac{\partial \Psi}{\partial S} \dot{S} + \frac{\partial \Psi}{\partial \mathbf{F}} : \dot{\mathbf{F}} + \frac{\partial \Psi}{\partial \mathbf{K}} \cdot \dot{\mathbf{K}} \right) dv, \quad (2.226)$$

$$P = \int_{\Omega} \left((\nabla \cdot \mathbf{P}) \cdot \dot{\mathbf{u}} + \mathbf{P} \cdot \dot{\mathbf{F}} \right) dv, \quad (2.227)$$

so that application to (2.225) with the absolute temperature $T = \partial \Psi / \partial S$ yields

$$\int_{\Omega} \left[T \dot{S} + \left(\frac{\partial \Psi}{\partial \mathbf{F}} - \mathbf{P} \right) : \dot{\mathbf{F}} + \frac{\partial \Psi}{\partial \mathbf{K}} \cdot \dot{\mathbf{K}} - (\nabla \cdot \mathbf{P}) \cdot \dot{\mathbf{u}} \right] dv = 0. \quad (2.228)$$

Like the first law of thermodynamics this relation must hold for an arbitrary volume Ω of the material body so that at every material point \mathbf{X} we have

$$T \dot{S} + \left(\frac{\partial \Psi}{\partial \mathbf{F}} - \mathbf{P} \right) : \dot{\mathbf{F}} + \frac{\partial \Psi}{\partial \mathbf{K}} \cdot \dot{\mathbf{K}} - (\nabla \cdot \mathbf{P}) \cdot \dot{\mathbf{u}} = 0. \quad (2.229)$$

Here and in the following, we tacitly presume that all relations hold in every material point \mathbf{X} without writing out this dependence. The particular case of rigid body motion (where the only non-zero rate is the velocity $\dot{\mathbf{u}}$) requires the well-known equilibrium condition (in the absence of body forces)

$$\nabla \cdot \mathbf{P} = 0. \quad (2.230)$$

Usually, a change of the internal variables of a mechanical system comes along with a dissipation of energy. Following Eq. (2.221), we introduce the dissipation \mathcal{D} as

$$\mathcal{D} = T \dot{S} = \left(\mathbf{P} - \frac{\partial \Psi}{\partial \mathbf{F}} \right) : \dot{\mathbf{F}} - \frac{\partial \Psi}{\partial \mathbf{K}} \cdot \dot{\mathbf{K}}. \quad (2.231)$$

Re-arranging the above relation, we arrive at the Clausius-Planck inequality,

$$\mathcal{D} = \mathbf{P} : \dot{\mathbf{F}} - \dot{\Psi} \geq 0. \quad (2.232)$$

The first term of (2.231) represents dissipation of the type of viscous damping, the second term characterizes dissipation due to changes of the internal variables. In general, we assume for problems of elasto-plasticity that no viscous damping is present (in contrast to problems of viscoelasticity or -plasticity), so that we arrive at the constitutive equation for the stresses (known as Coleman's method)

$$\mathbf{P} = \frac{\partial \Psi}{\partial \mathbf{F}}. \quad (2.233)$$

It becomes apparent that, following these principles and our previous definitions, \mathbf{P} is the first Piola-Kirchhoff stress tensor Σ^I . Furthermore, let us introduce a thermodynamically conjugate stress for the internal variables by defining

$$\mathbf{Q} = - \frac{\partial \Psi}{\partial \mathbf{K}} \quad (2.234)$$

so that we may also write the dissipation as

$$\mathcal{D} = - \frac{\partial \Psi}{\partial \mathbf{K}} \cdot \dot{\mathbf{K}} = \mathbf{Q} \cdot \dot{\mathbf{K}}. \quad (2.235)$$

The total dissipation of the body now reads

$$\mathcal{D} = \int_{\Omega} \mathbf{Q} \cdot \dot{\mathbf{K}} \, dv \geq 0. \quad (2.236)$$

We can restate the thermodynamic principle of maximizing the entropy in terms of the *principle of maximum dissipation* (because entropy production and dissipation are directly correlated)

$$\dot{\mathbf{K}} = \operatorname{argmax} \{ \mathcal{D}(\mathbf{X}, \dot{\mathbf{K}}, \mathbf{Q}) \mid \mathcal{D} = \dot{\mathbf{K}} \cdot \mathbf{Q} \}. \quad (2.237)$$

For problems in elasto-plasticity the internal variables may only evolve if a yield condition

$$\varphi(\mathbf{K}, \mathbf{Q}) = 0$$

is satisfied (φ bounds the yield surface in the stress space). If $\varphi(\mathbf{K}, \mathbf{Q}) < 0$ the body deforms elastically. If $\varphi(\mathbf{K}, \mathbf{Q}) = 0$, then the body exhibits plastic flow. Any state characterized by $\varphi(\mathbf{K}, \mathbf{Q}) > 0$ is prohibited. Therefore, it is convenient to introduce an indicator function $J(\mathbf{K}, \mathbf{Q})$, sometimes called the inelastic potential (Carstensen et al., 2002), defined at each material point by

$$J = \begin{cases} 0, & \text{for } \varphi(\mathbf{K}, \mathbf{Q}) \leq 0, \\ \infty, & \text{else.} \end{cases} \quad (2.238)$$

Instead of dealing with the indicator function, it is of more practical use to introduce a dissipation functional $\Delta(\mathbf{K}, \dot{\mathbf{K}})$, defined by the Legendre-Fenchel transform of J , which only depends on the internal variables and their rates:

$$\Delta(\mathbf{K}, \dot{\mathbf{K}}) = \sup \{ \dot{\mathbf{K}} \cdot \mathbf{Q} - J(\mathbf{K}, \mathbf{Q}) \mid \mathbf{Q} \}. \quad (2.239)$$

For irreversible processes in non-equilibrium thermodynamics the evolution of the internal variables is commonly defined by a flow rule of the type

$$\mathbf{Q} = \lambda \frac{\partial \Delta}{\partial \dot{\mathbf{K}}}. \quad (2.240)$$

In the following Chapters we will assume rate-independence of the plasticity models, which requires that Δ must be homogeneous of degree 1, i.e.

$$\Delta(\epsilon \cdot \dot{\mathbf{K}}, \mathbf{K}) = \epsilon \cdot \Delta(\dot{\mathbf{K}}, \mathbf{K}), \quad (2.241)$$

such that $\lambda = 1$ and as a consequence

$$\mathcal{D} = \Delta. \quad (2.242)$$

As a simple example, when dissipation occurs due to plastic slip γ (and for simplicity we here assume a single scalar internal variable γ only), we employ a dissipation functional of the type $\Delta(\dot{\gamma}) = c |\dot{\gamma}|$ with some material constant c . Then it is easy to verify that

$$\mathcal{D} = \frac{\partial \Delta}{\partial \dot{\mathbf{K}}} \cdot \dot{\mathbf{K}} = \frac{\partial \Delta(\dot{\gamma})}{\partial \dot{\gamma}} \dot{\gamma} = c |\dot{\gamma}| = \Delta(\dot{\gamma}). \quad (2.243)$$

Now, we can write the evolution equation for the internal variables in the form

$$\mathbf{Q} \in \frac{\partial \Delta}{\partial \dot{\mathbf{K}}} \quad (2.244)$$

or, by employing the Legendre transform, in an equivalent form as

$$\dot{\mathbf{K}} \in \frac{\partial J}{\partial \mathbf{Q}}. \quad (2.245)$$

We often use differential inclusions in the notation of flow rules as in (2.244) and (2.245) to also account for the elastic case.

Comparing Eqs. (2.234) and (2.244), we arrive at the well-known Biot equation for the evolution of the internal variables (Biot, 1965; Germain, 1973; Ziegler and Wehrli, 1987; Nguyen, 2000)

$$0 \in \frac{\partial \Psi}{\partial \mathbf{K}} + \frac{\partial \Delta}{\partial \dot{\mathbf{K}}}. \quad (2.246)$$

The complete evolution problem can now be described in terms of two principles. We obtain the actual deformation of the material body from the principle of minimum potential energy (2.222). The evolution of the internal variables results from Biot's equation (2.246). Hence, updates of all elastic variables can be determined from energy minimization, whereas the internal (plastic) variables change according to specified flow rules.

In Chapter 4 we will apply these two principles to derive the displacement field $\mathbf{u}(\mathbf{X})$ and the set of internal variables $\mathbf{K}(\mathbf{X})$ as continuous functions throughout the body Ω with given boundary conditions $\mathbf{u} = \mathbf{u}_0$ and $\mathbf{K} = \mathbf{K}_0$ on $\partial\Omega$. We compute the distribution of the internal variables in the material body under investigation and analyze microstructural pattern formation and characteristics of the dislocation network.

In problems of crystal plasticity, we usually investigate the time-continuous evolution of all variables involved. Therefore, it is convenient to modify the above formulation to allow for an iterative solution scheme, using finite time increments Δt . For a finite time interval $[t_n, t_{n+1}]$ with $t_{n+1} - t_n = \Delta t$, we define the stresses in the next time step according to the principle of minimum potential energy as

$$\Sigma_{n+1}^I = \frac{\partial \Psi(\mathbf{F}_{n+1})}{\partial \mathbf{F}}. \quad (2.247)$$

The question of how to define $\Psi(\mathbf{F}_{n+1})$ was first answered by Ortiz and Repetto (1999) with

$$\Psi(\mathbf{F}_{n+1}) = \inf_{\mathbf{K}(t)} \int_{t_n}^{t_{n+1}} \Sigma^I : \dot{\mathbf{F}} \, dt = \inf_{\mathbf{K}(t)} \int_{t_n}^{t_{n+1}} \left(\dot{\Psi} + \mathbf{Q} \cdot \dot{\mathbf{K}} \right) \, dt, \quad (2.248)$$

along with the boundary conditions $\mathbf{K}(t_n) = \mathbf{K}_n$ and $\mathbf{K}(t_{n+1}) = \mathbf{K}_{n+1}$. Carstensen et al. (2002) and Miehe et al. (2002) replaced the above relation by incorporating a general dissipation functional so that

$$\Psi(\mathbf{F}_{n+1}) = \inf_{\mathbf{K}(t)} \int_{t_n}^{t_{n+1}} \left(\dot{\Psi} + \Delta \right) \, dt. \quad (2.249)$$

For rate-independence (and hence a dissipation functional which is homogeneous of degree 1) these two formulations coincide. The proof that Eqs. (2.249) and (2.246) yield the same solution for a small time increment can be given as follows (Miehe et al., 2002).

First, we re-write Eq. (2.249) as

$$\Psi(\mathbf{F}_{n+1}) = \inf_{\mathbf{K}(t)} \left[\Psi(\mathbf{F}, \mathbf{K}) \Big|_{t_n}^{t_{n+1}} + \int_{t_n}^{t_{n+1}} \Delta(\dot{\mathbf{K}}, \mathbf{K}) \, dt \right], \quad (2.250)$$

and perform the minimization in (2.250) by applying the first variation:

$$\frac{\partial \Psi}{\partial \mathbf{K}} \cdot \delta \mathbf{K} \Big|_{t_n}^{t_{n+1}} + \int_{t_n}^{t_{n+1}} \left[\frac{\partial \Delta}{\partial \dot{\mathbf{K}}} \cdot \delta \dot{\mathbf{K}} + \frac{\partial \Delta}{\partial \mathbf{K}} \cdot \delta \mathbf{K} \right] \, dt = 0. \quad (2.251)$$

Integration by parts finally yields

$$\left(\frac{\partial \Psi}{\partial \mathbf{K}} + \frac{\partial \Delta}{\partial \dot{\mathbf{K}}} \right) \cdot \delta \mathbf{K} \Big|_{t_n}^{t_{n+1}} + \int_{t_n}^{t_{n+1}} \left[-\frac{d}{dt} \frac{\partial \Delta}{\partial \dot{\mathbf{K}}} + \frac{\partial \Delta}{\partial \mathbf{K}} \right] \cdot \delta \mathbf{K} \, dt = 0. \quad (2.252)$$

In the limit of an infinitesimal time increment $t_{n+1} - t_n \rightarrow dt$ and with $\delta \mathbf{K}(t_n) = 0$, we see that the state of the internal variables at time $t = t_{n+1}$ is obtained from

$$\frac{\partial \Psi}{\partial \mathbf{K}} + \frac{\partial \Delta}{\partial \dot{\mathbf{K}}} = 0, \quad (2.253)$$

and the minimizing path $\mathbf{K}(t)$ inside the time interval must satisfy the Euler equation

$$-\frac{d}{dt} \frac{\partial \Delta}{\partial \dot{\mathbf{K}}} + \frac{\partial \Delta}{\partial \mathbf{K}} = 0. \quad (2.254)$$

Therefore, as $t_{n+1} \rightarrow t_n$, Eq. (2.249) provides a point-wise approximation of Biot's equation (2.246). Note that this derivation must be modified if the free energy depends not only on the internal variables but also on their gradient, i.e. $\Psi = \Psi(\mathbf{F}, \mathbf{K}, \nabla \mathbf{K})$, as will be required in Section 4.

In Chapter 3 we investigate the time-incremental evolution of microstructures in finite plasticity so that it will be beneficial to replace the solution of Biot's equation by the aforementioned incremental formulation. Therefore, the so-called *minimum principle for the dissipation functional* is introduced, where we follow ideas presented by Ortiz and Repetto (1999), Carstensen et al. (2002) and Miehe (2002), which recasts (2.249) into the following form:

$$\dot{\mathbf{K}} = \arg \min \{ \mathcal{L}(\phi, \mathbf{K}, \dot{\mathbf{K}}) \mid \dot{\mathbf{K}} \}, \quad (2.255)$$

where we introduced a Lagrange functional following Eq. (2.249):

$$\mathcal{L}(\phi, \mathbf{K}, \dot{\mathbf{K}}) = \frac{d}{dt} \Psi(\nabla \phi, \mathbf{K}) + \Delta(\mathbf{K}, \dot{\mathbf{K}}). \quad (2.256)$$

Hackl and Fischer (2007) investigated the interrelation of the minimum principle for the dissipation functional (2.255) and the principle of maximum dissipation (2.237) and gave evidence for their agreement for those problems treated here (i.e., for homogeneous dissipation potentials) and various other examples.

So far we have focused on the evolution of internal parameters connected to plastic deformation and regarded the spatial distribution of microstructural characteristics as the material's microstructure. Modeling finite elasto-plasticity (see Section 3) as well as deformation twinning (see Section 5) or phase transformations, another problem arises which is connected to the formation of microstructural patterns and which we will focus on in the remaining part of this Chapter.

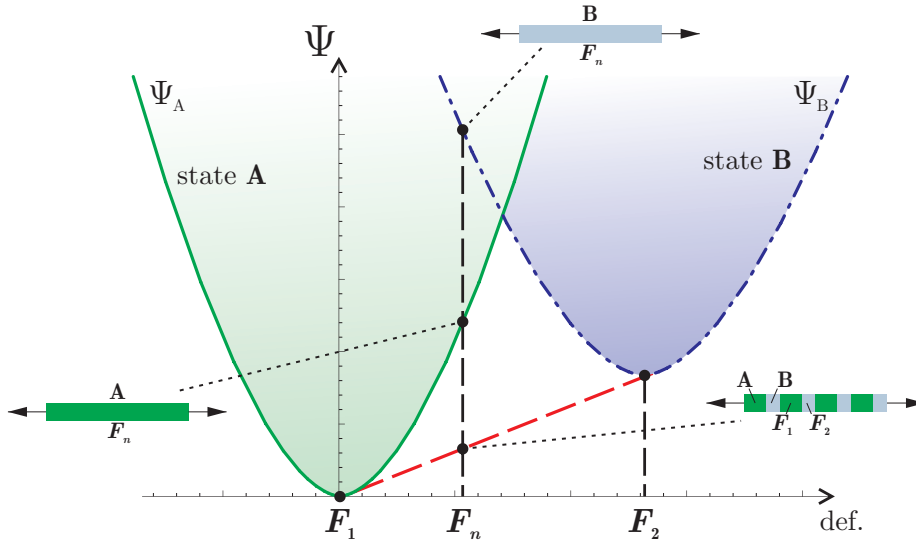


Figure 2.26: Non-convex energy landscape with two energy wells: For a given boundary condition F_n each energy well exhibits rather high energy values; the formation of a mixture of states F_1 and F_2 can accommodate the boundary conditions and achieve a state of lower energy.

2.5.2 Energy Minimizers, Minimizing Sequences and Microstructure

As we have seen, the state of deformation is governed by the free energy of the material and aims at attaining a state of minimum energy. In an ideal situation the energy landscape is (quasi-) convex, having a single global energy minimum (the energy is said to be single-welled). Then, the body accommodates the energy minimum by means of its deformation field. Very often, however, the energy landscape is not quasiconvex but multi-welled in nature (exhibiting several local minima), where each energy well represents a different state of the material (e.g. different transformation states for phase-transforming materials such as the austenite-martensite structures in steels, different values of the plastic distortion in finite plasticity, or different crystal orientations in parent and twin phase of deformation twins). A complicating change in the theory of plasticity as compared to phase transformations arises from the fact that, in plasticity, these energy wells are not located at fixed Bain strains but may evolve as well. In both cases, as seen in Section 2.2, a lack of quasiconvexity of the energy potential reveals that no minimizer exists.

Now, consider a homogeneous single-crystal of volume Ω subject to given boundary conditions on $\partial\Omega$. The crystal tends to achieve a state of minimum energy. If the prescribed boundary conditions correspond to a state at a possible energy well, the body will accommodate the energy minimum by means of a homogeneous deformation state. If, however, the boundary conditions enforce a deformation gradient F_n between e.g. two energy wells of states A and B, then no homogeneous minimizer exists. However, the material can satisfy both the boundary conditions and the energy minimum by forming a mixture of those states A and B at the energy wells (see Figure 2.26). Let us illustrate this with a very simple example in one dimension, which was presented (in a more elaborate form) by Ericksen (1975).

The simplest example in one dimension is a slender bar stretched along its principal axis. The deformation field simply reduces to only uniaxial displacements $u_x(x)$ and the only

non-zero components of the deformation gradient $\mathbf{F} = \nabla \mathbf{u}$ are given by $F_{11} = 1 + u_{x,x}$, $F_{22} = F_{33} = 1$. Now, assume a free energy density of the type

$$\Psi(\nabla \mathbf{u}) = \mu (\text{tr } \mathbf{F}^T \mathbf{F} - 4)^2 = \mu (u_{x,x}^2 - 1)^2. \quad (2.257)$$

It is not hard to verify that this choice of Ψ is clearly not quasiconvex (Figure 2.27). The total potential energy for a bar of length L reads

$$\mathcal{I}(\nabla \mathbf{u}) = \int_0^L \Psi(\nabla \mathbf{u}) \, dl. \quad (2.258)$$

Therefore, the energy comes to a minimum when the deformation gradient $u_{x,x}$ in every material point equals $+1$ or -1 . Now, however, assume the given boundary conditions

$$u_x(0) = 0, \quad u_x(L) = 0, \quad (2.259)$$

i.e. the displacement field is forced to vanish on both ends of the bar of length L (the bar is constrained between rigid supports). A problem arises from satisfying both conditions (2.259) and the principle of minimum potential energy. There exists no continuously differentiable solution for u_x which is 0 on the boundary but has gradient ± 1 inside the bar. Ericksen (1975) concluded that the bar can still satisfy both conditions by forming a mixture of alternating sections with gradient $+1$ and -1 as sketched in Figure 2.28. The boundary conditions are satisfied and the energy tends to zero. In general, the problem is more complex (Bhattacharya, 2003) and to explore the full mathematical concept one will have to modify the energy such that

$$\mathcal{I}(\mathbf{u}) = \int_0^L [\Psi(u_{x,x}) + (u_x)^2] \, dl. \quad (2.260)$$

Then one can show that the minimum energy (with \mathbf{u} satisfying the boundary conditions) is achieved as we make this mixture of alternating gradients finer and finer (see Figure 2.28). The obtained sequence of functions u_i is called a *minimizing sequence* and we can conclude that in the limit of an infinitely fine microstructure the energy will approach its minimum which is 0, i.e.

$$\lim_{n \rightarrow \infty} \mathcal{I}(u_n) = 0. \quad (2.261)$$

Therefore, the energy of the minimizing sequence is lower than that of a homogeneous solution satisfying the boundary conditions ($\nabla \mathbf{F} = \mathbf{0}$ and $\Psi(0) = 1$); i.e. the energy of the

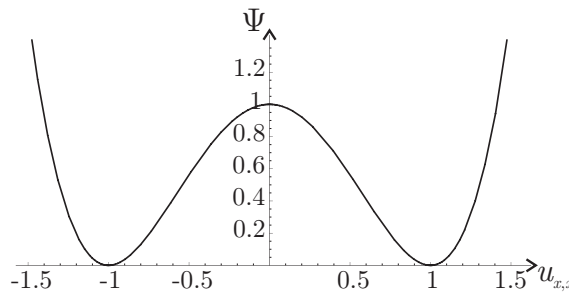


Figure 2.27: Free energy Ψ of the bar as a function of the strain $u_{x,x}$.

limit of deformation sequences (i.e. constant zero deformation) is greater than the limit of the energy of the refining phase mixture:

$$\mathcal{I}(\lim_{n \rightarrow \infty} u_n) > \lim_{n \rightarrow \infty} \mathcal{I}(u_n). \quad (2.262)$$

Note that the average deformation gradient on the total length of the bar is 0; thus, the average deformation gradient corresponds to the overall deformation gradient imposed by the boundary conditions. Furthermore, we see that the deformation u is continuous, the deformation gradient $u_{x,x}$, however, is not.

Whenever there exists a minimizing sequence ϕ_n which is capable of reducing the free energy \mathcal{I} beyond the free energy of a homogeneous deformation state ϕ in the limit $n \rightarrow \infty$, then we say the energy \mathcal{I} is not weakly lower semi-continuous, as *weakly lower semi-continuity* of the energy \mathcal{I} corresponds to

$$\mathcal{I}(\lim_{n \rightarrow \infty} \phi_n) \leq \lim_{n \rightarrow \infty} \mathcal{I}(\phi_n) \quad (2.263)$$

for all weakly converging sequences ϕ_n . As the condition of weakly lower semi-continuity is hard to check in actual problems, Morrey (1952) introduced the concept of *quasiconvexity*. The energy $\mathcal{I}(\phi)$ as defined in Eq. (2.217) is then weakly lower semi-continuous if the free energy density $\Psi(\phi)$ is quasiconvex (see Section 2.2). If the free energy density of a material for a given overall deformation gradient ϕ is not quasiconvex, there exists no solution to the minimization problem in the classical sense, and there is a minimizing sequence which can reduce the material's energy. If possible, the material will therefore accommodate the energy minimum by forming fine-scale microstructures with alternating gradients.

In problems of finite plasticity the description is more complex and in general three-dimensional. Therefore, the issue of the coherence of the deformation field arises, which was not the case in the simple one-dimensional example. For the general understanding, however, the problem in three dimensions is very similar to the one discussed above. Figure 2.29 illustrates the formation of fine mixtures for a two-dimensional problem in a square body. Differently than before, the mixture of states or deformation gradients is now arranged by forming thin laminate regions, and the boundary condition now must be accommodated by a thin boundary layer region. Figure 2.29a shows a first-order laminate which arises from a mixture of two energy wells and which mixes deformation gradients \mathbf{A} and \mathbf{B} to represent the average deformation gradient

$$\mathbf{F}_\lambda = \lambda \mathbf{A} + (1 - \lambda) \mathbf{B}, \quad (2.264)$$

where λ denotes the volume fraction of phase A. Figure 2.29b illustrates a second-order laminate which forms by mixing the states of four energy wells, where each deformation

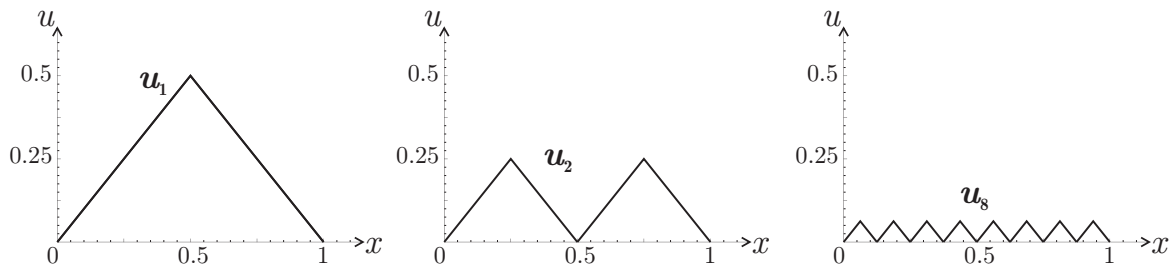


Figure 2.28: A sequence of deformations which minimize the total energy and, at the same time, satisfy the boundary conditions.

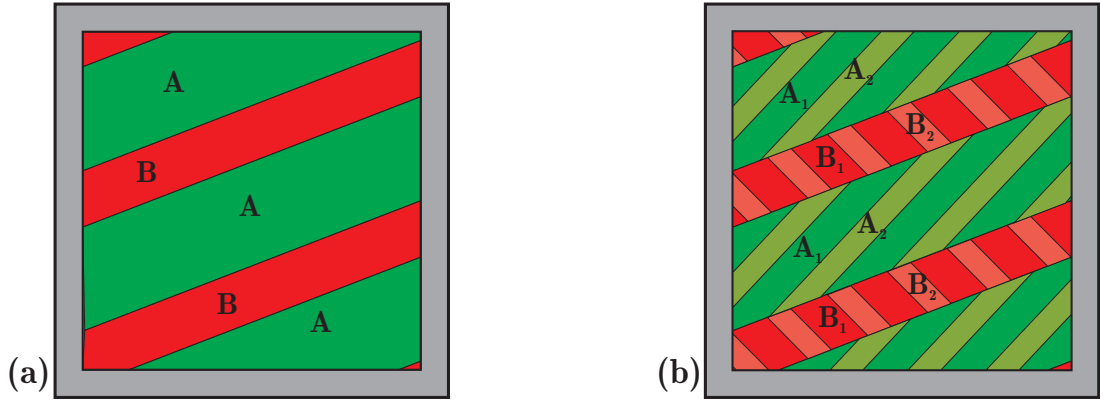


Figure 2.29: (a) First-order and (b) second-order laminate.

gradient \mathbf{A} and \mathbf{B} is again split into a mixture of finer laminates with deformation gradients \mathbf{A}_1 , \mathbf{A}_2 and \mathbf{B}_1 , \mathbf{B}_2 , respectively, i.e. here we have

$$\begin{aligned} \mathbf{F}_\lambda &= \lambda \mathbf{A} + (1 - \lambda) \mathbf{B}, \\ \mathbf{A} &= \lambda_A \mathbf{A}_1 + (1 - \lambda_A) \mathbf{A}_2, \\ \mathbf{B} &= \lambda_B \mathbf{B}_1 + (1 - \lambda_B) \mathbf{B}_2. \end{aligned} \quad (2.265)$$

As a conclusion, for a non-convex stored energy function Ψ there exists no solution to the minimization problem (2.222) in the classical sense. If possible, the material will accommodate the energy minimum by forming fine-scale alternating gradients, often referred to as fine-scale microstructures. Non-convex variational problems may have (depending on the boundary conditions) a unique, many or even no solution.

If the material can form microstructures, the non-existence of a minimum will lead to the development of small-scale oscillations or, in general, fluctuations of the deformation gradient. The characteristics of these microstructures can be described by employing mathematical relaxation theory. A *relaxation* is associated with a quasiconvexification of the non-convex function Ψ by constructing its *quasiconvex hull* $Q\Psi$, which was already introduced in Section 2.2. The minimization problem (2.222) is modified by considering the relaxed energy functional (Acerbi and Fusco, 1984; Dacorogna, 1989)

$$\mathcal{I}_Q(\phi) = \int_{\Omega} Q\Psi(\nabla \phi) \, dv - \ell(\phi), \quad (2.266)$$

where $Q\Psi$ denotes the quasiconvex hull of the original energy density Ψ , i.e.

$$Q\Psi(\nabla \phi) = \inf_{|\omega|} \frac{1}{|\omega|} \int_{\omega} \Psi(\mathbf{F} + \nabla \varphi) \, dv \quad \text{for all admissible } \varphi : \mathcal{R}^3 \rightarrow \mathcal{R}^3. \quad (2.267)$$

Physically, quasiconvexity is the passage from a microscopic energy to a macroscopic energy that is obtained from an averaging over fine-scale oscillations. Eq. (2.267) determines a micro-fluctuation field φ on the arbitrary domain ω . The relaxed minimization problem now reads

$$\phi = \arg \min \{ \mathcal{I}_Q(t, \phi) \mid \phi = \phi_0 \text{ on } \Gamma_u \}. \quad (2.268)$$

Note that, as the energy relaxation only affects the elastic variables, those principles presented in previous Sections to determine the evolution of the internal (plastic) variables are not

affected. A relaxation of the energy can be carried out beforehand. The relaxed problem is considered to be well-posed and as close as possible to the original unstable problem which has no solution. The stress tensor is obtained from the very same quasiconvex hull (and analogously the stiffness tangent tensor) to give

$$\Sigma^I = \frac{\partial Q \Psi}{\partial \mathbf{F}}. \quad (2.269)$$

Unfortunately, the quasiconvex hull is very hard to determine for many engineering problems. Therefore, it is often replaced by convex, polyconvex or rank-one-convex hulls (Dolzmann, 1999; Bartels et al., 2004; Carstensen et al., 2008). In our analyses in Section 3 we will make use of an approximation of the rank-one-convex hull and hence solve the minimization problem

$$\phi = \arg \min \{ \mathcal{I}_{R_1}(t, \phi) \mid \phi = \phi_0 \text{ on } \Gamma_u \} \quad (2.270)$$

with

$$\mathcal{I}_{R_1}(\phi) = \int_{\Omega} R_1 \Psi(\nabla \phi) \, dv - \ell(\phi), \quad (2.271)$$

where $R_1 \Psi$ is the rank-one-convex hull approximation as a first-order laminate ($N = 2$), defined by

$$R_1 \Psi(\phi) = \inf_{\lambda_i, \mathbf{F}_i} \left\{ \sum_{i=1}^2 \lambda_i \Psi(\mathbf{F}_i) \mid \text{constr.} \right\} \quad (2.272)$$

where the constraints read

$$0 \leq \lambda_i \leq 1, \quad \sum_{i=1}^2 \lambda_i = 1, \quad \sum_{i=1}^2 \lambda_i \mathbf{F}_i = \mathbf{F}, \quad \text{rank}(\mathbf{F}_1 - \mathbf{F}_2) \leq 1. \quad (2.273)$$

In general, the analogous conditions for more than two laminate phases ($N > 2$) are hard to determine. Instead, Kohn and Strang (1986) proposed a sequential construction where each phase further decomposes into a new laminate. The volume fractions λ_i can be considered as probability measures in the sense of Young (1969).

Given the rank-one-convex hull or its approximation (2.271), we can solve the well-posed minimization problem (2.270) instead of the original one to obtain the solution in terms of laminate microstructures.

2.5.3 Material Microstructures

The experimental determination of material microstructures has been limited for a long time in terms of the microscopic resolution capabilities. Nowadays, modern techniques such as transmission electron spectroscopy (TEM) or electron back scatter diffraction (EBSD) allow for a close look at dislocation structures at very fine scales. Indeed, experimental findings confirm, in agreement with the predictions presented in previous Sections, that the dislocation distributions in a strained material body are not random but very often exhibit distinct patterns with structural characteristics. These dislocation patterns are dictated by the crystal's energy and the dissipation required to form those structures.

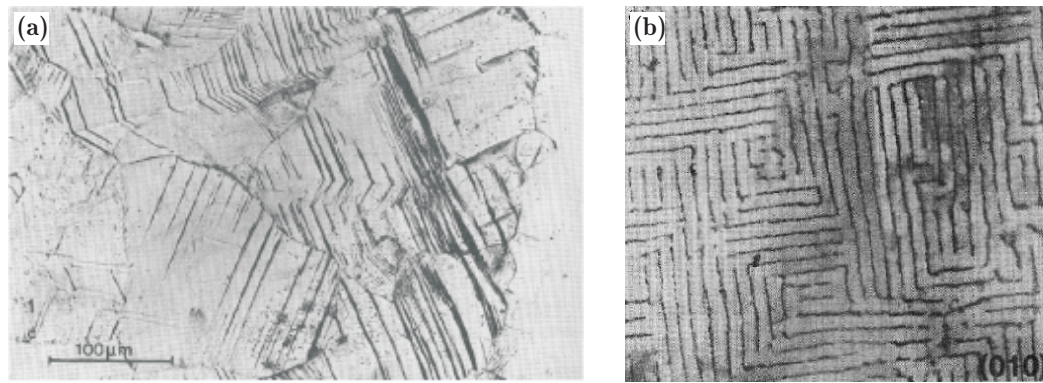


Figure 2.30: (a) Dislocation slip segregation into single-slip domains (Rasmussen and Pederson, 1980), (b) labyrinth-type dislocation structure in a fatigued copper single crystal (Jin and Winter, 1984). Images reprinted by permission.

Figure 2.30 shows exemplary TEM micrographs where dislocations and dislocation accumulations can be identified as dark lines. In Figure 2.30a, dislocations pile up at grain boundaries and obstacles and grow into the undistorted crystals along preferred slip systems; this behavior is known as slip segregation into single-slip domains. Figure 2.30b reveals a labyrinth-type dislocation structure which clearly indicates the formation of a strict pattern with preferred orientations for dislocation accumulation.

Other examples are illustrated in Figure 2.31 where in (a) parallel lamellar structures arise. The lamellar boundaries are constituted of dislocations leaving most lamellar interiors almost dislocation-free and forming dislocation sub-walls within the lamellae. In micrograph (b), a regular zig-zag pattern forms with alternating crystal orientations, commonly referred to as *micro-twins*.

Finally, Figure 2.32 gives two examples of experimentally observed microstructures which are linked to specific microstructural mechanisms: Micrograph (a) shows the formation of lamellar twin domains that form during the transformation of steel in its austenitic phase into martensite. Here, the origin of microstructures is based on the concept of phase transformations, see e.g. (Bhattacharya, 2003), and results from the different energy

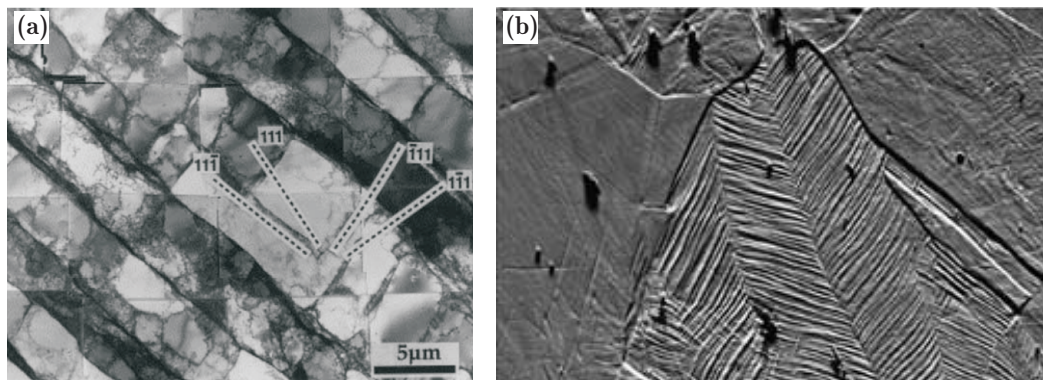


Figure 2.31: (a) Lamellar dislocation wall structures in cold-rolled, pure aluminum (Li et al., 2006), (b) twin-type laminate dislocation structures in compressed high manganese steel (Meng et al., 2007). Images reprinted by permission.

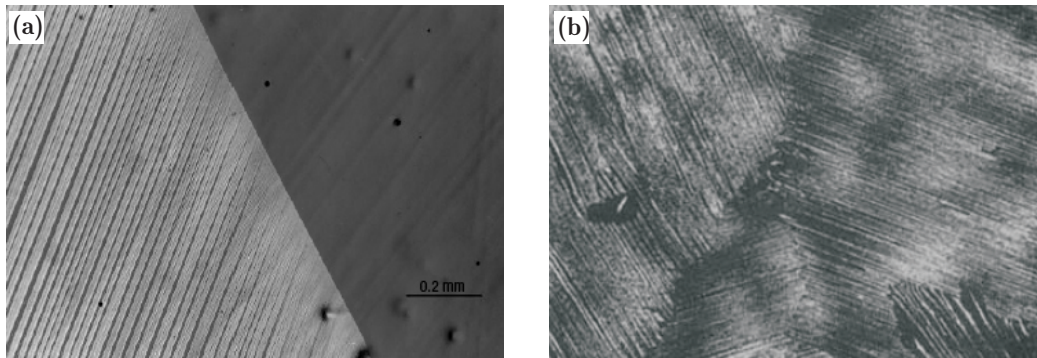


Figure 2.32: (a) Lamellar twin domains in martensite (Chu and James, 1995), (b) dislocation twin structures in manganese-added TiAl (Hanamura and Tanino, 1989). Images reprinted by permission.

wells of martensite and austenite variants. Two martensite variants form a lamellar pattern (reducing the crystal's energy beyond that of a homogeneous deformation gradient). Note the change of the lamellae into thin needles as they approach the austenite boundary (thus accommodating the aforementioned boundary region to satisfy the overall boundary constraints). Figure 2.32b shows a special type of microstructure, called *deformation twins*, in manganese-added TiAl. Here, two distinct energy wells (corresponding to different, symmetric slip system orientations) compete within one grain, giving rise to a zig-zag pattern with alternating lattice orientations to reduce the energy beyond that of a homogeneous single-crystal deforming in single slip. Under externally applied loads, the crystal lattice forms a lamellar structure with alternating symmetric slip systems. We will deal with this type of microstructure in more detail in Section 5.

Although there is a huge variety of experimentally observed microstructures in engineering materials, the underlying causal mechanisms obey the very same thermodynamic principles. The following Chapters present some selected examples of microstructures determined from those variational principles presented in the previous Sections and investigate the origin and subsequent evolution of these structures on the microscale. Of capital importance, all microstructural characteristics are collectively responsible for the macroscopic mechanical behavior of a material body. Therefore, it is crucial gain further understanding.

3 Time-Continuous Evolution of Inelastic Microstructures in Finite Plasticity

3.1 Introduction

The macroscopic response of a material body deforming plastically under the action of external forces is a direct result of physical mechanisms occurring on the body's microscale. Hence, microstructural lattice defects and related mechanisms are crucial in order to understand the macroscopic material behavior. The accommodation of plastic deformation by huge numbers of such defects is dictated by the concepts of free energy and dissipation. In elasto-plasticity the free energy is commonly assumed to stem from the uniform deformation of the periodic crystal lattice and aims at restoring the material body in a zero-stress state. It therefore comprises only energy due to elastic deformation. Dissipation arises as a consumption of energy due to irreversible changes of the microstructure. The internal state of the material's microstructure is commonly described in terms of so-called internal or history variables, a change of which causes dissipation. In crystalline solids dissipation may occur as a consequence of dislocation motion through gliding or climbing, or as a result of grain boundary motion, diffusion processes, phase transformations or sources of internal friction, to mention only a few.

Given the free energy and the dissipation of a deformed material body as functions of the displacement field and of the set of all internal variables, the principles of minimum potential energy (Truesdell and Noll, 1965), see (2.222), and the principle of maximum dissipation (Simo, 1988a,b), see (2.237), or of minimum dissipation potential (Carstensen et al., 2002; Hackl and Fischer, 2007), see (2.255), determine the actual configuration of the body. In rate-independent plasticity models the incremental evolution of the internal variables may also be described by a Lagrange functional consisting of the sum of elastic power and dissipation due to changes of the internal state of the material (Ortiz and Repetto, 1999; Carstensen et al., 2002).

Experimental evidence indicate very often that it is favorable for a material to accommodate an imposed deformation gradient not by a homogeneous deformation field but rather by forming microstructural patterns which accommodate the overall deformation by mixing different homogeneous states of minimum energy. Figure 3.1 shows the EBSD image of a copper single crystal deformed under simple shear. A laminate microstructure of alternating plastic slip and rotation becomes apparent. (For further examples of experimentally observed microstructures see Section 2.5.3.)

Microstructure formation has been observed e.g. in the context of phase transformations (Chu and James, 1995) and for deformation twin structures (Christian and Mahajan, 1995; Bhattacharya, 2003), or for dislocation walls in single-crystals (Canadinc et al., 2005). An interesting feature of all these microstructures is that they tend to form similar spatial patterns, hinting at a universal underlying mechanism. Ericksen (1975) was among the first to conclude microstructural patterns as a direct result of energy minimum principles, who-

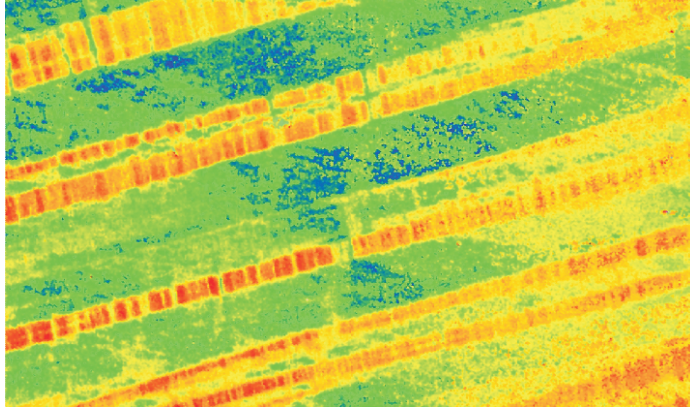


Figure 3.1: EBSD image of a copper single crystal deformed under simple shear, color difference represent deviation of the local configuration from the mean lattice orientation (Dmitrieva et al., 2009). Reprinted by permission.

se idea was expanded and enhanced later to a more complex theory predominantly for the treatment of phase transformations (Ball and James, 1987, 1992; Govindjee et al., 2003) and problems in elasto-plasticity (Ortiz and Repetto, 1999; Carstensen et al., 2002; Conti and Theil, 2005). In all of these examples, the free energy is non-quasiconvex and hence multi-welled in nature. As a consequence, the material body, aiming to reduce its energy, does not respond by means of a homogeneous deformation state but breaks up into multiple phases at local energy minima in such way that it is compatible with the overall imposed deformation field or any given boundary conditions. Solutions to describe these phase mixtures were developed by employing relaxation theory to find the quasiconvex hull of the free energy (Ball, 1977). This approach is based on small-scale fluctuations related to probability distributions of deformation gradients, so-called Young measures (Young, 1969). These small-scale fluctuations correspond to the observed material microstructures. The particular features of those, like orientation or volume fractions, can be calculated via relaxed potentials.

Microstructures in physical reality exhibit an enormous variety of appearances, the simplest example being a spatial lamination of different phases, i.e. regions with different deformation states are separated by parallel planes with a common normal vector indicating the laminate orientation. Values of the internal variables and of the deformation gradient differ from phase to phase, with the given constraints that these values are chosen such as to ensure compatibility and to match the boundary conditions. As the quasiconvex envelope in general is too complex to compute, it is often approximated by the rank-one-convex envelope of the free energy, see e.g. (Bartels et al., 2004; Carstensen et al., 2008), which corresponds to the energy of such a laminate microstructure.

Approaches to model microstructural patterns must account for the two crucial problems of the initiation of a forming microstructure and the subsequent evolution of the newly-formed structure. The initiation of a forming microstructure usually follows from a loss of stability. At a material point local instability corresponds to a state where the crystal can reduce its energy by breaking up the homogeneous deformation state into fine structures. For details on the differences between local and global stability for related problems see e.g. (Miehe et al., 2002). Here we resort to the common approach that a microstructure may form locally as soon as it becomes energetically preferable. By considering associated potentials in a time-incremental setting, several authors have investigated the initiation of microstruc-

tures (Ortiz and Repetto, 1999; Lambrecht et al., 2003; Bartels et al., 2004; Mielke, 2004; Conti and Theil, 2005) using a condensed energy functional. This method was successfully applied to the evolution of inelastic materials, see (Mielke and Ortiz, 2007; Conti and Ortiz, 2008). However, application of the condensed energy is based on the assumption that no microstructure is present at the beginning of a time step (therefore, it is suitable to model the onset of microstructure formation). Yet in order to model the time-continuous evolution of microstructures, we need to account for the dissipation required to change from one state in time to the next. Hence, the incremental update of the internal variables will depend on the set of internal variables at the end of the preceeding time step, so that the use of the condensed energy functional becomes rather unphysical. To overcome this problem, we develop an incremental formulation based on laminated Young measures. The application of a similar concept to shape-memory-alloys can be found in (Hackl et al., 2003a; Hackl, 2006; Hackl and Heinen, 2008).

In this Chapter we outline a novel method to model the time-continuous evolution of laminate microstructures, which accounts for the existing microstructure at the beginning of each time step. In Section 3.2 we first review the underlying variational principles and outline the concept of relaxed potentials, Young measures and lamination theory with application to inelastic materials. In Section 3.3 we then derive explicit evolution equations for the problem of single-slip crystal plasticity for a Neo-Hookean material and present a numerical algorithm by means of which the time-continuous evolution can be determined. This algorithm is based on a partially analytically relaxed energy and incrementally solves the evolution equations. Finally, we apply this method to different loading cases and slip system orientations, and we illustrate numerical results in Section 3.5. Section 3.6 concludes the present Chapter with a discussion of the results.

3.2 Application of Relaxation Theory to Inelastic Microstructures

3.2.1 Minimum Principles and Young Measures

We will first lay the basis for the derivation of evolution equations for material microstructures by briefly reviewing the underlying minimum principles, and we adopt their formulation to our problem by introducing appropriate Young measures. For a more thorough investigation of the underlying thermodynamic principles see Section 2.5.1. In an isothermal setting, the state of a general inelastic material is defined by its deformation gradient $\mathbf{F} = \nabla \phi$, where $\phi(\mathbf{X})$ represents the displacement field, and a collection of internal variables $\mathbf{K}(\mathbf{X})$. Denoting the specific Helmholtz free energy by $\Psi(\mathbf{F}, \mathbf{K})$, we introduce thermodynamically conjugate stresses by defining

$$\Sigma^I = \frac{\partial \Psi}{\partial \mathbf{F}}, \quad \mathbf{Q} = -\frac{\partial \Psi}{\partial \mathbf{K}}. \quad (3.1)$$

The evolution of \mathbf{K} is governed either by a so-called inelastic potential $J(\mathbf{K}, \mathbf{Q})$ or its Legendre-transform (Carstensen et al., 2002), the dissipation functional

$$\Delta(\mathbf{K}, \dot{\mathbf{K}}) = \sup \{ \dot{\mathbf{K}} : \mathbf{Q} - J(\mathbf{K}, \mathbf{Q}) \mid \mathbf{Q} \}. \quad (3.2)$$

Evolution equations for the internal variables are then given in the two equivalent forms

$$\dot{\mathbf{K}} \in \frac{\partial J}{\partial \mathbf{Q}}, \quad \mathbf{Q} \in \frac{\partial \Delta}{\partial \dot{\mathbf{K}}}. \quad (3.3)$$

Note that in this Section we will often make use of the subdifferential notation as in (3.3) to also account for the non-differentiable behavior of the dissipation potential (viz. to include the case $\dot{\mathbf{K}} = 0$).

The complete evolution problem can now be described in terms of two minimum principles where we follow ideas presented by Carstensen et al. (2002); Mielke (2002); Ortiz and Repetto (1999). We compute the total free energy of the entire body as

$$\mathcal{I}(t, \phi, \mathbf{K}) = \int_{\Omega} \Psi(\nabla \phi, \mathbf{K}) \, dv - \ell(t, \phi) \quad (3.4)$$

where $\ell(t, \phi)$ represents the potential of external forces, Ω is the body's volume and Γ_u denotes a subset of its boundary. The actual displacement field is then given by the principle of minimum potential energy, i.e.

$$\phi = \arg \min \{ \mathcal{I}(t, \phi, \mathbf{K}) \mid \phi = \phi_0 \text{ on } \Gamma_u \}. \quad (3.5)$$

Introducing the Lagrange functional

$$\mathcal{L}(\phi, \mathbf{K}, \dot{\mathbf{K}}) = \frac{d}{dt} \Psi(\nabla \phi, \mathbf{K}) + \Delta(\mathbf{K}, \dot{\mathbf{K}}), \quad (3.6)$$

we write the evolution equation (3.3) in the form

$$\dot{\mathbf{K}} = \arg \min \{ \mathcal{L}(\phi, \mathbf{K}, \dot{\mathbf{K}}) \mid \dot{\mathbf{K}} \}, \quad (3.7)$$

where the dot denotes differentiation with respect to time. For a thorough investigation of this principle and its relation to the principle of maximum dissipation, see (Hackl and Fischer, 2007). For rate-independent materials, principle (3.7) allows to account for instantaneous changes of the value of \mathbf{K} , as it can be integrated to yield the balance law

$$\Psi(\nabla \phi, \mathbf{K}_1) - \Psi(\nabla \phi, \mathbf{K}_0) = -D(\mathbf{K}_0, \mathbf{K}_1), \quad (3.8)$$

where

$$D(\mathbf{K}_0, \mathbf{K}_1) = \inf \left\{ \int_0^1 \Delta(\mathbf{K}(s), \dot{\mathbf{K}}(s)) \, ds \mid \mathbf{K}(0) = \mathbf{K}_0, \mathbf{K}(1) = \mathbf{K}_1 \right\} \quad (3.9)$$

is the so-called dissipation distance (Mielke, 2002). When applied to a finite time-increment $[t_n, t_{n+1}]$, Eq. (3.8) allows for an approximate formulation where ϕ_{n+1} and \mathbf{K}_{n+1} at time t_{n+1} are determined for given loading at time t_{n+1} and the known value of the internal variables \mathbf{K}_n at time t_n via the following principle (Carstensen et al., 2002; Mielke, 2002)

$$\begin{aligned} \{ \phi_{n+1}, \mathbf{K}_{n+1} \} = \\ \arg \min \left\{ \int_{\Omega} \{ \Psi(\nabla \phi, \mathbf{K}) + D(\mathbf{K}_n, \mathbf{K}) \} \, dV - \ell(t_{n+1}, \phi) \mid \phi, \mathbf{K} \right\}. \end{aligned} \quad (3.10)$$

Carrying out the minimization with respect to \mathbf{K} in (3.10) beforehand gives the so-called condensed energy

$$\Psi_{\mathbf{K}_n}^{\text{cond}}(\mathbf{F}) = \inf \{ \Psi(\mathbf{F}, \mathbf{K}) + D(\mathbf{K}_n, \mathbf{K}) \mid \mathbf{K} \} \quad (3.11)$$

which has been used in the literature to calculate the onset of microstructures (Ortiz and Repetto, 1999; Lambrecht et al., 2003; Bartels et al., 2004; Mielke, 2004; Conti and Theil,

2005). This approach, however, is based on the assumption that the material is homogeneous and does not exhibit a microstructure at the beginning of the time increment. Hence, it is not suitable to describe the evolution of already existing microstructures, as for each time step the internal variables already exhibit a microstructure at the beginning of the time increment as a result of a relaxation process in the preceding time-increment. Therefore, it is convenient to express the internal variables in the form of so-called Young measures.

Young measures are probability distributions $\lambda_{\mathbf{F}}(\mathbf{X}) \geq 0$ (given e.g. for the deformation gradient, i.e. on $\text{GL}(d)$) which satisfy the following properties:

$$\int \lambda_{\mathbf{F}} d\mathbf{F} = 1, \quad \int \lambda_{\mathbf{F}} \bar{\mathbf{F}} d\bar{\mathbf{F}} = \mathbf{F}. \quad (3.12)$$

Moreover, in the case of the deformation gradient the probability distribution must ensure spatial compatibility, i.e. the distributed deformation gradient must be realizable by some deformation field ϕ in Ω . This means that for some representative volume Ω_{rep}

$$\frac{1}{\Omega_{\text{rep}}} \int_{\Omega_{\text{rep}}} \Psi(\nabla \phi) dV = \int_{\text{GL}(d)} \lambda_{\bar{\mathbf{F}}} \Psi(\bar{\mathbf{F}}) d\bar{\mathbf{F}} \quad (3.13)$$

must hold for all quasiconvex potentials Ψ . In this case we call $\lambda_{\mathbf{F}} \in \text{GYM}$ a gradient Young measure.

It is now, at least in principle, possible to define a relaxed energy and dissipation functional Hackl (2005, 2006) via cross-quasiconvexification by

$$\begin{aligned} \Psi^{\text{rel}}(\mathbf{F}, \lambda_{\mathbf{K}}) = \inf \{ & \int \Lambda_{\bar{\mathbf{F}}, \bar{\mathbf{K}}} \Psi(\bar{\mathbf{F}}, \bar{\mathbf{K}}) d\bar{\mathbf{K}} d\bar{\mathbf{F}} \mid \Lambda_{\bar{\mathbf{F}}, \bar{\mathbf{K}}}; \int \Lambda_{\bar{\mathbf{F}}, \bar{\mathbf{K}}} d\bar{\mathbf{K}} d\bar{\mathbf{F}} = 1, \\ & \int \Lambda_{\bar{\mathbf{F}}, \bar{\mathbf{K}}} d\bar{\mathbf{K}} \in \text{GYM}, \int \Lambda_{\bar{\mathbf{F}}, \bar{\mathbf{K}}} d\bar{\mathbf{F}} = \lambda_{\mathbf{K}}, \int \Lambda_{\bar{\mathbf{F}}, \bar{\mathbf{K}}} \bar{\mathbf{F}} d\bar{\mathbf{K}} d\bar{\mathbf{F}} = \mathbf{F} \}, \end{aligned} \quad (3.14)$$

$$\begin{aligned} \Delta^*(\dot{\lambda}_{\mathbf{K}}) = \inf \{ & \int \Lambda_{\mathbf{K}_0, \mathbf{K}_1} D(\mathbf{K}_0, \mathbf{K}_1) d\mathbf{K}_0 d\mathbf{K}_1 \mid \Lambda_{\mathbf{K}_0, \mathbf{K}_1}; \\ & \int \Lambda_{\mathbf{K}_0, \mathbf{K}_1} d\mathbf{K}_0 d\mathbf{K}_1 = 1, \int \Lambda_{\mathbf{K}_0, \mathbf{K}_1} d\mathbf{K}_0 = \dot{\lambda}_{\mathbf{K}}, \int \Lambda_{\mathbf{K}_0, \mathbf{K}_1} d\mathbf{K}_1 = -\dot{\lambda}_{\mathbf{K}} \}. \end{aligned} \quad (3.15)$$

Related concepts have already been introduced and discussed in different settings by Mielke (2004). With these definitions we recover the original principles (3.5) and (3.7), with the only difference that the internal variables \mathbf{K} have been replaced by the Young measures $\lambda_{\mathbf{K}}$.

3.2.2 Approximation via Lamination

In general, expressions (3.14) and (3.15) will be hard to compute. One possible approximation is via so-called lamination. Applications of this procedure to the time-incremental problem can be found e.g. in (Bartels et al., 2004). For brevity, we will restrict ourselves here to first-order laminates. Everything stated in subsequent Sections can be extended to general laminates in an essentially straightforward manner, but the details of this may become very cumbersome.

A laminate of first order is characterized by N volume fractions λ_i separated by parallel planes with normal vector \mathbf{b} , as sketched in Figure 3.2. To every volume fraction there corresponds a value \mathbf{K}_i of the internal variables. Moreover, in every volume fraction we have a deformation gradient which we write in the form

$$\mathbf{F}_i = \mathbf{F}(\mathbf{I} + \mathbf{a}_i \otimes \mathbf{b}). \quad (3.16)$$

By choosing this form, deformation gradients differ only by tensors of rank one, enforcing compatibility at laminate interfaces and hence ensuring the existence of a corresponding deformation field. We need to impose the volume average of the deformation gradient,

$$\sum_{i=1}^N \lambda_i \mathbf{F}_i = \mathbf{F}, \quad (3.17)$$

which is equivalent to

$$\sum_{i=1}^N \lambda_i \mathbf{a}_i = \mathbf{0}. \quad (3.18)$$

Let us consider the normal vector \mathbf{b} as ingrained into the material because any change of \mathbf{b} would require a change of the internal variables and thus lead to dissipation. The amplitudes \mathbf{a}_i on the other hand can be changed purely elastically. This suggests to define a relaxed energy as

$$\Psi^{\text{rel}}(\mathbf{F}, \lambda, \mathbf{K}, \mathbf{b}) = \inf \left\{ \sum_{i=1}^N \lambda_i \Psi(\mathbf{F}_i, \mathbf{K}_i) \mid \mathbf{a}_i; \sum_{i=1}^N \lambda_i \mathbf{a}_i = \mathbf{0} \right\}, \quad (3.19)$$

where we introduced the abbreviations $\lambda = \{\lambda_1, \dots, \lambda_N\}$ and $\mathbf{K} = \{\mathbf{K}_1, \dots, \mathbf{K}_N\}$. If we further assume that the lamination respects the ordering $\{1, \dots, N\}$ and that the normal vector remains fixed, the relaxation of the dissipation is given by

$$\begin{aligned} \Delta^*(\lambda, \mathbf{K}, \dot{\lambda}, \dot{\mathbf{K}}) &= \sum_{i=1}^N \lambda_i \Delta(\mathbf{K}_i, \dot{\mathbf{K}}_i) + \inf \left\{ \sum_{i,j=1}^N \Delta \lambda_{ij} D(\mathbf{K}_i, \mathbf{K}_j) \mid \Delta \lambda_{ij}; \right. \\ &\quad \left. \sum_{i=1}^N \Delta \lambda_{ij} = \dot{\lambda}_j, \sum_{j=1}^N \Delta \lambda_{ij} = \dot{\lambda}_i, \Delta \lambda_{ij} = 0 \text{ for } |(i-j) \bmod N| \neq 1 \right\}. \end{aligned} \quad (3.20)$$

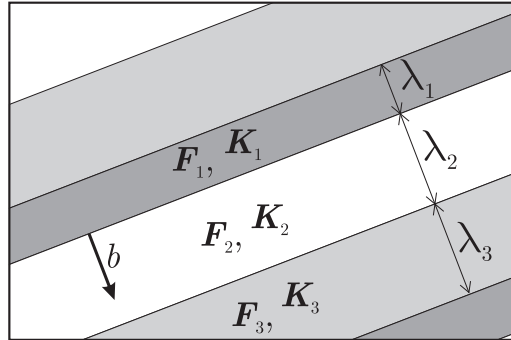


Figure 3.2: Sketch of a first-order laminate for $N = 3$ with normal vector \mathbf{b} .

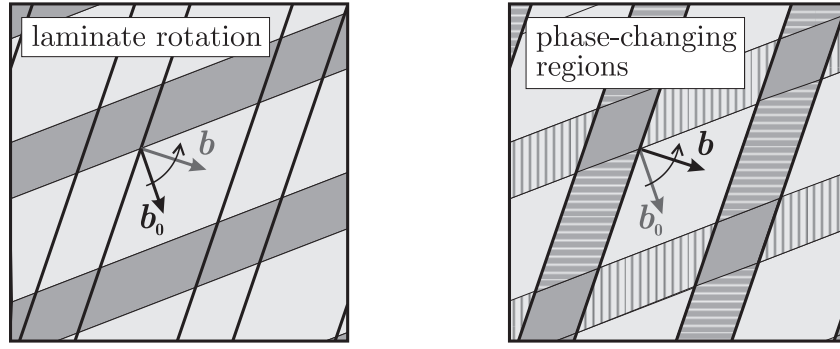


Figure 3.3: Rotation of the original laminate with old normal vector \mathbf{b}_0 to the new normal vector \mathbf{b} . The right graphic highlights the hatched regions which have changed their phase membership upon rotation and hence caused dissipation.

Now, once again from (3.7), we obtain evolution equations for λ and \mathbf{K} for fixed \mathbf{b} . As can be seen from Figure 3.3, however, a change of \mathbf{b} results in changes of the plastic slip in certain regions of the deformed body and is hence associated with a fixed amount of dissipation given by

$$D_{\mathbf{b}}(\lambda, \mathbf{K}) = \sum_{i=1}^N \sum_{j=1}^N \lambda_i \lambda_j D(\mathbf{K}_i, \mathbf{K}_j). \quad (3.21)$$

$D_{\mathbf{b}}$ is proportional to the total area of exchanged volume fractions (the hatched area in Figure 3.3) and the dissipation required for microstructurally changing these regions. We assume that a change of orientation will take place as soon as it becomes energetically favorable. This gives

$$\inf \{ \Psi^{\text{rel}}(\mathbf{F}, \lambda, \mathbf{K}, \mathbf{b}) - \Psi^{\text{rel}}(\mathbf{F}, \lambda, \mathbf{K}, \mathbf{b}_0) \mid \mathbf{b}; |\mathbf{b}| = 1 \} + D_{\mathbf{b}}(\lambda, \mathbf{K}) \leq 0 \quad (3.22)$$

for given \mathbf{b}_0 , λ , \mathbf{K} . The description of the inelastic evolution of a first order laminate is hence complete by Eq. (3.22). In the following we will specify this method to the case of crystal plasticity.

3.3 Incompressible Neo-Hooke Material in Single-Slip Plasticity

3.3.1 Constitutive Framework for a Single Active Slip System

We are going to demonstrate the general scheme introduced above by applying it to the crystal plasticity model introduced originally by Carstensen et al. (2002). In the following, we study the evolution of microstructures by employing a Neo-Hookean material with its free energy density

$$\Psi(\mathbf{F}_e) = \frac{1}{2} \mu [\text{tr} \mathbf{F}_e^T \mathbf{F}_e - 3] + \frac{K}{4} \left[j^2 - 2 \left(1 + 2 \frac{\mu}{K} \right) \ln j - 1 \right], \quad (3.23)$$

where \mathbf{F}_e denotes the elastic deformation gradient tensor, $j = \det \mathbf{F}_e$, and $\mu > 0$ and $K > 0$ are the shear and bulk moduli, respectively. To account for material hardening, let us introduce an internal hardening history variable p . In most of the subsequent analyses

we will limit our considerations to incompressible material behavior (a simplifying but approximately justified assumption for many materials) so that $j = \det \mathbf{F}_e = 1$. Note that incompressibility requires that not only $\det \mathbf{F}_p = 1$ but also $\det \mathbf{F}_e = \det \mathbf{F} = 1$. Then, the above energy reduces to

$$\Psi(\mathbf{F}_e, p) = \frac{1}{2}\mu (\text{tr } \mathbf{F}_e^T \mathbf{F}_e - 3) + \kappa p^\alpha, \quad \det \mathbf{F} = 1, \quad (3.24)$$

where $\kappa > 0$ is a hardening modulus of the material and α is commonly 2 (linear hardening) or 4. Multiplicative split of the deformation gradient into an elastic part \mathbf{F}_e and an irreversible, plastic part \mathbf{F}_p yields the standard multiplicative decomposition

$$\mathbf{F} = \mathbf{F}_e \mathbf{F}_p. \quad (3.25)$$

A slip system is characterized by its unit vectors \mathbf{s} and \mathbf{m} ($|\mathbf{s}| = |\mathbf{m}| = 1$, $\mathbf{s} \cdot \mathbf{m} = 0$), where \mathbf{s} characterizes the slip direction, and \mathbf{m} denotes the unit vector normal to the corresponding slip plane. If we have n active slip systems, the flow rule can be given in the form

$$\dot{\mathbf{F}}_p \mathbf{F}_p^{-1} = \sum_i^n \dot{\gamma}_i \mathbf{s}_i \otimes \mathbf{m}_i \quad (3.26)$$

with plastic slip rates $\dot{\gamma}_i$ and the initial conditions $\gamma_i(0) = 0$. Time-integration of (3.26) reduces to a neat analytical form if we assume that all slip directions lie in the same slip plane, i.e. $\mathbf{m} = \mathbf{m}_i \forall i$. Then, by time-integration (Carstensen et al., 2002) we infer

$$\mathbf{F}_p^{-1} = \mathbf{I} - \sum_i^n \gamma_i \mathbf{s}_i \otimes \mathbf{m}. \quad (3.27)$$

In this Section we limit our analysis to only one active slip system (single-slip plasticity or infinite latent hardening) so that the above condition further reduces to

$$\mathbf{F}_p^{-1} = \mathbf{I} - \gamma \mathbf{s} \otimes \mathbf{m}. \quad (3.28)$$

Furthermore, consider the additional flow rule (Carstensen et al., 2002)

$$\dot{p} = |\dot{\gamma}| \quad (3.29)$$

with the initial condition $p(0) = 0$. For the dissipation functional (with only one active slip system) we assume

$$\Delta(\dot{\gamma}) = r|\dot{\gamma}|, \quad (3.30)$$

with a positive constant r (the critical resolved shear stress), see (Carstensen et al., 2002) for details.

Due to a non-convex condensed energy, microstructures arise as energy minimizers. Let us assume a first-order laminate microstructure with N phases having interfaces with unit normal \mathbf{b} . We define the deformation gradient in phase i according to Eq. (3.16). To ensure incompressibility of each laminate phase, we must enforce that for every phase i we have $\det \mathbf{F}_i = 1$, which is equivalent to

$$\mathbf{a}_i \cdot \mathbf{b} = 0. \quad (3.31)$$

Taking this constraint into account, the laminate energy may be written as

$$\Psi^{\text{lam}}(\mathbf{F}, \lambda, \gamma, p, \mathbf{b}) = \frac{\mu}{2} \sum_i^N [\lambda_i \text{tr} \mathbf{C}_{e,i} - 2\lambda_i \mathbf{\Lambda} \cdot \mathbf{a}_i - 2\lambda_i \rho_i \mathbf{a}_i \cdot \mathbf{b}] - \frac{3}{2} \mu + \kappa \sum_i^N \lambda_i p_i^\alpha \quad (3.32)$$

where $\mathbf{C}_{e,i} = \mathbf{F}_{e,i}^\top \mathbf{F}_{e,i}$ denotes the elastic right Cauchy-Green tensor in phase i with

$$\mathbf{F}_{e,i} = \mathbf{F}(\mathbf{I} + \mathbf{a}_i \otimes \mathbf{b})(\mathbf{I} - \gamma_i \mathbf{s} \otimes \mathbf{m}), \quad (3.33)$$

and $\mathbf{\Lambda}$ and ρ_i are Lagrange multipliers to enforce constraints (3.18) and (3.31). Minimizing (3.32) with respect to the unknown quantities \mathbf{a}_i , we arrive at

$$\frac{\partial \Psi^{\text{lam}}}{\partial \mathbf{a}_i} = \mathbf{0} \Leftrightarrow 2\lambda_i \mathbf{C}(\mathbf{I} + \mathbf{a}_i \otimes \mathbf{b})(\mathbf{I} - \gamma_i \mathbf{s} \otimes \mathbf{m})(\mathbf{I} - \gamma_i \mathbf{m} \otimes \mathbf{s}) \cdot \mathbf{b} - 2\lambda_i \mathbf{\Lambda} - 2\lambda_i \rho_i \mathbf{b} = \mathbf{0}, \quad (3.34)$$

where $\mathbf{C} = \mathbf{F}^\top \mathbf{F}$ denotes the right Cauchy-Green tensor. Let us define

$$\mathbf{b}_i = \mathbf{b} - \gamma_i(\mathbf{b} \cdot \mathbf{m} \mathbf{s} + \mathbf{b} \cdot \mathbf{s} \mathbf{m}) + \gamma_i^2 \mathbf{b} \cdot \mathbf{s} \mathbf{s} \quad (3.35)$$

to re-arrange the above equation to

$$\mathbf{a}_i \mathbf{b}_i \cdot \mathbf{b} = \mathbf{C}^{-1} \mathbf{\Lambda} + \rho_i \mathbf{C}^{-1} \mathbf{b} - \mathbf{b}_i, \quad (3.36)$$

from which follows that

$$\begin{aligned} \rho_i &= \frac{\mathbf{b}_i \cdot \mathbf{b}}{\mathbf{b} \cdot \mathbf{C}^{-1} \mathbf{b}}, \\ \mathbf{\Lambda} &= \frac{\mathbf{C}}{\sum_i \frac{\lambda_i}{\mathbf{b}_i \cdot \mathbf{b}}} \left(\sum_i \frac{\lambda_i}{\mathbf{b}_i \cdot \mathbf{b}} \mathbf{b}_i - \frac{1}{\mathbf{b} \cdot \mathbf{C}^{-1} \mathbf{b}} \mathbf{C}^{-1} \mathbf{b} \right), \\ \mathbf{a}_i &= \frac{1}{\mathbf{b}_i \cdot \mathbf{b}} \mathbf{C}^{-1} \mathbf{\Lambda} + \frac{1}{\mathbf{b} \cdot \mathbf{C}^{-1} \mathbf{b}} \mathbf{C}^{-1} \mathbf{b} - \frac{1}{\mathbf{b}_i \cdot \mathbf{b}} \mathbf{b}_i. \end{aligned} \quad (3.37)$$

Application of (3.37) to (3.32) yields the relaxed energy in the form

$$\begin{aligned} \Psi^{\text{rel}}(\mathbf{F}, \lambda, \gamma, p, \mathbf{b}) &= \inf \{ \Psi^{\text{lam}}(\mathbf{F}, \lambda, \gamma, p, \mathbf{b}) \mid \mathbf{a}_i \} \\ &= \kappa \sum_i^N \lambda_i p_i^\alpha + \frac{\mu}{2} \left[\frac{1}{\sum_i^N \frac{\lambda_i}{\mathbf{b}_i \cdot \mathbf{b}}} \left(\sum_j^N \sum_k^N \frac{\lambda_j \lambda_k \mathbf{b}_j \cdot \mathbf{C} \mathbf{b}_k}{\mathbf{b}_j \cdot \mathbf{b} \mathbf{b}_k \cdot \mathbf{b}} - \frac{1}{\mathbf{b} \cdot \mathbf{C}^{-1} \mathbf{b}} \right) \right. \\ &\quad \left. + \sum_i^N \lambda_i \left(\frac{\mathbf{b}_i \cdot \mathbf{b}}{\mathbf{b} \cdot \mathbf{C}^{-1} \mathbf{b}} - \frac{\mathbf{b}_i \cdot \mathbf{C} \mathbf{b}_i}{\mathbf{b}_i \cdot \mathbf{b}} \right) + \text{tr} \mathbf{C} + \sum_i^N \lambda_i (\gamma_i^2 \mathbf{s} \cdot \mathbf{C} \mathbf{s} - 2\gamma_i \mathbf{s} \cdot \mathbf{C} \mathbf{m}) - 3 \right] \end{aligned} \quad (3.38)$$

with $\gamma = \{\gamma_1, \dots, \gamma_N\}$, $p = \{p_1, \dots, p_N\}$.

The non-convexity of the employed free energy density can easily be verified by investigating the behavior of the unrelaxed solution for a single phase ($N = 1$), which gives the condensed energy

$$\Psi^{\text{cond}}(\mathbf{F}) = \inf \left\{ \Psi(\mathbf{F}, \gamma, p) + r|\gamma| \mid \gamma : p = |\gamma| \right\}. \quad (3.39)$$

The condensed energy is illustrated in Figure 3.4 for plane-strain simple shear ($\mathbf{F} = \mathbf{I} + \gamma \mathbf{e}_1 \otimes \mathbf{e}_2$), where the in-plane orientation of the laminate phase normal vector is defined

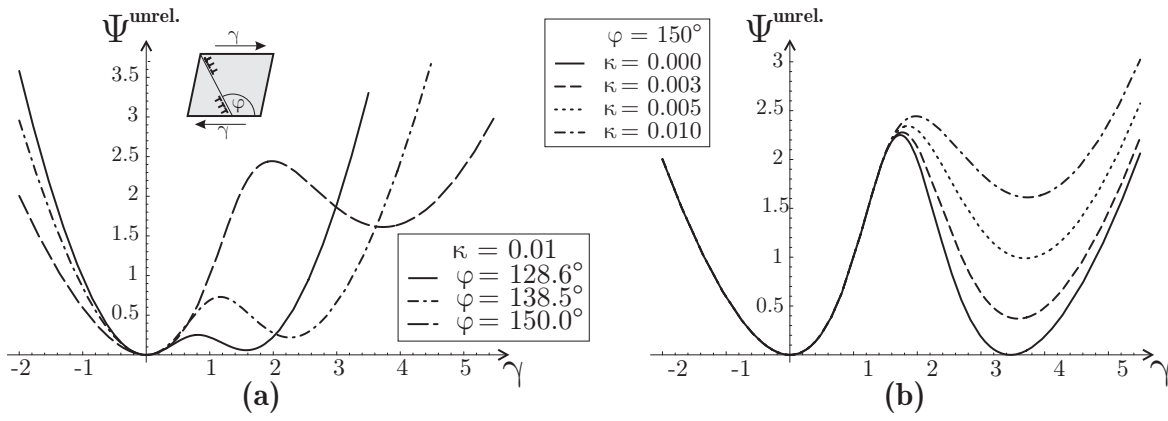


Figure 3.4: Unrelaxed condensed energy of a homogeneous single crystal with one active slip system. The energy is clearly not convex for positive γ whereas convex for negative γ . a) Condensed energy for fixed hardening and varying slip system orientation, b) condensed energy for fixed slip system orientation and varying hardening parameter values.

by $\mathbf{b} = (\cos \varphi, \sin \varphi, 0)^T$, for different orientations φ and varying hardening parameter κ ($\alpha = 4$). Note that upon positive loading ($\gamma > 0$) the energy is clearly non-convex giving rise to instability and hence to the formation of microstructure whereas during negative loading ($\gamma < 0$) no such non-convexity is observed, as has already been discussed e.g. by Carstensen et al. (2002) or Lambrecht et al. (2003).

For simplicity let us reduce the present model to a two-phase laminate ($N = 2$) and define the volume fraction of phase 2 as λ such that by taking into account (3.30) the dissipation potential defined in (3.20) may be written in the form

$$\Delta^*(\lambda, \gamma_i, \dot{\lambda}, \dot{\gamma}_i) = r \left(\left| \dot{\lambda}(\gamma_1 - \gamma_2) \right| + (1 - \lambda) |\dot{\gamma}_1| + \lambda |\dot{\gamma}_2| \right), \quad (3.40)$$

and the Lagrange functional corresponding to (3.6) now becomes

$$\mathcal{L}(\mathbf{F}, \lambda, \gamma_i, p_i, \dot{\lambda}, \dot{\gamma}_i, \mathbf{b}) = \frac{d}{dt} \Psi^{\text{rel}}(\mathbf{F}, \lambda, \gamma_i, p_i, \mathbf{b}) + \Delta^*(\lambda, \gamma_i, \dot{\lambda}, \dot{\gamma}_i). \quad (3.41)$$

Here, one of the major differences of the present model to previous approaches becomes apparent from the first term of (3.40): A change of the volume fractions (here, of λ) causes dissipation. However, we do not consider the dissipation required to transform some region with originally no plastic history into a part of the increasing phase. Instead, we correctly account for the transformation of some part originally of phase 1 into a part of the expanding phase 2 (hence, $\Delta^* = \dot{\lambda} |\gamma_1 - \gamma_2|$). Therefore, the dissipation (and thus the evolution of the internal variables) depends on the microstructure at the beginning of each time step.

3.3.2 Time-Continuous Evolution for a Single Active Slip System

Via the principle given in (3.7) we now arrive at evolution equations for λ and γ_i from the above Lagrange functional as

$$-r |\gamma_1 - \gamma_2| \text{sign } \dot{\lambda} \in -q = \frac{\partial \Psi^{\text{rel}}}{\partial \lambda}, \quad (3.42)$$

$$-r(1 - \lambda) \text{sign } \dot{\gamma}_1 \in \frac{\partial \Psi^{\text{rel}}}{\partial \gamma_1} + \frac{\partial \Psi^{\text{rel}}}{\partial p_1} \text{sign } \dot{\gamma}_1, \quad (3.43)$$

$$-r\lambda \text{sign } \dot{\gamma}_2 \in \frac{\partial \Psi^{\text{rel}}}{\partial \gamma_2} + \frac{\partial \Psi^{\text{rel}}}{\partial p_2} \text{sign } \dot{\gamma}_2. \quad (3.44)$$

For the above model the driving forces (i.e. the derivatives of the free energy) can analytically be computed as

$$\begin{aligned} \frac{\partial \Psi^{\text{rel}}}{\partial \lambda} = & \frac{\mu}{2} [\text{tr } \mathbf{C}_{e,2} - \text{tr } \mathbf{C}_{e,1} - 2\mathbf{\Lambda} \cdot (\mathbf{a}_2 - \mathbf{a}_1) - 2(\rho_2 \mathbf{a}_2 - \rho_1 \mathbf{a}_1) \cdot \mathbf{b}] \\ & + \kappa (p_2^\alpha - p_1^\alpha), \end{aligned} \quad (3.45)$$

$$\frac{\partial \Psi^{\text{rel}}}{\partial \gamma_1} = -\frac{\mu}{2}(1 - \lambda) \text{tr} [\mathbf{m} \otimes \mathbf{s}(\mathbf{I} + \mathbf{b} \otimes \mathbf{a}_1)\mathbf{C}(\mathbf{I} + \mathbf{a}_1 \otimes \mathbf{b})(\mathbf{I} - \gamma_1 \mathbf{s} \otimes \mathbf{m})], \quad (3.46)$$

$$\frac{\partial \Psi^{\text{rel}}}{\partial \gamma_2} = -\frac{\mu}{2}\lambda \text{tr} [\mathbf{m} \otimes \mathbf{s}(\mathbf{I} + \mathbf{b} \otimes \mathbf{a}_2)\mathbf{C}(\mathbf{I} + \mathbf{a}_2 \otimes \mathbf{b})(\mathbf{I} - \gamma_2 \mathbf{s} \otimes \mathbf{m})], \quad (3.47)$$

with $\mathbf{\Lambda}$ and ρ_i from Eqs. (3.37). Note that we may use the (for numerical computations simpler) partial derivatives, since for all internal variables y involved (e.g. λ, γ_i) we have

$$\frac{d\Psi^{\text{rel}}}{dy} = \frac{\partial \Psi^{\text{rel}}}{\partial y} + \frac{\partial \Psi^{\text{rel}}}{\partial \mathbf{a}_i} \frac{\partial \mathbf{a}_i}{\partial y} = \frac{\partial \Psi^{\text{rel}}}{\partial y}. \quad (3.48)$$

Instead of solving the stationarity conditions one can also numerically minimize the Lagrange functional

$$\begin{aligned} \mathcal{L}(\mathbf{F}, \lambda, \gamma_i, p_i, \dot{\lambda}, \dot{\gamma}_i, \dot{p}_i, \mathbf{b}) = & \frac{\partial \Psi^{\text{rel}}}{\partial \lambda} \dot{\lambda} + \sum_{i=1}^2 \frac{\partial \Psi^{\text{rel}}}{\partial \gamma_i} \dot{\gamma}_i + \alpha \kappa \sum_{i=1}^2 p_i^{\alpha-1} |\dot{\gamma}_i| \\ & + r \left[\dot{\lambda}(\gamma_1 - \gamma_2) \right] + r(1 - \lambda) |\dot{\gamma}_1| + r\lambda |\dot{\gamma}_2|, \end{aligned} \quad (3.49)$$

with respect to the rates of all internal variables.

With our goal of computing the evolution of plastic microstructures in mind, we need to find an incremental formulation to be solved numerically, using finite deformation increments $[\mathbf{F}_n, \mathbf{F}_{n+1}]$ with known initial conditions $\mathbf{F}_n, \gamma_{i,n}, \lambda_n, p_{i,n}$ at the beginning of each time step (i.e. at time t_n) and the known deformation gradient \mathbf{F}_{n+1} at the end of the time step, i.e. at time $t_{n+1} = t_n + \Delta t$. For a small time step we approximate the rate of change of the internal variables as

$$\dot{y} = \frac{y_{n+1} - y_n}{\Delta t} = \frac{\Delta y}{\Delta t}. \quad (3.50)$$

Eqs. (3.42)-(3.44) can then be used to compute the updates

$$\Delta \lambda = \lambda_{n+1} - \lambda_n, \quad \Delta \gamma_i = \gamma_{i,n+1} - \gamma_{i,n}, \quad \Delta p_i = p_{i,n+1} - p_{i,n}. \quad (3.51)$$

Before outlining the numerical scheme, we need to discuss three important steps of our model. Firstly, any change of λ results in mixing the formerly pure phases in a small part of Ω (as mentioned above); e.g. an increase in λ will raise the volume fraction of phase 2 (with history variable p_2) by certain regions which were previously associated with phase 1 and hence exhibited history variable value p_1 . We propose to obtain the updated p -values in both phases by taking the energetic average. For $\lambda_{n+1} = \lambda_n + \Delta\lambda$ and $\Delta\lambda > 0$ we have

$$(\lambda_n + \Delta\lambda) p_{2,n+1}^\alpha = \lambda_n p_{2,n}^\alpha + \Delta\lambda p_{1,n}^\alpha, \quad p_{1,n+1} = p_{1,n}, \quad (3.52)$$

and analogously for $\Delta\lambda < 0$

$$(1 - \lambda_n - \Delta\lambda) p_{1,n+1}^\alpha = (1 - \lambda_n) p_{1,n}^\alpha - \Delta\lambda p_{2,n}^\alpha, \quad p_{2,n+1} = p_{2,n}. \quad (3.53)$$

Secondly, once a laminate microstructure exists, changes of the orientation vector \mathbf{b} will be treated using the criterion given in (3.22). We check upon each load increment whether or not a rotation of the laminate is energetically admissible by means of (3.22), i.e. by finding \mathbf{b}_{n+1} from

$$\Psi^{\text{rel}}(\mathbf{F}_n, \lambda_n, \gamma_{i,n}, p_{i,n}, \mathbf{b}_{n+1}) - \Psi^{\text{rel}}(\mathbf{F}_n, \lambda_n, \gamma_{i,n}, p_{i,n}, \mathbf{b}_n) + 2r\lambda_n(1 - \lambda_n) |\gamma_{1,n} - \gamma_{2,n}| \leq 0, \quad (3.54)$$

where the last term represents the dissipation given by (3.21).

Thirdly, a crucial issue is the initiation of the laminate microstructure from the originally uniform single crystal. Here, two equally sensible methods are relevant. On the one hand, it is possible to numerically compute the condensed relaxed energy, see (3.11),

$$\Psi_{n+1}^{\text{cond,rel}}(\mathbf{F}_{n+1}) = \min \left\{ \Psi^{\text{rel}}(\mathbf{F}_{n+1}, \gamma_{1,n}, \gamma_2, \lambda, \mathbf{b}) + r |\lambda(\gamma_2 - \gamma_{1,n})| \mid \gamma_2, \lambda, \mathbf{b} : \right. \\ \left. p_2 = |\gamma_2|, 0 \leq \lambda \leq 1, |\mathbf{b}| = 1 \right\} \quad (3.55)$$

and check whether or not $\Psi_{n+1}^{\text{cond,rel}} \leq \Psi_{n+1}^{\text{cond}}$, i.e. if the formation of a laminate can reduce the energy below that of the homogeneous crystal. If $\Psi_{n+1}^{\text{cond,rel}} \leq \Psi_{n+1}^{\text{cond}}$, then a laminate forms with $(\gamma_2, \lambda, \mathbf{b}) = \text{argmin} \Psi_{n+1}^{\text{cond,rel}}$ from (3.55). On the other hand, one can treat the laminate initiation as follows. At the beginning of each time increment n , one computes the driving force $q_{\lambda,n}$ on the volume fractions in the limit of a marginal amount of phase 2, i.e.

$$q_{\lambda,n}(\mathbf{F}_{n+1}, \gamma_{1,n}, \gamma_{2,n+1}, p_{1,n}, p_{2,n+1}, \mathbf{b}_{n+1}) = \lim_{\lambda \rightarrow 0} q(\mathbf{F}_{n+1}, \lambda, \gamma_{1,n}, \gamma_{2,n+1}, p_{1,n}, p_{2,n+1}, \mathbf{b}_{n+1}). \quad (3.56)$$

Maximizing this driving force with respect to \mathbf{b}_{n+1} and $\gamma_{2,n+1}$, one can determine the energetically favored values of these quantities in the arising phase 2, i.e.

$$(\mathbf{b}_{n+1}, \gamma_{2,n+1}) = \text{argmax} \left\{ q_{\lambda,n} \mid p_{2,n+1} = |\gamma_{2,n+1}|, |\mathbf{b}_{n+1}| = 1 \right\}. \quad (3.57)$$

One then determines the actual value of λ_{n+1} by solving

$$r |\gamma_{1,n} - \gamma_{2,n+1}| = q(\mathbf{F}_{n+1}, \lambda_{n+1}, \gamma_{1,n}, \gamma_{2,n+1}, p_{1,n}, p_{2,n+1} = |\gamma_{2,n+1}|, \mathbf{b}_{n+1}). \quad (3.58)$$

If there exists a solution λ_{n+1} , a laminate forms with phase 2 having the determined values of λ_{n+1} , $\gamma_{2,n+1}$ and \mathbf{b}_{n+1} .

Algorithm 1: Incremental solution for a single active slip system

(a) incremental load update: $\mathbf{F}_{n+1} = \mathbf{F}_n + \Delta \mathbf{F}$

(b) find λ_{n+1} (assume $\gamma_i = \gamma_{i,n} = \text{const.}$):

- for the initially uniform single-crystal ($\lambda_n = 0$) find \mathbf{b}_{n+1} and $\gamma_{2,n+1}$ from

$$\max_{\mathbf{b}_{n+1}, \gamma_{2,n+1}} \left\{ \lim_{\epsilon \rightarrow 0} q(\mathbf{F}_{n+1}, \lambda = \epsilon, \gamma_{1,n}, p_{1,n}, \gamma_{2,n+1}, p_{2,n+1} = |\gamma_{2,n+1}|, \mathbf{b}_{n+1}) \right\}$$

and λ_{n+1} from

$$r |\gamma_{1,n} - \gamma_{2,n+1}| = q(\mathbf{F}_{n+1}, \lambda_{n+1}, \gamma_{1,n}, \gamma_{2,n+1}, p_{1,n}, p_{2,n+1} = |\gamma_{2,n+1}|, \mathbf{b}_{n+1}).$$

$$\Rightarrow \text{if } 0 \leq \lambda_{n+1} \leq 1, \text{ update } \lambda_{n+1}, \gamma_{2,n+1}, \mathbf{b}_{n+1}$$

- for an existing laminate microstructure ($\lambda_n > 0$) solve:

$$q(\mathbf{F}_{n+1}, \lambda_n + \Delta \lambda, \gamma_{i,n}, p_{i,n}) \text{sign } \Delta \lambda = r |\gamma_{1,n} - \gamma_{2,n}|$$

$$\Rightarrow \lambda_{n+1} = \lambda_n + \Delta \lambda$$

- check for a laminate rotation by finding \mathbf{b}_{n+1} such that:

$$\min_{\mathbf{b}_{n+1}} \Psi^{\text{rel}}(\mathbf{b}_{n+1}) - \Psi^{\text{rel}}(\mathbf{b}_n) + 2r \lambda_{n+1} (1 - \lambda_{n+1}) |\gamma_{1,n} - \gamma_{2,n}| \stackrel{?}{\leq} 0$$

- update $p_{i,n+1}$ according to (3.52) or (3.53)

(c) find $\gamma_{i,n+1}$ (assume $\lambda = \lambda_{i,n+1} = \text{const.}$) by solving:

$$\left[\begin{array}{l} \frac{\partial \Psi^{\text{rel}}}{\partial \gamma_1} + \frac{\partial \Psi^{\text{rel}}}{\partial p_1} \text{sign } \Delta \gamma_1 \\ \frac{\partial \Psi^{\text{rel}}}{\partial \gamma_2} + \frac{\partial \Psi^{\text{rel}}}{\partial p_2} \text{sign } \Delta \gamma_2 \end{array} \right]_{\substack{\gamma_{i,n} + \Delta \gamma_i \\ p_{i,n} + |\Delta \gamma_i|}} = \begin{array}{l} -r (1 - \lambda_{n+1}) \text{sign } \Delta \gamma_1 \\ -r \lambda_{n+1} \text{sign } \Delta \gamma_2 \end{array}$$

$$\Rightarrow \gamma_{i,n+1} = \gamma_{i,n} + \Delta \gamma_i, \quad p_{i,n+1} = p_{i,n} + |\Delta \gamma_i|$$

3.3.3 Numerical Scheme for a Single Active Slip System

Our numerical scheme takes the form outlined in Algorithm 1. This algorithm computes the microstructure evolution (i.e. the updates of the plastic slips $\Delta\gamma_i$, the history variable update Δp_i , and the volume fraction update $\Delta\lambda$) by incrementally minimizing functional (3.41). Since we are using the relaxed energy and dissipation functional, this constitutes a well-posed problem and we can resort to solving the stationarity conditions (3.42) through (3.44). For a given load increment $[\mathbf{F}_n, \mathbf{F}_{n+1}]$ each step starts with the current state as initial conditions $\lambda_n, \gamma_{i,n}, p_{i,n}$, and solves the stationarity conditions in order to update all internal variables at time t_{n+1} with known load \mathbf{F}_{n+1} . For the initially homogeneous material the interface normal \mathbf{b}_{n+1} as well as the internal variables of the originating second laminate phase, $\gamma_{2,n+1}$ and $p_{2,n+1}$, are determined from (3.57), and the initial value of λ is obtained from (3.58). Alternatively, one can find the initial laminate by employing the condensed energy functional. Once a laminate has formed the evolution of the variables λ, γ_i and p_i is computed by a staggered scheme. In a first step a time-discretized version of (3.42) is solved for the increment $\Delta\lambda$ for fixed γ_1 and γ_2 . Afterwards, p_1 and p_2 are updated via (3.52) or (3.53). Then in a second step, (3.43) and (3.44) are solved for the increments $\Delta\gamma_1$ and $\Delta\gamma_2$ for fixed λ , and the p_i -values are again updated according to (3.29). Finally the updated values of $\lambda, \gamma_1, \gamma_2, p_1, p_2$ are transferred to the next time-step.

3.4 Generalization to Multiple Active Slip Systems

3.4.1 Constitutive Framework for Multiple Active Slip Systems

Analogously to the constitutive framework outlined in the previous Section, we employ the energy density for an incompressible neo-Hookean material of the form

$$\Psi(\mathbf{F}_e, \mathbf{p}) = \frac{1}{2}\mu (\text{tr } \mathbf{F}_e^T \mathbf{F}_e - 3) + \kappa \sum_i^n p_i^\alpha, \quad \det \mathbf{F} = 1. \quad (3.59)$$

Each of the now n active slip systems i is characterized by its slip direction \mathbf{s}_i and slip plane normal \mathbf{m}_i ($|\mathbf{s}_i| = |\mathbf{m}_i| = 1, \mathbf{s}_i \cdot \mathbf{m}_i = 0$). Cross hardening could be accounted for by replacing the above hardening term by $\sum_i \sum_j \kappa_{ij} |p_i p_j|^{\alpha/2}$ but here we limit our analysis to the above form. We consider the same flow rules as before, with slip-rates $\dot{\gamma}_i$,

$$\dot{\mathbf{F}}_p \mathbf{F}_p^{-1} = \sum_i^n \dot{\gamma}_i \mathbf{s}_i \otimes \mathbf{m}_i, \quad \dot{p}_i = |\dot{\gamma}_i| \quad (3.60)$$

with initial conditions $\gamma_i(0) = 0$ and $p_i(0) = 0$. We limit our considerations here to slip systems with a common slip plane normal $\mathbf{m}_i = \mathbf{m}$. In this case, we can infer via time-integration that

$$\mathbf{F}_p^{-1} = \mathbf{I} - \sum_i^n \gamma_i \mathbf{s}_i \otimes \mathbf{m}. \quad (3.61)$$

We assume the same first-order laminate microstructure as before with N phases having interfaces with unit normal \mathbf{b} . We define the deformation gradient in phase i according to Eq.

(3.16). For multiple slip systems, the relaxed energy for a first-order laminate analogously to (3.38) takes the form

$$\begin{aligned} \Psi^{\text{rel}}(\mathbf{F}, \lambda, \gamma_{ij}, p_{ij}, \mathbf{b}) &= \kappa \sum_i^N \lambda_i \sum_j^n p_{ij}^\alpha + \frac{\mu}{2} \left[\frac{1}{\sum_i^N \frac{\lambda_i}{\mathbf{b}_i \cdot \mathbf{b}}} \left(\sum_j^N \sum_k^N \frac{\lambda_j \lambda_k \mathbf{b}_j \cdot \mathbf{C} \mathbf{b}_k}{\mathbf{b}_j \cdot \mathbf{b} \mathbf{b}_k \cdot \mathbf{b}} - \frac{1}{\mathbf{b} \cdot \mathbf{C}^{-1} \mathbf{b}} \right) \right. \\ &\quad + \sum_i^N \lambda_i \left(\frac{\mathbf{b}_i \cdot \mathbf{b}}{\mathbf{b} \cdot \mathbf{C}^{-1} \mathbf{b}} - \frac{\mathbf{b}_i \cdot \mathbf{C} \mathbf{b}_i}{\mathbf{b}_i \cdot \mathbf{b}} \right) + \text{tr } \mathbf{C} - 3 \\ &\quad \left. + \sum_i^N \lambda_i \text{tr} \left(\mathbf{I} - \sum_j^n \gamma_{ij} \mathbf{m} \otimes \mathbf{s}_j \right) \mathbf{C} \left(\mathbf{I} - \sum_j^n \gamma_{ij} \mathbf{s}_j \otimes \mathbf{m} \right) \right], \end{aligned} \quad (3.62)$$

where

$$\mathbf{b}_i = \left(\mathbf{I} - \sum_j^n \gamma_{ij} \mathbf{s}_j \otimes \mathbf{m} \right) \left(\mathbf{I} - \sum_j^n \gamma_{ij} \mathbf{m} \otimes \mathbf{s}_j \right) \cdot \mathbf{b}. \quad (3.63)$$

$\mathbf{C} = \mathbf{F}^\top \mathbf{F}$ is the right Cauchy-Green tensor, p_{ij} is the hardening history and γ_{ij} the plastic slip in phase i on slip system j .

For simplicity let us reduce the present model to a two-phase laminate ($N = 2$) with two active slip systems ($n = 2$). We define the volume fraction of phase 2 as λ such that the dissipation potential for only one slip system was given in the form (Hackl and Kochmann, 2008)

$$\Delta^*(\lambda, \gamma_i, \dot{\lambda}, \dot{\gamma}_i) = r \left((1 - \lambda) |\dot{\gamma}_1| + \lambda |\dot{\gamma}_2| + \left| \dot{\lambda}(\gamma_1 - \gamma_2) \right| \right). \quad (3.64)$$

For multiple slip systems, the definition of Δ^* is no longer unique. We assume a dissipation potential of the following type:

$$\begin{aligned} \Delta^*(\lambda, \gamma_{ij}, \dot{\lambda}, \dot{\gamma}_{ij}) &= r \left[(1 - \lambda) (|\dot{\gamma}_{11}| + |\dot{\gamma}_{12}|) + \lambda (|\dot{\gamma}_{21}| + |\dot{\gamma}_{22}|) \right. \\ &\quad \left. + |\dot{\lambda}(\gamma_{11} - \gamma_{12})| + |\dot{\lambda}(\gamma_{21} - \gamma_{22})| \right]. \end{aligned} \quad (3.65)$$

This form implies that motion of dislocations occurs on both slip systems independently and without interference.

The Lagrange functional corresponding to (3.6) now takes the form

$$\mathcal{L}(\mathbf{F}, \lambda, \gamma_{ij}, p_{ij}, \dot{\lambda}, \dot{\gamma}_{ij}, \mathbf{b}) = \frac{d}{dt} \Psi^{\text{rel}}(\mathbf{F}, \lambda, \gamma_{ij}, p_{ij}, \mathbf{b}) + \Delta^*(\lambda, \gamma_{ij}, \dot{\lambda}, \dot{\gamma}_{ij}). \quad (3.66)$$

Via the principle given in (3.7) we now arrive at five evolution equations for λ and γ_{ij} from the above Lagrange functional (for $j = 1, 2$)

$$-r [|\gamma_{11} - \gamma_{12}| + |\gamma_{21} - \gamma_{22}|] \text{sign } \dot{\lambda} \in -q = \frac{\partial \Psi^{\text{rel}}}{\partial \lambda}, \quad (3.67)$$

$$-r (1 - \lambda) \text{sign } \dot{\gamma}_{1j} \in \frac{\partial \Psi^{\text{rel}}}{\partial \gamma_{1j}} + \frac{\partial \Psi^{\text{rel}}}{\partial p_{1j}} \text{sign } \dot{\gamma}_{1j}, \quad (3.68)$$

$$-r \lambda \text{sign } \dot{\gamma}_{2j} \in \frac{\partial \Psi^{\text{rel}}}{\partial \gamma_{2j}} + \frac{\partial \Psi^{\text{rel}}}{\partial p_{2j}} \text{sign } \dot{\gamma}_{2j}. \quad (3.69)$$

To obtain a numerical scheme for computing the evolution of plastic microstructures, we make use of an incremental formulation to be solved numerically for finite deformation increments $[\mathbf{F}_n, \mathbf{F}_{n+1}]$. Note that a change of λ results in mixing the formerly pure phases in a small part of Ω . We proposed to obtain the updated p values by taking the energetic average (Hackl and Kochmann, 2008). Here, we adopt this in principle but for each slip system independently (no slip system interaction), i.e. for $\lambda_{n+1} = \lambda_n + \Delta\lambda$ and e. g. $\Delta\lambda > 0$ we have

$$(\lambda_n + \Delta\lambda) p_{21,n+1}^\alpha = \lambda p_{21,n}^\alpha + \Delta\lambda p_{11,n}^\alpha, \quad p_{11,n+1} = p_{11,n}, \quad (3.70)$$

$$(\lambda_n + \Delta\lambda) p_{22,n+1}^\alpha = \lambda p_{22,n}^\alpha + \Delta\lambda p_{12,n}^\alpha, \quad p_{21,n+1} = p_{21,n}. \quad (3.71)$$

To find the onset of microstructure formation, we investigate upon each increment if there exists a combination $(\mathbf{b}, \gamma_{21}, \gamma_{22}, \lambda)$ which can reduce the crystal's energy below the unrelaxed energy of a homogeneous single crystal. If so, the unstable homogeneous deformation state breaks up into a laminate microstructure with the determined values of $\mathbf{b}, \gamma_{21}, \gamma_{22}, \lambda$. Otherwise, no microstructure originates. Once the laminate has formed, we check with each further increment whether or not a rotation of the laminate is energetically admissible by means of (3.22), i.e. by finding \mathbf{b}_{n+1} from

$$\Psi^{\text{rel}}(\mathbf{b}_{n+1}) - \Psi^{\text{rel}}(\mathbf{b}_n) + 2r\lambda_n(1 - \lambda_n)(|\gamma_{12,n} - \gamma_{22,n}| + |\gamma_{21,n} - \gamma_{22,n}|) \leq 0, \quad (3.72)$$

where the last term represents the dissipation given by (3.21).

3.4.2 Numerical Scheme for Double-Slip

Our numerical scheme is outlined in Algorithm 2. This algorithm computes the microstructure evolution (i.e. plastic slips γ_{ij} and volume fraction λ) by incrementally minimizing functional (3.66). As we still use the relaxed energy and dissipation functional, this constitutes a well-posed problem and we can resort to solving the stationarity conditions (3.67), (3.68) and (3.69). Each step starts with the current state as the initial condition and solves the stationarity conditions in order to update the internal variables. For initially homogeneous material (i.e. no laminate present) the interface normal \mathbf{b} as well as the slips γ_{2j} for the originating second laminate phase are determined via maximization of the driving force. Once a laminate has formed, the evolution of variables λ and γ_{ij} is computed by a staggered algorithm: In a first step a time-discretized version of (3.67) is solved for the increment $\Delta\lambda$ for fixed γ_{ij} . Afterwards, p_{ij} are updated via (3.70) and (3.71). Then in a second step, (3.68) and (3.69) (for $j = 1, 2$) are solved for the increments $\Delta\gamma_{ij}$ for fixed λ . Again, we accomplish this in a staggered form (γ_{1j} are updated first, then follow γ_{2j}) to reduce complexity of the minimization problem. Numerical experiments indicate a rather negligible influence of the order of the staggered algorithm with a sufficiently small time step. Finally, the updated values of λ and γ_{ij} are transferred to the next time-step.

Algorithm 2: Incremental evolution for double-slip plasticity

(a) incremental load update: $\mathbf{F}_{n+1} = \mathbf{F}_n + \Delta \mathbf{F}$

(b) find λ_{n+1} (assume $\gamma_{ij} = \text{const.} = \gamma_{ij,n}$):

- for the initially uniform single-crystal ($\lambda_n = 0$) find \mathbf{b}_{n+1} and $\gamma_{2j,n+1}$ from ($j = 1, 2$)

$$\max_{\mathbf{b}_{n+1}, \gamma_{2j,n+1}} \left\{ \lim_{\epsilon \rightarrow 0} q(\mathbf{F}_{n+1}, \lambda = \epsilon, \gamma_{1j,n}, \gamma_{2j,n+1}, p_{1j,n}, p_{2j,n+1} = |\gamma_{2,n+1}|, \mathbf{b}_{n+1}) \right\}$$

and λ_{n+1} from

$$r (|\gamma_{11,n} - \gamma_{21,n}| + |\gamma_{12,n} - \gamma_{22,n}|) = q(\mathbf{F}_{n+1}, \lambda_{n+1}, \gamma_{ij,n}, p_{ij,n})$$

$$\Rightarrow \text{if } 0 \leq \lambda_{n+1} \leq 1, \text{ update } \lambda_{n+1}, \gamma_{21,n+1}, \gamma_{22,n+1}, \mathbf{b}_{n+1}$$

- for an existing laminate microstructure ($\lambda_n > 0$) solve:

$$q(\mathbf{F}_{n+1}, \lambda_n + \Delta \lambda, \gamma_{ij,n}, p_{ij,n}) \text{ sign } \Delta \lambda = r (|\gamma_{11,n} - \gamma_{21,n}| + |\gamma_{12,n} - \gamma_{22,n}|) \Rightarrow \lambda_{n+1} = \lambda_n + \Delta \lambda$$

- check for laminate rotation by finding \mathbf{b}_{n+1} from (3.72).
- update $p_{ij,n}$ according to (3.70) and (3.71) or the analogous forms for $\Delta \lambda < 0$

(c) find $\gamma_{ij,n+1}$ (assume $\lambda = \text{const.} = \lambda_{n+1}$) by solving in a staggered form:

$$\begin{aligned} \left[\begin{aligned} \frac{\partial \Psi^{\text{rel}}}{\partial \gamma_{11}} + \frac{\partial \Psi^{\text{rel}}}{\partial p_{11}} \text{sign } \Delta \gamma_{11} \Big|_{\substack{\gamma_{1j,n} + \Delta \gamma_{1j} \\ p_{1j,n} + |\Delta \gamma_{1j}|}} &= -r (1 - \lambda_{n+1}) \text{sign } \Delta \gamma_{11} \\ \frac{\partial \Psi^{\text{rel}}}{\partial \gamma_{12}} + \frac{\partial \Psi^{\text{rel}}}{\partial p_{12}} \text{sign } \Delta \gamma_{12} \Big|_{\substack{\gamma_{1j,n} + \Delta \gamma_{1j} \\ p_{1j,n} + |\Delta \gamma_{1j}|}} &= -r (1 - \lambda_{n+1}) \text{sign } \Delta \gamma_{12} \end{aligned} \right. \\ \Rightarrow \gamma_{1j,n+1} = \gamma_{1j,n} + \Delta \gamma_{1j}, \quad p_{1j,n+1} = p_{1j,n} + |\Delta \gamma_{1j}| \end{aligned}$$

$$\begin{aligned} \left[\begin{aligned} \frac{\partial \Psi^{\text{rel}}}{\partial \gamma_{21}} + \frac{\partial \Psi^{\text{rel}}}{\partial p_{21}} \text{sign } \Delta \gamma_{21} \Big|_{\substack{\gamma_{2j,n} + \Delta \gamma_{2j} \\ p_{2j,n} + |\Delta \gamma_{2j}|}} &= -r \lambda_{n+1} \text{sign } \Delta \gamma_{21} \\ \frac{\partial \Psi^{\text{rel}}}{\partial \gamma_{22}} + \frac{\partial \Psi^{\text{rel}}}{\partial p_{22}} \text{sign } \Delta \gamma_{22} \Big|_{\substack{\gamma_{2j,n} + \Delta \gamma_{2j} \\ p_{2j,n} + |\Delta \gamma_{2j}|}} &= -r \lambda_{n+1} \text{sign } \Delta \gamma_{22} \end{aligned} \right. \\ \Rightarrow \gamma_{2j,n+1} = \gamma_{2j,n} + \Delta \gamma_{2j}, \quad p_{2j,n+1} = p_{2j,n} + |\Delta \gamma_{2j}| \end{aligned}$$

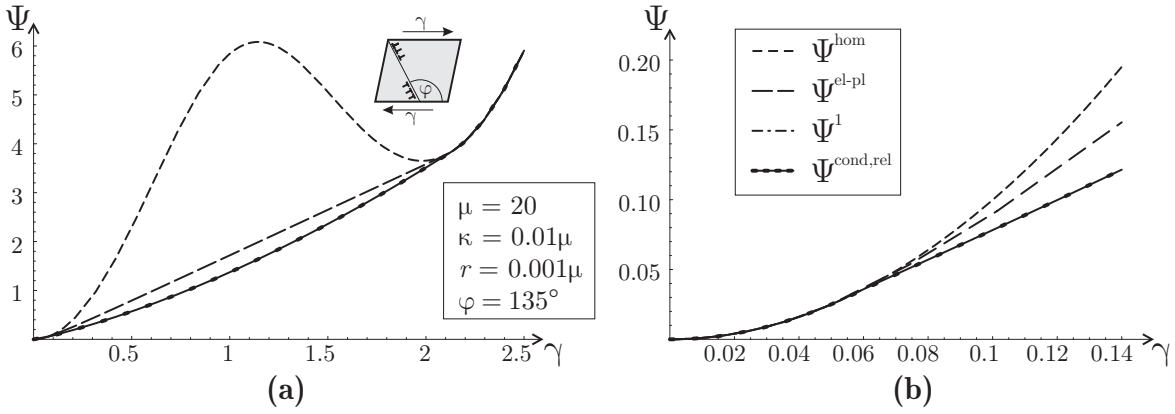


Figure 3.5: Unrelaxed condensed energy Ψ^{hom} for a homogeneous deformation state and possible relaxations as defined in Section 3.5.1 for a plane-strain simple shear test with linear hardening. The right image shows a magnification of the initial section of the left one.

3.5 Results

3.5.1 Relaxed and Condensed Energy

As a first result it is interesting to present the condensed energy functional for the two-phase laminate (now employing the relaxed laminate energy density derived above), i.e.

$$\Psi^{\text{cond,rel}}(\mathbf{F}) = \min \left\{ \Psi^{\text{rel}}(\mathbf{F}, \lambda, \gamma_i, p_i, \mathbf{b}) + r(1 - \lambda)|\gamma_1| + r\lambda|\gamma_2| \mid \gamma_i, \lambda, \mathbf{b} : \right. \\ \left. p_i = |\gamma_i|, 0 \leq \lambda \leq 1, |\mathbf{b}| = 1 \right\}, \quad (3.73)$$

which has been used in the literature in a different setting to compute laminate microstructures, see e.g. (Bartels et al., 2004; Carstensen et al., 2008). Note that here it is assumed that the orientation vector \mathbf{b} can be chosen purely elastically and also we do not account for dissipation due to changes of the volume fractions. (Furthermore, this approach does not account for an existing microstructure at the beginning of a time step and is hence only suitable for one time increment when a laminate forms.) As the energy is semi-relaxed with respect to amplitudes \mathbf{a}_i already, minimization with respect to the remaining unknowns can conveniently be performed numerically.

As shown e.g. in (Carstensen et al., 2008), approximations of the above condensed energy can be determined for specific microstructures, for which a solution can easily be found. Figure 3.5 illustrates the unrelaxed energy Ψ^{hom} for a homogeneous deformation state (which is clearly non-convex) along with a comparison of several relaxation results based on the present energy formulation. The highest of these relaxed energy curves shown is obtained from mixing one purely elastic phase with one elasto-plastic phase ($\gamma_1 = 0, \gamma_2 \neq 0$):

$$\Psi^{\text{el-pl}}(\mathbf{F}) = \min \left\{ \Psi^{\text{rel}}(\mathbf{F}, \lambda, \gamma_i, p_i, \mathbf{b}) + r\lambda|\gamma_2| \mid \lambda, \gamma_2, \mathbf{b} : \gamma_1 = p_1 = 0, p_2 = |\gamma_2|, \right. \\ \left. 0 \leq \lambda \leq 1, |\mathbf{b}| = 1 \right\}. \quad (3.74)$$

Another possible relaxation corresponds to a laminate approximation where both phases are

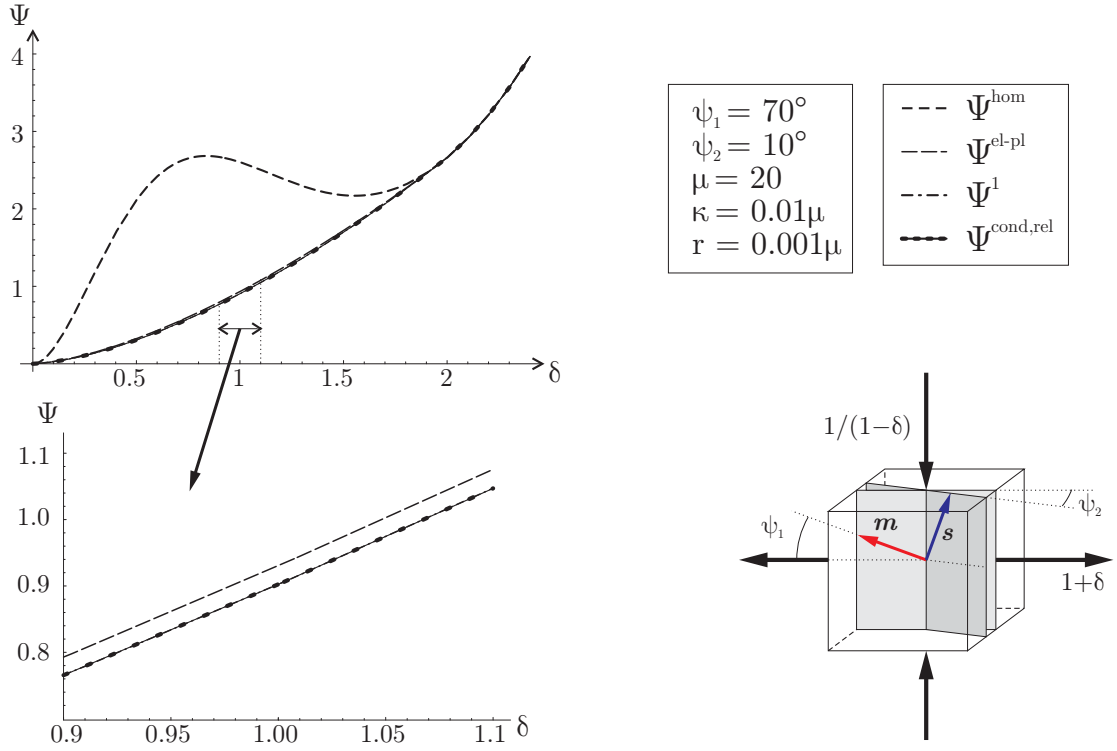


Figure 3.6: Unrelaxed condensed energy Ψ^{hom} for a homogeneous deformation state and possible relaxations as defined in Section 3.5.1 for a three-dimensional tension-compression test with non-aligned slip system and with linear hardening. The bottom image shows a magnification of the indicated region.

elasto-plastic but with equal amounts of plastic slip of opposite signs ($\gamma_1 = -\gamma_2 = \gamma$):

$$\begin{aligned} \Psi^1(\mathbf{F}) = \min \{ & \Psi^{\text{rel}}(\mathbf{F}, \lambda, \gamma_i, p_i, \mathbf{b}) + r |\gamma| \mid \lambda, \gamma, \mathbf{b} : \gamma_2 = -\gamma_1 = \gamma, \\ & p_1 = p_2 = |\gamma|, 0 \leq \lambda \leq 1, |\mathbf{b}| = 1 \}. \end{aligned} \quad (3.75)$$

A comparison of all three energy curves is shown in Figure 3.5 for a simple shear test with $\mathbf{F} = \gamma \mathbf{e}_1 \otimes \mathbf{e}_2$. Clearly, the elastic-plastic energy $\Psi^{\text{el-pl}}$ lies higher than the relaxed condensed energy $\Psi^{\text{cond,rel}}$ as well as the energy curve of Ψ^1 (the latter two almost coincide). Computations were performed with $\mu = 20$, $\kappa = 0.01\mu$, $r = 0.001\mu$. Note that the results in Figure 3.5 (and also Figure 3.6) are for linear hardening ($\alpha = 2$) to allow for a comparison with literature results as e.g. in (Carstensen et al., 2008). Unless otherwise noted, all subsequent results are plotted for $\alpha = 4$.

Another comparison of these energy paths is shown in Figure 3.6 for a tension-compression test with the macroscopic deformation gradient (this particular form is chosen to ensure incompressibility)

$$\mathbf{F} = \begin{pmatrix} 1 + \delta & 0 & 0 \\ 0 & 1/(1 + \delta) & 0 \\ 0 & 0 & 1 \end{pmatrix}. \quad (3.76)$$

Note that the active slip system does not lie in the same plane as the deformation to present a fully three-dimensional example.

Although only partially relaxed, the quality of the relaxed energy Ψ^{rel} in (3.38) can be estimated by a comparison with the convex energy lower bound. A convex energy hull be

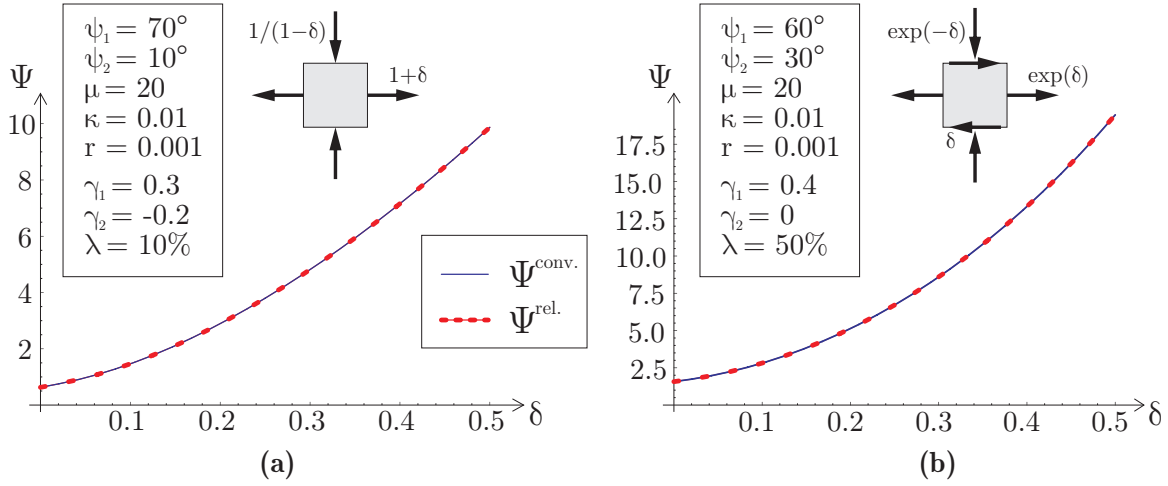


Figure 3.7: Comparison of the relaxed energy with the convex energy hull for fixed internal variables λ , γ_i , and $p_i = |\gamma_i|$, for different slip system orientations and loading cases and with linear hardening ($\alpha = 2$).

defined by

$$\Psi^{\text{conv}}(\mathbf{F}, \lambda, \gamma_i, p_i) = \min \{ (1 - \lambda)\Psi(\mathbf{F}_1, \gamma_1, p_1) + \lambda\Psi(\mathbf{F}_2, \gamma_2, p_2) \mid \mathbf{F}_1, \mathbf{F}_2 : \det \mathbf{F}_1 = \det \mathbf{F}_2 = 1, (1 - \lambda)\mathbf{F}_1 + \lambda\mathbf{F}_2 = \mathbf{F}, p_i = |\gamma_i| \}, \quad (3.77)$$

Unlike for the laminate energy hulls (with additional constraint $\text{rank}(\mathbf{F}_1 - \mathbf{F}_2) \leq 1$), deformation gradients in the two phases of the convex energy hull do not guarantee compatibility.

To estimate the quality of the relaxed energy Ψ^{rel} (the semi-analytical relaxation with respect to the amplitude vectors was derived in previous Sections) one can compare the fully relaxed laminate energy to the convex energy hull for given values of λ, γ_i and p_i and for a given deformation path. By fully relaxed we mean the energy $\Psi^{\text{rel}*}$ obtained from numerical minimization with respect to the orientation vector \mathbf{b} , i.e.

$$\Psi^{\text{rel}*}(\mathbf{F}, \lambda, \gamma_i, p_i) = \min \{ \Psi^{\text{rel}}(\mathbf{F}, \lambda, \gamma_i, p_i, \mathbf{b}) \mid \mathbf{b} : |\mathbf{b}| = 1 \}. \quad (3.78)$$

Results are illustrated in Figure 3.7 for the given values of the internal variables; note that the relaxed energy is obtained from numerical minimization with respect to \mathbf{b} . Examples comprise a tension-compression test with the overall deformation gradient \mathbf{F}_a and a mixed tension-compression-shear test with \mathbf{F}_b with slip system orientations defined according to Figure 3.6:

$$\mathbf{F}_a = \begin{pmatrix} 1 + \delta & 0 & 0 \\ 0 & 1/(1 + \delta) & 0 \\ 0 & 0 & 1 \end{pmatrix}, \quad \mathbf{F}_b = \begin{pmatrix} e^\delta & \delta & 0 \\ 0 & e^{-\delta} & 0 \\ 0 & 0 & 1 \end{pmatrix} \quad (3.79)$$

The difference between the relaxed energy and the convex energy curve is small: for the example in Figure 3.7a the relative deviation of the relaxed energy from the convex hull is less than 1% everywhere (and, of course, the relaxed energy lies above the convex hull). The right example shows a larger relative error for small strains δ of less than 5%. With increasing strain δ the deviation rapidly decreases to less than 0.5%, which hints at a good approximation of the quasiconvex envelope by the (semi-)relaxed energy, since the quasiconvex energy hull is bounded from above and below by the rank-one-convex hull and the convex hull, respectively.

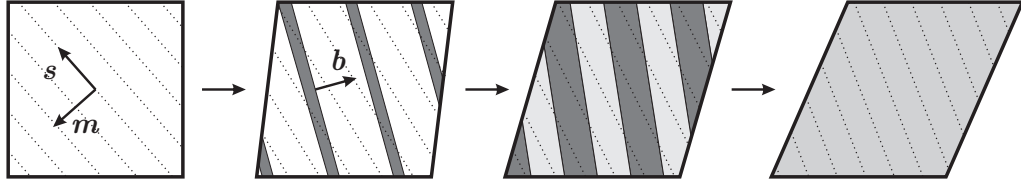


Figure 3.8: Microstructure development of a first-order laminate for a simple shear test with a single active slip system. Two bifurcated laminate phases arise with common surface normal \mathbf{b} . The newly nucleated phase 2 exhibits finite plastic slip already at the onset of lamination whereas the original phase 1 remains elastic first and finally yields plastically, too. Volume fractions develop to finally recover the crystal in a stable homogeneous state with uniform plastic slip.

3.5.2 Single-Slip Plasticity for a First-Order Laminate

For modeling the incremental evolution of the microstructure, the numerical scheme outlined in previous Sections can be applied to arbitrary deformations, so long as the deformation remains volume-preserving to account for the assumption of incompressibility. In the following, we present examples of applying Algorithm 1 to different three-dimensional examples with varying hardening parameters and active slip systems. For simplicity, we use for all results $\mu = 2$ and $r = 0.001$, and we name results obtained from this method *relaxed* compared to the *unrelaxed* solution for a homogeneous deformation state. Whenever the example is in plane-strain, the slip system orientation is characterized by the angle φ of the slip direction \mathbf{s} with the x-axis.

When plotting the stress components as functions of the overall strain, we must specify a zero stress niveau because of the backstress arising from the enforcement of incompressibility. Assuming a general neo-Hookean free energy formulation of the type

$$\Psi(\mathbf{F}_e) = \frac{1}{2}\mu [\text{tr}(\mathbf{F}_e^T \mathbf{F}_e) - 3] + \frac{K}{4} \left[j^2 - 2 \left(1 + 2\frac{\mu}{K} \right) \ln j - 1 \right], \quad (3.80)$$

we obtain the first Piola-Kirchhoff stress in our model as

$$\Sigma^I = \left. \frac{\partial \Psi}{\partial \mathbf{F}} \right|_{\det \mathbf{F}=1} = \mu (\mathbf{F}_e - \mathbf{F}_e^{-T}) \mathbf{F}_p^{-T}, \quad (3.81)$$

from which the Cauchy stress follows as

$$\boldsymbol{\sigma} = \mu (\mathbf{F}_e \mathbf{F}_e^T - \mathbf{I}). \quad (3.82)$$

Note that the constraint of incompressibility gives rise to the hydrostatic back stress in (3.82).

Figure 3.8 illustrates the general nature of solutions obtained for those problems considered here: First, the crystal behaves in a homogeneous elastic manner. (Depending on the non-aligned slip system, plastic flow may also occur before the onset of lamination.) At the onset of lamination, a second phase arises out of the originally uniform single crystal. This newly nucleated phase exhibits a finite amount of plastic slip already, whereas the original phase may still evolve elastically, and it occupies only a small volume fraction of the crystal. Upon further loading both phases eventually exhibit plastic flow and all internal variables

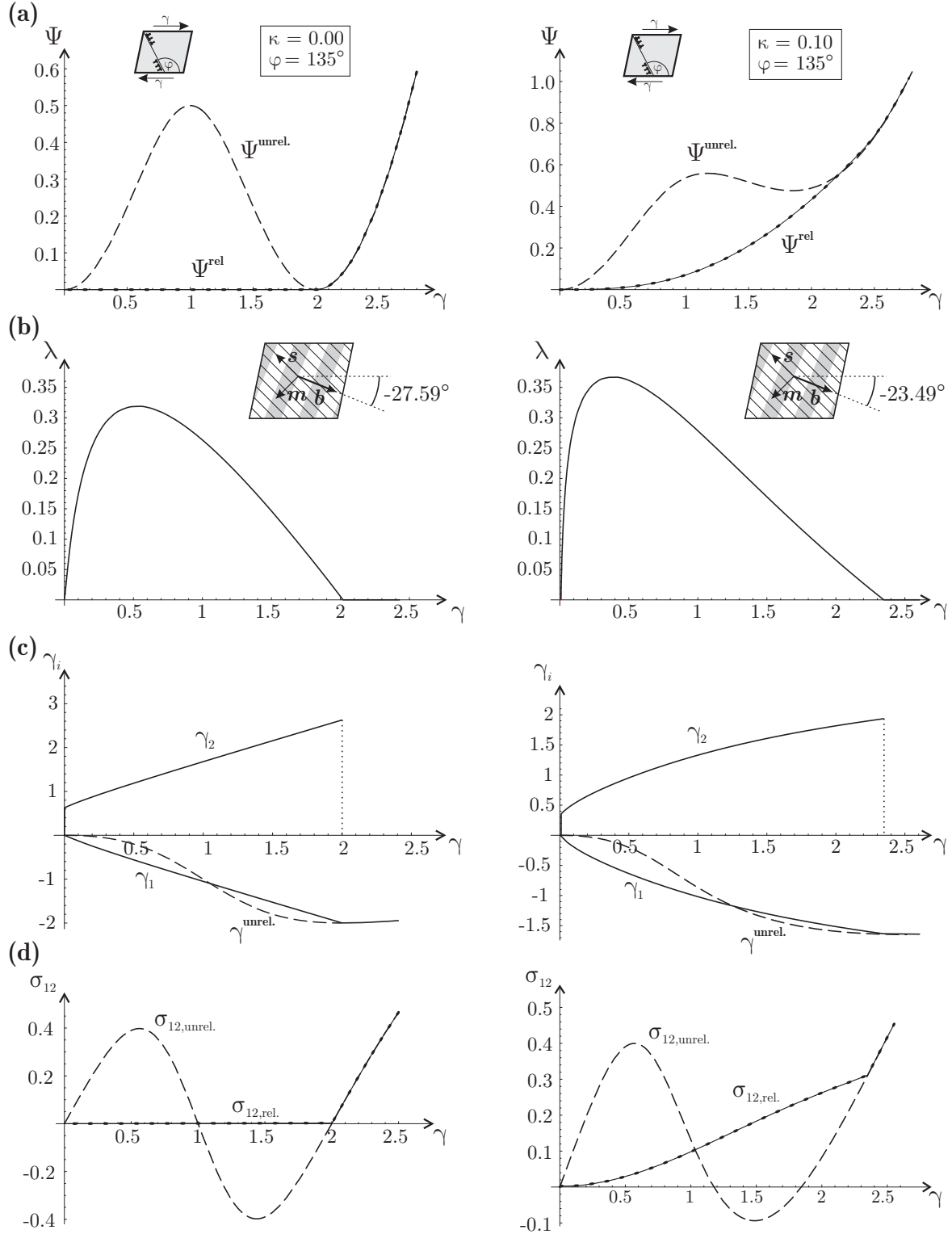


Figure 3.9: Plane-strain simple shear test for zero and non-zero hardening ($\kappa = 0$ and $\kappa = 0.1$, respectively): (a) comparison of unrelaxed and relaxed energy (energy computed via the incremental method), (b) origin and evolution of the volume fraction λ of phase 2, (c) evolution of the plastic slips γ_i for both laminate phases compared to the unrelaxed slip, (d) comparison of unrelaxed and relaxed Cauchy shear stress.

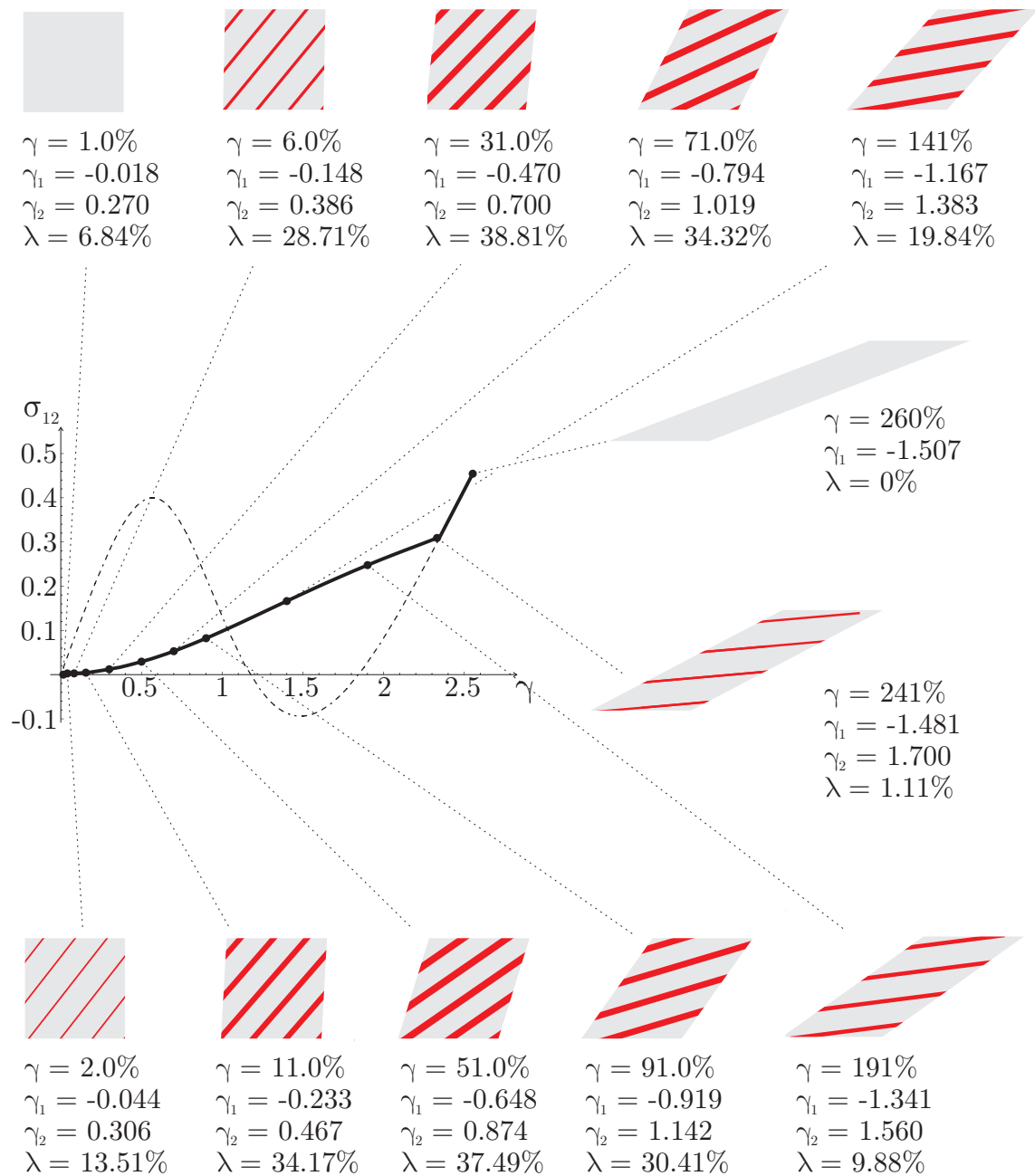


Figure 3.10: Illustration of the evolving laminate phases during a plane-strain simple shear test.

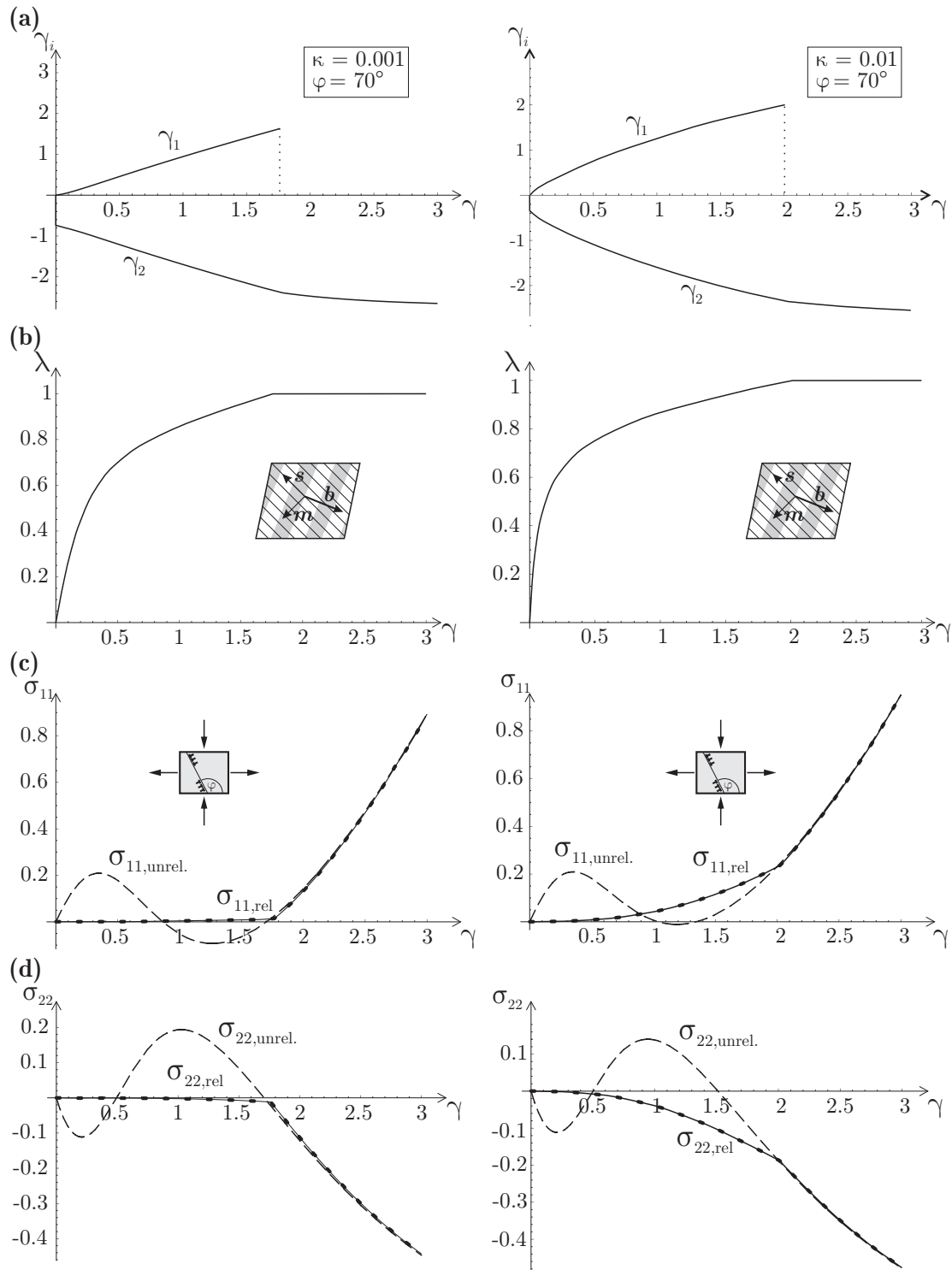


Figure 3.11: Plane-strain tension-compression test: (a) evolution of plastic slips γ_i for both phases, (b) origin and evolution of the volume fraction λ of phase 2, (c) and (d) comparison of unrelaxed and relaxed Cauchy stress components.

evolve. Finally, only one phase remains at the recovery of convexity of the unrelaxed energy, leaving the crystal in a homogeneous stable state with uniform plastic slip.

The first example investigates the microstructure evolution during a plane-strain simple shear test parametrized by the macroscopic deformation gradient

$$\mathbf{F} = \begin{pmatrix} 1 & \gamma & 0 \\ 0 & 1 & 0 \\ 0 & 0 & 1 \end{pmatrix}. \quad (3.83)$$

Results in Figure 3.9 are for $\kappa = 0$ (no hardening) and $\kappa = 0.1\mu$, computed with constant load increments of $\Delta\gamma = 5 \cdot 10^{-4}$ up to a maximum of $\gamma_{\max} = 2.8$. The exact step size of the load increment is of minor importance so long as the increment is kept small. (This is of particular importance for finding the initial laminate.) The slip system is oriented under an angle of $\varphi = 135^\circ$. Because of the non-aligned slip system the material stability of the homogeneous deformation is lost and microstructures arise. Due to the convexity of the unrelaxed energy Ψ^{unrel} for $\gamma < 0$, no microstructures form with negative strain γ . Figure 3.9 summarizes the evolution of the laminate microstructure by illustrating the paths of energy, the evolution of the volume fraction λ of phase 2, plastic slips γ_i and the Cauchy shear stress σ_{12} upon straining. Also included is a sketch of the originating laminate and the resultant normal vector \mathbf{b} . Note that for simple shear without hardening ($\kappa = 0$) the orientation of the laminate (i.e. the orientation of \mathbf{b} with the x-axis) results under an angle of approximately -27.59° , whereas in the case of hardening ($\kappa = 0.1$) the orientation changes to -23.49° . Figure 3.10 exemplarily illustrates the evolution of the laminate microstructure during the simple shear test.

As a second example, we investigate the microstructure evolution during a plane-strain tension-compression test with the macroscopic deformation gradient

$$\mathbf{F} = \begin{pmatrix} 1 + \delta & 0 & 0 \\ 0 & 1/(1 + \delta) & 0 \\ 0 & 0 & 1 \end{pmatrix}. \quad (3.84)$$

Computations were carried out for different hardening parameters ($\kappa = 0.001$ and $\kappa = 0.01$) and with constant load increments $\Delta\delta = 5 \cdot 10^{-4}$ up to the maximum load of $\delta_{\max} = 3$. The slip system was oriented under an angle of $\varphi = 70^\circ$. Again, due to the loss of rank-one convexity, the homogeneous deformation state is not stable and decomposes into micro-deformations. Figure 3.11 shows the microstructure evolution, displaying the evolution of plastic slips, volume fractions, and Cauchy stress components upon straining. The corresponding paths of the energy are provided in Figure 3.12.

In these examples the body behaves elastically first, until a second phase with finite, non-zero slip γ_2 originates from the uniform ground state, until finally phase 1 exhibits plastic flow, too (cf. Figure 3.8). Once the laminate has formed with a distinct orientation vector \mathbf{b} , we do not observe laminate rotations due to the large amount of dissipation necessary for a rotation. Rotation commonly only occurs when the body is in an almost uniform state (i.e. if $\lambda \approx 0$ or $\lambda \approx 1$).

A very important aspect of the present model is the updating procedure for the internal hardening variables p_i . In the literature the condensed energy functional is often used for a single time step only to model the entire course of microstructure evolution, i.e. one assumes no microstructure at the beginning of the time step. As for the hardening variables,

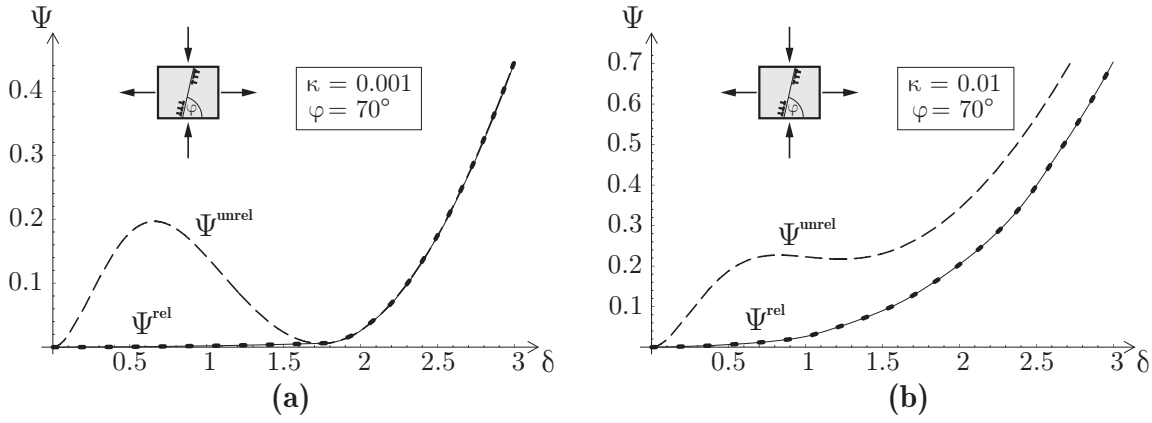


Figure 3.12: Relaxed and unrelaxed energy of a plane-strain tension-compression test with different hardening parameters; results correspond to curves and data shown in Figure 3.11.

these models presume that $p_i = |\gamma_i|$ at each time step. In reality, however, changes of the volume fractions result in a mixture of phases and hence a mixture of previous p_i -values. The present approach accounts for this mixture by the energetic averaging, see Eqs. (3.52) and (3.53). The effect becomes apparent when considering e.g. tension-compression examples as parametrized by (3.84). Figures 3.13 and 3.14 illustrate examples of the very same macroscopic deformation gradient (3.84) but with a slip system orientation which is not in the same plane to obtain a fully three-dimensional problem.

The example in Figure 3.13 shows a typical evolution of all parameters involved. Note that due to the slip system orientation the second energy well is no longer zero (even for zero hardening) but bears some finite value. Results in Figure 3.14 are the analogous solution at non-zero hardening ($\kappa = 0.004$). One interesting aspect to be observed is the deviation of the relaxed energy path from the unrelaxed energy curve even beyond the recovery of convexity of the unrelaxed solution. An analogous but smaller deviation also holds true for the Cauchy stress components plotted here. An even stronger such effect is visible in Figure 3.12. This deviation stems from the updating procedure of the hardening variables. Therefore, let us investigate the influence of the hardening parameters more in detail.

The influence of the hardening variable updates can best be inspected by a comparison of the curves of energy. Figure 3.15 illustrates results from the simplest example of a plane-strain simple shear test with in-plane slip system orientation. The unrelaxed energy of a homogeneous deformation state is clearly non-convex (the right image shows a magnification of the non-convex region of the left graphic). The dashed line represents the solution obtained from the condensed energy functional when assuming one purely elastic phase and one elasto-plastic phase, i.e. using (3.74). The dot-dash line results from employing the fully relaxed condensed energy (3.73). The two remaining curves are obtained from the present incremental approach: the higher one, labeled $\Psi^{\text{num},1}$, results from the present approach without updating the hardening variables due to volume changes, the lower one, labeled $\Psi^{\text{num},2}$, from the proposed updating procedure. It becomes obvious that the energy path without updates lies slightly above the relaxed energy curve from condensation – due to a different form of the dissipation functional: the condensed energy functional cannot correctly capture the actual amount of dissipation required to change the volume fractions. The solution from the present approach with updates considerably reduces the energy during straining

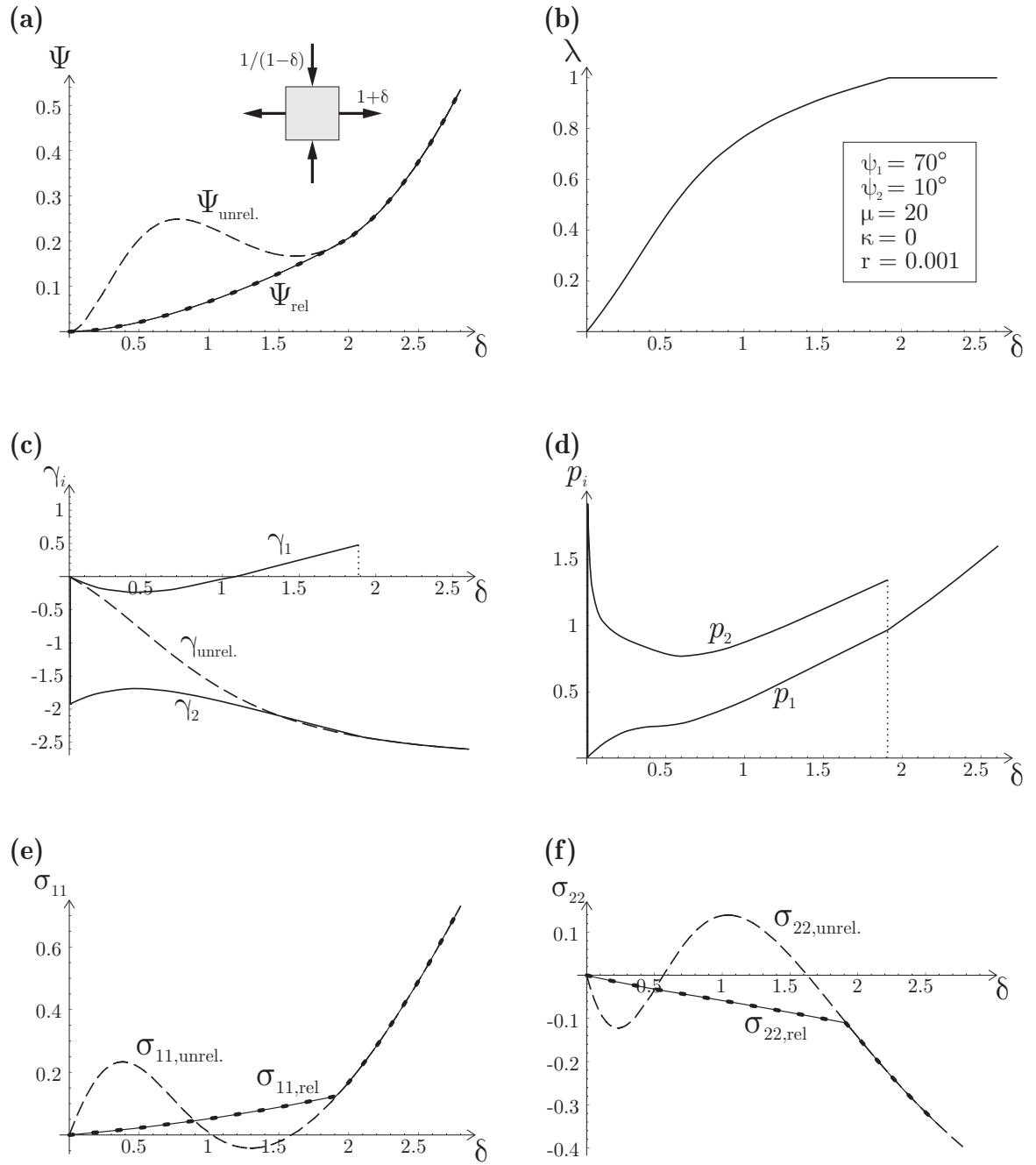


Figure 3.13: Tension-compression test (slip system orientation is not in-plane) with zero hardening: (a) energy path, (b) volume fraction λ of phase 2, (c) evolution of plastic slips γ_i and (d) the hardening variables p_i , (e) and (f) comparison of unrelaxed and relaxed Cauchy stress components.

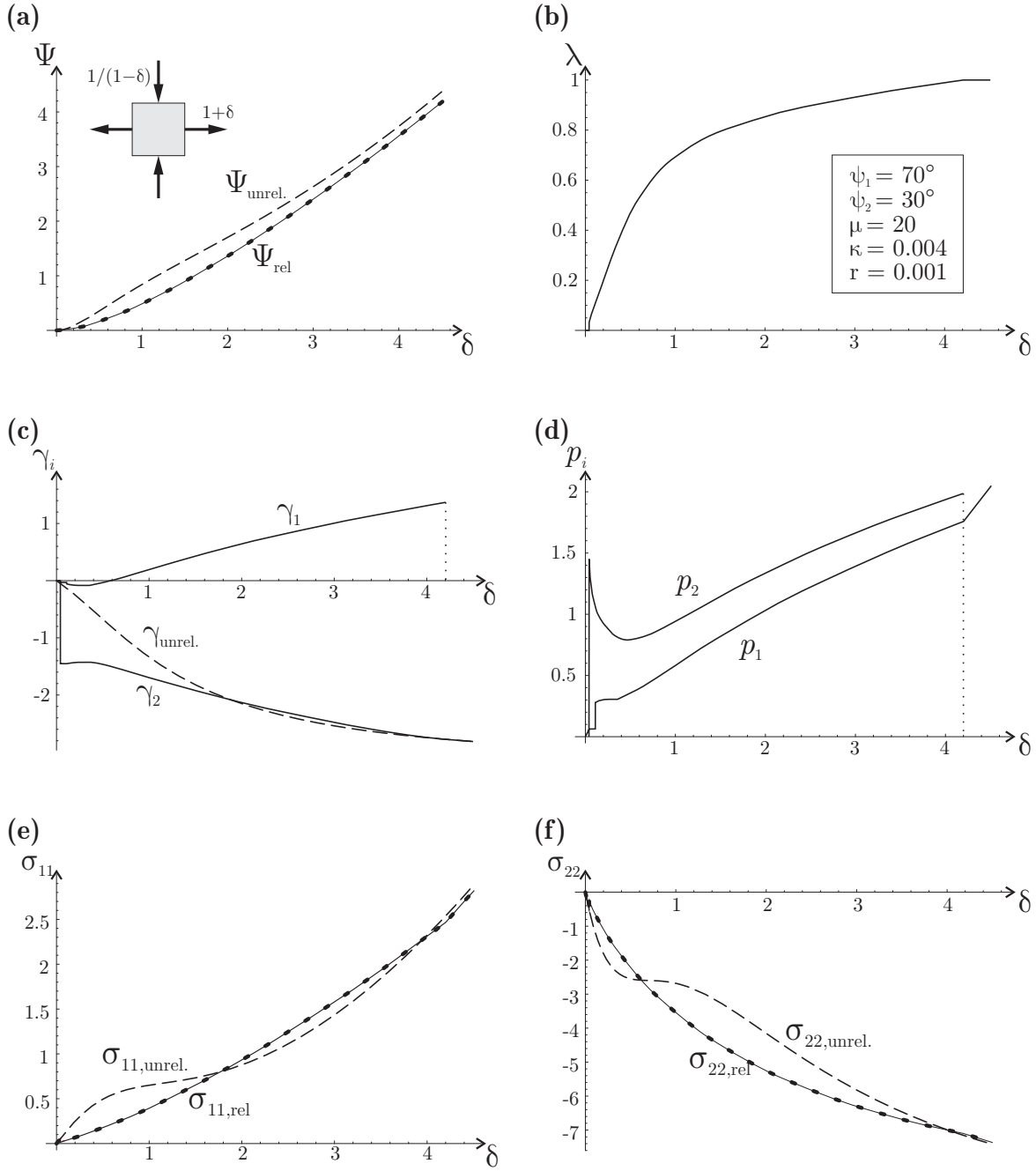


Figure 3.14: Tension-compression test (slip system orientation is not in-plane) with non-zero hardening: (a) energy path, (b) volume fraction λ of phase 2, (c) evolution of plastic slips γ_i and (d) the hardening variables p_i , (e) and (f) comparison of unrelaxed and relaxed Cauchy stress components.

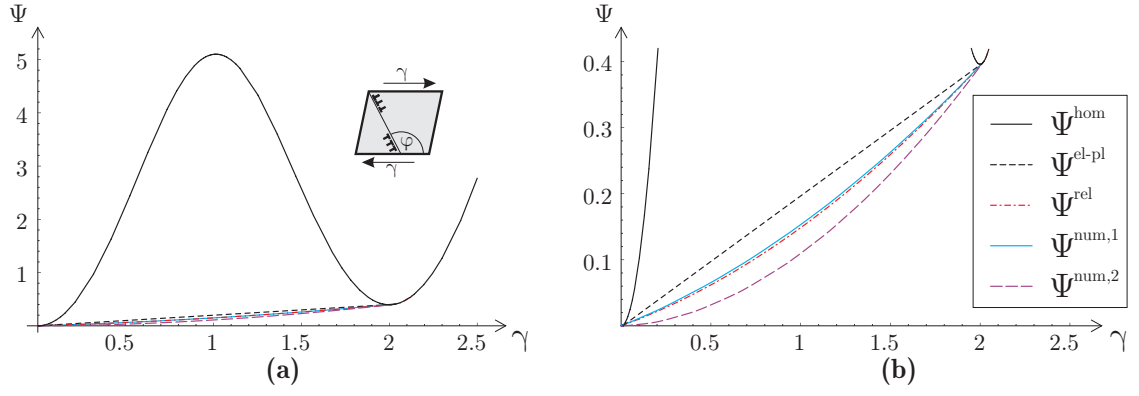


Figure 3.15: Comparison of the energy paths obtained from condensation and from the present approach for a plane-strain simple shear test (the right image shows a magnification of the left).

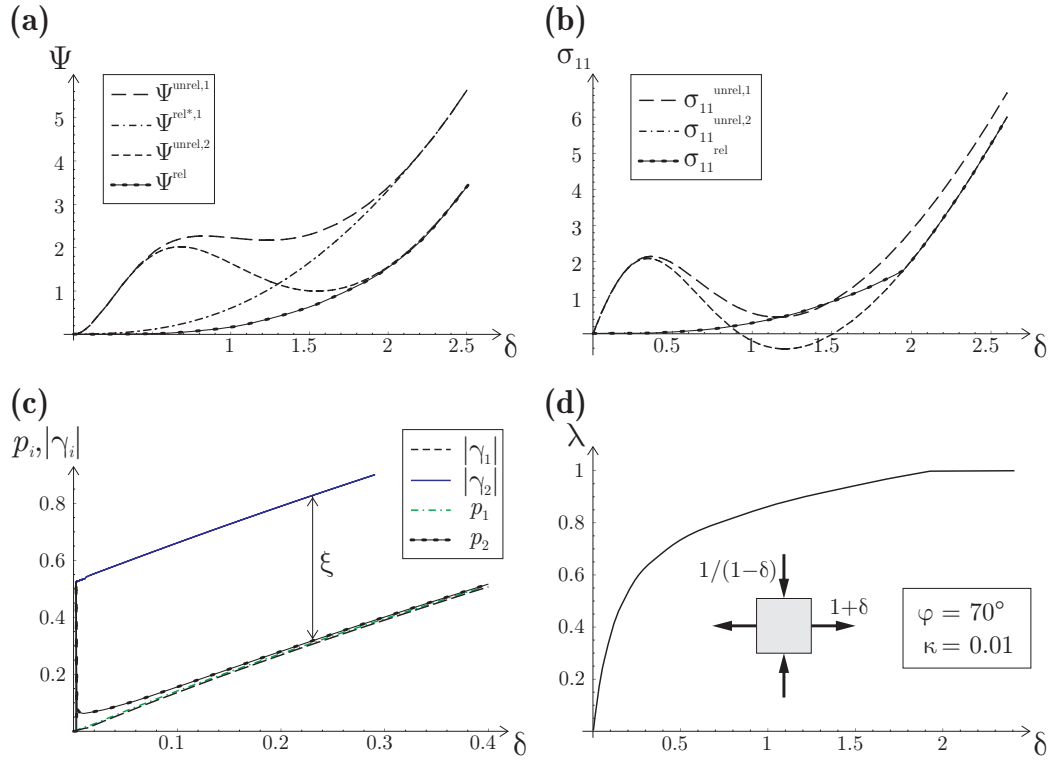


Figure 3.16: Difference between the present approach and results from energy condensation for a single time step: Evolution of plastic slips and hardening variables, the volume fraction of phase 2, the energy path and the Cauchy stress σ_{11} .

(essentially below the energy obtained from the condensed approach). This indicates that the material can indeed lower its energy by changing the volume fractions of an evolving microstructure, but also that any approach dealing with the condensed energy functional and employing a single time step only cannot capture this release of energy.

This effect becomes elucidating from the tension-compression tests in Figures 3.13, 3.15, 3.16. Let us investigate Figure 3.16. The two bottom images clearly show a similar behavior, i.e. here, the energy from the present approach Ψ^{rel} does not only lie considerably below the

condensed solution $\Psi^{\text{rel},1}$ but even shows an essentially lower energy at the recovery of convexity of the unrelaxed energy $\Psi^{\text{unrel},1}$. The two top images explain the causal mechanism: The left image shows the evolution of (the absolute value of) the plastic slips γ_i as well as the hardening parameters p_i . It is clear that we still have $p_1 \cong |\gamma_1|$, but p_2 rapidly decreases from the initial value $|\gamma_2|$ (in the forming laminate) to lower values to finally approach approximately the value of p_1 . As the final homogeneous material after lamination contains only phase 2 (see the course of λ to the right), the homogeneous body exhibits values γ_2 and p_2 where p_2 is $|\gamma_2| - \xi$ (here, ξ is approximately 0.5122). Assuming $p_2 = |\gamma_2| - \xi$ in the unrelaxed (condensed) energy functional results in the curve $\Psi^{\text{unrel},2}$, which very well fits into the picture. Here, it becomes more apparent that the present approach can reduce the crystal energy during laminate evolution considerably below the energy predicted by using the condensed energy functional in a single time step. The corresponding effect can also be observed for the Cauchy stress (see the bottom right image). The very same effect of a rapidly decreasing p_2 -value after the onset of lamination can also be noted for Figures 3.13 and 3.14.

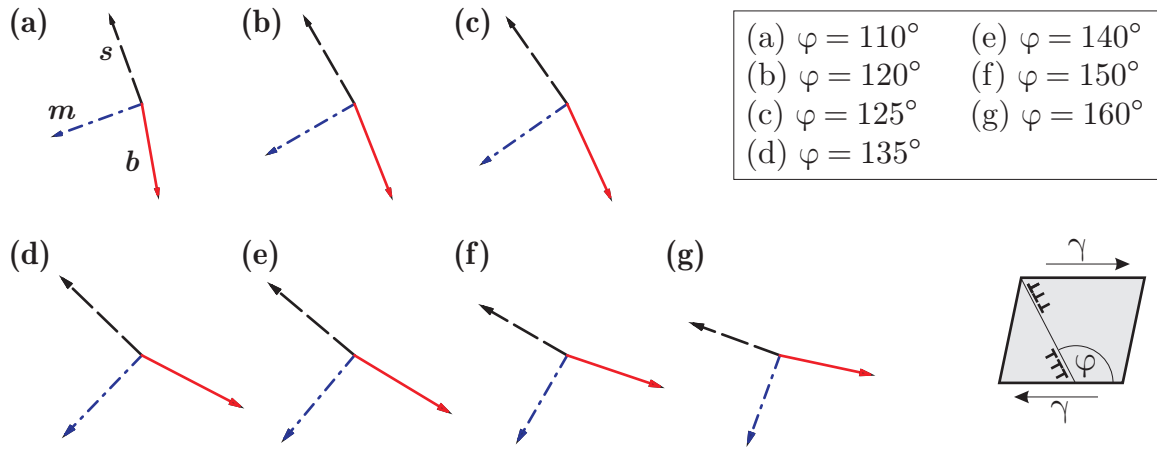


Figure 3.17: Orientation vector \mathbf{b} of the forming laminate for different orientations of the active slip system (\mathbf{s}, \mathbf{m}) for $\kappa = 0.1$ and plane-strain simple shear.

The orientation of the laminate (characterized by vector \mathbf{b} which is normal to the laminate interfaces) highly depends on the choice of the material parameters and the orientation of the

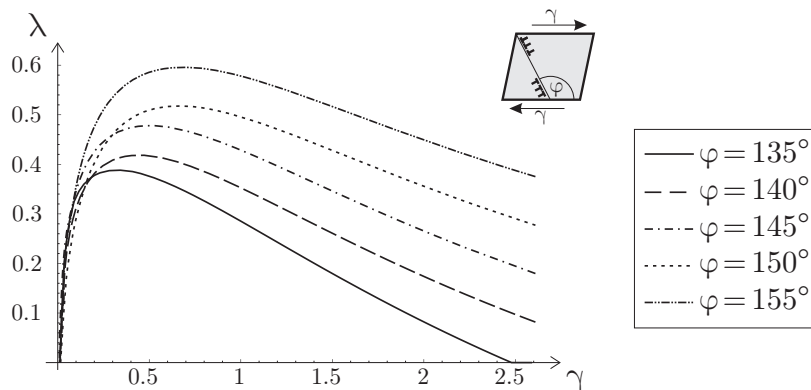


Figure 3.18: Volume fraction λ of phase 2 for different orientations of the active slip system (characterized by φ) for $\kappa = 0.1$ and plane-strain simple shear.

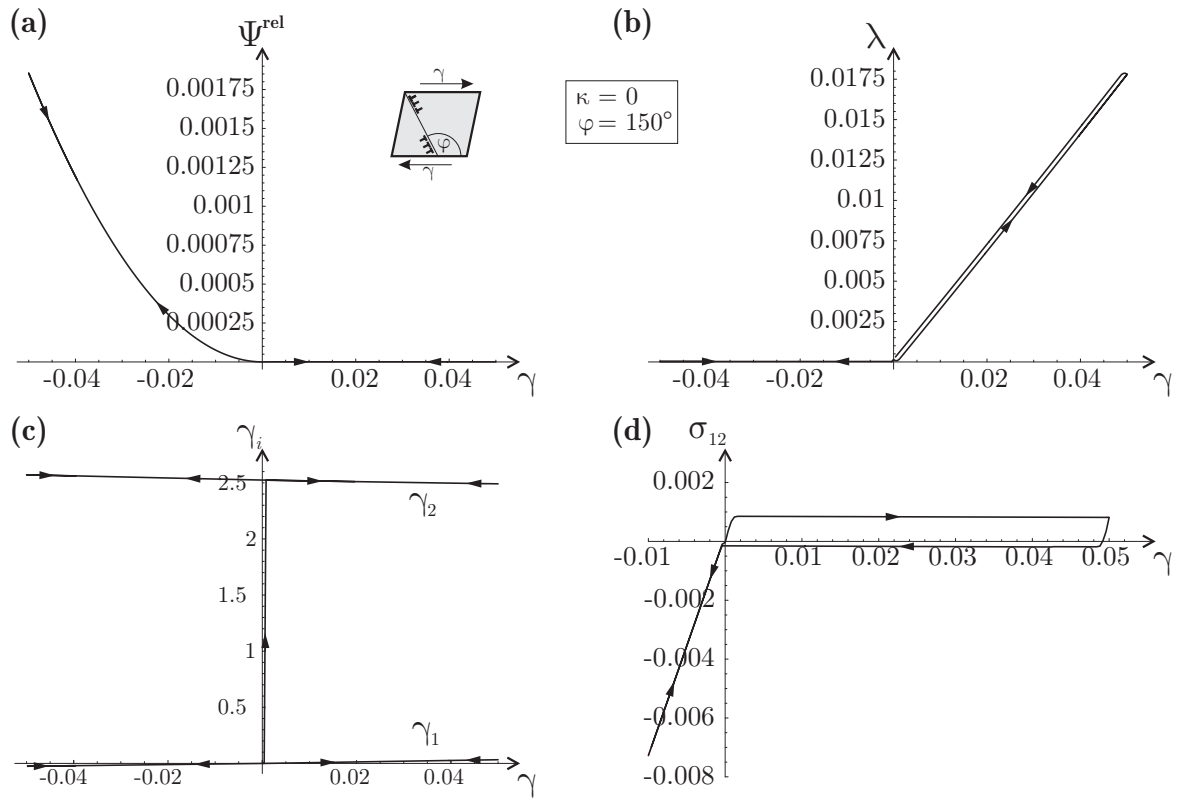


Figure 3.19: Cyclic simple shear test at zero hardening: evolution of (a) the relaxed energy, (b) the volume fraction of phase 2, (c) the plastic slips, (d) the Cauchy shear stress.

active slip system. The latter dependence can best be illustrated for a plane problem where \mathbf{b} is in-plane, too. Figure 3.17 shows the changing laminate orientation \mathbf{b} for different active slip systems (\mathbf{s}, \mathbf{m}) in a plane-strain simple shear test with non-zero hardening. It becomes apparent that (for this particular example) the laminate normal vector \mathbf{b} commonly arranges close to the direction of plastic slip. Note the change of the orientation as the active slip system passes 135° : below, the laminate orientation deviates from the slip system orientation clockwise; above, the deviation appears counter-clockwise. Not only the orientation of the laminate changes but so do the evolving laminate characteristics. Figure 3.18 illustrates the volume fraction of phase 2 during the same simple shear test and with varying slip system orientations. Of course, the presented results are valid only for this particular example which, however, stresses the influence of the choice of the active slip system.

Finally, let us investigate the behavior of the present model during cyclic loading. Figure 3.19 illustrates the numerical results of a cyclic test in plane-strain simple shear, see Eq. (3.83). Computations were carried out with $\mu = 2$, $\kappa = 0$ (no hardening), $r = 0.001$, and with constant increments $\Delta\gamma = 4 \cdot 10^{-4}$ up to the maximal load of $\gamma = \pm 0.05$. The slip system was oriented under an angle of $\varphi = 150^\circ$. Due to the lack of hardening all curves follow unaltered paths during subsequent loading cycles. The stress-strain curve exhibits a typical hysteresis loop.

Figure 3.20 illustrates the results from the same simple shear experiment but with non-zero hardening ($\kappa = 0.01$). It becomes apparent that the stress-strain hysteresis considerably alters its path with increasing number of load cycles. This can be understood by aid of a comparison of the evolving laminate volume fractions at zero and non-zero hardening.

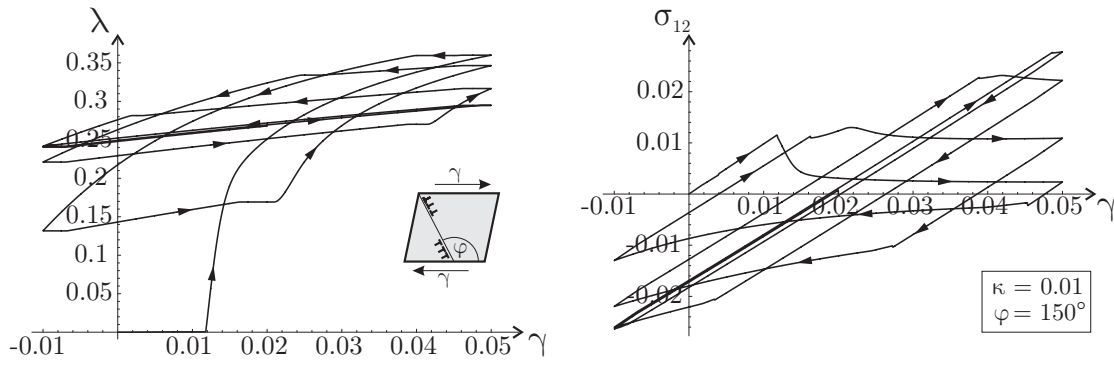


Figure 3.20: Cyclic simple shear test at non-zero hardening: evolution of the volume fraction of phase 2 and the Cauchy shear stress.

If material hardening is absent, the volume fractions evolve along the same paths during subsequent cycles. At non-zero hardening, however, the volume fractions tend to approach a constant limit as can be seen from Figure 3.20: the volume fraction of phase 2 eventually exhibits a value between 25% and 30%. This (more or less permanent) established laminate results in the stiff stress-strain hysteresis shown. Of course, this behavior highly depends on the choice of the material parameters and of the slip system orientation chosen.

3.5.3 Double-Slip Plasticity for a First-Order Laminate

Based on Algorithm 2 we can also analyze the microstructure evolution with two active slip systems (assuming no cross-slip). Again we perform a plane-strain simple shear experiment, now on a sample with two active slip systems. The orientations of the two active slip systems are depicted in Figure 3.21, with $\varphi = 150^\circ$, $\alpha_1 = 5.71^\circ$, $\alpha_2 = 16.70^\circ$, where $\mathbf{m}_1 = \mathbf{m}_2 = \mathbf{m} = (-\sin \varphi, \cos \varphi, 0)^T$. Results for the relaxed energy, the volume fractions, plastic slips and the Cauchy shear stress are summarized in Figure 3.21.

We see that the non-convex energy density gives rise to the formation of a laminate microstructure of the same type as before. The material first deforms elastically, now along both slip directions on the common slip plane. Then, a second laminate phase arises with already finite plastic slips γ_{21} and γ_{22} along the two slip directions, respectively. Due to the non-symmetric alignment of both slip directions, the plastic slips in the two directions are not the same. The originating laminate exhibits an orientation as sketched in Figure 3.21. Of course, relaxation of the energy via lamination also affects the stress-strain behavior, as can clearly be seen from the plotted Cauchy shear stress. This approach can equally be applied to arbitrary three-dimensional loading cases and slip system orientations, but we limit our overview here to this illustrative example.

3.6 Discussion and Conclusions

In this Chapter we have summarized a novel incremental approach to model the origin and subsequent evolution of laminate microstructures in elasto-plasticity at finite strains. The non-convexity of the free energy for an incompressible Neo-Hookean material gives rise to the formation of fine-scale microstructures as energy minimizers. A Lagrange functional

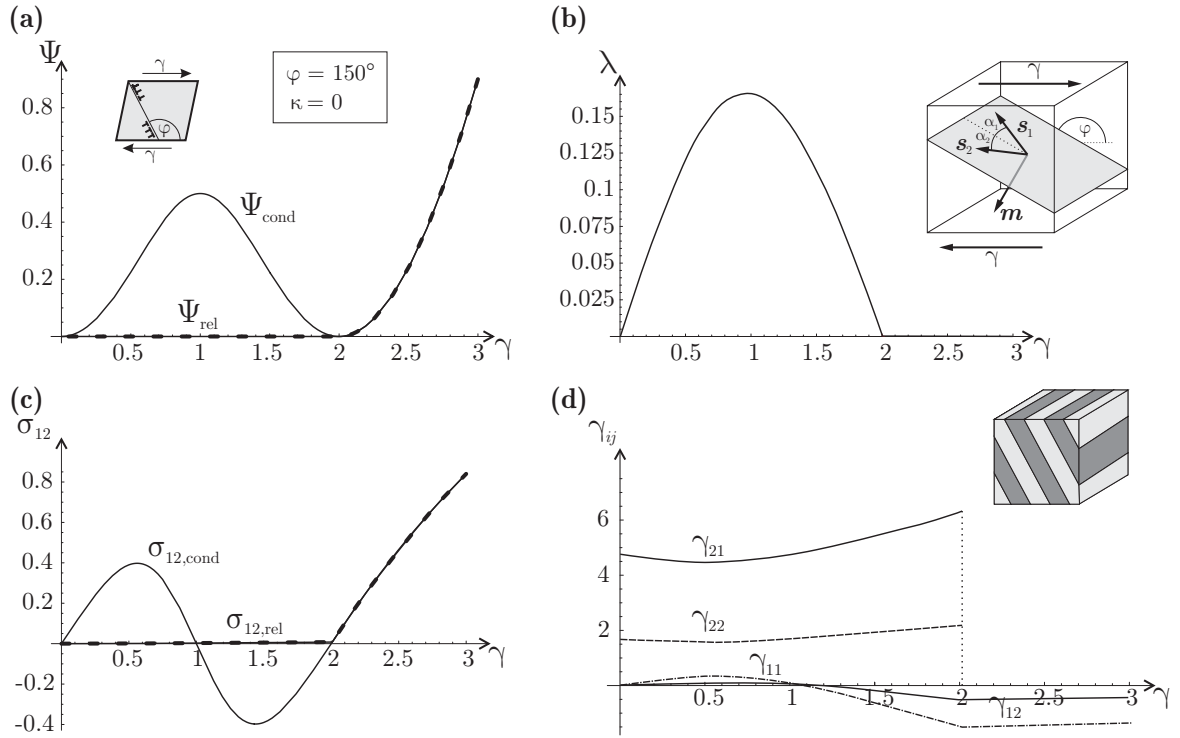


Figure 3.21: Plane-strain simple shear test with two active slip systems: (a) comparison of condensed and relaxed energy, (b) volume fraction of phase 2, (c) Cauchy shear stress, (d) plastic slips γ_{ij} .

(i.e., the sum of the rate of the free energy and a dissipation potential) is introduced to be employed in the principle of minimum dissipation potential. Integration of this principle for rate-independent processes yields the so-called condensed energy which has been used to compute the evolution of microstructures. However, the condensed energy does not account for a microstructured state of the material at the beginning of the time increment. Instead, authors have employed the condensed energy to model the microstructure by always presuming a homogeneous state at the beginning of each time step. Also, the condensed energy does not account for the actual amount of dissipation required to change the volume fractions of an existing laminate. Therefore, it is reasonable to employ an incremental formulation that does account for the state of the internal variables at the beginning of each time step, as does the present method.

We have analytically relaxed the energy of an incompressible Neo-Hookean material with respect to the elastic variables. The relaxed energy is employed in the Lagrange functional to incrementally solve the stationarity conditions at each time step. Thereby, we model the evolution of all internal variables for a given path of deformation. Results indicate that the incremental approach and the related updating of the hardening variables essentially impact the path of energy during straining. Updating the hardening variables upon each change of the volume fractions results in a path of energy that lies considerably below the solution obtained from employing the condensed energy functional for a single time step only. As a consequence, the present method is more appropriate to capture the physical effects of a material lamination. In this context, we have also introduced a new form of the dissipation functional which does not only account for the dissipation required to change the volume fractions but also characterizes the amount of dissipation required for a laminate rotation.

In conclusion, the present approach is more appropriate to model the evolution of laminate microstructures in finite plasticity, but it is also numerically more involved. The minimization of a condensed energy functional is certainly of less numerical effort than is the solution of the stationarity equations for each time step (especially as the time step size must be kept small). Note that the present model bears its limitations in terms of the model assumption: We only model an incompressible Neo-Hookean material. Also, we only accounted for a first-order laminate with one and two active slip systems. A generalization to second-order laminates and to multiple slip systems is a rather technical issue and can be performed by modifications of the above solution procedure. Research in all of these directions is under way at present.

4 Modeling Microstructures via Continuum Dislocation Theory

4.1 Introduction to Continuum Dislocation Theory

4.1.1 Motivation

The plastic deformation of polycrystalline materials depends to a high degree on the mechanisms related to the dislocation network. In order to accommodate plastic distortion and to reduce the crystal's energy, new dislocations are nucleated and pile up near the grain or phase boundaries, thereby giving rise to material strengthening. The nucleation and motion of dislocations is hence an essential mechanism for explaining plastic yielding and work hardening as well as size effects and hysteresis effects in crystal plasticity, and it needs embedding into the constitutive framework of modeling materials with microstructure. An important aspect of modeling dislocation microstructures by a continuum approach lies in a sensible representation of those effects stemming from the characteristics of the discrete crystal lattice which, in particular, prohibits too high a local dislocation concentration. Such a saturation behavior gives rise to numerous experimentally observed effects, some of which are analyzed in this Section.

Dislocations are not only a key microstructural defect for the plastic deformation of materials but are also the core ingredient for forming microstructural patterns and substructures that may give rise to outstanding material performance. One of these dislocation-based mechanisms, which may give rise to excellent material performance, is the formation of deformation twins (Hirth and Lothe, 1982; Christian and Mahajan, 1995). The increase of strength and work hardening during microstructure refinement by twinning in manganese steels or other TWIP-alloys (twinning induced plasticity; see e.g. (Allain et al., 2004), and the references therein) is one example which has remained until now not quite well understood. Perhaps the dislocation pile-up near the phase boundaries (raising the boundary energy) and the related size-effect play an important role here. It is believed that the finite phase boundary energies accompanying the pile-up of dislocations limit the refinement of microstructure and hence are responsible for the formation of twin patterns. In order to propose a model capable of describing this complex phenomenon we must in the first step be able to analyze the most simple situation, namely the dislocation pile-ups at the phase boundaries of a bicrystal. This simplified model of a bicrystal of the shape of a thin strip has already been employed in the literature to investigate the dislocation nucleation from interfaces and grain boundaries (Spearot et al., 2007a; Capolungo et al., 2007) as well as the structure and strength of grain boundaries (Tschopp et al., 2007; Spearot et al., 2007b) and to model the constitutive behavior of polycrystals (Evers et al., 2002).

The thin strip bicrystal is only one example of an important aspect of plasticity theory: Experiments indicate that many effects of plasticity exhibit an underlying size effect – i.e. the size of the body under consideration influences its plastic behavior. Hall (1951) and Petch (1953) were among the first to report an inversely proportional effect of the grain si-

ze in a polycrystal on its yield strength. The well-known Hall-Petch relation $\sigma_y \propto d^{-1/2}$ holds for a large variety of metals and for a large range of grain diameters d . This effect can be understood by the restrictions imposed on the mean travel distance of dislocations in a polycrystal, see also (Taylor, 1934). It has been observed, however, that this relationship breaks down for small grain sizes well in the lower micro- and nano-meter range (Louchet et al., 2006). Here, the strength of a crystal increases faster with decreasing grain size, an effect experimentally observed e.g. during equal channel extrusion (Le and Kochmann, 2009). Besides this influence of the grain size in polycrystals, a similar size effect can be observed for single crystals with decreasing size. In particular, the mechanical behavior of thin metallic films with respect to their strength and hardness considerably depends on the film thickness, see (Nicola et al., 2003) and the references therein. Freund (1987) and Nix (1998) have proposed a model based on the confined motion of a threading dislocation in a single crystal film, which suggests that the yield strength scales with the film thickness. Hartmaier et al. (1998) have discussed the role of thickness on the possibility of the generation of new dislocations. Again, the nucleation and subsequent pile-up of dislocations on the crystal boundaries are in some sense responsible for causing the size effects.

These size effects are not captured by the classical continuum plasticity theories as they lack an internal length scale. This difficulty can be overcome by employing continuum dislocation theory along with an energetic formulation that includes the effect of dislocation saturation. The present approach adopts the energy formulation proposed by Berdichevsky (2006b) to account for dislocation saturation and describe related size effects on small scales.

This Chapter is structured as follows: After this short introduction, we first discuss the development of continuum dislocation theory and then derive its equilibrium and constitutive equations for our purposes in this Section. Sections 4.2-4.6 analyze thin strip bicrystals under plane-constrained shear, uniaxial extension and a combination of shear and extension, both at zero and non-zero dissipation. Then, Section 4.8 introduces a variational formulation to numerically investigate two-dimensional plane-strain examples of dislocation microstructure evolution at zero and non-zero dissipation by employing finite element methods. The finite element procedure at non-zero dissipation thereby requires the extension of the variational formulation for general standard media and incremental time steps, as proposed by Ortiz and Repetto (1999) and Carstensen et al. (2002), to include gradients of the internal variables. Section 4.9 illustrates various numerical examples. Finally, Section 4.10 discusses the obtained results and possible generalizations, and it concludes this Chapter.

4.1.2 Continuum Dislocation Theory

Continuum dislocation theory deals with the ensembles of a large number of dislocations by the methods of continuum mechanics. The complexity of the system makes the phenomenological approach unavoidable. Guiding principles for finding an appropriate phenomenological formulation are the laws of thermodynamics (see also Section 2.5.1).

For simplicity we restrict in this Chapter to the geometrically linear theory. For a crystal deforming in single slip the plastic distortion produced by this slip system is given by $\beta = \beta(x) \mathbf{s} \otimes \mathbf{m}$, with \mathbf{s} being the slip direction and \mathbf{m} the unit normal vector to the slip plane. If the crystal has n active slip systems, the plastic distortion is the sum of those produced by

these slip systems

$$\boldsymbol{\beta}(\mathbf{x}) = \sum_{i=1}^n \beta_i(\mathbf{x}) \mathbf{s}_i \otimes \mathbf{m}_i. \quad (4.1)$$

One can easily verify that consequently continuous plastic distortions do not cause any volumetric change.

The plastic strain tensor $\boldsymbol{\varepsilon}_p$ and the plastic rotations $\boldsymbol{\omega}$ are the symmetric and skew-symmetric parts of the plastic distortion

$$\boldsymbol{\varepsilon}_p = \frac{1}{2}(\boldsymbol{\beta} + \boldsymbol{\beta}^T), \quad \boldsymbol{\omega} = \frac{1}{2}(\boldsymbol{\beta} - \boldsymbol{\beta}^T). \quad (4.2)$$

The elastic strain tensor is defined as the difference between the total compatible strains and the incompatible plastic strains, cf. Eq. (2.130),

$$\boldsymbol{\varepsilon}_e = \boldsymbol{\varepsilon} - \boldsymbol{\varepsilon}_p = \frac{1}{2}(\nabla \mathbf{u} + \mathbf{u} \nabla) - \boldsymbol{\varepsilon}_p, \quad (4.3)$$

with \mathbf{u} being the displacement vector.

In the sequel we employ the dislocation density tensor introduced by Nye (1953),

$$\boldsymbol{\alpha} = \text{curl } \boldsymbol{\beta}. \quad (4.4)$$

For an arbitrary infinitesimal surface da with the unit normal \mathbf{n} , $\boldsymbol{\alpha} \cdot \mathbf{n} da$ gives the resultant Burgers' vector of all dislocations whose dislocation lines cut the surface da . For a crystal deforming in single slip, we write in components

$$\alpha_{ij} n_j = s_i \epsilon_{jkl} \beta_{,k} m_l n_j, \quad (4.5)$$

so the resultant Burgers' vector turns out to be parallel to the slip direction. The number of dislocations per unit area can then be computed as

$$\rho = \frac{1}{b} |\epsilon_{jkl} \beta_{,k} m_l n_j|, \quad (4.6)$$

with b the magnitude of Burgers' vector. Within this kinematic setting the methods of non-equilibrium thermodynamics can be applied to obtain the governing equations. The equations of the continuum dislocation theory were derived by Berdichevsky and Sedov (1967) by using the variational approach of Sedov (1965), see also (Le and Stumpf, 1996a,b). With this set of equations the firm framework of dislocation theory was laid down.

4.1.3 Energy of Dislocations and Constitutive Framework

Within the framework of continuum dislocation theory, each model describing dislocations is based on a specific choice of the type of the energy and dissipation. For a single crystal deforming in single slip we adopt in the present approach the formulation proposed by Berdichevsky (2006a,b)

$$\Psi_\rho(\rho) = k\mu \ln \frac{1}{1 - \rho/\rho_s}, \quad (4.7)$$

where k is a material constant and ρ_s is the saturated dislocation density. The logarithmic term ensures a linear increase of the energy for a small dislocation density (where the self-energies of non-interacting dislocations dominate), and it tends to infinity as ρ approaches the saturated dislocation density ρ_s (the interaction energies of closely-packed dislocations dominate). Due to the minimum principle of potential energy, the energy hence asymptotically penalizes any dislocation density approaching ρ_s .

Deriving the constitutive framework, we follow principles and definitions from Section 2.5.1. However, in contrast to the standard problem presented there, we need to account for the chosen type of the dislocation energy, i.e. we must deal with an energy that additionally depends on the gradient of internal variables: $\Psi = \Psi(\varepsilon_e, \mathbf{K}, \nabla \mathbf{K})$. Here, \mathbf{K} summarizes the plastic distortion β , the dislocation density tensor α and (for a most general derivation) the entropy S .

Let Ω be any regular, bounded sub-region of the crystal in its initial ground state. Following (2.217), the energy of the crystal confined in the region Ω reads

$$\mathcal{I} = \int_{\Omega} \Psi(\varepsilon_{ij}, \beta_{ij}, \alpha_{ij}, S) \, dv. \quad (4.8)$$

Here and in the sequel, we employ index notation for all quantities for conciseness. According to the first law of thermodynamics (2.224), the energy rate equals the power of the external forces (for simplicity we here neglect the heat supply by considering adiabatic processes)

$$\dot{\mathcal{I}} = \frac{d}{dt} \int_{\Omega} \Psi(\varepsilon_{ij}, \beta_{ij}, \alpha_{ij}, S) \, dv = P. \quad (4.9)$$

The structure of the power of external forces, P , must be controlled by the form of the energy (Sedov, 1965). In our case the power is given by

$$P = \int_{\partial\Omega} (\sigma_{ij} n_j \dot{u}_i + \sigma_{ijk} n_k \dot{\beta}_{ij}) \, da, \quad (4.10)$$

where $\partial\Omega$ is the boundary of Ω with \mathbf{n} being the unit outward vector normal to $\partial\Omega$. We see that some stresses of higher order enter into the theory as a result of the dependence of the stored energy density on the gradient of the plastic distortion.

Transforming the surface integral in (4.10) into a volume integral by Gauß' theorem and requiring that (4.9) is satisfied for arbitrary Ω , we arrive at

$$\begin{aligned} T\dot{S} + \left(\frac{\partial \Psi}{\partial \varepsilon_{ij}} - \sigma_{ij} \right) \dot{u}_{i,j} + \left(\frac{\partial \Psi}{\partial \beta_{ij}} - \sigma_{ijk,k} \right) \dot{\beta}_{ij} \\ + \left(\frac{\partial \Psi}{\partial \alpha_{im}} \epsilon_{mkj} - \sigma_{ijk} \right) \dot{\beta}_{ij,k} - \sigma_{ij,j} \dot{u}_i = 0, \end{aligned} \quad (4.11)$$

where $T = \partial \Psi / \partial S$ is the absolute temperature.

For rigid translations the energy does not change while $\dot{u}_{i,j}$, $\dot{\beta}_{ij}$ and $\dot{\beta}_{ij,k}$ are zero. Therefore the stress must obey the equilibrium equation (in the absence of body forces)

$$\sigma_{ij,j} = 0. \quad (4.12)$$

Similarly, the first law of thermodynamics can be satisfied for arbitrary rigid rotations only if the stress tensor is symmetric

$$\sigma_{ij} = \sigma_{ji}. \quad (4.13)$$

Let us introduce the following abbreviations

$$\tau_{ij} = \sigma_{ij} - \frac{\partial \Psi}{\partial \varepsilon_{ij}}, \quad \tau_{ijk} = \sigma_{ijk} - \frac{\partial \Psi}{\partial \alpha_{im}} \epsilon_{mkj}, \quad (4.14)$$

$$\varkappa_{ij} = -\frac{\partial \Psi}{\partial \beta_{ij}} + \sigma_{ijk,k}. \quad (4.15)$$

Then the first law of thermodynamics becomes

$$T\dot{S} = \tau_{ij}\dot{u}_{i,j} + \varkappa_{ij}\dot{\beta}_{ij} + \tau_{ijk}\dot{\beta}_{ij,k}. \quad (4.16)$$

Eq. (4.16) shows that τ_{ij} and τ_{ijk} are those parts of the stresses and the higher order stresses which cause heating of the crystal. Tensor τ_{ij} describes heating in a non-uniform flow, so it has the meaning of viscous stresses. Tensors \varkappa_{ij} and τ_{ijk} describe heating caused by homogeneous and inhomogeneous plastic deformation, respectively.

The widely used closure of non-equilibrium thermodynamics assumes that the right hand side of (4.16), i.e. the dissipation \mathcal{D} is a given function of $\dot{u}_{i,j}$, $\dot{\beta}_{ij}$, and $\dot{\beta}_{ij,k}$, cf. (2.231),

$$T\dot{S} = \mathcal{D}(\dot{u}_{i,j}, \dot{\beta}_{ij}, \dot{\beta}_{ij,k}), \quad (4.17)$$

and that the tensors τ_{ij} , \varkappa_{ij} , and τ_{ijk} controlling the irreversible processes are linked to $\dot{u}_{i,j}$, $\dot{\beta}_{ij}$, and $\dot{\beta}_{ij,k}$ by the relations

$$\tau_{ij} = \lambda \frac{\partial \mathcal{D}}{\partial \dot{u}_{i,j}}, \quad \varkappa_{ij} = \lambda \frac{\partial \mathcal{D}}{\partial \dot{\beta}_{ij}}, \quad \tau_{ijk} = \lambda \frac{\partial \mathcal{D}}{\partial \dot{\beta}_{ij,k}}. \quad (4.18)$$

Then the parameter λ is determined from (4.16) and (4.18) as

$$\lambda = \frac{\mathcal{D}}{\frac{\partial \mathcal{D}}{\partial \dot{u}_{i,j}} \dot{u}_{i,j} + \frac{\partial \mathcal{D}}{\partial \dot{\beta}_{ij}} \dot{\beta}_{ij} + \frac{\partial \mathcal{D}}{\partial \dot{\beta}_{ij,k}} \dot{\beta}_{ij,k}}. \quad (4.19)$$

The set of equations (4.12), (4.13), (4.14), (4.15) and (4.18) is closed with respect to the unknown functions u_i and β_{ij} . Eq. (4.16) can be used to determine the temperature.

The simplest model assumes that the dissipation is zero. In this case all tensors τ_{ij} , \varkappa_{ij} and τ_{ijk} vanish, and functions u_i and β_{ij} should be found from pure energy minimization. The next model, also quite simple, neglects the viscous effect as well as the dissipation caused by $\dot{\beta}_{ij,k}$. In this model \mathcal{D} is assumed to depend only on $\dot{\beta}_{ij}$ so that $\tau_{ij} = 0$ and $\tau_{ijk} = 0$ and

$$\sigma_{ij} = \frac{\partial \Psi}{\partial \varepsilon_{ij}}, \quad \sigma_{ijk} = \frac{\partial \Psi}{\partial \alpha_{im}} \epsilon_{mkj}. \quad (4.20)$$

If, furthermore, \mathcal{D} is a homogeneous function of first order with respect to $\dot{\beta}_{ij}$, then again $\lambda = 1$ and Eq. (4.18)₂ becomes

$$\varkappa_{ij} = \frac{\partial \mathcal{D}}{\partial \dot{\beta}_{ij}}. \quad (4.21)$$

We will consider in what follows only these simplified dissipation potentials. For a more thorough investigation of this relation see Eqns. (2.240)-(2.244) in Section 2.5.1.

We further require that the stored energy density depends only on the elastic strain ε_{ij}^e and on the dislocation density α_{ij} :

$$\Psi = \Psi(\varepsilon_{ij}^e, \alpha_{ij}). \quad (4.22)$$

In this case the stress is given (as usually) by

$$\sigma_{ij} = \frac{\partial \Psi}{\partial \varepsilon_{ij}^e}, \quad (4.23)$$

while Eq. (4.21) can be written in the variational form (for rate-independence $\mathcal{D} \equiv \Delta$)

$$\frac{\partial \Delta}{\partial \dot{\beta}_{ij}} = -\frac{\delta_\varepsilon \Psi}{\delta \beta_{ij}} = -\frac{\partial \Psi}{\partial \beta_{ij}} + \frac{\partial}{\partial x_k} \frac{\partial \Psi}{\partial \beta_{ij,k}} \bigg|_{\varepsilon_{ij}}. \quad (4.24)$$

Based on this constitutive framework, Berdichevsky and Le (2007) found the analytical solution of an anti-plane-constrained shear problem for single crystals. Their results show how nucleated dislocations pile up at the boundaries. Interesting features of their solution comprise energetic and dissipative yielding thresholds, Bauschinger translational work hardening and a size effect typical for problems of crystal plasticity. The dislocation nucleation admits a clear characterization by the variational principle for the final plastic states (Berdichevsky, 2006b). Le and Sembring (2008a) obtained the solution for a plane-constrained shear problem of a single crystal strip, which exhibits the same features as that of Berdichevsky and Le (2007).

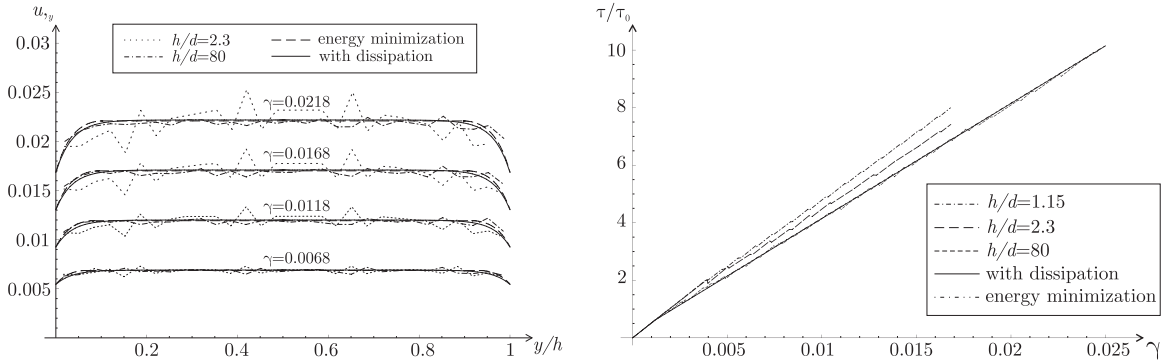


Figure 4.1: Comparison of results obtained from this approach and from discrete dislocation dynamics, modified after (Le and Sembring, 2008a): Overall strain profile and stress-strain behavior of a single crystal under simple shear deformation.

A comparison with the results of discrete dislocation simulations reported by Needleman and Van der Giessen (2001) and Shu et al. (2001) shows good agreement between the discrete and the present continuum approach. Figure 4.1 compares results from the present approach and discrete dislocation simulations at the example of a simple shear test of a single crystal (Le and Sembring, 2008a). Results indicate that for a single crystal strip with decreasing slip plane distance d (here h/d must be sufficiently large, where h is the height of the strip) good agreement of various results is achieved when ρ_s and k are obtained from curve-fitting stress-strain curves. Le and Sembring (2008b) investigated the influence of a second slip system, using the present approach, and also showed agreement with discrete dislocation simulations. Here, we go a step beyond and investigate the deformation under shear, tension and combined loading of a bicrystal, which may lay the basis for a continuum description of deformation twinning (see Section 5). Also, we employ a finite element description to model general polycrystals.

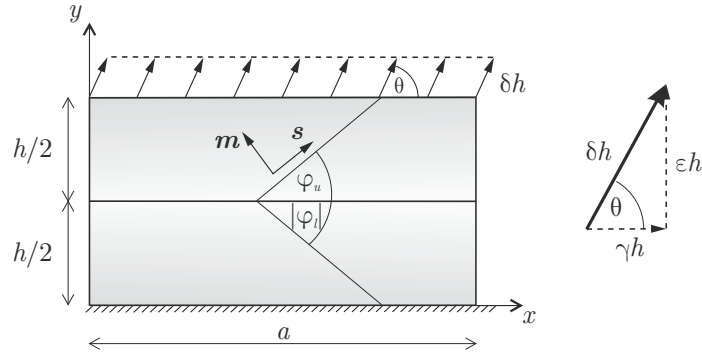


Figure 4.2: Combined deformation of uniaxial extension (ε) and simple shear (γ) of a bicrystal with one active slip-system within each of the two perfectly bonded single crystals.

4.2 Plastic Deformation of Bicrystals: Boundary Value Problem

We now consider a bicrystal consisting of a strip made up of two perfectly bonded single crystals of equal heights $h/2$, which undergoes a plane-strain deformation of mixed shear and extension, as illustrated in Figure 4.2. Let the cross-section of the strip be a rectangle of width a and height h , $0 \leq x \leq a$, $0 \leq y \leq h$. Displacements at the upper and lower sides of the bicrystal are rigidly enforced in a hard device as

$$u(0) = 0, \quad v(0) = 0, \quad u(h) = \gamma h, \quad v(h) = \varepsilon h, \quad (4.25)$$

where $u(y)$ and $v(y)$ are the longitudinal and transverse displacements, respectively, with ε denoting the overall tensile strain and γ the overall shear strain. We can as well introduce the total prescribed displacement δh applied under an angle θ as sketched in Figure 4.2 such that

$$\varepsilon = \delta \sin \theta, \quad \gamma = \delta \cos \theta. \quad (4.26)$$

We assume that the thickness in the z -direction of the strip, L , is large, and the width a is much greater than the height h ($L \gg a \gg h$) to neglect end effects and to have the stresses and strains depending only on one variable y in the central part of the strip. For the plane-strain state the components of the strain tensor are

$$\varepsilon_{xx} = 0, \quad \varepsilon_{xy} = \varepsilon_{yx} = \frac{1}{2}u_{,y}, \quad \varepsilon_{yy} = v_{,y}. \quad (4.27)$$

If the overall strain is sufficiently small, the bicrystal deforms elastically and $u = \gamma y$, $v = \varepsilon y$ everywhere in the strip. If the applied load exceeds some critical threshold, edge dislocations may appear to reduce the crystal's energy. We assume that each layer admits only one active slip system, with the slip directions (or the directions of the Burgers' vectors) perpendicular to the z -axis and inclined at an angle $\varphi(y)$ with the x -axis and the dislocation lines parallel to the z -axis. In this problem, the angle $\varphi(y)$ is piecewise constant, i.e.

$$\varphi(y) = \begin{cases} \varphi_l, & \text{for } 0 < y < h/2, \\ \varphi_u, & \text{for } h/2 < y < h. \end{cases} \quad (4.28)$$

In general, one may wish to incorporate multiple slip systems to better represent the physical reality. Multiple slip systems can easily be included into the present model; the influence

of multiple slip systems on the plane-constrained shear in single crystals was investigated by Le and Sembring (2008b). Here, we limit our analysis to the case of only one active slip system within each layer of our model bicrystal to avoid complexity and hence allow for a closed-form analytical solution. This corresponds to the assumption of infinite latent hardening (Ortiz and Repetto, 1999).

Since each layer has only one active slip system, we have for the plastic distortion $\beta_{ij} = \beta s_i m_j$, with $\mathbf{s} = (\cos \varphi, \sin \varphi, 0)^T$ being the slip direction and $\mathbf{m} = (-\sin \varphi, \cos \varphi, 0)^T$ the unit normal vector to that slip plane. Due to the geometry we may assume translational invariance to have β depending on one variable one, viz. $\beta = \beta(y)$. Because of the prescribed displacements (4.25), dislocations cannot penetrate the boundaries $y = 0$ and $y = h$, therefore

$$\beta(0) = \beta(h) = 0. \quad (4.29)$$

Note that we assume that dislocations cannot leave the bicrystal at the boundaries. This can be interpreted as a grain constrained by neighboring grains with different slip system orientation such that dislocation penetration of the boundary is impeded. Furthermore, let us assume that dislocations cannot penetrate the phase boundary either because the neighboring crystal does not admit the same slip system, so

$$\beta(h/2) = 0. \quad (4.30)$$

This assumption, of course, is a simplification of the physical reality as effects such as dislocation emission from grain boundaries, grain boundary sliding or grain boundary diffusion are not accounted for.

The components of the plastic strain tensor $\varepsilon_{ij}^p = \frac{1}{2}(\beta_{ij} + \beta_{ji})$ follow as

$$\varepsilon_{xx}^p = -\frac{1}{2}\beta \sin 2\varphi, \quad \varepsilon_{xy}^p = \frac{1}{2}\beta \cos 2\varphi, \quad \varepsilon_{yy}^p = \frac{1}{2}\beta \sin 2\varphi. \quad (4.31)$$

With (4.27) and (4.31) we obtain the components of the elastic strain tensor $\varepsilon_{ij}^e = \varepsilon_{ij} - \varepsilon_{ij}^p$,

$$\varepsilon_{xx}^e = \frac{1}{2}\beta \sin 2\varphi, \quad \varepsilon_{xy}^e = \frac{1}{2}(u_{,y} - \beta \cos 2\varphi), \quad \varepsilon_{yy}^e = v_{,y} - \frac{1}{2}\beta \sin 2\varphi. \quad (4.32)$$

As β depends only on y , there are two non-zero components of Nye's dislocation density tensor $\alpha_{ij} = \epsilon_{jkl}\beta_{il,k}$ (Nye, 1953), with ϵ_{jkl} being the permutation symbol,

$$\alpha_{xz} = \beta_{,y} \sin \varphi \cos \varphi, \quad \alpha_{yz} = \beta_{,y} \sin^2 \varphi. \quad (4.33)$$

Thus, the resultant Burgers' vector of all dislocations whose lines cut the area perpendicular to the z -axis is parallel to the slip direction \mathbf{s} . The scalar dislocation density equals

$$\rho = \frac{1}{b} \sqrt{\alpha_{xz}^2 + \alpha_{yz}^2} = \frac{1}{b} |\beta_{,y} \sin \varphi|. \quad (4.34)$$

Assuming that both single crystals are elastically isotropic with equal elastic moduli, we write for the energy per unit volume (Berdichevsky, 2006a,b)

$$\Psi(\varepsilon_{ij}^e, \alpha_{ij}) = \frac{1}{2} \lambda (\varepsilon_{ii}^e)^2 + \mu \varepsilon_{ij}^e \varepsilon_{ij}^e + \mu k \ln \frac{1}{1 - \frac{|\beta_{,y} \sin \varphi|}{b \rho_s}}, \quad (4.35)$$

where μ and λ are the Lamé elastic moduli, ρ_s is the saturated dislocation density, and k a material constant. The logarithmic term ensures a linearly increasing energy for small dislocation density ρ and tends to infinity with ρ approaching the saturated dislocation density ρ_s , hence providing an energetic barrier against over-saturation. The first and second term of (4.35) describe the elastic energy, the third term is the energy of the dislocation network.

With our aim in mind to derive closed-form analytical solutions, let us furthermore reduce the complexity of the model by assuming first that the active slip systems are symmetric with respect to the interface, i.e. we analyze twins with $-\varphi_l = \varphi_u = \varphi$. As we assume that both single crystals are elastically isotropic with equal elastic moduli, the total energy functional becomes, using (4.35),

$$\begin{aligned} \mathcal{I}(u, v, \beta) = aL \int_0^h & \left[\frac{1}{2} \lambda v_{,y}^2 + \frac{1}{2} \mu (u_{,y} - \beta \cos 2\varphi)^2 + \frac{1}{4} \mu \beta^2 \sin^2 2\varphi \right. \\ & \left. + \mu (v_{,y} - \frac{1}{2} \beta \sin 2\varphi)^2 + \mu k \ln \frac{1}{1 - \frac{|\beta_{,y} \sin \varphi|}{b\rho_s}} \right] dy. \end{aligned} \quad (4.36)$$

Functional (4.36) can be reduced to a functional depending on $\beta(y)$ only. Indeed, by first fixing $\beta(y)$ and taking the variation of (4.36) with respect to u and v , we derive the equilibrium equations

$$\begin{aligned} \mu (u_{,y} - \beta \cos 2\varphi)_{,y} &= 0, \\ [(\lambda + 2\mu) v_{,y} - \mu \beta \sin 2\varphi]_{,y} &= 0. \end{aligned} \quad (4.37)$$

Integration of these equations and use of the boundary conditions (4.25) as well as the continuity of displacements and tractions at the phase boundary $y = h/2$ yield

$$\begin{aligned} u_{,y} &= \gamma + \beta \cos 2\varphi - \langle \beta \cos 2\varphi \rangle, \\ v_{,y} &= \varepsilon + \bar{\kappa}(\beta \sin 2\varphi - \langle \beta \sin 2\varphi \rangle), \end{aligned} \quad (4.38)$$

where we introduced

$$\omega = \frac{\lambda}{\mu}, \quad \bar{\kappa} = \frac{\mu}{\lambda + 2\mu}, \quad \langle \cdot \rangle = \frac{1}{h} \int_0^h \cdot dy. \quad (4.39)$$

Substitution of (4.38) into (4.36) leads to the sought energy functional in terms of β only:

$$\begin{aligned} \mathcal{I}(\beta) = aL\mu \int_0^h & \left[\frac{1}{2} \omega [\varepsilon + \bar{\kappa}(\beta \sin 2\varphi - \langle \beta \sin 2\varphi \rangle)]^2 + \frac{1}{2} (\gamma - \langle \beta \cos 2\varphi \rangle)^2 \right. \\ & \left. + \frac{1}{4} \beta^2 \sin^2 2\varphi + [\varepsilon + (\bar{\kappa} - 1/2)\beta \sin 2\varphi - \bar{\kappa} \langle \beta \sin 2\varphi \rangle]^2 + k \ln \frac{1}{1 - |\beta_{,y} \sin \varphi|} \right] dy \end{aligned} \quad (4.40)$$

For brevity, we make use of the dimensionless definitions

$$E = \frac{b\rho_s}{aL\mu} \mathcal{I}, \quad \xi = b\rho_s y, \quad H = b\rho_s h. \quad (4.41)$$

For small up to moderate dislocation densities the logarithmic term in (4.40) may be approximated by keeping the first two terms of a Taylor expansion only, i.e.

$$\ln \frac{1}{1 - \frac{|\beta_{,y} \sin \varphi|}{b\rho_s}} \cong \frac{|\beta_{,y} \sin \varphi|}{b\rho_s} + \frac{1}{2} \frac{\beta_{,y}^2 \sin^2 \varphi}{(b\rho_s)^2}, \quad (4.42)$$

so that the dimensionless energy functional becomes

$$E(\beta) = \int_0^H \left[\frac{1}{2} \omega [\varepsilon + \bar{\kappa}(\beta \sin 2\varphi - \langle \beta \sin 2\varphi \rangle)]^2 + \frac{1}{2} (\gamma - \langle \beta \cos 2\varphi \rangle)^2 + \frac{1}{4} \beta^2 \sin^2 2\varphi + [\varepsilon + (\bar{\kappa} - 1/2)\beta \sin 2\varphi - \bar{\kappa} \langle \beta \sin 2\varphi \rangle]^2 + k(|\beta'| \sin \varphi| + \frac{1}{2} \beta'^2 \sin^2 \varphi) \right] d\xi, \quad (4.43)$$

where the prime denotes differentiation with respect to ξ . If the dissipation of energy is negligible, then the plastic distortion β minimizes (4.43) under the constraints (4.29) and (4.30). The overall strain is regarded as a given function of time, so we can study the evolution of the dislocation network which accompanies changes of ε and γ .

If the resistance to dislocation motion cannot be neglected, the energy minimization with respect to β must be replaced by a flow rule which, in case of rate-independent plasticity, for $\dot{\beta} \neq 0$ reads

$$\frac{\partial \Delta}{\partial \dot{\beta}} = - \frac{\delta_{\varepsilon, \gamma} \Psi}{\delta \beta}, \quad (4.44)$$

with the dissipation potential

$$\Delta(\dot{\beta}) = \tau_{\text{crit}}(\xi) |\dot{\beta}|, \quad (4.45)$$

where $\tau_{\text{crit}}(\xi)$ is the critical resolved shear stress ($\tau_{\text{crit}} = \tau_{\text{cr},l}$ for $\xi \in (0, H/2)$ and $\tau_{\text{crit}} = \tau_{\text{cr},u}$ for $\xi \in (H/2, H)$) and

$$\varkappa \equiv - \frac{\delta_{\varepsilon, \gamma} \Psi}{\delta \beta} = - \frac{\partial \Psi}{\partial \beta} + \frac{\partial}{\partial \xi} \frac{\partial \Psi}{\partial \beta_{,\xi}} \Big|_{\varepsilon, \gamma}. \quad (4.46)$$

For $\dot{\beta} = 0$, the evolution equation (4.44) does not have to be satisfied: It is replaced by $\dot{\beta} = 0$.

4.3 Energetic Threshold for Dislocation Nucleation

The results in (Le and Berdichevsky, 2001; Le and Sembring, 2008a,b) show that, for the variational problem of this type, we can find a threshold value δ_{en} such that when $\delta < \delta_{en}$ no dislocations are nucleated and $\beta = 0$. The threshold stress has an energetic origin: Below it the crystal reaches a global energy minimum elastically without geometrically necessary dislocations. Above the energetic threshold the energy minimum of the deformed crystal is accommodated by means of newly nucleated dislocations. Near the threshold value the dislocation density must be small so that the quadratic term containing β' in (4.43) can be neglected. Besides, the width of the boundary layers tends to zero as $\delta \rightarrow \delta_{en}$. This gives rise to the idea of finding the threshold value by employing a minimizing sequence (Ball and James, 1987) of the form

$$\beta(\xi) = \begin{cases} \frac{\beta_l}{\epsilon} \xi, & \text{for } \xi \in (0, \epsilon), \\ \beta_l, & \text{for } \xi \in (\epsilon, H/2 - \epsilon), \\ \frac{\beta_l}{\epsilon} (H/2 - \xi), & \text{for } \xi \in (H/2 - \epsilon, H/2), \\ \frac{\beta_u}{\epsilon} (\xi - H/2), & \text{for } \xi \in (H/2, H/2 + \epsilon), \\ \beta_u, & \text{for } \xi \in (H/2 + \epsilon, H - \epsilon), \\ \frac{\beta_u}{\epsilon} (H - \xi), & \text{for } \xi \in (H - \epsilon, H), \end{cases} \quad (4.47)$$

where β_l and β_u are unknowns, and ϵ is a small unknown length which tends to zero as $\delta \rightarrow \delta_{en}$. Substituting (4.47) into (4.43) and minimizing the energy with respect to β_u and β_l , we determine the threshold value δ_{en} for any given combination of slip system orientation φ and load direction θ .

For the particular cases of plane-constrained shear (Kochmann and Le, 2008a) and uniaxial extension (Kochmann and Le, 2008b) we can derive neat analytical solutions. First, we investigate the case of plane-constrained shear ($\theta = 0$ and $\delta = \gamma$). Substituting (4.47) into the energy functional (4.43) (with the quadratic term in β' being removed) and neglecting all small terms of order ϵ and higher, we obtain after some algebraic manipulations

$$E(\beta_l, \beta_u) = \frac{H}{8} \left[2(1 - \bar{\kappa})(\beta_l^2 + \beta_u^2) \sin^2 2\varphi + \bar{\kappa}(\beta_u - \beta_l)^2 \sin^2 2\varphi + (2\gamma - (\beta_l + \beta_u) \cos 2\varphi)^2 \right] + 2k(|\beta_l| + |\beta_u|) |\sin \varphi|. \quad (4.48)$$

A rather simple analysis shows that for $\varphi \in (0^\circ, 45^\circ)$ the energy minimum requires a symmetric solution, i.e.

$$\beta_l = \beta_u = \frac{2\gamma \cos 2\varphi - 8k |\sin \varphi| / H}{2 - \bar{\kappa} + \bar{\kappa} \cos 4\varphi} > 0, \quad (4.49)$$

and for $\varphi \in (45^\circ, 90^\circ)$ we have

$$\beta_l = \beta_u = \frac{2\gamma \cos 2\varphi + 8k |\sin \varphi| / H}{2 - \bar{\kappa} + \bar{\kappa} \cos 4\varphi} < 0 \quad (4.50)$$

if (in both cases)

$$\gamma > \gamma_{en} = \frac{4k}{hb\rho_s} \frac{|\sin \varphi|}{|\cos 2\varphi|}. \quad (4.51)$$

In the case of uniaxial extension ($\theta = \pi/2$ and $\delta = \epsilon$), we obtain the energy from the minimizing sequence approach:

$$E(\beta_l, \beta_u) = \frac{H}{8} \left[4\frac{\epsilon^2}{\bar{\kappa}} - 4\epsilon(\beta_u - \beta_l) \sin 2\varphi + (\beta_u + \beta_l)^2 \cos^2 2\varphi + \bar{\kappa}(\beta_u - \beta_l)^2 \sin^2 2\varphi + 2(1 - \bar{\kappa})(\beta_u^2 + \beta_l^2) \sin^2 2\varphi \right] + 2k(|\beta_l| + |\beta_u|) |\sin \varphi| \quad (4.52)$$

We conclude that, for $\varphi \in (0^\circ, 90^\circ)$, the energy minimum is achieved for antisymmetric β with

$$\beta_u = -\beta_l = 2\frac{\epsilon \sin 2\varphi - 4k \sin \varphi / H}{\sin^2 2\varphi} > 0, \quad (4.53)$$

and for $\varphi \in (90^\circ, 180^\circ)$ the minimum is achieved at

$$\beta_u = -\beta_l = 2\frac{\epsilon \sin 2\varphi + 4k \sin \varphi / H}{\sin^2 2\varphi} < 0, \quad (4.54)$$

if (in both cases)

$$\epsilon > \epsilon_{en} = \frac{4k}{hb\rho_s} \frac{\sin \varphi}{|\sin 2\varphi|}. \quad (4.55)$$

After these simple examples let us find the energetic threshold for general loading. Decomposing the plastic distortion $\beta(\xi)$ into a symmetric function $\beta_s(\xi)$ and an antisymmetric function $\beta_a(\xi)$, i.e.

$$\beta(\xi) = \begin{cases} \beta_s(\xi) + \beta_a(\xi) & \text{for } 0 < \xi < H/2, \\ \beta_s(\xi) - \beta_a(\xi) & \text{for } H/2 < \xi < H, \end{cases} \quad (4.56)$$

a rather simple analysis shows that we have to consider four cases for the determination of the threshold value δ_{en} (see also Figure 4.4):

Case 1: $0 < \varphi < 45^\circ$ and $\tan \theta < -\frac{1}{\tan 2\varphi(\bar{\kappa}-1/\sin^2 2\varphi)}$:

We obtain a positive distortion β across the entire height of the bicrystal, i.e.

$$\beta_l = \beta_s + \beta_a > 0 \quad \text{and} \quad \beta_u = \beta_s - \beta_a > 0, \quad (4.57)$$

with

$$\beta_s = \frac{\gamma \cos 2\varphi - 4|\sin \varphi|k/H}{1 - \bar{\kappa} \sin^2 2\varphi}, \quad \beta_a = -\frac{\varepsilon}{\sin 2\varphi}. \quad (4.58)$$

Applying the definition of γ and ε in terms of the loading parameter δ (see Eq. (4.26)), we obtain the threshold value

$$\delta > \delta_{en} = \frac{4|\sin \varphi|k/H}{\cos \theta \cos 2\varphi + \sin \theta \sin 2\varphi(\bar{\kappa} - 1/\sin^2 2\varphi)}. \quad (4.59)$$

Case 2: $0 < \varphi < 45^\circ$ and $\tan \theta > -\frac{1}{\tan 2\varphi(\bar{\kappa}-1/\sin^2 2\varphi)}$:

Now, we have unequal signs of β throughout the height of the bicrystal, i.e.

$$\beta_l = \beta_s + \beta_a < 0 \quad \text{and} \quad \beta_u = \beta_s - \beta_a > 0, \quad (4.60)$$

with

$$\beta_s = \frac{\gamma \cos 2\varphi}{1 - \bar{\kappa} \sin^2 2\varphi}, \quad \beta_a = \frac{-\varepsilon \sin 2\varphi + 4|\sin \varphi|k/H}{\sin^2 2\varphi}. \quad (4.61)$$

In terms of the loading parameter δ , we obtain the threshold value

$$\delta > \delta_{en} = \frac{4|\sin \varphi|k/H(\bar{\kappa} - 1/\sin^2 2\varphi)}{\cos \theta \cos 2\varphi + \sin \theta \sin 2\varphi(\bar{\kappa} - 1/\sin^2 2\varphi)}. \quad (4.62)$$

Case 3: $45^\circ < \varphi < 90^\circ$ and $\tan \theta < \frac{1}{\tan 2\varphi(\bar{\kappa}-1/\sin^2 2\varphi)}$:

In this case we obtain a negative β throughout the height of the bicrystal, i.e.

$$\beta_l = \beta_s + \beta_a < 0 \quad \text{and} \quad \beta_u = \beta_s - \beta_a < 0, \quad (4.63)$$

with

$$\beta_s = \frac{\gamma \cos 2\varphi + 4|\sin \varphi|k/H}{1 - \bar{\kappa} \sin^2 2\varphi}, \quad \beta_a = \frac{-\varepsilon}{\sin 2\varphi} \quad (4.64)$$

The threshold value now reads

$$\delta > \delta_{en} = -\frac{4|\sin \varphi|k/H}{\cos \theta \cos 2\varphi - \sin \theta \sin 2\varphi(\bar{\kappa} - 1/\sin^2 2\varphi)}. \quad (4.65)$$

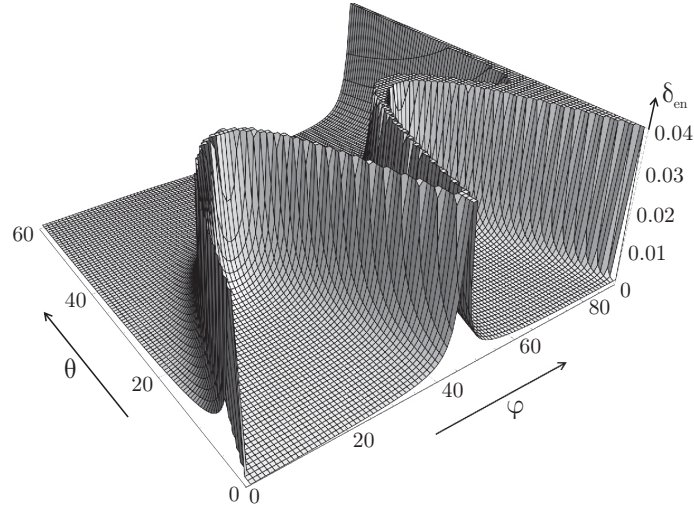


Figure 4.3: Energetic threshold value δ_{en} for the nucleation of dislocations in a symmetric bicrystal with varying angles φ and θ .

Case 4: $45^\circ < \varphi < 90^\circ$ and $\tan \theta > \frac{1}{\tan 2\varphi(\bar{\kappa}-1/\sin^2 2\varphi)}$:

Finally, in this case, we conclude that again

$$\beta_l = \beta_s + \beta_a < 0 \quad \text{and} \quad \beta_u = \beta_s - \beta_a > 0, \quad (4.66)$$

with the same β_s and β_a as in Case 2 but with the threshold value

$$\delta > \delta_{en} = -\frac{4 |\sin \varphi| k/H(\bar{\kappa} - 1/\sin^2 2\varphi)}{\cos \theta \cos 2\varphi - \sin \theta \sin 2\varphi(\bar{\kappa} - 1/\sin^2 2\varphi)}. \quad (4.67)$$

The general solution for varying angles φ and θ is illustrated in Figure 4.3 with material properties from Table 4.1 and $h = 1\mu\text{m}$ ($H = 0.349$).

It is remarkable that all of these threshold values are twice that of a single crystal, showing clearly the size effect that was already observed for single crystals. Also, the model predicts increasing nucleation strength with decreasing height h of the bicrystal.

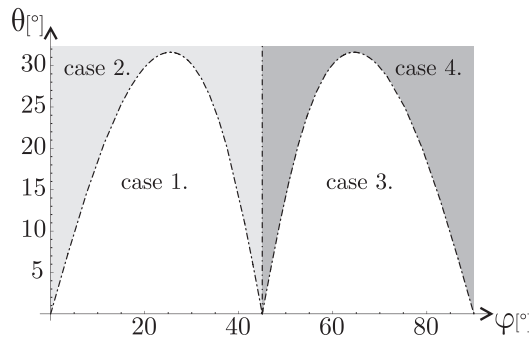


Figure 4.4: Plot of the φ - θ -plane identifying four different regions for the energetic threshold value δ_{en} and for the evolution of the plastic distortion. Labeling refers to cases 1. through 4. as explained above.

material	μ (GPa)	ν	b (Å)	ρ_s (m ⁻²)	k
aluminum	26.3	0.33	2.5	$1.396 \cdot 10^{15}$	$1.15 \cdot 10^{-3}$

Table 4.1: Material characteristics

4.4 Plane-Constrained Shear of Single-Slip Bicrystals

Before we analyze the general loading situation with arbitrary angle θ , we limit our analysis to particular cases first. In the following, we investigate the evolution of plastic slip and the dislocation density at zero and non-zero dissipation for the special case of a plane-constrained shear deformation of our model bicrystal with symmetric slip systems, following (Kochmann and Le, 2008a). We present the derivation of this problem in some more detail to demonstrate the general solution method and to abbreviate the remaining problems later.

4.4.1 Plane-Constrained Shear at Zero Dissipation

Based on the previous analysis (see solutions (4.49) and (4.50)), we now assume that for plane-constrained shear we have symmetry of β in the bicrystal, i.e. $\beta(H/2 + \xi) = \beta(\xi)$ for $\xi \in (0, H/2)$. Thus, $\langle \beta \sin 2\varphi \rangle = 0$ and the dimensionless energy functional reduces to

$$E(\beta) = \int_0^H \left[\frac{1}{2}(1 - \bar{\kappa})\beta^2 \sin^2 2\varphi + \frac{1}{2}(\gamma - \langle \beta \rangle \cos 2\varphi)^2 + k|\beta'| |\sin \varphi| + \frac{1}{2}k\beta'^2 \sin^2 \varphi \right] d\xi, \quad (4.68)$$

Due to the boundary conditions, β' should change its sign on the interval $(0, H/2)$. Our previous results suggest to seek the minimizer in the form

$$\beta(\xi) = \begin{cases} \beta_1(\xi), & \text{for } \xi \in (0, l), \\ \beta_m, & \text{for } \xi \in (l, H/2 - l), \\ \beta_1(H/2 - \xi), & \text{for } \xi \in (H/2 - l, H/2), \end{cases} \quad (4.69)$$

where β_m is a constant, l an unknown length, $0 \leq l \leq \frac{H}{4}$, and $\beta_1(l) = \beta_m$ at $\xi = l$. We need to find $\beta_1(\xi)$ and the constants β_m and l . With β from (4.69) the energy functional (4.68) becomes

$$E = 4 \int_0^l \left[\frac{1}{2}(1 - \bar{\kappa})\beta_1^2 \sin^2 2\varphi + \frac{1}{2}(\gamma - \langle \beta \rangle \cos 2\varphi)^2 + k|\beta'_1 \sin \varphi| + \frac{1}{2}k\beta_1'^2 \sin^2 \varphi \right] d\xi + 2 \left[\frac{1}{2}(1 - \bar{\kappa})\beta_m^2 \sin^2 2\varphi + \frac{1}{2}(\gamma - \langle \beta \rangle \cos 2\varphi)^2 \right] (H/2 - 2l), \quad (4.70)$$

where

$$\langle \beta \rangle = \frac{1}{H} \left(4 \int_0^l \beta_1 d\xi + 2(H/2 - 2l)\beta_m \right). \quad (4.71)$$

Varying functional (4.70) with respect to $\beta_1(\xi)$, we obtain the differential equation

$$(1 - \bar{\kappa})\beta_1 \sin^2 2\varphi + (\varepsilon - \bar{\kappa}\langle\beta \sin 2\varphi\rangle) \sin 2\varphi - k\beta_1'' \sin^2 \varphi = 0 \quad (4.72)$$

on $(0, l)$ where $\beta_1(\xi)$ is subject to the boundary conditions

$$\beta_1(0) = 0, \quad \beta_1(l) = \beta_m. \quad (4.73)$$

The variation of (4.70) with respect to l gives the additional boundary condition

$$\beta_1'(l) = 0, \quad (4.74)$$

which means that the dislocation density must be continuous at $\xi = l$. Varying the energy functional with respect to β_m , we obtain a condition for β_m at $y = l$, which reads

$$4k|\sin \varphi| \text{sign} \beta_1' + [(1 - \bar{\kappa})\beta_m \sin^2 2\varphi + (\varepsilon - \bar{\kappa}\langle\beta \sin 2\varphi\rangle) \sin 2\varphi](H - 4l) = 0. \quad (4.75)$$

Eqs. (4.72), (4.73)₁ and (4.74) yield the solution

$$\beta_1(\xi) = \beta_{1p} (1 - \cosh \eta \xi + \tanh \eta l \sinh \eta \xi), \quad 0 \leq \xi \leq l \quad (4.76)$$

with

$$\beta_{1p} = \frac{\gamma \cos 2\varphi - \langle\beta\rangle \cos^2 2\varphi}{(1 - \bar{\kappa}) \sin^2 2\varphi}, \quad \beta_m = \beta_{1p} \left(1 - \frac{1}{\cosh \eta l}\right), \quad (4.77)$$

and

$$\eta = 2\sqrt{\frac{1 - \bar{\kappa}}{k}} |\cos \varphi|. \quad (4.78)$$

The average of β can be obtained as

$$\langle\beta\rangle = \frac{\gamma \cos 2\varphi \left(4 \left(l - \frac{\tanh \eta l}{\eta}\right) + \left(1 - \frac{1}{\cosh \eta l}\right) (H - 4l)\right)}{g(l)}, \quad (4.79)$$

with

$$g(l) = H(1 - \bar{\kappa}) \sin^2 2\varphi + \cos^2 2\varphi \left[4 \left(l - \frac{\tanh \eta l}{\eta}\right) + \left(1 - \frac{1}{\cosh \eta l}\right) (h - 4l)\right]. \quad (4.80)$$

The unknown boundary thickness l must be determined numerically from the equation

$$4k|\sin \varphi| \text{sign} \beta_1' - \frac{\gamma \cos 2\varphi - \langle\beta\rangle \cos^2 2\varphi}{\cosh \eta l} (H - 4l) = 0. \quad (4.81)$$

Figure 4.5 shows the evolution of $\beta(\xi)$ with increasing γ , for $\varphi = 30^\circ$ (continuous lines) and $\varphi = 60^\circ$ (dashed lines), where $\xi = yb\rho_s$. For the numerical simulation we take the material parameters from Table 4.1 as well as $h = 1\mu\text{m}$ so that $H = hb\rho_s = 0.349$. Clearly, β is symmetric in the bicrystal.

It is interesting to plot the shear stress

$$\tau = \mu(\gamma - \langle\beta\rangle \cos 2\varphi) \quad (4.82)$$

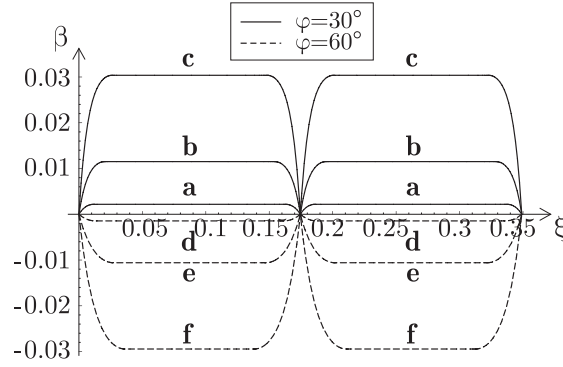


Figure 4.5: Evolution of β for constrained shear of a bicrystal at zero dissipation: a,d) $\gamma = 0.005$, b,e) $\gamma = 0.02$, c,f) $\gamma = 0.05$

as a function of the shear strain. As we know, for $\gamma < \gamma_{en}$ no dislocations are nucleated and $\beta = 0$, so the shear stress $\tau = \mu\gamma$. For $\gamma > \gamma_{en}$ we take $\langle\beta\rangle$ from (4.79) to compute the shear stress.

Figure 4.6 illustrates the normalized shear stress versus shear strain curve **OAB** for $\varphi = 30^\circ$ (continuous lines) and **OA'B'** for $\varphi = 60^\circ$ (dashed lines), with material properties from Table 4.1 and $H = hb\rho_s = 0.349$. Note the work hardening section **AB** for $\gamma > \gamma_{en}$ caused by the dislocation pile-up. Due to the absence of dissipation, however, there is no residual strain as we unload the twin by decreasing γ . The stress-strain curve follows the same path **BAO**. So, the plastic deformation is completely reversible, and no energy dissipation occurs. During unloading the nucleated dislocations annihilate, and as we approach point **A**, all dislocations disappear.

4.4.2 Plane-Constrained Shear at Non-Zero Dissipation

If the resistance to dislocation motion (and hence the dissipation) cannot be neglected, the plastic distortion may evolve only if the yield condition $|\varkappa| = \tau_{crit}(\xi)$ is fulfilled, see (4.46). If $|\varkappa| < \tau_{crit}(\xi)$, then β is frozen, the dislocation density remains unaltered and the bicrystal deforms elastically. Again we conclude symmetry of β from our threshold analysis, i.e. we

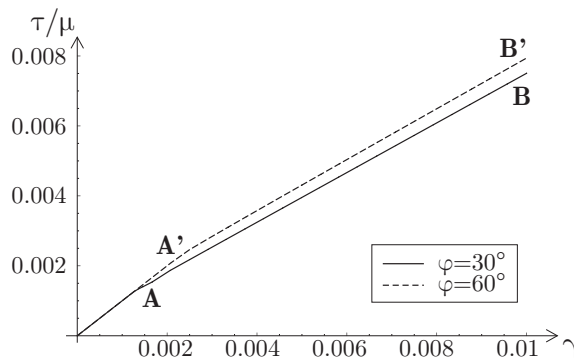


Figure 4.6: Normalized shear stress versus shear strain curve for a constrained shear test of a bicrystal at zero dissipation.

assume $\beta(H/2 + \xi) = \beta(\xi)$ for $\xi \in (0, H/2)$, and due to the symmetry of slip systems $\tau_{cr,l} = \tau_{cr,u} = \tau_{crit}$. Thus, the energy functional is the same as in (4.68). Computing the variational derivative of (4.68), we derive from (4.44) the yield condition

$$|-(1 - \bar{\kappa})\beta \sin^2 2\varphi + \cos 2\varphi(\gamma - \langle\beta\rangle \cos 2\varphi) + k\beta'' \sin^2 \varphi| = \tau_{crit}/\mu = \gamma_{cr} \cos 2\varphi, \quad (4.83)$$

where we introduced $\gamma_{cr} = \tau_{crit}/\mu \cos 2\varphi$.

Consider the case $\varphi < 45^\circ$ first. We regard γ as a given function of time and try to determine $\beta(t, y)$. We consider the loading path shown in Figure 4.7. The rate of change of $\gamma(t)$ does not affect the results due to the rate independence of dissipation. The problem is to determine the evolution of β as a function of t and ξ , provided $\beta(0, \xi) = 0$.

Since the plastic distortion β is initially zero, we see from (4.83) that $\beta = 0$ as long as $\gamma < \gamma_{cr}$. Thus, the dissipative threshold stress (the yield stress) is $\sigma_y = \tau_{crit}$. For small $\beta(t, \xi)$ and $\gamma > \gamma_{cr}$, the yield condition becomes

$$-(1 - \bar{\kappa})\beta \sin^2 2\varphi + \cos 2\varphi(\gamma - \langle\beta\rangle \cos 2\varphi) + k\beta'' \sin^2 \varphi = \gamma_{cr} \cos 2\varphi. \quad (4.84)$$

Let us introduce the deviation of $\gamma(t)$ from the critical shear γ_{cr} ,

$$\gamma_r = \gamma - \gamma_{cr} \quad (4.85)$$

and rearrange (4.84) to obtain

$$(1 - \bar{\kappa})\beta \sin^2 2\varphi - \cos 2\varphi(\gamma_r - \langle\beta\rangle \cos 2\varphi) - k\beta'' \sin^2 \varphi = 0. \quad (4.86)$$

As this equation is linear, β is proportional to γ_r such that $\beta = \gamma_r \beta_1$, where β_1 is the solution of (4.86) with $\gamma_r = 1$. As in the zero-dissipation case, we conclude that the solution for the plastic distortion is symmetric within each crystal, i.e.

$$\beta_1(\xi) = \beta_1(H/2 - \xi) \quad \text{for} \quad \xi \in (H/4, H/2). \quad (4.87)$$

Function $\beta_1(\xi)$ is determined from Eq. (4.86) (with $\gamma = 1$) and the boundary conditions

$$\beta_1(0) = 0, \quad \beta_1'(H/4) = 0. \quad (4.88)$$

As before, the first condition means that dislocations cannot reach the boundary of the region. The second condition follows from the continuity of plastic distortion and the symmetry property (4.87).

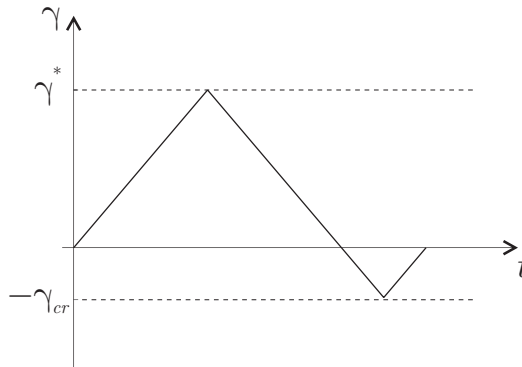


Figure 4.7: A closed loading path.

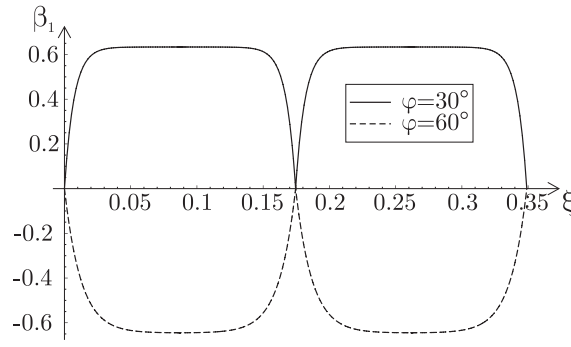


Figure 4.8: Graphs of $\beta_1(\xi)$ for constrained shear of a bicrystal at non-zero dissipation

Eqs. (4.86) and (4.88) admit the solution

$$\beta_1 = \beta_{1p} \left(1 - \cosh \eta \xi + \tanh \eta \frac{H}{4} \sinh \eta \xi \right), \quad 0 \leq \xi \leq \frac{H}{4}, \quad (4.89)$$

with

$$\beta_{1p} = \frac{\cos 2\varphi - \cos^2 2\varphi \langle \beta_1 \rangle}{(1 - \bar{\kappa}) \sin^2 2\varphi}, \quad (4.90)$$

and η from (4.78). The average of β_1 is given by

$$\langle \beta_1 \rangle = \frac{\cos 2\varphi \left(1 - \frac{4 \tanh \eta \frac{H}{4}}{\eta H} \right)}{(1 - \bar{\kappa}) \sin^2 2\varphi + \cos^2 2\varphi \left(1 - \frac{4 \tanh \eta \frac{H}{4}}{\eta H} \right)}. \quad (4.91)$$

Figure 4.8 shows the graphs of $\beta_1(\xi)$ for $\varphi = 30^\circ$ (continuous lines) and $\varphi = 60^\circ$ (dashed lines). For the numerical simulation we took the same material data as before and $H = 0.349$.

After reaching $\gamma^* > \gamma_{cr}$, we unload the crystal by decreasing γ . Since \varkappa becomes smaller than τ_{crit} , β does not change ($\beta = \beta^*(\xi)$) until

$$-(1 - \bar{\kappa})\beta^* \sin^2 2\varphi + \cos 2\varphi(\gamma - \langle \beta^* \rangle \cos 2\varphi) + k\beta^{*''} \sin^2 \varphi = -\gamma_{cr} \cos 2\varphi, \quad (4.92)$$

where $\beta^*(\xi)$ is the solution of (4.86) for $\gamma(t) = \gamma^*$. From (4.92) we can identify the onset of plastic flow at $\gamma - (\gamma^* - \gamma_{cr}) = -\gamma_{cr}$, i.e. when $\gamma = \gamma_* = \gamma^* - 2\gamma_{cr}$. From that value of γ , the yield condition reads $\varkappa = -\tau_{crit}$ leading to a decrease of β which now must be determined from

$$-(1 - \bar{\kappa})\beta \sin^2 2\varphi + \cos 2\varphi(\gamma - \langle \beta \rangle \cos 2\varphi) + k\beta'' \sin^2 \varphi = -\gamma_{cr} \cos 2\varphi. \quad (4.93)$$

Since for $\gamma \in (-\gamma_{cr}, \gamma_*)$ the deviation $\gamma_l = \gamma + \gamma_{cr}$ is positive, Eq. (4.93) can again be transformed to equation (4.86) and solved in exactly the same way by replacing $\gamma_r = \gamma - \gamma_{cr}$ in all formulae (4.89)-(4.91) by

$$\gamma_l = \gamma + \gamma_{cr}. \quad (4.94)$$

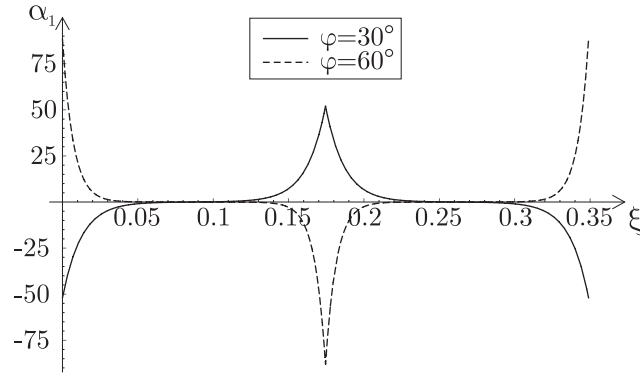


Figure 4.9: Graphs of the normalized dislocation density $\alpha_1(\xi)$ for constrained shear of a bicrystal at non-zero dissipation

As γ approaches $-\gamma_{cr}$, β tends to zero as $\gamma_l \rightarrow 0$. Further increase of γ from $-\gamma_{cr}$ to zero does not cause change of β which remains zero. The complete solution for $\varphi > 45^\circ$ can be found in an analogous way and is omitted here for conciseness.

The normalized dislocation density

$$\alpha(\xi) = \beta_{,\xi} \sin \varphi(\xi) \quad (4.95)$$

can be calculated from (4.89). Since $\beta(\xi)$ is proportional to γ_r , so is $\alpha(\xi)$ such that $\alpha(\xi) = \gamma_r \alpha_1(\xi)$. For $\xi \in (0, H/4)$ we have

$$\alpha_1(\xi) = -\beta_{1p} \left(-\eta \sinh \eta \xi + \eta \cosh \eta \xi \tanh \frac{\eta H}{4} \right) \sin \varphi(\xi) \quad (4.96)$$

with β_{1p} from (4.90) and η from (4.78). For $\xi \in (H/4, H/2)$, we have $\alpha_1(\xi) = -\alpha_1(H/2 - \xi)$ due to symmetry. Figure 4.9 illustrates the graphs of $\alpha_1(\xi)$ for $\varphi = 30^\circ$ (continuous lines) and $\varphi = 60^\circ$ (dashed lines), computed with material properties from Table 4.1 and $H = hb\rho_s = 0.349$. It becomes apparent that dislocations pile up at the crystal boundaries, leaving the central parts of both single crystals dislocation-free. The changing signs in Figure 4.9 simply represent dislocations of different orientations.

Finally, let us calculate the shear stress τ , an experimentally measurable quantity. During loading we have for the normalized shear stress

$$\frac{\tau}{\mu} = \gamma_{cr} + \gamma_r \left[1 - \left(1 - \frac{4 \tanh \frac{\eta H}{4}}{\eta H} \right) \beta_{1p} \cos 2\varphi \right], \quad (4.97)$$

with β_{1p} from (4.90). The second term of (4.97) causes hardening due to the dislocation pile-up and depends on the height H . Eq. (4.97) hence describes the size effect in this model: With decreasing height of the bicrystal the hardening rate increases. During inverse loading, when the yield condition $\varkappa = -\tau_{crit}$ holds true, Eq. (4.97) changes into

$$\frac{\tau}{\mu} = -\gamma_{cr} + \gamma_l \left[1 - \left(1 - \frac{4 \tanh \frac{\eta H}{4}}{\eta H} \right) \beta_{1p} \cos 2\varphi \right]. \quad (4.98)$$

Figure 4.10 shows the normalized shear stress versus shear strain curve for the loading path of Figure 4.7, with $\tau_{crit} = 23.67$ MPa, $\gamma^* = 0.01$, $\varphi = 30^\circ$, while all other parameters

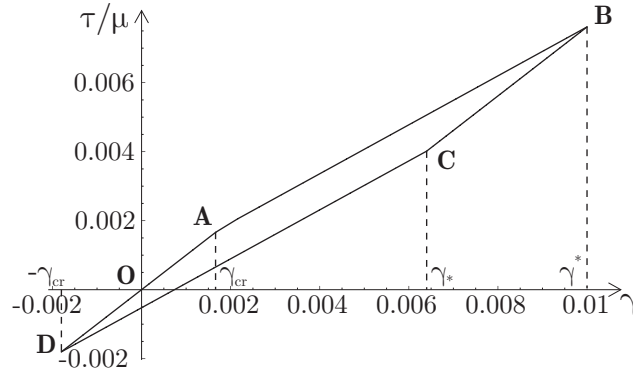


Figure 4.10: Normalized shear stress versus shear strain curve for a constrained shear test of a bicrystal at non-zero dissipation, for $\varphi = 30^\circ$

remain the same as before. The straight line **OA** corresponds to purely elastic loading with γ increasing from zero to γ_{cr} . Line **AB** corresponds to plastic yielding with $\varkappa = \tau_{crit}$. Plastic flow begins at point **A** with the yield stress $\tau_y = \tau_{crit} / \cos 2\varphi$, and we observe a work hardening effect (due to the dislocation pile-up), described by the second term of (4.97) and (4.98).

During unloading, as γ decreases from γ^* to $\gamma_* = \gamma^* - 2\gamma_{cr}$ (line **BC**), the plastic distortion $\beta = \beta^*$ is frozen. As γ decreases further from γ_* to $-\gamma_{cr}$, plastic yielding occurs with $\varkappa = -\tau_{crit}$ (line **CD**). It is seen from Figure 4.10 that the yield stress $\tau_y = \tau^* - 2\tau_{crit} / \cos 2\varphi$ at point **C**, where the inverse plastic flow begins, is larger than $-\tau_{crit} / \cos 2\varphi$ (because $\tau^*/\mu > \gamma_{cr} = \tau_{crit}/(\mu \cos 2\varphi)$). Along line **CD**, as γ decreases, the nucleated dislocations annihilate, and at point **D** all dislocations have disappeared. Finally, as γ increases from $-\gamma_{cr}$ to zero, the crystal behaves elastically with $\beta = 0$. In this closed cycle **OABCD**, dissipation only occurs along lines **AB** and **CD**. Note that lines **DA** and **BC** are parallel and have the same length. In phenomenological plasticity theory this property is known as the so-called Bauschinger effect (a translational shift of the yield surface in the stress space).

4.4.3 Numerical Solution for Plane-Constrained Shear with Non-Symmetric Active Slip Systems

Analyzing the plane-constrained shear problem of a bicrystal with arbitrary non-symmetric active slip systems, we notice that a neat closed-form analytical solution is no longer feasible. However, we can easily obtain a numerical solution for the evolution of β for given slip orientations φ_l and φ_u by means of a finite element procedure. In the special case of symmetric slip planes, the analytical solution confirms the correctness of the numerical solution.

Based on the previous results for dislocation pile-ups as well as from discrete dislocation dynamics (Needleman and Van der Giessen, 2001), we again assume the plastic distortion β to be constant in the middle of each layer at zero dissipation. This means, in terms of dislocations, that dislocations nucleated within the two layers pile up at the boundaries, forming thin boundary layers and leaving the center of each crystal dislocation-free. Furthermore, we assume the solution to be symmetric within each layer as has been found for all cases before. The major advantage of formulating the numerical problem this way lies in the small number of degrees of freedom needed for minimization. Computations in this Section were

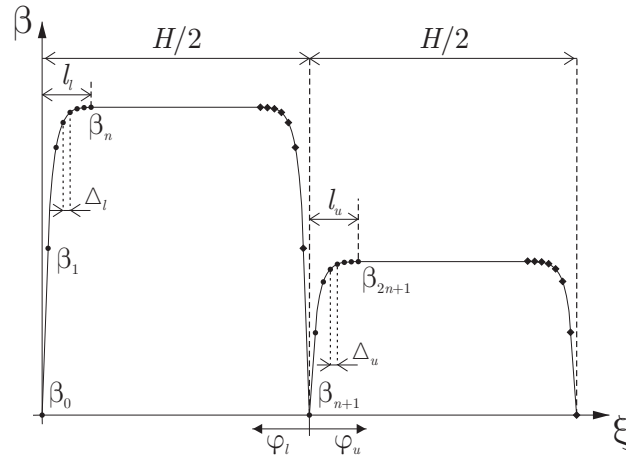


Figure 4.11: Sketch illustrating the finite element model used to compute the numerical solution. Plastic distortion β is assumed to be symmetric within each layer of the bicrystal (i.e. values at square-nodes are obtained from dot-nodes via symmetry).

performed with as few as 20 elements per boundary layer to show agreement with analytical results in the symmetric case (with the largest relative error less than 0.1%).

With these assumptions we employ linear elements to model the plastic distortion β over the height of the bicrystal under consideration as sketched in Figure 4.11. To model each boundary layer with n elements, it requires $2n + 2$ degrees of freedom at nodes plus the unknown boundary layer thicknesses in the lower layer and in the upper layer, l_l and l_u , respectively. Boundary conditions along with the assumption that $\beta = 0$ at the interface yield the constraints

$$\beta_0 = \beta_{n+1} = 0. \quad (4.99)$$

The dimensionless energy can now be written in the form (using the same dimensionless definitions as before),

$$E = E(\beta_i, l_l, l_u). \quad (4.100)$$

For the example of pure shear the energy functional can be written as

$$E = \frac{H}{2} (\gamma - \langle \beta \cos 2\varphi \rangle)^2 + \frac{H}{2} (1 - \bar{\kappa}) \langle \beta^2 \sin^2 2\varphi \rangle + \frac{H}{2} \bar{\kappa} \langle \beta \sin 2\varphi \rangle^2 + kR_1 + kR_2, \quad (4.101)$$

with the following average values

$$\begin{aligned} \langle \beta \cos 2\varphi \rangle = \frac{1}{H} & \left[\beta_n \cos 2\varphi_l \left(\frac{H}{2} - 2l_l \right) + \beta_{2n+1} \cos 2\varphi_u \left(\frac{H}{2} - 2l_u \right) \right. \\ & \left. + \Delta_l \cos 2\varphi_l \sum_{i=1}^n (\beta_i + \beta_{i-1}) + \Delta_u \cos 2\varphi_u \sum_{i=n+1}^{2n} (\beta_i + \beta_{i+1}) \right], \end{aligned} \quad (4.102)$$

$$\langle \beta \sin 2\varphi \rangle = \frac{1}{H} \left[-\beta_n \sin 2\varphi_l \left(\frac{H}{2} - 2l_l \right) + \beta_{2n+1} \sin 2\varphi_u \left(\frac{H}{2} - 2l_u \right) - \Delta_l \sin 2\varphi_l \sum_{i=1}^n (\beta_i + \beta_{i-1}) + \Delta_u \sin 2\varphi_u \sum_{i=n+1}^{2n} (\beta_i + \beta_{i+1}) \right], \quad (4.103)$$

$$\begin{aligned} \langle \beta^2 \sin^2 2\varphi \rangle = \frac{1}{H} & \left[\beta_n^2 \sin^2 2\varphi_l \left(\frac{H}{2} - 2l_l \right) + \beta_{2n+1}^2 \sin^2 2\varphi_u \left(\frac{H}{2} - 2l_u \right) \right. \\ & + \frac{2}{3} \Delta_l \sin^2 2\varphi_l \sum_{i=1}^n (\beta_i^2 + \beta_i \beta_{i-1} + \beta_{i-1}^2) \\ & \left. + \frac{2}{3} \Delta_u \sin^2 2\varphi_u \sum_{i=n+1}^{2n} (\beta_i^2 + \beta_i \beta_{i+1} + \beta_{i+1}^2) \right] \end{aligned} \quad (4.104)$$

and

$$R_1 = \int_0^H |\beta'(\xi) \sin 2\varphi| d\xi = 2 |\sin \varphi_l| \sum_{i=1}^n |\beta_i - \beta_{i-1}| + 2 |\sin \varphi_u| \sum_{i=n+1}^{2n} |\beta_i - \beta_{i+1}|,$$

$$R_2 = \frac{1}{2} \int_0^H \beta'^2(\xi) \sin^2 2\varphi d\xi = \frac{2}{\Delta_l} \sin^2 \varphi_l \sum_{i=1}^n (\beta_i - \beta_{i-1})^2 + \frac{2}{\Delta_u} \sin^2 \varphi_u \sum_{i=n+1}^{2n} (\beta_i - \beta_{i+1})^2,$$

where

$$\Delta_l = \frac{l_l}{n} \quad \text{and} \quad \Delta_u = \frac{l_u}{n}. \quad (4.105)$$

Note that the minus signs in $\langle \beta \sin 2\varphi \rangle$ result from the definition of φ_l . Minimizing the energy functional with respect to the vector (β_i, l_l, l_u) and with additional constraints

$$0 \leq l_l \leq \frac{H}{4}, \quad 0 \leq l_u \leq \frac{H}{4}, \quad (4.106)$$

one obtains the numerical solution for the plastic distortion β .

To illustrate the numerical solution for non-symmetric active slip planes in the two layers of our model bicrystal, let us consider the case of $\varphi_l = -60^\circ$ and $\varphi_u = 30^\circ$, i.e. the active slip planes in the two layers are perpendicular to each other but not symmetric with respect to the interface. Note that, according to the analytical solution in the symmetric case, we can expect positive β in the upper layer and negative β in the lower layer. Figure 4.12 illustrates the evolution of β in the two layers with increasing strain γ for the case of zero dissipation. For the numerical simulation we took $\mu = 26.3 \text{ GPa}$, $\nu = 0.33$, $k = 3.8 \cdot 10^{-4}$, $\rho_s = 3 \cdot 10^{14} \text{ m}^{-2}$, $b = 2.5 \cdot 10^{-10} \text{ m}$ and $h = 10 \mu\text{m}$.

The critical threshold value for the nucleation of dislocations for this special case of $\varphi_l = -60^\circ$ and $\varphi_u = 30^\circ$ can be obtained analytically by employing a minimizing sequence like in previous Sections, yielding

$$\gamma_{en} = \frac{k}{hb\rho_s} \frac{(13 - \sqrt{3}) - 6\bar{\kappa}(1 + \sqrt{3})}{3(1 - \bar{\kappa})}. \quad (4.107)$$

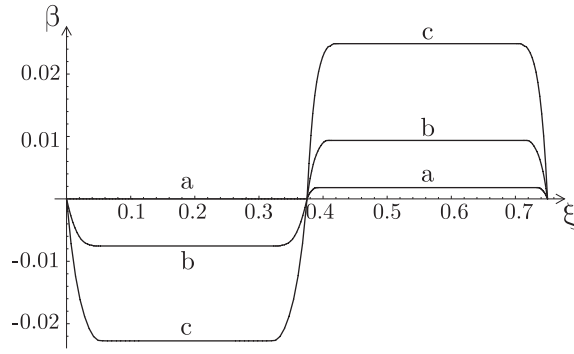


Figure 4.12: Evolution of $\beta(\xi)$ for a constrained shear test at zero dissipation, for $\varphi_l = -60^\circ$ and $\varphi_u = 30^\circ$: a) $\gamma = 0.005$, b) $\gamma = 0.02$, c) $\gamma = 0.05$.

However, due to the different orientations of the active slip systems in upper and lower layer and the resulting difference of the resolved shear stresses, one of the slip system may remain passive even at $\gamma > \gamma_{en}$. Indeed, one can see in Figure 4.12 that β is already well-developed in the upper layer at $\gamma = 0.005$ whereas it only starts to evolve in the lower layer at the same overall shear strain.

The stress-strain curve corresponding to the evolution of β in Figure 4.12 is shown in Figure 4.13. Note the steep slope of the stress-strain curve beyond the onset of dislocation nucleation due to the active slip systems chosen here.

In the case of non-zero dissipation the evolution of β must be obtained from solving the flow rule instead of minimizing the energy functional. However, adding an artificial term of dissipation to the energy functional and omitting the term with β' , one can numerically find the solution by minimizing the modified energy functional E^* . $E^*(\beta)$ can be regarded as an accumulated energy functional for standard dissipative solids, and it is simple to verify that the minimizer of E^* automatically satisfies the evolution equations, as they are the exact Euler equations thereof, see e.g. (Kochmann and Le, 2008a, 2009a). For the simple shear

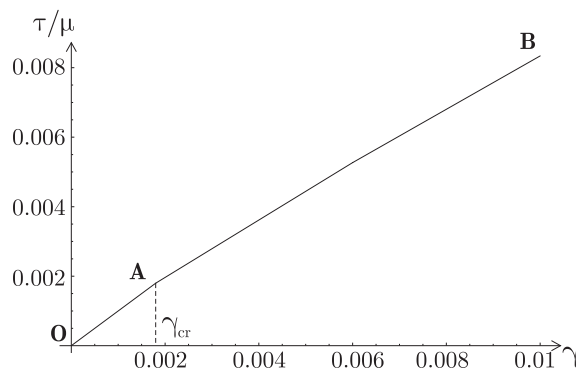


Figure 4.13: Normalized shear stress versus shear strain curve for a plane-constrained shear test at zero dissipation for $\varphi_l = -60^\circ$ and $\varphi_u = 30^\circ$.

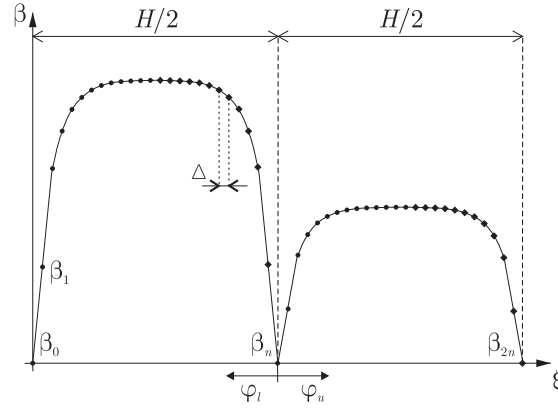


Figure 4.14: Sketch illustrating the finite element model used to compute the numerical solution in the case with dissipation. Symmetry requires square-nodes to have the same value as the corresponding symmetric dot-nodes, thus reducing the number of degrees of freedom.

example, we have

$$E^* = \frac{h}{2}(1 - \bar{\kappa})\langle\beta^2 \sin^2 2\varphi\rangle + \frac{h}{2}\bar{\kappa}\langle\beta \sin 2\varphi\rangle^2 + \frac{h}{2}(\gamma^2 + \langle\beta \cos 2\varphi\rangle^2) - h\gamma_r\langle\beta \cos 2\varphi\rangle + kR_2 \quad (4.108)$$

where

$$\gamma_r = \gamma - \gamma_{cr}. \quad (4.109)$$

Here, we assume for simplicity that $\gamma_{cr,l} = \gamma_{cr,u} = \gamma_{cr}$, i.e. the threshold value γ_{cr} is the same in both layers. (Of course, one may expect different threshold values in the two layers due to the orientations of their active slip systems as shown in the case without dissipation.) As before, the minimizer depends on γ_r only. Regarding the analytical solution in the previous Sections, we do not expect the same boundary layer-type solution as in the previous case without dissipation. Therefore, we now employ linear finite elements throughout the entire height of each layer without assuming a constant region in the middle of each layer (see Figure 4.14).

Then, the components of the energy functional can then be written as

$$\langle\beta \cos 2\varphi\rangle = \frac{\Delta}{2H} \left(\cos 2\varphi_l \sum_{i=1}^n (\beta_i + \beta_{i-1}) + \cos 2\varphi_u \sum_{i=n+1}^{2n} (\beta_i + \beta_{i-1}) \right), \quad (4.110)$$

$$\langle\beta \sin 2\varphi\rangle = \frac{\Delta}{2H} \left(-\sin 2\varphi_l \sum_{i=1}^n (\beta_i + \beta_{i-1}) + \sin 2\varphi_u \sum_{i=n+1}^{2n} (\beta_i + \beta_{i-1}) \right), \quad (4.111)$$

$$\begin{aligned} \langle\beta^2 \sin^2 2\varphi\rangle = \frac{\Delta}{3H} & \left(\sin^2 2\varphi_l \sum_{i=1}^n (\beta_i^2 + \beta_i \beta_{i-1} + \beta_{i-1}^2) \right. \\ & \left. + \sin^2 2\varphi_u \sum_{i=n+1}^{2n} (\beta_i^2 + \beta_i \beta_{i-1} + \beta_{i-1}^2) \right), \end{aligned} \quad (4.112)$$

$$R_2 = \frac{1}{2\Delta} \left(\sin^2 \varphi_l \sum_{i=1}^n (\beta_i - \beta_{i-1})^2 + \sin^2 \varphi_u \sum_{i=n+1}^{2n} (\beta_i - \beta_{i-1})^2 \right), \quad (4.113)$$

where

$$\Delta = \frac{H}{2n}. \quad (4.114)$$

Boundary conditions (i.e. zero plastic distortion at the boundaries and at the interface) read

$$\beta_0 = \beta_n = \beta_{2n} = 0. \quad (4.115)$$

Furthermore, we assume the plastic distortion β to be symmetric within each layer of the bicrystal, as has been found in all previous solutions, i.e. we require

$$\beta_{n-i} = \beta_i \quad \text{for } i = 0 \dots n/2 \quad \text{and} \quad \beta_{2n-j} = \beta_{n+j} \quad \text{for } j = 0 \dots n/2 \quad (4.116)$$

and thereby reduce the number of degrees of freedom by a factor of 2. A comparison with the analytical solution for twins with $n = 100$ shows a relative error less than 0.3%. For the numerical simulations we took (for pure copper and the chosen upper slip system) $\gamma_{cr} = 0.0018$.

Figure 4.15 illustrates the evolution of β in the two layers of the bicrystal with increasing strain γ_r for the case with dissipation and with non-symmetric angles $\varphi_l = -30^\circ$ and $\varphi_u = 40^\circ$. Observe the difference in the height of the β -curves due to the different angles of the active slip systems.

Finally, the stress-strain curve is computed for the above non-symmetric example with $\varphi_l = -30^\circ$ and $\varphi_u = 40^\circ$, following the closed strain path as in previous Sections: We increase γ from zero to the arbitrary value $\gamma^* = 0.01$, then decrease γ to $-\gamma_{cr}$ and finally increase γ back to zero. Due to the rate independence of dissipation, the strain rate $\dot{\gamma}$ does not affect the results. Figure 4.16 illustrates the normalized shear stress versus shear strain curve. A similar hardening behavior as in previous Sections can be observed. The Bauschinger effect can be noted as well.

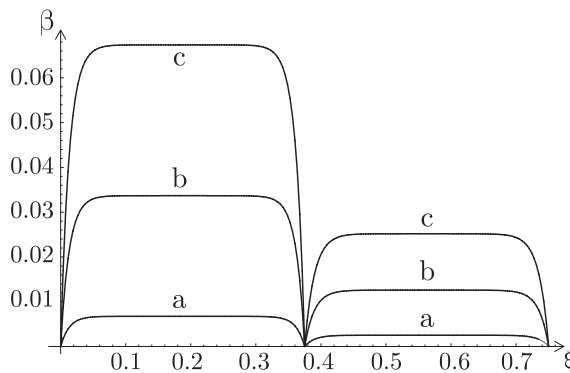


Figure 4.15: Evolution of β for plane-constrained shear at non-zero dissipation with non-symmetric slip system orientations: a) $\gamma_r = 0.01$, b) $\gamma_r = 0.05$, c) $\gamma_r = 0.1$

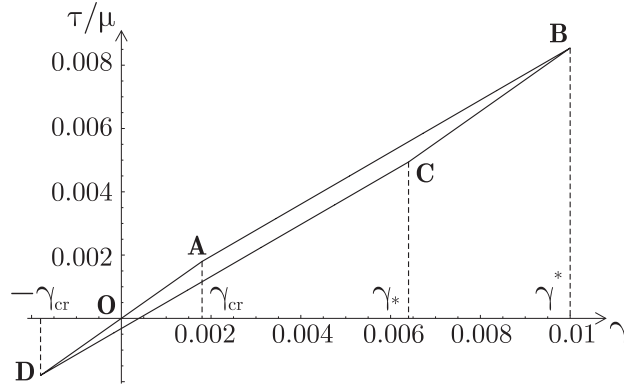


Figure 4.16: Normalized shear stress versus shear strain curve at non-zero dissipation with non-symmetric slip system orientations, $\varphi_l = -30^\circ$ and $\varphi_u = 40^\circ$.

4.5 Plane-Strain Uniaxial Extension of Single-Slip Bicrystals

Following our analysis of the plane-constrained shear problem, the solution for the uniaxial extension problem is briefly presented in the following. We derive closed-form analytical solutions for the case of plane-strain uniaxial extension of the bicrystal with symmetric active slip-systems, thereby following (Kochmann and Le, 2008b). We will first analyze the deformation of a bicrystal at zero dissipation and later take into account the dissipation of energy due to dislocation motion.

4.5.1 Plane-Strain Uniaxial Extension at Zero Dissipation

Based on the threshold analysis (see solutions (4.53) and (4.54)), we now assume that, in contrast to the shear problem, β is antisymmetric in the bicrystal with respect to the interface, i.e. $\beta(H/2 + \xi) = -\beta(\xi)$ for $\xi \in (0, H/2)$. Thus, in this case $\langle \beta \cos 2\varphi \rangle = 0$ and the dimensionless energy functional (4.43) reduces to

$$E(\beta) = \int_0^H \left[\frac{1}{2} \omega \left(\varepsilon + \bar{\kappa} (\beta \sin 2\varphi - \langle \beta \sin 2\varphi \rangle) \right)^2 + \frac{1}{4} \beta^2 \sin^2 2\varphi \right. \\ \left. + \left(\varepsilon + \left(\bar{\kappa} - \frac{1}{2} \right) \beta \sin 2\varphi - \bar{\kappa} \langle \beta \sin 2\varphi \rangle \right)^2 + k(|\beta'| \sin \varphi| + \frac{1}{2} \beta'^2 \sin^2 \varphi) \right] d\xi. \quad (4.117)$$

The results obtained in previous Sections suggest to seek the minimizer again in the form (4.69), with β_m being a constant quantity, l the unknown boundary layer thickness ($0 \leq l \leq \frac{H}{4}$) and $\beta_1(l) = \beta_m$. With β from (4.69) the energy functional (4.117) becomes

$$E = \frac{\varepsilon^2 H}{2\bar{\kappa}} + 4 \int_0^l \left[\frac{1}{2} (1 - \bar{\kappa}) \beta_1^2 \sin^2 2\varphi + \left(\varepsilon - \frac{\bar{\kappa}}{2} \langle \beta \sin 2\varphi \rangle \right) \beta_1 \sin 2\varphi + k|\beta'_1 \sin \varphi| \right. \\ \left. + \frac{1}{2} k \beta_1'^2 \sin^2 \varphi \right] d\xi + 2 \left[\frac{1}{2} (1 - \bar{\kappa}) \beta_m^2 \sin^2 2\varphi + \left(\varepsilon - \frac{\bar{\kappa}}{2} \langle \beta \sin 2\varphi \rangle \right) \beta_m \right] (H/2 - 2l), \quad (4.118)$$

where

$$\langle \beta \sin 2\varphi \rangle = -\frac{1}{H} \left(4 \int_0^l \beta_1 d\xi + 2(H/2 - 2l) \beta_m \right) \sin 2\varphi. \quad (4.119)$$

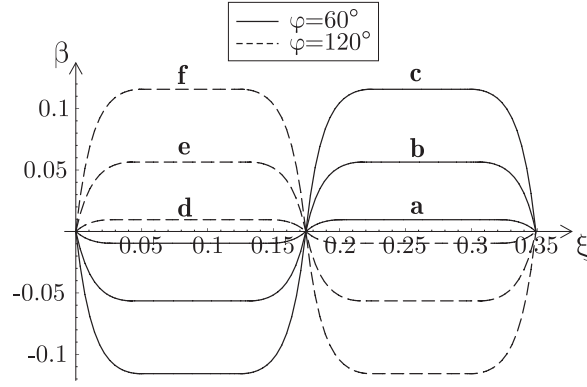


Figure 4.17: Evolution of β for uniaxial extension of a bicrystal at zero dissipation for a,d) $\varepsilon = 0.01$, b,e) $\varepsilon = 0.05$, c,f) $\varepsilon = 0.1$

Varying functional (4.118) with respect to $\beta_1(y)$, l and β_m , we obtain the solution for this case, which is of the same type as before, cf. (4.76),

$$\beta_1(\xi) = \beta_{1p} (1 - \cosh \eta \xi + \tanh \eta l \sinh \eta \xi), \quad 0 \leq \xi \leq l \quad (4.120)$$

with η from (4.78), but now with

$$\beta_{1p} = -\frac{\varepsilon - \bar{\kappa} \langle \beta \sin 2\varphi \rangle}{(1 - \bar{\kappa}) \sin 2\varphi}, \quad \beta_m = \beta_{1p} \left(1 - \frac{1}{\cosh \eta l} \right). \quad (4.121)$$

The average of $\beta \sin 2\varphi$ yields

$$\langle \beta \sin 2\varphi \rangle = \frac{\varepsilon \left[4 \left(l - \frac{\tanh \eta l}{\eta} \right) + \left(1 - \frac{1}{\cosh \eta l} \right) (H - 4l) \right]}{g(l)}, \quad (4.122)$$

where

$$g(l) = H(1 - \bar{\kappa}) + \bar{\kappa} \left[4 \left(l - \frac{\tanh \eta l}{\eta} \right) + \left(1 - \frac{1}{\cosh \eta l} \right) (H - 4l) \right]. \quad (4.123)$$

The following equation must be solved numerically to determine the boundary layer thickness l

$$4k |\sin \varphi| \text{sign} \beta'_1 + (\varepsilon - \bar{\kappa} \langle \beta \sin 2\varphi \rangle) \frac{\sin^2 2\varphi - \cosh \eta l + 1}{\sin 2\varphi \cosh \eta l} (H - 4l) = 0. \quad (4.124)$$

Figure 4.17 shows the evolution of $\beta(\xi)$ as ε increases, for $\varphi = 60^\circ$ (continuous lines) and $\varphi = 120^\circ$ (dashed lines), where $\xi = y b \rho_s$. Note that the solution exhibits antisymmetry of cases a) and d), b) and e) as well as c) and f), respectively, which is physically reasoned by the symmetry of the problem. For the numerical simulation we used the same data as before.

Similarly to the shear problem, let us plot a measurable quantity, here in terms of the dimensionless normal tensile stress

$$\frac{\sigma_{yy}}{\lambda + 2\mu} = \varepsilon - \bar{\kappa} \langle \beta \sin 2\varphi \rangle \quad (4.125)$$

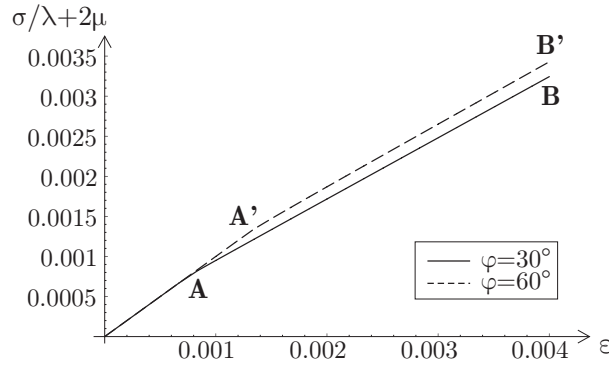


Figure 4.18: Normalized tensile stress versus strain curve for the uniaxial extension test of a bicrystal at zero dissipation

as a function of the strain ε . As we know, for $\varepsilon < \varepsilon_{en}$ no dislocations are nucleated and $\beta = 0$, so the tensile stress evolves elastically and $\sigma_{yy} = (\lambda + 2\mu)\varepsilon$. For $\varepsilon > \varepsilon_{en}$ we employ $\langle \beta \sin 2\varphi \rangle$ from (4.122) to obtain the stress σ_{yy} according to the above relation.

Figure 4.18 illustrates the normalized tensile stress versus strain curve **OAB** for $\varphi = 30^\circ$ (continuous lines) and **OA'B'** for $\varphi = 60^\circ$ (dashed lines), computed with material properties from Table 4.1 and $H = hb\rho_s = 0.349$. Note the work hardening section **AB** (or **A'B'**) for $\varepsilon > \varepsilon_{en}$ ($\varepsilon > \varepsilon'_{en}$) caused by the dislocation pile-ups. However, there is no residual strain as we unload the twins by decreasing ε . The stress-strain curve follows the same path **BAO** since the plastic deformation is completely reversible, as already discussed in Section 4.4.1.

4.5.2 Plane-Strain Uniaxial Extension at Non-Zero Dissipation

Let us complete this Section by investigating the uniaxial extension problem at non-zero dissipation so that the plastic distortion may evolve only if the yield condition $|\varkappa| = \tau_{crit}(\xi)$ is satisfied. As before, if $|\varkappa| < \tau_{crit}(\xi)$, then β is frozen and the bicrystal behaves elastically. We limit our analysis to the evolution of β in the special case of symmetric active slip systems where $-\varphi_l = \varphi_u = \varphi$ (i.e. for twins) for which we may again assume antisymmetry, i.e. $\beta(H/2 + \xi) = -\beta(\xi)$ for $\xi \in (0, H/2)$ and $\tau_{cr,l} = \tau_{cr,u} = \tau_{crit}$. Thus, $\langle \beta \cos 2\varphi \rangle = 0$ and the energy functional takes the form (4.117).

First, let us consider the case $0 < \varphi < 90^\circ$. Computing the variational derivative of (4.117), we derive from (4.44) the dimensionless yield condition for the lower layer (with the same dimensionless notation employed before)

$$|-(1 - \bar{\kappa})\beta \sin^2 2\varphi - \sin 2\varphi(\varepsilon - \bar{\kappa}\langle \beta \sin 2\varphi \rangle) + k\beta'' \sin^2 \varphi| = \tau_{crit}/\mu = \varepsilon_{cr} \sin 2\varphi, \quad (4.126)$$

where we introduced $\varepsilon_{cr} = \tau_{crit}/\mu \sin 2\varphi$. Unlike for the shear problem, where the plastic distortion was identical in both single crystals due to symmetry, we now have different differential equations to determine β for the lower and upper layer because of antisymmetry. The analogous yield condition for the upper layer is identical except for a changed sign in front of the second term resulting from the definition of $\varphi = -\varphi_l = \varphi_u$. Both yield conditions provide identical results for our model bicrystal as we assume β to be antisymmetric in the two single crystals. Therefore, in the following we may deal with the evolution of β in the lower layer only.

We regard ε as the driving variable and determine $\beta(t, \xi)$. We consider a loading path analogous to the one shown in Figure 4.7: ε is first increased from zero to some arbitrary value $\varepsilon^* > \varepsilon_{cr}$, then decreased to $-\varepsilon_{cr}$, and finally increased to zero. Again, the rate of change of $\varepsilon(t)$ has no impact on the results due to the rate independence of dissipation. The problem is to determine the evolution of β as a function of t and ξ with the initial condition $\beta(0, \xi) = 0$.

As β is initially zero, we see from (4.126) that $\beta = 0$ as long as $\varepsilon < \varepsilon_{cr}$. Thus, the dissipative threshold stress (the yield stress) is $\sigma_y = \tau_{crit}$. Let us introduce the deviation of $\varepsilon(t)$ from the critical strain ε_{cr} ,

$$\varepsilon_r = \varepsilon - \varepsilon_{cr}. \quad (4.127)$$

For small $\beta(t, \xi)$ and $\varepsilon > \varepsilon_{cr}$ the yield condition in the lower layer becomes (again for $0 < \varphi < 90^\circ$)

$$(1 - \bar{\kappa})\beta \sin^2 2\varphi + \sin 2\varphi(\varepsilon_r - \bar{\kappa}\langle\beta \sin 2\varphi\rangle) - k\beta'' \sin^2 \varphi = 0. \quad (4.128)$$

As this equation is linear, β is proportional to ε_r (note that in the simple shear problem β is proportional to γ_r in a similar manner) such that we may write again $\beta = \varepsilon_r \beta_1$. Here, we obtain the solution

$$\beta_1(\xi) = \beta_{1p} \left(1 - \cosh \eta \xi + \tanh \eta \frac{H}{4} \sinh \eta \xi \right), \quad 0 \leq \xi \leq \frac{H}{4}, \quad (4.129)$$

with η from (4.78) and

$$\beta_{1p} = \frac{\bar{\kappa}\langle\beta_1 \sin 2\varphi\rangle - 1}{(1 - \bar{\kappa}) \sin 2\varphi}. \quad (4.130)$$

The average of $\beta_1 \sin 2\varphi$ is obtained in the form

$$\langle\beta_1 \sin 2\varphi\rangle = \frac{1 - \frac{4 \tanh \eta \frac{H}{4}}{\eta H}}{(1 - \bar{\kappa}) + \bar{\kappa} \left(1 - \frac{4 \tanh \eta \frac{H}{4}}{\eta H} \right)}. \quad (4.131)$$

Note the similarity of results obtained here and in the problem of plane-constrained shear in the previous Section.

Figure 4.19 shows the graphs of $\beta_1(\xi)$ for $\varphi = 60^\circ$ (continuous lines) and $\varphi = 120^\circ$ (dashed lines). Again, note the symmetric solution for these two angles due to the symmetry of the problem. The same material parameters were used as in previous Sections.

After reaching ε^* , we unload the bicrystal by decreasing ε . Since \varkappa becomes smaller than τ_{crit} , β does not change ($\beta = \beta^*(\xi)$ where β^* denotes the solution of (4.128 for $\varepsilon(t) = \varepsilon^*$) until

$$(1 - \bar{\kappa})\beta^* \sin^2 2\varphi + \sin 2\varphi(\varepsilon - \bar{\kappa}\langle\beta^* \sin 2\varphi\rangle) - k\beta^{*''} \sin^2 \varphi = -\varepsilon_{cr} \sin 2\varphi, \quad (4.132)$$

where $\beta^*(\xi)$ is the solution of the flow condition for positive loading and for $\varepsilon(t) = \varepsilon^*$. From (4.132) it becomes apparent that plastic flow begins when $\varepsilon - (\varepsilon^* - \varepsilon_{cr}) = -\varepsilon_{cr}$, i.e. for $\varepsilon = \varepsilon_* = \varepsilon^* - 2\varepsilon_{cr}$. From that value of ε the yield condition $\varkappa = -\tau_{crit}$ holds true leading to a decrease of β .

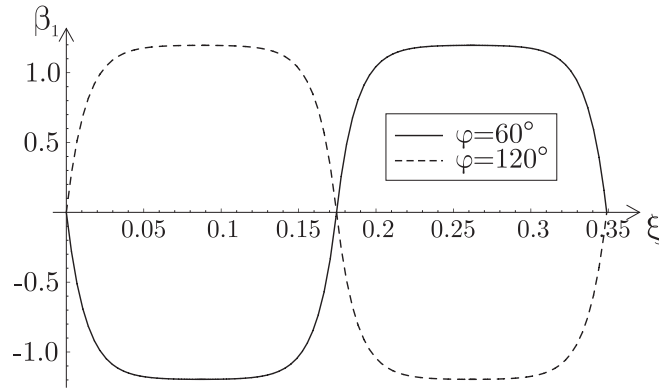


Figure 4.19: Graphs of $\beta_1(\xi)$ for uniaxial extension of a bicrystal at non-zero dissipation

For $\varepsilon \in (-\varepsilon_{cr}, \varepsilon_*)$ the deviation

$$\varepsilon_l = \varepsilon + \varepsilon_{cr} \quad (4.133)$$

is positive and the solution can be obtained in exactly the same manner as in the shear problem, i.e. by replacing $\varepsilon_r = \varepsilon - \varepsilon_{cr}$ by $\varepsilon_l = \varepsilon + \varepsilon_{cr}$ in all formulae (4.129) through (4.131). As ε approaches $-\varepsilon_{cr}$, β tends to zero because $\varepsilon_l \rightarrow 0$. The further increase of ε from $-\varepsilon_{cr}$ to zero does not cause change in β which remains zero.

The above construction can easily be modified to find the solution for $\varphi > 90^\circ$.

The normalized dislocation density $\alpha(\xi) = \beta_{,\xi} \sin \varphi(\xi)$ can be calculated from the above solution (4.129). As $\beta(\xi)$ is proportional to ε_r , so is $\alpha(\xi)$ such that $\alpha(\xi) = \varepsilon_r \alpha_1(\xi)$. For $\xi \in (0, H/4)$ we have

$$\alpha_1(\xi) = -\beta_{lp} \left(-\eta \sinh \eta \xi + \eta \cosh \eta \xi \tanh \frac{\eta H}{4} \right) \sin \varphi, \quad (4.134)$$

with β_{lp} from (4.90) and η from (4.78). For $\xi \in (H/4, H/2)$ we have $\alpha_1(\xi) = -\alpha_1(H/2 - \xi)$ due to symmetry of the plastic distortion β . Due to symmetry, the solution in the upper layer is the same.

Let us now complete this Section by determining the tensile stress σ_{yy} . During loading we have for the normalized average stress

$$\frac{\sigma_{yy}}{\lambda + 2\mu} = \varepsilon_{cr} + \varepsilon_r (1 - \bar{\kappa} \langle \beta_1 \sin 2\varphi \rangle) \quad (4.135)$$

with $\langle \beta_1 \sin 2\varphi \rangle$ from (4.131). The second term of (4.135) causes hardening due to the dislocation pile-up and describes the size effect in this model. Decreasing the height $H (= hb\rho_s)$ results in an increasing hardening rate.

During inverse loading when the yield condition $\varkappa = -\tau_{crit}$ holds true, Eq. (4.135) changes into

$$\frac{\sigma_{yy}}{\lambda + 2\mu} = -\varepsilon_{cr} + \varepsilon_l (1 - \bar{\kappa} \langle \beta_1 \sin 2\varphi \rangle) \quad (4.136)$$

with

$$\varepsilon_l = \varepsilon + \varepsilon_{cr}. \quad (4.137)$$

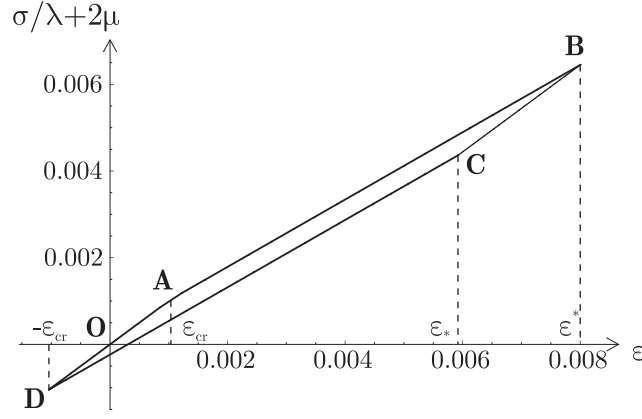


Figure 4.20: Normalized tensile stress versus strain curve for uniaxial extension of a bicrystal at non-zero dissipation, for $\varphi = 60^\circ$

Figure 4.20 shows the normalized tensile stress versus strain curve for the loading path as before, with $\tau_{\text{crit}} = 23.67\text{MPa}$, $\varepsilon^* = 0.008$, $\varphi = 60^\circ$, while all other parameters remain the same. The straight line OA corresponds to the purely elastic loading with ε increasing from zero to ε_{cr} . Line AB corresponds to plastic yielding with $\varkappa = \tau_{\text{crit}}$. The onset of plastic flow is at point A, and we can observe a work hardening section due to the dislocation pile-ups, which is described by the second term of (4.135). During unloading, as ε decreases from ε^* to $\varepsilon_* = \varepsilon^* - 2\varepsilon_{\text{cr}}$ (line BC), the plastic distortion $\beta = \beta^*$ is frozen. As ε decreases further from ε_* to $-\varepsilon_{\text{cr}}$, plastic yielding occurs with $\varkappa = -\tau_{\text{crit}}$ (line CD). Along line CD, as ε is decreased, the nucleated dislocations annihilate, and at point D all dislocations have disappeared. Finally, as ε increases from $-\varepsilon_{\text{cr}}$ to zero, the crystal deforms elastically with $\beta = 0$. In this closed cycle OABCD O dissipation again occurs only along lines AB and CD. It is interesting to note that again lines DA and BC are parallel and of the same length (Bauschinger effect).

4.5.3 Numerical Solution for Uniaxial Extension for Non-Symmetric Active Slip Systems and for Arbitrary Crystal Heights

As presented in Section 4.4.3, we can obtain the solution for arbitrary non-symmetric active slip systems by employing a finite element approximation to solve for the plastic distortion in the general case. This can also be applied to the problem of uniaxial extension. Here, the dimensionless energy at zero dissipation may be written in the form (using the same dimensionless definitions as before)

$$E = E(\beta_i, l_l, l_u), \quad (4.138)$$

where l_l and l_u are the unknown boundary layer thicknesses in the lower and upper crystal, respectively, and β_i is the plastic distortion at node i . For a uniaxial extension strain ε the energy functional reads

$$E = \frac{\varepsilon^2 H}{2\bar{\kappa}} - \varepsilon H \langle \beta \sin 2\varphi \rangle + \frac{H}{2} \langle \beta \cos 2\varphi \rangle^2 + \frac{H}{2} \bar{\kappa} \langle \beta \sin 2\varphi \rangle^2 + \frac{H}{2} (1 - \bar{\kappa}) \langle \beta^2 \sin^2 2\varphi \rangle + kR_1 + kR_2, \quad (4.139)$$

where the same average values may be used as in Section 4.4.3. Analogously to the constrained-shear problem we assume that for the uniaxial extension problem at zero dissipation there

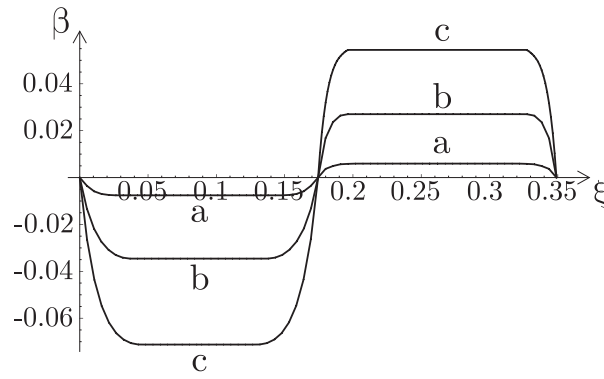


Figure 4.21: Evolution of $\beta(\xi)$ for uniaxial extension at zero dissipation with non-symmetric slip system orientations, for a) $\varepsilon = 0.01$, b) $\varepsilon = 0.04$, c) $\varepsilon = 0.08$.

is a constant part in the middle of each crystal whereas at non-zero dissipation there is none (see Section 4.4.3 for details).

Figure 4.21 shows the evolution of the plastic distortion $\beta(\xi)$ during a uniaxial extension test at zero dissipation with non-symmetric active slip systems, $\varphi_l = -60^\circ$ and $\varphi_u = 20^\circ$, with increasing overall extension strain $\varepsilon = 0.01, 0.04, 0.08$. Figure 4.22 illustrates the evolution of $\beta(\xi)$ during uniaxial extension at non-zero dissipation with $\varphi_l = -20^\circ$ and $\varphi_u = 60^\circ$, for strains of $\varepsilon_r = 0.001, 0.005, 0.01$, and exemplarily the dimensionless dislocation density $\alpha(\xi)$ for $\varepsilon_r = 0.01$ only (for clarity). Both Figures make use of the same material parameters presented before.

Finally, for completeness Figure 4.23 illustrates the influence of changing crystal heights on the present results. Figure 4.23 shows the plastic distortion β at fixed uniaxial extension strain $\varepsilon_r = 0.01$ at non-zero dissipation for symmetric active slip systems, $\varphi_u = -\varphi_l = 30^\circ$, but for changing crystal heights. The total height $H = hb\rho_s = 0.349$ remains constant while the interface changes its position in the illustrated manner, where h_u/h_l denotes the ratio of the heights of upper to lower crystal.

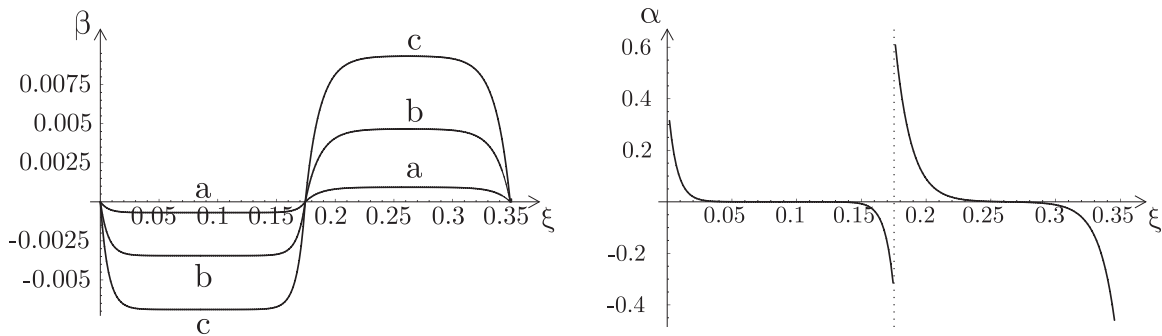


Figure 4.22: Evolution of $\beta(\xi)$ for uniaxial extension at zero dissipation with non-symmetric slip system orientations, for a) $\varepsilon_r = 0.001$, b) $\varepsilon_r = 0.005$, c) $\varepsilon_r = 0.01$, and the dimensionless dislocation density $\alpha(\xi)$ at $\varepsilon_r = 0.01$.

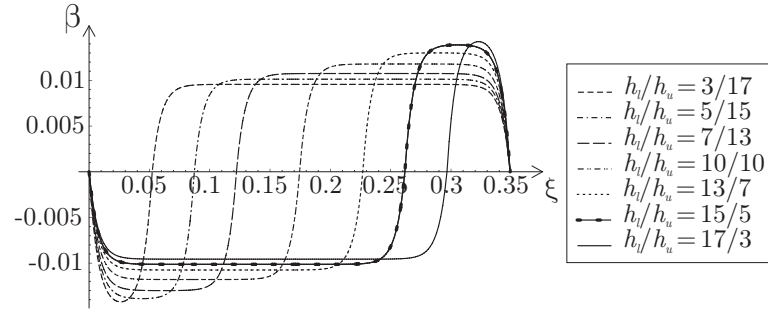


Figure 4.23: Plastic distortion $\beta(\xi)$ for uniaxial extension at non-zero dissipation with symmetric slip system orientations for changing ratio of the crystal heights.

4.6 Combined Shear and Extension of Single-Slip Bicrystals

Now that we have obtained analytical solutions for the particular problems of shear and extension of the bicrystal, let us investigate the combined loading situation already sketched in Figure 4.2. Loading the bicrystal in a hard device with the prescribed displacement δh applied under an angle θ as sketched in Figure 4.2, we can decompose any such deformation into tensile and shear strains by

$$\varepsilon = \delta \sin \theta, \quad \gamma = \delta \cos \theta, \quad (4.140)$$

respectively. The energetic threshold for this combined case was already presented in Section 4.3. It would be useful to conclude a general solution for β , which is based on previous results obtained for the independent cases of shear and extension. To do so, we will decompose the plastic distortion β as shown in Figure 4.24, i.e. we write β as the sum of a symmetric and an antisymmetric function. To demonstrate the benefit, we will focus on the plastic deformation at non-zero dissipation first, where this decomposition can be applied successfully, and later show the solution at zero dissipation.

4.6.1 Combined Shear and Extension at Non-Zero Dissipation

Any arbitrary admissible solution $\beta(\xi)$ in the bicrystal can be decomposed into a symmetric function $\beta_s(\xi)$ and an antisymmetric function $\beta_a(\xi)$ (see Figure 4.24), i.e. we write

$$\beta(\xi) = \begin{cases} \beta_s(\xi) + \beta_a(\xi) & \text{for } 0 < \xi < H/2, \\ \beta_s(\xi) - \beta_a(\xi) & \text{for } H/2 < \xi < H. \end{cases} \quad (4.141)$$

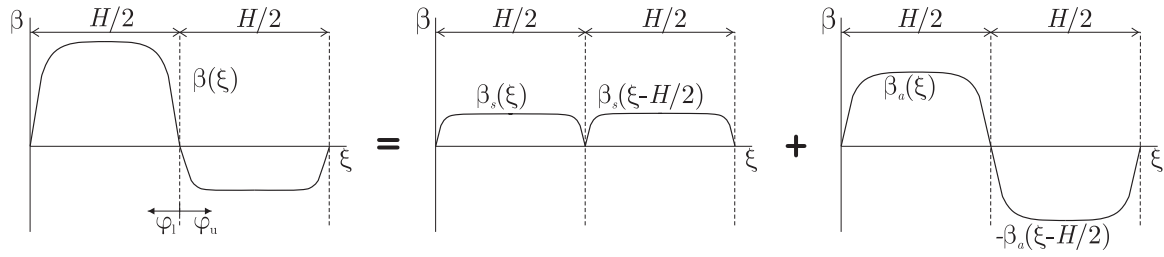


Figure 4.24: Additive decomposition of the plastic distortion β into a symmetric function β_s and an antisymmetric function β_a .

In this case, it is easy to verify that the average quantities follow for symmetric slip system orientations (i.e. $-\varphi_l = \varphi_u = \varphi$) as

$$\langle \beta \sin 2\varphi \rangle = \langle \beta_a \sin 2\varphi \rangle = -\frac{2}{H} \sin 2\varphi \int_0^{H/2} \beta_a \, d\xi, \quad (4.142)$$

$$\langle \beta \cos 2\varphi \rangle = \langle \beta_s \cos 2\varphi \rangle = \frac{2}{H} \cos 2\varphi \int_0^{H/2} \beta_s \, d\xi, \quad (4.143)$$

$$\langle \beta \sin 2\varphi \rangle^2 = \frac{4}{H^2} \sin^2 2\varphi \left[\int_0^{H/2} \beta_a \, d\xi \right]^2, \quad (4.144)$$

$$\langle \beta \cos 2\varphi \rangle^2 = \frac{4}{H^2} \cos^2 2\varphi \left[\int_0^{H/2} \beta_s \, d\xi \right]^2, \quad (4.145)$$

$$\langle \beta^2 \sin^2 2\varphi \rangle = \langle (\beta_a^2 + \beta_s^2) \sin^2 2\varphi \rangle = \frac{2}{H} \sin^2 2\varphi \int_0^{H/2} (\beta_s^2 + \beta_a^2) \, d\xi. \quad (4.146)$$

Now, we apply the same flow rule as before, now generalized to combined loading, i.e.

$$\frac{\partial \Delta}{\partial \dot{\beta}} = -\frac{\delta_{\varepsilon, \gamma} \Psi}{\delta \dot{\beta}} \quad \text{with } \Delta = \tau_{\text{crit}}(\xi) |\dot{\beta}|. \quad (4.147)$$

Varying the energy functional (4.43) with respect to β , we obtain the flow condition in the lower layer

$$\begin{aligned} & \left| (1 - \bar{\kappa}) \beta \sin^2 2\varphi + \sin 2\varphi (\varepsilon - \bar{\kappa} \langle \beta \sin 2\varphi \rangle) - \cos 2\varphi (\gamma - \langle \beta \cos 2\varphi \rangle) \right. \\ & \quad \left. - k^2 \beta'' \sin^2 \varphi \right| = \tau_{\text{crit}} / \mu. \end{aligned} \quad (4.148)$$

Initially, β is zero and hence we obtain the critical condition for the onset of plastic flow for $0 < \varphi < 45^\circ$,

$$\varepsilon \sin 2\varphi + \gamma \cos 2\varphi = \tau_{\text{crit}} / \mu. \quad (4.149)$$

Now, let us decompose the critical resolved shear stress into $\tau_{\text{crit}} = \tau_\varepsilon + \tau_\gamma$ with

$$\tau_\varepsilon = \frac{\tau_{\text{crit}}}{1 + \cot 2\varphi \cot \theta}, \quad \tau_\gamma = \frac{\tau_{\text{crit}}}{1 + \tan 2\varphi \tan \theta}. \quad (4.150)$$

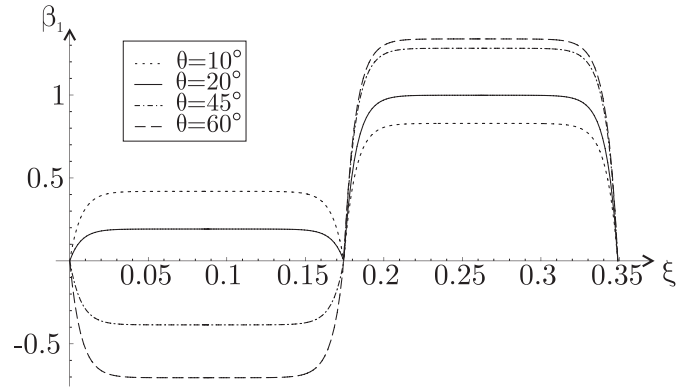


Figure 4.25: Graphs of $\beta_1(\xi)$ for combined loading of a bicrystal at non-zero dissipation, for $\varphi = 30^\circ$

As a consequence, we can decompose our flow condition into separate conditions involving β_s and β_a . We employ the above definitions and again make use of the deviation of both ε and γ from the critical values,

$$\varepsilon_r = \varepsilon - \varepsilon_{cr}, \quad \gamma_r = \gamma - \gamma_{cr}, \quad \text{with} \quad \varepsilon_{cr} = \tau_\varepsilon / \mu \sin 2\varphi, \quad \gamma_{cr} = \tau_\gamma / \mu \cos 2\varphi, \quad (4.151)$$

so that we finally arrive at the differential equations during positive loading (valid in the lower layer only, to allow for a comparison with previous results)

$$(1 - \bar{\kappa})\beta_a \sin^2 2\varphi + \sin 2\varphi(\varepsilon_r - \bar{\kappa}\langle\beta_a \sin 2\varphi\rangle) - k\beta_a'' \sin^2 \varphi = 0, \quad (4.152)$$

$$(1 - \bar{\kappa})\beta_s \sin^2 2\varphi - \cos 2\varphi(\gamma_r - \langle\beta_s \cos 2\varphi\rangle) - k\beta_s'' \sin^2 \varphi = 0. \quad (4.153)$$

Like in previous Sections, the analogous conditions for the upper layer are identical except for a changed sign in front of the second term in the first equation due to the definition of $\varphi = -\varphi_l = \varphi_u$. We will limit our analysis to investigating only the lower layer because the solution in the upper layer is obtained automatically via antisymmetry.

A comparison with the corresponding conditions obtained for uniaxial extension (4.128) and for constrained shear (4.86) reveals that $\beta_s = \beta_{\text{shear}}$ and $\beta_a = \beta_{\text{extension}}$ with $\tau_{\text{crit}} = \tau_\gamma$ or $\tau_{\text{crit}} = \tau_\varepsilon$, respectively. Therefore, the general solution for the combined deformation at non-zero dissipation can be obtained from a linear superposition of the solutions for the two particular cases treated before. Note that the solution for each of the two deformation cases was linear with respect to the applied load so that we obtain the general solution in the form

$$\beta(\xi) = \varepsilon_r \beta_{a,1}(\xi) + \gamma_r \beta_{s,1}(\xi) = \delta_r [\beta_{a,1}(\xi) \sin \theta + \beta_{s,1}(\xi) \cos \theta], \quad (4.154)$$

with $\delta_r = \delta - \delta_{cr}$ and $\beta_{a,1} = \beta_1$ from (4.129) and $\beta_{s,1} = \beta_1$ from (4.89). Exemplary graphs of β_1 are illustrated in Figure 4.25 for different angles θ (computed with material properties from Table 4.1 and $H = hb\rho_s = 0.349$) for $\varphi = 30^\circ$. Dislocation density, stress-strain curves etc. can be obtained analogously via superposition.

For a combined loading case the stress-strain curve should be replaced by a plot of the principal stresses as there are normal and shear stresses present in the bicrystal. For these examples we can plot all three average principal stresses σ_1 , σ_2 and σ_3 and the angle of the principal stresses in the x - y -plane, which be denoted by $\hat{\varphi}$. Figures 4.26 and 4.27 illustrate

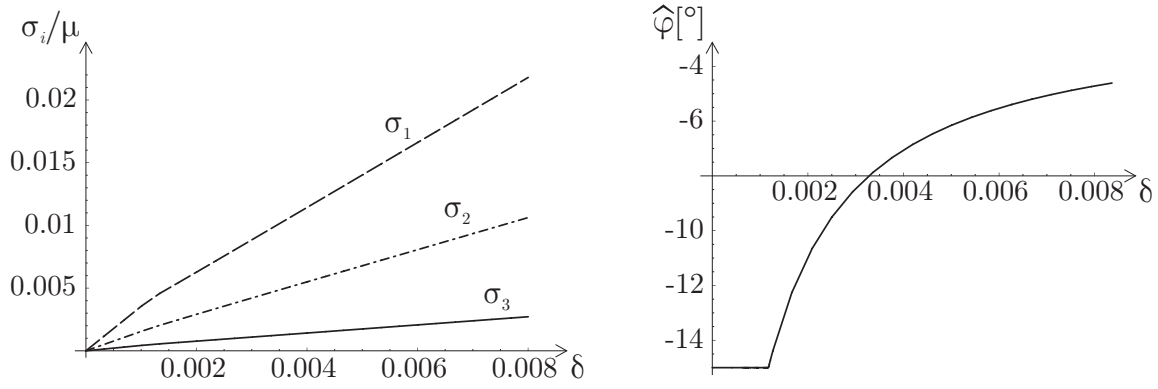


Figure 4.26: Principal stresses and angle of the in-plane principal stresses for $\varphi = 10^\circ$ and $\theta = 60^\circ$ with material parameters as before.

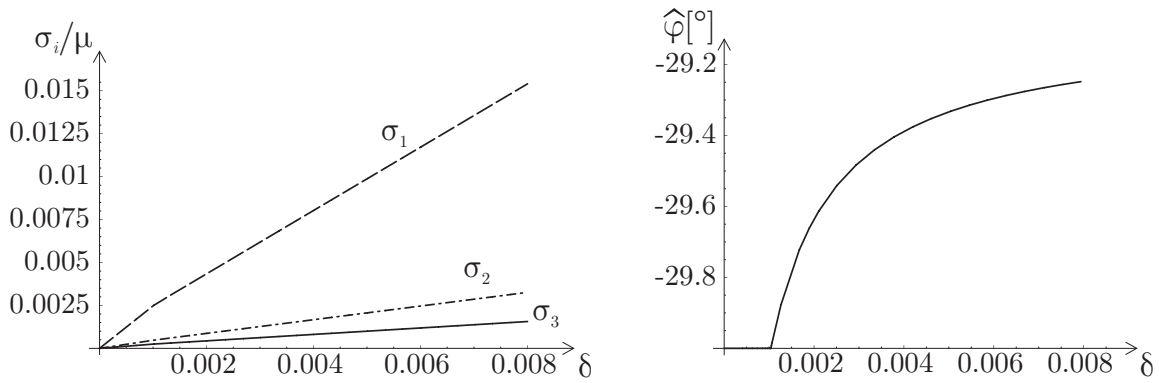


Figure 4.27: Principal stresses and angle of the in-plane principal stresses for $\varphi = 30^\circ$ and $\theta = 30^\circ$ with material parameters as before.

two examples with different slip system orientations and loading directions. Graphics present the principal stresses (note the change from elastic to plastic deformation at δ_{cr}) and the changing in-plane principal stress angle versus the overall applied deformation δ .

To complete this Section, Figure 4.28 gives an overview of the evolution of both the plastic distortion β and the dimensionless dislocation density α for increasing strain δ_r (shear and extension with $\theta = 60^\circ$) at non-zero dissipation with symmetric slip system orientations ($\varphi_u = -\varphi_l = \varphi = 30^\circ$).

4.6.2 Combined Shear and Extension at Zero Dissipation

In Section 4.4.3 we discussed a numerical routine to compute the evolution of the plastic distortion and the dislocation density at zero and non-zero dissipation for arbitrary non-symmetric active slip systems, first for the case of plane-constrained shear and later, in Section 4.5.3, for plane uniaxial extension. We can easily modify the numerical procedure outlined above to cases of general loading.

Analyzing the combined deformation of the bicrystal at zero dissipation, we notice that a decomposition of β into symmetric and antisymmetric part is feasible but does not provide a neat closed-form analytical solution in terms of superposed solutions of the single deforma-

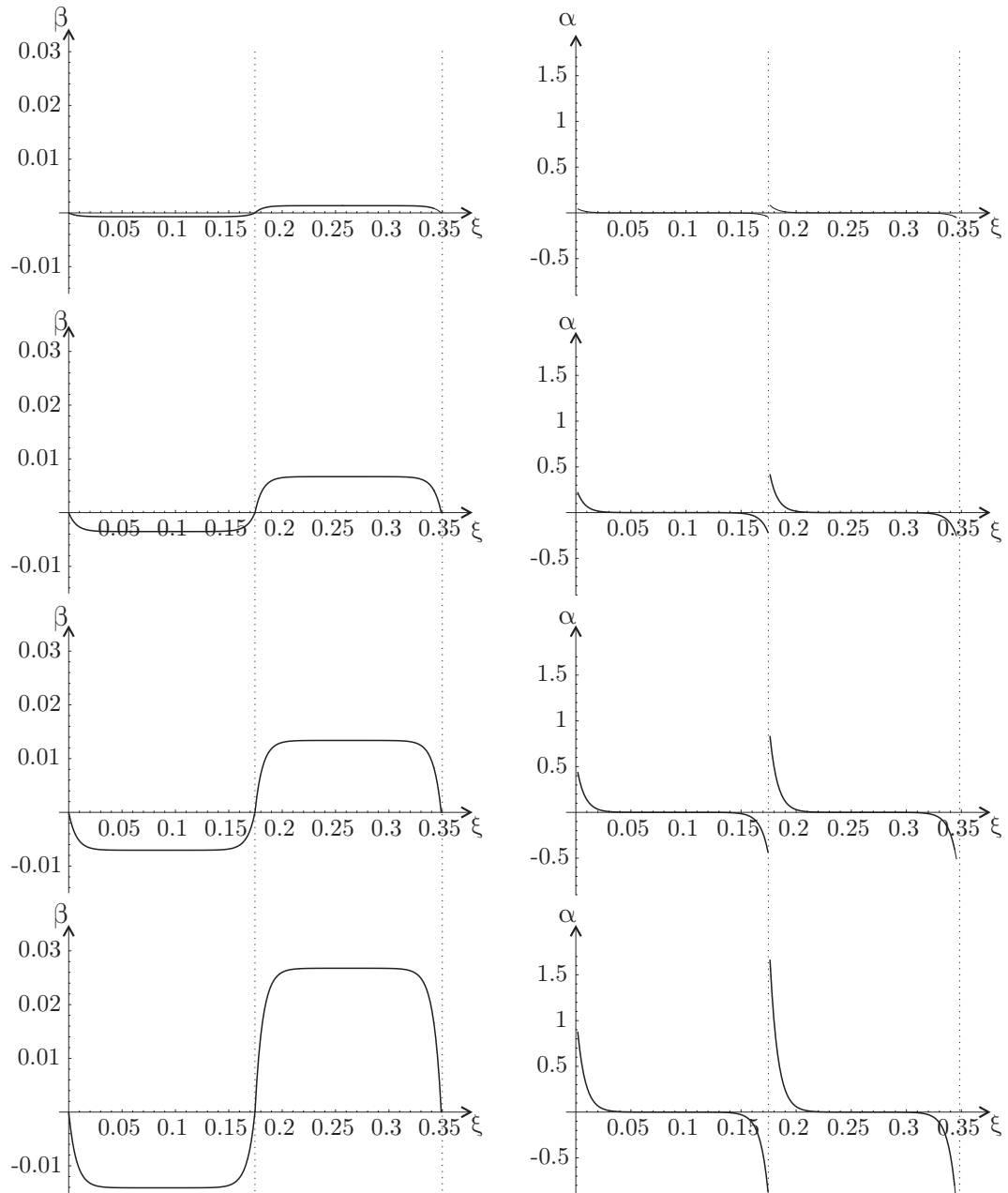


Figure 4.28: Evolution of the plastic distortion $\beta(\xi)$ and the dimensionless dislocation density $\alpha(\xi)$ for plane-constrained shear of a bicrystal at non-zero dissipation, for $\gamma_r = 0.001, 0.005, 0.01, 0.02$.

tion states as before. However, we can easily obtain a numerical solution. The total energy now reads

$$E = \frac{\varepsilon^2 H}{2\bar{\kappa}} + \frac{\gamma^2 H}{2} - \gamma H \langle \beta \cos 2\varphi \rangle - \varepsilon H \langle \beta \sin 2\varphi \rangle + \frac{H}{2} \langle \beta \cos 2\varphi \rangle^2 + \frac{H}{2} \bar{\kappa} \langle \beta \sin 2\varphi \rangle^2 + \frac{H}{2} (1 - \bar{\kappa}) \langle \beta^2 \sin^2 2\varphi \rangle + kR_1 + kR_2, \quad (4.155)$$

with the same average values and abbreviations presented in Section 4.4.3. Minimizing the energy functional numerically, we obtain the sought solution for combined loading at zero dissipation.

Figure 4.29 exemplarily compares the plastic distortion β at fixed load $\delta = 0.05$ and $\varphi = 30^\circ$ for different angles θ , with material properties from Table 4.1 and $H = hb\rho_s = 0.349$. The evolution of the dislocation density as well as the stress-strain curve can be obtained analogously for arbitrary loading and arbitrary slip system orientations.

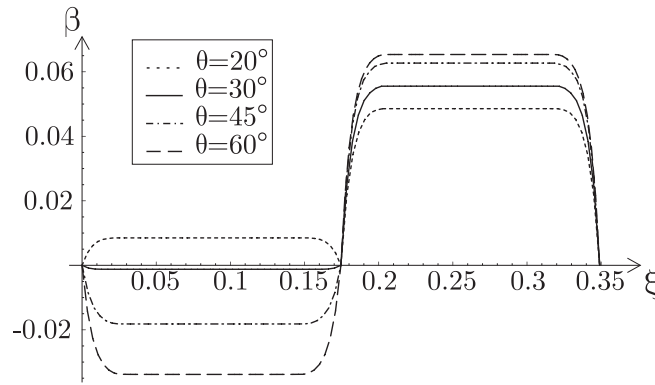


Figure 4.29: Plastic distortion β at zero dissipation and at fixed strain $\delta = 0.05$ for $\varphi = 30^\circ$ for a bicrystal under combined loading

4.7 Size Effects of the Bicrystal Problem

Many of the results in previous Sections exhibit a size effect typical of problems of crystal plasticity. In particular, the energetic threshold for the onset of plastic flow depends inversely proportional on the crystal height, see e.g. (4.51) and (4.55) for pure shear and uniaxial extension. This type of size effect does not correspond to the Hall-Petch relation but matches well the deviating law observed for small specimen sizes. Furthermore, all results indicate a dependence of the hardening rate on the crystal height both at zero and non-zero dissipation. Both effects become apparent in Figure 4.30 where the stress-strain curve (for constant $\varphi = 30^\circ$ and all other parameters as before) is plotted for different heights h of the bicrystal. With decreasing crystal size the yield stress increases as well as the hardening rate.

This macroscopic observation corresponds, of course, to a microscopic effect: With decreasing crystal height the mean free length for dislocation pile-ups also decreases, which results in higher dislocation densities at the boundaries. Due to the chosen form of the dislocation energy and its saturation effect, the local dislocation concentration is bounded so that dislocation pile-ups are forced to extend more and more into the crystal interior with decreasing crystal height, which considerably effects – among others – the inner back-stresses of

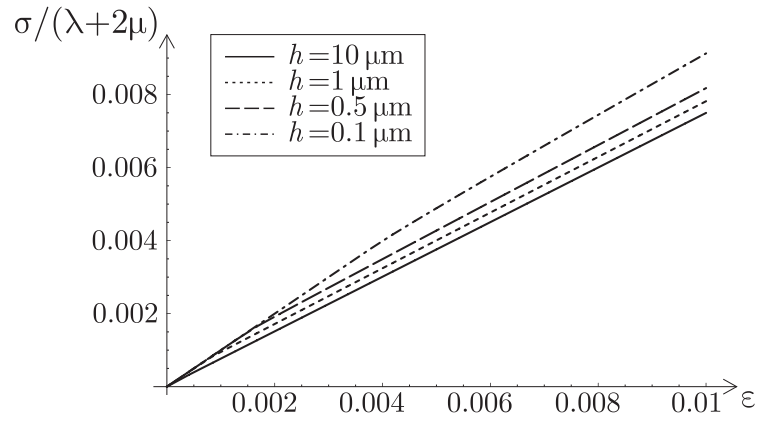


Figure 4.30: Normalized average tensile stress versus strain curve for the uniaxial extension test of a bicrystal at zero dissipation with changing crystal height

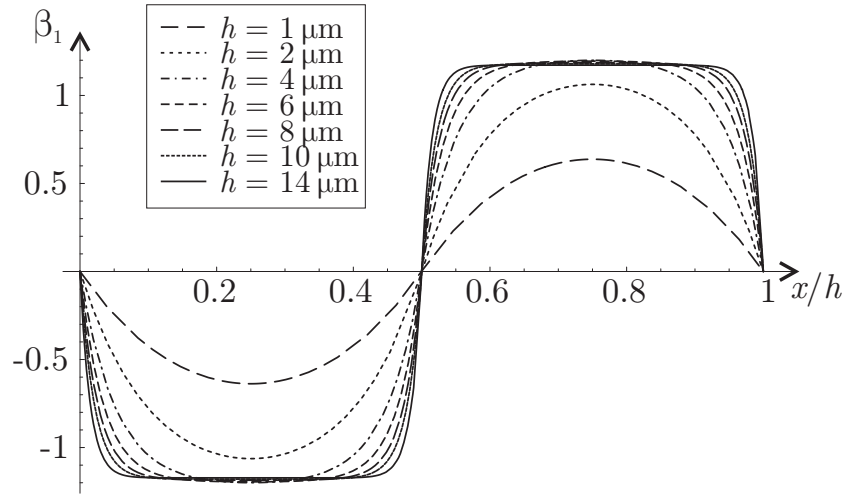


Figure 4.31: Normalized plastic distortion β_1 in a bicrystal with decreasing crystal height h (the abscissa is normalized with respect to h) for plane-strain uniaxial extension at non-zero dissipation with $\varphi = 30^\circ$ and the common material parameters.

dislocations. Figure 4.31 illustrates the normalized plastic distortion of a bicrystal in a tension test with decreasing crystal height (normalized to its height), and the aforementioned effect becomes obvious.

4.8 Variational Formulation

4.8.1 Finite Element Formulation at Zero Dissipation

We will now derive a variational formulation for a general 2D boundary value problem, which can be solved numerically by the finite element method. To this end, we discretize the material body under consideration and derive a set of equations to be solved numerically. We follow notations introduced in Section 2.3.5 and in (Cook et al., 2002). In this Section we limit our analysis to plane-strain deformations only. The extension of the present formulation to three-dimensional problems is a rather technical issue and can easily be obtained by some modifications to the model presented here. In a state of plane strain we only consider deformation in the x - y -plane. The total energy of a homogeneous, isotropic, linear elasto-plastic body is given by the sum of the elastic strain energy and the energy of the microstructure, i.e. here of the dislocation network,

$$\Psi(\boldsymbol{\varepsilon}, \boldsymbol{\beta}) = \frac{1}{2}(\boldsymbol{\varepsilon} - \boldsymbol{\varepsilon}_p)^T : \mathcal{C} : (\boldsymbol{\varepsilon} - \boldsymbol{\varepsilon}_p) + \Psi_\rho(\boldsymbol{\beta}). \quad (4.156)$$

For numerical computations it is easier to introduce vectors for the elastic and plastic strain (Cook et al., 2002). We therefore formulate the total energy as

$$\tilde{\Psi}(\tilde{\boldsymbol{\varepsilon}}, \boldsymbol{\beta}) = \frac{1}{2}(\tilde{\boldsymbol{\varepsilon}} - \tilde{\boldsymbol{\varepsilon}}_p)^T \cdot \mathbf{E} \cdot (\tilde{\boldsymbol{\varepsilon}} - \tilde{\boldsymbol{\varepsilon}}_p) + \Psi_\rho(\boldsymbol{\beta}) \quad (4.157)$$

where, due to the assumption of plane strain, we can reduce the components of the elastic and plastic strain vectors in Voigt notation to

$$\tilde{\boldsymbol{\varepsilon}} = (\varepsilon_{xx}, \varepsilon_{yy}, \gamma_{xy})^T, \quad \tilde{\boldsymbol{\varepsilon}}_p = (\varepsilon_{xx,p}, \varepsilon_{yy,p}, \gamma_{xy,p})^T. \quad (4.158)$$

Analogously, the stress tensor is written as a stress vector in Voigt notation as

$$\tilde{\boldsymbol{\sigma}} = (\sigma_{xx}, \sigma_{yy}, \sigma_{xy})^T. \quad (4.159)$$

For isotropic plane strain the elasticity tensor in the above formulation reads

$$\mathbf{E} = \frac{E}{(1+\nu)(1-2\nu)} \begin{pmatrix} 1-\nu & \nu & 0 \\ \nu & 1-\nu & 0 \\ 0 & 0 & \frac{1}{2}(1-2\nu) \end{pmatrix}, \quad (4.160)$$

where E denotes Young's modulus and ν Poisson's ratio. The stress component σ_{zz} can easily be obtained from the resultant stress vector $\tilde{\boldsymbol{\sigma}}$ via the equation (obtained from requiring that $\varepsilon_{zz} = 0$)

$$\sigma_{zz} = \nu(\sigma_{xx} + \sigma_{yy}). \quad (4.161)$$

Furthermore, the in-plane components of the displacement field at a given point can be arranged in a vector of the form

$$\mathbf{u} = (u, v)^T. \quad (4.162)$$

The energy of the dislocation network is assumed to be of the type

$$\Psi_\rho(\rho) = k\mu \ln \frac{1}{1 - \rho/\rho_s}, \quad (4.163)$$

with k being a material constant and ρ_s denoting the saturated dislocation density which results from the discrete nature of the atomic lattice. Plastic slip is assumed to occur only along one given slip system (infinite latent hardening) characterized by the slip direction $\mathbf{s} = (\cos \varphi, \sin \varphi, 0)^T$ and the slip plane unit normal $\mathbf{m} = (-\sin \varphi, \cos \varphi, 0)^T$ so that

$$\boldsymbol{\beta} = \beta \mathbf{s} \otimes \mathbf{m} = \beta \begin{pmatrix} -\sin \varphi \cos \varphi & \cos^2 \varphi \\ -\sin^2 \varphi & \sin \varphi \cos \varphi \end{pmatrix} \quad (4.164)$$

and

$$\boldsymbol{\varepsilon}_p = \text{sym } \boldsymbol{\beta} = \frac{1}{2} \beta \begin{pmatrix} -\sin 2\varphi & \cos 2\varphi \\ \cos 2\varphi & \sin 2\varphi \end{pmatrix}. \quad (4.165)$$

Comparison with the above Voigt notation of the elastic strain vector $\tilde{\boldsymbol{\varepsilon}}$ leads to

$$\tilde{\boldsymbol{\varepsilon}}_p = \begin{pmatrix} \varepsilon_{p,xx} \\ \varepsilon_{p,xy} \\ \gamma_{p,xy} \end{pmatrix} = \frac{1}{2} \beta \begin{pmatrix} -\sin 2\varphi \\ \sin 2\varphi \\ 2 \cos 2\varphi \end{pmatrix}. \quad (4.166)$$

Now, let us compute the scalar dislocation density which is obtained from Nye's dislocation density tensor

$$\boldsymbol{\alpha} = \text{curl } \boldsymbol{\beta} \quad (4.167)$$

with the only non-zero components

$$\alpha_{xz} = \beta_{,y} \sin \varphi \cos \varphi + \beta_{,x} \cos^2 \varphi, \quad (4.168)$$

$$\alpha_{yz} = \beta_{,y} \sin^2 \varphi + \beta_{,x} \sin \varphi \cos \varphi. \quad (4.169)$$

The scalar dislocation density hence yields

$$\rho = \frac{1}{b} \sqrt{\alpha_{xz}^2 + \alpha_{yz}^2} = \frac{1}{b} |\beta_{,x} \cos \varphi + \beta_{,y} \sin \varphi|, \quad (4.170)$$

where b is Burgers' vector. If translational invariance may be assumed, i.e. $\beta = \beta(y)$, the dislocation density reduces to (4.34).

Consider the boundary conditions

$$\boldsymbol{\sigma} \cdot \mathbf{n} = \mathbf{f}_t \quad \text{on } \Gamma_t, \quad (4.171)$$

$$\mathbf{u} = \mathbf{u}_0 \quad \text{on } \Gamma_u. \quad (4.172)$$

Following Section 2.3.5, we transform the given boundary value problem into a minimization problem by first calculating the total energy potential whose minimum can then be obtained from variational calculus (for the related energy principles, see Section 2.5.1):

$$\mathcal{I} = \int_{\Omega} \left[\frac{1}{2} (\tilde{\boldsymbol{\varepsilon}} - \tilde{\boldsymbol{\varepsilon}}_p)^T \cdot \mathbf{E} \cdot (\tilde{\boldsymbol{\varepsilon}} - \tilde{\boldsymbol{\varepsilon}}_p) + \Psi_{\rho}(\beta) \right] dv - \int_{\Gamma_t} \mathbf{u} \cdot \mathbf{f}_t ds - \int_{\Gamma_u} \mathbf{t} \cdot (\mathbf{u} - \mathbf{u}_0) ds. \quad (4.173)$$

Note that for plane problems \mathcal{I} represents the energy per thickness. In order to numerically treat this variational problem, let us discretize the body Ω and the unknown continuously distributed quantities \mathbf{u} and β . The body Ω is subdivided into a finite number n_e of bilinear quadrilateral elements of volume Ω^e ($e = 1 \dots n_e$), which allows for a transition from the

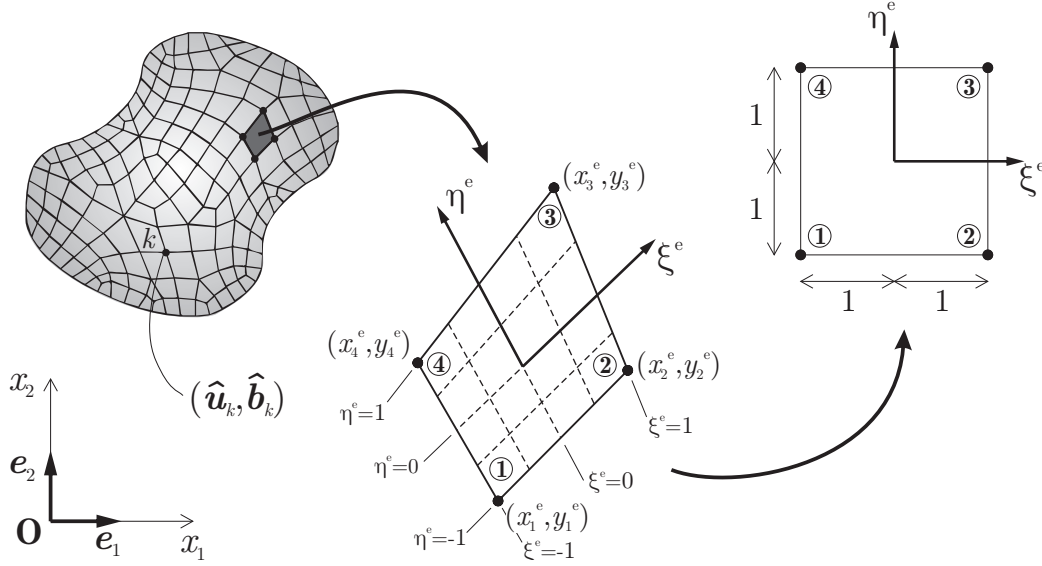


Figure 4.32: Discretization of the material body Ω into bilinear isoparametric elements. The vector and scalar quantities $\hat{\mathbf{u}}_k$ and $\hat{\mathbf{b}}_k$ are defined at each node k . The magnifications show exemplarily one element in the physical space and then mapped into the ξ - η -space with the definition of the node numbering order.

continuously distributed vector field \mathbf{u} and the scalar field β to a discrete set of nodal variables $\hat{\mathbf{u}}_k$ and $\hat{\beta}_k$ at each node k . Each element Ω^e is mapped from the physical space in the x - y -plane onto an auxiliary or reference coordinate system in the ξ - η -plane where each element has the shape of a square. Shape functions are introduced to interpolate both the displacement field \mathbf{u} , the plastic distortion β and the element geometry throughout the element while values of these quantities are only stored and updated at nodes. For each element we hence have a local displacement vector with displacements $\hat{\mathbf{u}}_i^e$ at node i and a local vector for the plastic distortion $\hat{\beta}_i^e$ at node i , so

$$\hat{\mathbf{u}}^e = (\hat{u}_1^e, \hat{v}_1^e, \hat{u}_2^e, \hat{v}_2^e, \hat{u}_3^e, \hat{v}_3^e, \hat{u}_4^e, \hat{v}_4^e), \quad (4.174)$$

$$\hat{\mathbf{b}}^e = (\hat{\beta}_1^e, \hat{\beta}_2^e, \hat{\beta}_3^e, \hat{\beta}_4^e). \quad (4.175)$$

We interpolate the displacement field \mathbf{u}^e and the scalar plastic distortion field β^e across the entire element Ω_e from their nodal values $\hat{\mathbf{u}}^e$ and $\hat{\mathbf{b}}^e$, respectively. Therefore, we have the interpolation rules

$$\mathbf{u}^e = \sum_{i=1}^4 N_i^e \hat{\mathbf{u}}_i^e = \mathbf{N}^e \cdot \hat{\mathbf{u}}^e, \quad \beta^e = \sum_{i=1}^4 \tilde{N}_i^e \hat{\beta}_i^e = \tilde{\mathbf{N}}^e \cdot \hat{\mathbf{b}}^e, \quad (4.176)$$

which must ensure that $\mathbf{u}^e = (\hat{u}_i^e, \hat{v}_i^e)$ and $\beta^e = \hat{\beta}_i^e$ at each node i . The choice of shape functions \mathbf{N}^e and $\tilde{\mathbf{N}}^e$ determines the order of interpolation of the node data across the element; they do not necessarily have to be of the same type. Here and in the following, we linearly interpolate both \mathbf{u}^e and β^e , using the shape functions

$$\mathbf{N}^e = \begin{pmatrix} N_1^e & 0 & N_2^e & 0 & N_3^e & 0 & N_4^e & 0 \\ 0 & N_1^e & 0 & N_2^e & 0 & N_3^e & 0 & N_4^e \end{pmatrix} \quad (4.177)$$

and

$$\tilde{\mathbf{N}}^e = (N_1^e, N_2^e, N_3^e, N_4^e)^T \quad (4.178)$$

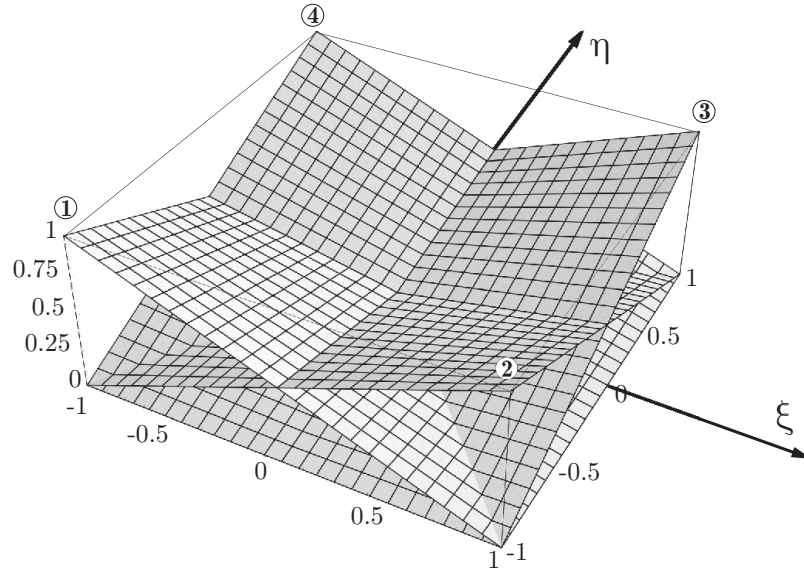


Figure 4.33: Shape functions N_i^e in one element e , where N_i^e equals 1 at node i and 0 at all other nodes.

with

$$N_1^e = \frac{1}{4}(1 - \xi)(1 - \eta), \quad N_2^e = \frac{1}{4}(1 + \xi)(1 - \eta), \quad (4.179)$$

$$N_3^e = \frac{1}{4}(1 + \xi)(1 + \eta), \quad N_4^e = \frac{1}{4}(1 - \xi)(1 + \eta), \quad (4.180)$$

for plane isoparametric, bilinear (quadrilateral) elements. These shape functions are designed such that (4.176) is fulfilled automatically. Shape function N_i^e equals 1 at node i and 0 at all three other nodes (see Figure 4.33).

As we map the current configuration of the bilinear element isoparametrically from the physical space onto the square element, there is a difference between the actual position of points of the element in the physical space (x_i^e, y_i^e) and of those in the mapped square element. Due to this mapping and the functional dependence $x = x(\xi, \eta)$ and $y = y(\xi, \eta)$ spatial derivatives also require a transformation, governed by the Jacobian matrix \mathbf{J}^e defined for element e by

$$\mathbf{J}^e = \begin{pmatrix} x_{,\xi}^e & y_{,\xi}^e \\ x_{,\eta}^e & y_{,\eta}^e \end{pmatrix} = \frac{1}{4} \begin{pmatrix} -(1 - \eta) & (1 - \eta) & (1 + \eta) & -(1 + \eta) \\ -(1 - \xi) & -(1 + \xi) & (1 + \xi) & (1 - \xi) \end{pmatrix} \cdot \begin{pmatrix} x_1^e & y_1^e \\ x_2^e & y_2^e \\ x_3^e & y_3^e \\ x_4^e & y_4^e \end{pmatrix}, \quad (4.181)$$

where (x_i^e, y_i^e) are the coordinates of the four nodes of the quadrilateral element in the physical space, listed in the common order (beginning with the left bottom node and proceeding counterclockwise). We denote the determinant of the Jacobian by $J^e = \det \mathbf{J}^e$ and its inverse by $\mathbf{\Gamma}^e = (\mathbf{J}^e)^{-1}$.

With all of the above definitions we can write the elastic strain vector in an element e in its discrete version as

$$\tilde{\boldsymbol{\varepsilon}}^e = \mathbf{B}^e \cdot \hat{\mathbf{u}}^e \quad (4.182)$$

with

$$\mathbf{B}^e = \boldsymbol{\partial} \mathbf{N} = \begin{pmatrix} 1 & 0 & 0 & 0 \\ 0 & 0 & 0 & 1 \\ 0 & 1 & 1 & 0 \end{pmatrix} \cdot \begin{pmatrix} \Gamma_{11}^e & \Gamma_{12}^e & 0 & 0 \\ \Gamma_{21}^e & \Gamma_{22}^e & 0 & 0 \\ 0 & 0 & \Gamma_{11}^e & \Gamma_{12}^e \\ 0 & 0 & \Gamma_{21}^e & \Gamma_{22}^e \end{pmatrix} \cdot \begin{pmatrix} N_{1,\xi}^e & 0 & N_{2,\xi}^e & 0 & N_{3,\xi}^e & 0 & N_{4,\xi}^e & 0 \\ N_{1,\eta}^e & 0 & N_{2,\eta}^e & 0 & N_{3,\eta}^e & 0 & N_{4,\eta}^e & 0 \\ 0 & N_{1,\xi}^e & 0 & N_{2,\xi}^e & 0 & N_{3,\xi}^e & 0 & N_{4,\xi}^e \\ 0 & N_{1,\eta}^e & 0 & N_{2,\eta}^e & 0 & N_{3,\eta}^e & 0 & N_{4,\eta}^e \end{pmatrix}. \quad (4.183)$$

Accordingly, we can discretize the plastic strain $\tilde{\boldsymbol{\varepsilon}}_p^e$ within element e by introducing

$$\tilde{\boldsymbol{\varepsilon}}_p^e = \frac{1}{2} \begin{pmatrix} -\sin 2\varphi \\ \sin 2\varphi \\ 2 \cos 2\varphi \end{pmatrix} (\tilde{\mathbf{N}}^e \cdot \hat{\mathbf{b}}^e) = \left[\frac{1}{2} \begin{pmatrix} -\sin 2\varphi \\ \sin 2\varphi \\ 2 \cos 2\varphi \end{pmatrix} \otimes \tilde{\mathbf{N}}^e \right] \cdot \hat{\mathbf{b}}^e = \mathbf{Q}^e \cdot \hat{\mathbf{b}}^e \quad (4.184)$$

with

$$\mathbf{Q}^e = \frac{1}{2} \begin{pmatrix} -N_1^e \sin 2\varphi & -N_2^e \sin 2\varphi & -N_3^e \sin 2\varphi & -N_4^e \sin 2\varphi \\ N_1^e \sin 2\varphi & N_2^e \sin 2\varphi & N_3^e \sin 2\varphi & N_4^e \sin 2\varphi \\ 2N_1^e \cos 2\varphi & 2N_2^e \cos 2\varphi & 2N_3^e \cos 2\varphi & 2N_4^e \cos 2\varphi \end{pmatrix}. \quad (4.185)$$

Having discretized all field variables, we can write for the total energy of a single element e

$$\begin{aligned} \Pi^e(\hat{\mathbf{u}}^e, \hat{\mathbf{b}}^e) = \int_{\Omega^e} \left[\frac{1}{2} (\hat{\mathbf{u}}^{e,T} \mathbf{B}^{e,T} - \hat{\mathbf{b}}^{e,T} \mathbf{Q}^{e,T}) \mathbf{E}^e (\mathbf{B}^e \hat{\mathbf{u}}^e - \mathbf{Q}^e \hat{\mathbf{b}}^e) + \Psi_\rho(\hat{\rho}^e) \right] dv \\ - \int_{\Gamma_t^e} \hat{\mathbf{u}}^{e,T} \cdot \mathbf{N}^{e,T} \mathbf{f}_t^e ds - \int_{\Gamma_u^e} \mathbf{t} \cdot (\mathbf{N}^e \hat{\mathbf{u}}^e - \mathbf{u}_0) ds. \end{aligned} \quad (4.186)$$

To deal with the energy of the dislocation network Ψ_ρ , we write the scalar dislocation density within an element e in terms of the discretization defined above, i.e.

$$\hat{\rho}^e = \frac{1}{b} |\beta_{,x}^e \cos \varphi + \beta_{,y}^e \sin \varphi| = \frac{1}{b} |(\cos \varphi \tilde{\mathbf{N}}_{,x} + \sin \varphi \tilde{\mathbf{N}}_{,y}) \cdot \hat{\mathbf{b}}^e| = \frac{1}{b} |\mathbf{N}^{e*} \cdot \hat{\mathbf{b}}^e|, \quad (4.187)$$

with \mathbf{N}^{e*} resulting as

$$\mathbf{N}^{e*} = \begin{pmatrix} \cos \varphi \\ \sin \varphi \end{pmatrix} \cdot \boldsymbol{\Gamma}^e \cdot \begin{pmatrix} N_{1,\xi}^e & N_{2,\xi}^e & N_{3,\xi}^e & N_{4,\xi}^e \\ N_{1,\eta}^e & N_{2,\eta}^e & N_{3,\eta}^e & N_{4,\eta}^e \end{pmatrix}. \quad (4.188)$$

In special cases we may want to reduce complexity by employing specific elements only. In particular, it might be helpful to employ rectangular elements only because then $x = x(\xi)$ and $y = y(\eta)$ and as a consequence \mathbf{J} and $\boldsymbol{\Gamma}$ are diagonal. In this case, we obtain the simple form

$$\mathbf{N}^{e*} = \frac{\cos \varphi}{J_{11}^e} \begin{pmatrix} N_{1,\xi}^e \\ N_{2,\xi}^e \\ N_{3,\xi}^e \\ N_{4,\xi}^e \end{pmatrix} + \frac{\sin \varphi}{J_{22}^e} \begin{pmatrix} N_{1,\eta}^e \\ N_{2,\eta}^e \\ N_{3,\eta}^e \\ N_{4,\eta}^e \end{pmatrix}. \quad (4.189)$$

In order to formulate the boundary value problem for the entire body, which comprises n_e elements and n_n nodes, we need to deal with the global node variables \hat{u}_k , \hat{v}_k and $\hat{\beta}_k$

(at nodes $k = 1 \dots n_n$) instead of the local node variables \hat{u}^e , \hat{v}^e and $\hat{\beta}^e$ (defined in every element $e = 1 \dots n_e$). Let us introduce the global vectors of all nodal values

$$\hat{\mathbf{u}} = (\hat{u}_1, \hat{v}_1, \dots, \hat{u}_k, \hat{v}_k)^T, \quad (4.190)$$

$$\hat{\mathbf{b}} = (\hat{\beta}_1, \dots, \hat{\beta}_k)^T. \quad (4.191)$$

These global vectors $\hat{\mathbf{u}}$ and $\hat{\mathbf{b}}$ are obtained from the local vectors $\hat{\mathbf{u}}^e$ and $\hat{\mathbf{b}}^e$ via an assembly operator $\mathcal{A}_{e=1}^{n_e}$ (Hughes, 1987):

$$\hat{\mathbf{u}} = \mathcal{A}_{e=1}^{n_e}(\hat{\mathbf{u}}^e), \quad \hat{\mathbf{b}} = \mathcal{A}_{e=1}^{n_e}(\hat{\mathbf{b}}^e). \quad (4.192)$$

The total energy of a body Ω can be written as the sum of the energies of each element Ω^e , i.e.

$$\hat{\mathcal{I}}(\hat{\mathbf{u}}, \hat{\mathbf{b}}) = \Pi(\hat{\mathbf{u}}, \hat{\mathbf{b}}) = \sum_{e=1}^{n_e} \Pi^e(\hat{\mathbf{u}}^e, \hat{\mathbf{b}}^e). \quad (4.193)$$

As a consequence, the discretized total energy follows as

$$\begin{aligned} \hat{\mathcal{I}}(\hat{\mathbf{u}}, \hat{\mathbf{b}}) = \int_{\Omega} \left[\frac{1}{2} (\hat{\mathbf{u}}^T \mathbf{B}^T - \hat{\mathbf{b}}^T \mathbf{Q}^T) \mathbf{E} (\mathbf{B} \hat{\mathbf{u}} - \mathbf{Q} \hat{\mathbf{b}}) + \Psi_{\rho}(\hat{\mathbf{b}}) \right] dv \\ - \int_{\Gamma_t} \hat{\mathbf{u}}^T \cdot \mathbf{N}^T \mathbf{f}_t ds - \int_{\Gamma_u} \mathbf{t} \cdot (\mathbf{N} \hat{\mathbf{u}} - \mathbf{u}_0) ds, \end{aligned} \quad (4.194)$$

where the global matrices \mathbf{E} , \mathbf{B} and \mathbf{Q} are obtained from the local matrices \mathbf{E}^e , \mathbf{B}^e and \mathbf{Q}^e via the same assembly operator $\mathcal{A}_{e=1}^{n_e}$:

$$\mathbf{E} = \mathcal{A}_{e=1}^{n_e}(\mathbf{E}^e), \quad \mathbf{B} = \mathcal{A}_{e=1}^{n_e}(\mathbf{B}^e), \quad \mathbf{Q} = \mathcal{A}_{e=1}^{n_e}(\mathbf{Q}^e). \quad (4.195)$$

The minimum of the energy potential is attained when $\delta \hat{\mathcal{I}}(\hat{\mathbf{u}}, \hat{\mathbf{b}}) = 0$, where the first variation of the above energy potential yields

$$\begin{aligned} \int_{\Omega} \left[\delta \hat{\mathbf{u}}^T \mathbf{B}^T \mathbf{E} (\mathbf{B} \hat{\mathbf{u}} - \mathbf{Q} \hat{\mathbf{b}}) - \delta \hat{\mathbf{b}}^T \mathbf{Q}^T \mathbf{E} (\mathbf{B} \hat{\mathbf{u}} - \mathbf{Q} \hat{\mathbf{b}}) + \delta \hat{\mathbf{b}}^T \cdot \frac{\partial \Psi_{\rho}}{\partial \hat{\mathbf{b}}} \right] dv \\ - \int_{\Gamma_t} \delta \hat{\mathbf{u}}^T \cdot \mathbf{N}^T \mathbf{f}_t ds - \int_{\Gamma_u} \delta \mathbf{t} \cdot (\mathbf{N} \hat{\mathbf{u}} - \mathbf{u}_0) ds = 0, \end{aligned} \quad (4.196)$$

from which we obtain the equilibrium condition

$$\int_{\Omega} \mathbf{B}^T \mathbf{E} (\mathbf{B} \hat{\mathbf{u}} - \mathbf{Q} \hat{\mathbf{b}}) dv - \int_{\Gamma_t} \mathbf{N}^T \mathbf{f}_t ds = 0 \quad (4.197)$$

and the microstructural equilibrium condition

$$- \int_{\Omega} \mathbf{Q}^T \mathbf{E} (\mathbf{B} \hat{\mathbf{u}} - \mathbf{Q} \hat{\mathbf{b}}) dv + \int_{\Omega} \frac{\partial \Psi_{\rho}}{\partial \hat{\mathbf{b}}} dv = 0 \quad (4.198)$$

along with the boundary conditions

$$\mathbf{N} \cdot \widehat{\mathbf{u}} = \mathbf{u}_0 \quad \text{on } \Gamma_{\mathbf{u}}, \quad \widetilde{\mathbf{N}} \cdot \widehat{\mathbf{b}} = \beta_0 \quad \text{on } \Gamma_{\beta}. \quad (4.199)$$

For solving the problem numerically we introduce the global matrices

$$\mathbf{K}_{BB} = \int_{\Omega} \mathbf{B}^T \mathbf{E} \mathbf{B} \, dv, \quad \mathbf{K}_{BQ} = \int_{\Omega} \mathbf{B}^T \mathbf{E} \mathbf{Q} \, dv, \quad (4.200)$$

$$\mathbf{K}_{QQ} = \int_{\Omega} \mathbf{Q}^T \mathbf{E} \mathbf{Q} \, dv, \quad (4.201)$$

and the vector of internal microstructural forces

$$\mathbf{f}_{\text{int}}(\widehat{\mathbf{b}}) = \int_{\Omega} \frac{\partial \Psi_{\rho}}{\partial \widehat{\mathbf{b}}} \, dv. \quad (4.202)$$

As all matrices \mathbf{E} , \mathbf{B} and \mathbf{Q} are obtained from an assembly of the corresponding element matrices \mathbf{E}^e , \mathbf{B}^e and \mathbf{Q}^e , the above defined global matrices \mathbf{K}_{BB} , \mathbf{K}_{BQ} and \mathbf{K}_{QQ} can be obtained in the same manner, i.e. via

$$\mathbf{K}_{BB} = \mathcal{A}_{e=1}^{n_e}(\mathbf{K}_{BB}^e), \quad \mathbf{K}_{BQ} = \mathcal{A}_{e=1}^{n_e}(\mathbf{K}_{BQ}^e), \quad (4.203)$$

$$\mathbf{K}_{QQ} = \mathcal{A}_{e=1}^{n_e}(\mathbf{K}_{QQ}^e), \quad (4.204)$$

and the element matrices are defined by

$$\begin{aligned} \mathbf{K}_{BB}^e &= \int_{-1}^1 \int_{-1}^1 \mathbf{B}^{e,T} \mathbf{E}^e \mathbf{B}^e t J^e \, d\xi \, d\eta, & \mathbf{K}_{BQ}^e &= \int_{-1}^1 \int_{-1}^1 \mathbf{B}^{e,T} \mathbf{E}^e \mathbf{Q}^e t J^e \, d\xi \, d\eta, \\ \mathbf{K}_{QQ}^e &= \int_{-1}^1 \int_{-1}^1 \mathbf{Q}^{e,T} \mathbf{E}^e \mathbf{Q}^e t J^e \, d\xi \, d\eta, \end{aligned} \quad (4.205)$$

where t is the constant thickness of the body Ω . Note that due to the choice of the finite element interpolation (linear with respect to \mathbf{u} and \mathbf{b}), matrix dimensions follow as $\mathbf{K}_{BB}^e \in \mathcal{R}^{8 \times 8}$, $\mathbf{K}_{BQ}^e \in \mathcal{R}^{4 \times 8}$ and $\mathbf{K}_{QQ}^e \in \mathcal{R}^{4 \times 4}$. As a consequence, the dimensions of the global matrices must have dimensions $2n_n \times 2n_n$ for \mathbf{K}_{BB} , $n_n \times 2n_n$ for \mathbf{K}_{BQ} , and $n_n \times n_n$ for \mathbf{K}_{QQ} .

Analogously, we can obtain the vector of external forces and the vector of internal microstructural forces via assembly, i.e.

$$\mathbf{f}_{\text{int}}(\widehat{\mathbf{b}}) = \mathcal{A}_{e=1}^{n_e} \left(\mathbf{f}_{\text{int}}^e(\widehat{\mathbf{b}}^e) \right), \quad \mathbf{f}_{\text{ext}} = \mathcal{A}_{e=1}^{n_e} (\mathbf{f}_{\text{ext}}^e), \quad (4.206)$$

where

$$\mathbf{f}_{\text{int}}^e(\widehat{\mathbf{b}}^e) = \int_{-1}^1 \int_{-1}^1 \frac{\partial \Psi_{\rho}}{\partial \widehat{\mathbf{b}}^e} t J^e \, d\xi \, d\eta. \quad (4.207)$$

The vector of external forces follows analogously as

$$\mathbf{f}_{\text{ext}}^e = \int_{\Gamma_t^e} \mathbf{N}^{e,T} \mathbf{f}_t \, ds. \quad (4.208)$$

Then, we can arrange the set of equations to be solved numerically for the unknown vector of all discrete nodal values

$$\hat{U} = (\hat{u}, \hat{b})^T \quad (4.209)$$

in the following manner:

$$\begin{pmatrix} \mathbf{K}_{BB} & -\mathbf{K}_{BQ} \\ -\mathbf{K}_{BQ}^T & \mathbf{K}_{QQ} \end{pmatrix} \cdot \begin{pmatrix} \hat{u} \\ \hat{b} \end{pmatrix} = \begin{pmatrix} \mathbf{f}_{\text{ext}} \\ -\mathbf{f}_{\text{int}}(\hat{b}) \end{pmatrix}, \quad \mathbf{N} \cdot \hat{u} = u_0 \quad \text{on } \Gamma_u, \quad (4.210)$$

In the sequel, we employ the abbreviations

$$\mathbf{K} = \begin{pmatrix} \mathbf{K}_{BB} & -\mathbf{K}_{BQ} \\ -\mathbf{K}_{BQ}^T & \mathbf{K}_{QQ} \end{pmatrix}, \quad \mathbf{f}(\hat{U}) = \begin{pmatrix} \mathbf{f}_{\text{ext}} \\ -\mathbf{f}_{\text{int}}(\hat{b}) \end{pmatrix}, \quad (4.211)$$

such that we arrive at the concise form

$$\mathbf{K} \cdot \hat{U} = \mathbf{f}(\hat{U}). \quad (4.212)$$

Within each element integration of all \mathbf{K}_{ab} -matrices can be accomplished exactly by a 2×2 point Gauß quadrature rule since all integrands are of polynomial order $\xi^2 \eta^2$ or lower, i.e.

$$\int_{-1}^1 \int_{-1}^1 \phi(\xi, \eta) d\xi d\eta = \sum_{i=1}^2 \sum_{j=1}^2 \phi(W_i, W_j) \quad (4.213)$$

with Gauß integration points located at $W_i = \pm 1/\sqrt{3}$. The same holds true for the vector of external forces. Unfortunately, the integration of the vector of internal forces $\mathbf{f}_{\text{int}}(\hat{b})$ cannot be performed as simply due to the occurrence of sign and absolute value functions rendering the integrand non-polynomial and hard to integrate. Therefore, a numerical integration scheme with a large number of Gauß points is employed to obtain a force vector as accurate as possible, i.e.

$$\mathbf{f}_{\text{int}}(\mathbf{b}) = \int_{-1}^1 \int_{-1}^1 \frac{\partial \Psi_\rho}{\partial \mathbf{b}} tJ d\xi d\eta \cong \sum_{i=1}^N \sum_{j=1}^N w_i w_j tJ \left. \frac{\partial \Psi_\rho}{\partial \mathbf{b}} \right|_{\xi=z_i, \eta=z_j}, \quad (4.214)$$

where z_i and z_j are the Gauß points (obtained from solving the appropriate Legendre equations, see e.g. Hughes (1987)) and w_i and w_j the corresponding weight factors. In subsequent computations we commonly use $N = 25$.

Having assembled all matrices and forces, we account for boundary conditions of the two types

$$(\hat{u}_k, \hat{v}_k) = \mathbf{u}_0, \quad \hat{\beta}_k = \beta_0. \quad (4.215)$$

The first condition is a pure displacement boundary condition, arising automatically from the equilibrium equations. The second condition arises from artificially fixing the plastic distortion, e.g. at grain boundaries or surfaces where an obstacle impedes penetration by dislocations. When numerically solving Eq. (4.212), we must ensure the boundary conditions (4.215), which can be achieved by replacing entries in \mathbf{K} and \mathbf{f} such that the equation for the corresponding nodal parameter \hat{u}_k or $\hat{\beta}_k$ is replaced by $\hat{u}_k = u_{k,0}$ or $\hat{\beta}_k = \beta_{k,0}$, respectively. Also, vector \mathbf{f} must be modified accordingly, see e.g. (Cook et al., 2002).

For solving Eq. (4.212) it is convenient to write the problem as

$$\mathbf{G}(\hat{\mathbf{U}}) = \mathbf{K} \cdot \hat{\mathbf{U}} - \mathbf{f}(\hat{\mathbf{U}}) \quad (4.216)$$

and employ a damped Newton-Raphson iteration scheme, which updates the current solution vector $\hat{\mathbf{U}}$ at each iteration step by

$$\hat{\mathbf{U}}_{n+1} = \hat{\mathbf{U}}_n - \alpha \mathbf{T}_n^{-1}(\hat{\mathbf{U}}_n) \cdot \mathbf{G}(\hat{\mathbf{U}}_n), \quad (4.217)$$

where

$$\mathbf{T}_n(\hat{\mathbf{U}}_n) = \left. \frac{\partial \mathbf{G}}{\partial \hat{\mathbf{U}}} \right|_{\hat{\mathbf{U}}_n} = \mathbf{K} - \left. \frac{\partial \mathbf{f}(\hat{\mathbf{U}})}{\partial \hat{\mathbf{U}}} \right|_{\hat{\mathbf{U}}_n} \quad (4.218)$$

is the tangent stiffness matrix at time step n , and α is a numerical damping parameter. This damping parameter is very important as the absolute value and sign functions in the internal force vector indeed impede a fast and unproblematic convergence. It is therefore convenient to choose a high numerical damping parameter (e.g. $\alpha = 1$) during the first few iterations and then decrease α to values below 1%. The progress of each iteration step is measured by means of the norm of the residue, i.e.

$$\Delta \hat{\mathbf{U}}_n = \| \mathbf{K} \cdot \hat{\mathbf{U}}_n - \mathbf{f}(\hat{\mathbf{U}}_n) \| . \quad (4.219)$$

The numerical procedure can be automated as to adjust the damping parameter α according to the quality of each iteration step. If the norm decreases, α can be kept constant (or even be increased); if the norm increases or hardly decreases, α should be decreased.

In order to avoid numerical problems arising from the (numerically) inconvenient sign and absolute value functions in the internal force vector \mathbf{f}_{int} , we consider the following representation of the sign function

$$\text{sign}(x) = \lim_{v \rightarrow \infty} \frac{2}{1 + e^{-vx}} - 1, \quad (4.220)$$

from which we reduce a numerical approximation of the sign function, the sigmoid function $\text{sig}_v(x)$,

$$\text{sign}(x) \cong \text{sig}_v(x) = \frac{2}{1 + e^{-vx}} - 1, \quad (4.221)$$

with $v \in \mathcal{R}$ being sufficiently big (and positive). Hence, it follows that the derivative of the sign function can be approximated by

$$\text{sign}'(x) \cong \text{sig}'_v(x) = \text{sig}_v(x) (1 - \text{sig}_v(x)). \quad (4.222)$$

Besides, the sigmoid function can be employed to numerically approximate the absolute value function:

$$|x| \cong \text{abs}_v(x) = x \cdot \text{sig}_v(x). \quad (4.223)$$

The quality of the approximate functions with increasing v is demonstrated in Figure 4.34. Computational results in subsequent Sections were usually obtained from a value of $v = 2.5 \cdot 10^5$.

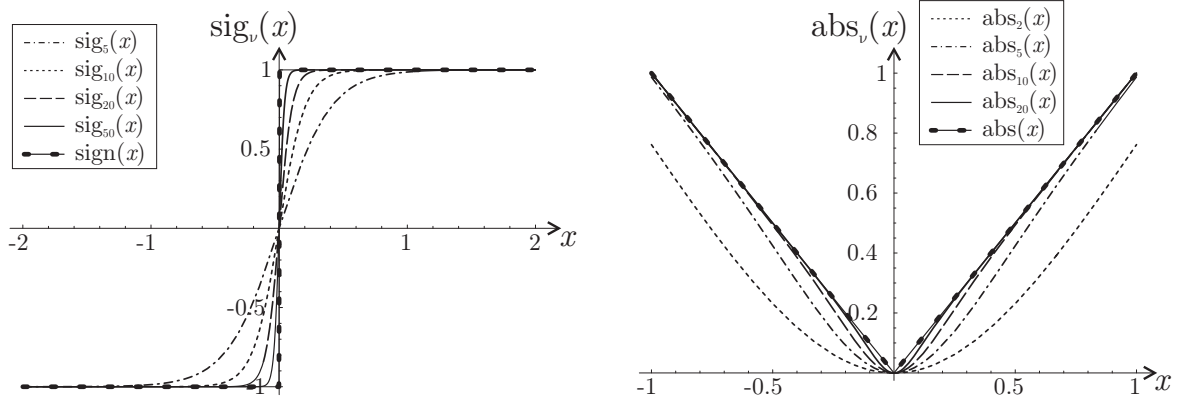


Figure 4.34: Quality of the approximate functions for sign and absolute value functions with varying parameter v .

The logarithmic energy form proposed by Berdichevsky (2006a) is well suited for the analytical treatment. For a numerical solution scheme, however, this type of energy is rather uncomfortable as it is not defined for $\rho > \rho_s$. A simple change by introducing the absolute value so that $\Psi_\rho = k\mu \ln 1/|1 - \rho/\rho_s|$ will overcome this difficulty but bears a new and even more risky disadvantage for numerical computations. The driving force $\Psi_{,\rho}$ is now defined for $\rho > \rho_s$ but it points into the wrong direction – once $\rho > \rho_s$, the driving force $\Psi_{,\rho}$ will favor an even higher increase of ρ , which should be prohibited to grow larger than ρ_s . For all these reasons let us introduce a new type of the energy of the dislocation network, which is very similar to that of Berdichevsky (2006a) but allows for a safe numerical treatment. We choose an energy which is identical to that of Berdichevsky (2006a) for small ρ and only deviates as ρ approaches ρ_s :

$$\Psi_\rho(\rho) = k\mu \left[\sum_{i=1}^n \frac{1}{i} \left(\frac{\rho}{\rho_s} \right)^i + e^{c(\rho/\chi\rho_s-1)} - e^{-c} \right] \quad (4.224)$$

or in the discrete version

$$\widehat{\Psi}_\rho(\widehat{\mathbf{b}}) = k\mu \left[\sum_{i=1}^n \frac{1}{i} \left(\frac{\left| \frac{1}{b} \mathbf{N}^* \cdot \widehat{\mathbf{b}} \right|}{\rho_s} \right)^i + e^{c(|\frac{1}{b} \mathbf{N}^* \cdot \widehat{\mathbf{b}}|/\chi\rho_s-1)} - e^{-c} \right], \quad (4.225)$$

where n can be chosen according to the sought precision, c and χ are constants with c being large and χ close to 1 but less than 1 (we commonly use $n = 3$, $c = 90$ and $\chi = 0.95$), and the last term simply ensures that $\widehat{\Psi}_\rho(0) = 0$. Figure 4.35 illustrates the deviation of the above approximation as compared to the exact energy form proposed by Berdichevsky (2006a), Eq. (4.163). Graphics demonstrate the influence of all three parameters: the number of Taylor terms n , and the two constant parameters c and χ .

To compute the vector of internal forces and the tangent stiffness matrix for the Newton-Raphson iteration, we need the first and second derivative of the energy of the dislocation

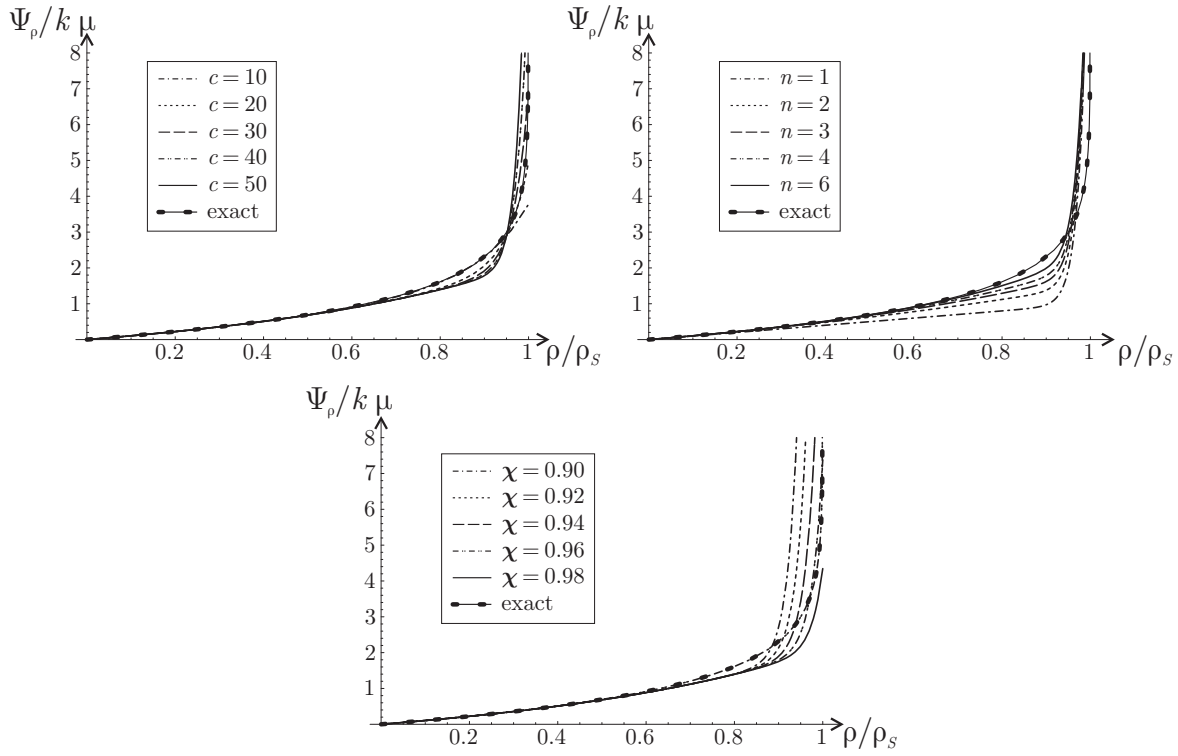


Figure 4.35: Approximate energy (4.224) with varying parameter c (while $\chi = 0.95$ and $n = 4$), χ (while $c = 40$ and $n = 4$) and n (while $c = 40$ and $\chi = 0.95$), as compared to the exact form (4.163).

network which can easily be obtained as

$$\frac{\partial \widehat{\Psi}_\rho}{\partial \widehat{\mathbf{b}}} = \frac{k\mu}{b\rho_s} \left[\sum_{i=1}^n \left(\frac{\left| \frac{1}{b} \mathbf{N}^* \cdot \widehat{\mathbf{b}} \right|}{\rho_s} \right)^{i-1} + \frac{c}{\chi} e^{c \left(\left| \frac{1}{b} \mathbf{N}^* \cdot \widehat{\mathbf{b}} \right| / \chi \rho_s - 1 \right)} \right] \cdot \text{sig} \left(\frac{1}{b} \mathbf{N}^* \cdot \widehat{\mathbf{b}} \right) \mathbf{N}^*, \quad (4.226)$$

$$\begin{aligned} \frac{\partial^2 \widehat{\Psi}_\rho}{(\partial \widehat{\mathbf{b}})^2} = & \frac{k\mu}{(b\rho_s)^2} \left\{ \rho_s \left[\sum_{i=1}^n \left(\frac{\left| \frac{1}{b} \mathbf{N}^* \cdot \widehat{\mathbf{b}} \right|}{\rho_s} \right)^{i-1} + \frac{c}{\chi} e^{c \left(\left| \frac{1}{b} \mathbf{N}^* \cdot \widehat{\mathbf{b}} \right| / \chi \rho_s - 1 \right)} \right] \cdot \text{sig}' \left(\frac{1}{b} \mathbf{N}^* \cdot \widehat{\mathbf{b}} \right) \right. \\ & \left. + \left[\sum_{i=2}^n (i-1) \left(\frac{\left| \frac{1}{b} \mathbf{N}^* \cdot \widehat{\mathbf{b}} \right|}{\rho_s} \right)^{i-2} + \frac{c^2}{\chi^2} e^{c \left(\left| \frac{1}{b} \mathbf{N}^* \cdot \widehat{\mathbf{b}} \right| / \chi \rho_s - 1 \right)} \right] \cdot \text{sig}^2 \left(\frac{1}{b} \mathbf{N}^* \cdot \widehat{\mathbf{b}} \right) \right\} \mathbf{N}^* \otimes \mathbf{N}^*. \end{aligned} \quad (4.227)$$

The latter derivative is required for the tangent stiffness matrix during the Newton-Raphson iteration.

With all above definitions we can finally employ the algorithm summarized in Algorithm 3 to compute the solution of \widehat{U} .

Algorithm 3: Numerical scheme to compute displacements and plastic distortion.

- (a) compute the global stiffness matrix \mathbf{K}
 - (b) for each load step, update the applied boundary conditions
 - (c) enforce boundary conditions by modifying \mathbf{K} and \mathbf{f}
 - (d) for each iteration n
 - compute the force vector $\mathbf{f}(\mathbf{U}_n)$
 - compute the tangent stiffness matrix $\mathbf{T}(\mathbf{U}_n)$
 - compute the residue $\Delta\mathbf{U}_n$ and its norm $\|\Delta\mathbf{U}_n\|$
 - if $\|\Delta\mathbf{U}_n\| < \|\Delta\mathbf{U}_{n-1}\|$ then $\mathbf{U}_{n+1} = \mathbf{U}_n - \alpha\mathbf{T}^{-1}\mathbf{f}(\mathbf{U}_n)$, else $\alpha \leftarrow 0.9\alpha$
 - if $\|\Delta\mathbf{U}_n\| < \delta_{\text{tol}}$ then $\mathbf{U}_{n+1} = \mathbf{U}_n - \alpha\mathbf{T}^{-1} \cdot \mathbf{f}(\mathbf{U}_n)$, exit
-

4.8.2 Finite Element Formulation at Non-Zero Dissipation

In case dissipation due to dislocation motion is no longer negligible, the minimization of the free energy is replaced by a flow rule. For classical plasticity theories Biot's equation may be employed. For gradient-type plasticity we must modify Biot's equation like in previous Sections and solve the variational flow rule

$$\frac{\delta\Psi}{\delta\beta} + \frac{\partial\Delta}{\partial\dot{\beta}} = 0. \quad (4.228)$$

Let us show that this differential equation can be replaced by a minimization problem for small time increments, similarly to the derivation shown in Chapter 2.5.1 for the evolution of microstructures in finite plasticity by following Ortiz and Repetto (1999) and Carstensen et al. (2002). We assume that the above variational form of Biot's equation may again be replaced by the minimization problem

$$\int_{\Omega} [\dot{\Psi} + \Delta] \, dv \rightarrow \min, \quad (4.229)$$

where in rate-independent plasticity we can write

$$\Delta(\dot{\beta}) = \tau_{\text{crit}}|\dot{\beta}|. \quad (4.230)$$

τ_{crit} is the critical resolved shear stress and $\dot{\beta}$ simply represents the rate of change of the plastic distortion. In general, we have

$$\Delta = \Delta(\beta, \dot{\beta}). \quad (4.231)$$

Let us define the incremental energy

$$W(\boldsymbol{\varepsilon}_{n+1}) = \inf_{\beta_{n+1}} \int_{t_n}^{t_{n+1}} \int_{\Omega} (\dot{\Psi} + \Delta) \, dv \, dt. \quad (4.232)$$

so that the stress at time t_{n+1} is defined by

$$\boldsymbol{\sigma}_{n+1} = \frac{\partial W(\boldsymbol{\varepsilon}_{n+1})}{\partial \boldsymbol{\varepsilon}}. \quad (4.233)$$

We rewrite Eq. (4.232) as

$$W(\varepsilon_{n+1}) = \inf_{\beta(x,t)} \left[\int_{\Omega} \Psi(\varepsilon, \beta, \nabla \beta) dv \Big|_{t_n}^{t_{n+1}} + \int_{\Omega} \int_{t_n}^{t_{n+1}} \Delta(\beta, \dot{\beta}) dt dv \right], \quad (4.234)$$

and minimize the term in brackets by computing the first variation which must vanish:

$$\int_{\Omega} \left(\frac{\partial \Psi}{\partial \beta} \delta \beta + \frac{\partial \Psi}{\partial \nabla \beta} \cdot \delta \nabla \beta \right) dv \Big|_{t_n}^{t_{n+1}} + \int_{\Omega} \int_{t_n}^{t_{n+1}} \left(\frac{\partial \Delta}{\partial \dot{\beta}} \delta \dot{\beta} + \frac{\partial \Delta}{\partial \beta} \delta \beta \right) dv dt = 0. \quad (4.235)$$

Integration by parts finally yields

$$\begin{aligned} & \int_{\Omega} \left(\frac{\partial \Psi}{\partial \beta} + \nabla \cdot \frac{\partial \Psi}{\partial \nabla \beta} \right) \delta \beta dv \Big|_{t_n}^{t_{n+1}} + \int_{\partial \Omega} \frac{\partial \Psi}{\partial \nabla \beta} \cdot \mathbf{n} \delta \beta da \Big|_{t_n}^{t_{n+1}} \\ & + \int_{\Omega} \frac{\partial \Delta}{\partial \dot{\beta}} \delta \dot{\beta} dv \Big|_{t_n}^{t_{n+1}} + \int_{t_n}^{t_{n+1}} \int_{\Omega} \left[-\frac{d}{dt} \frac{\partial \Delta}{\partial \dot{\beta}} + \frac{\partial \Delta}{\partial \beta} \right] \cdot \delta \beta dv dt = 0 \end{aligned} \quad (4.236)$$

or

$$\begin{aligned} & \int_{\Omega} \left(\frac{\delta \Psi}{\delta \beta} + \frac{\partial \Delta}{\partial \dot{\beta}} \right) \delta \beta dv \Big|_{t_n}^{t_{n+1}} + \int_{\partial \Omega} \mathbf{q}_{\beta} \delta \beta da \Big|_{t_n}^{t_{n+1}} \\ & + \int_{t_n}^{t_{n+1}} \int_{\Omega} \left[-\frac{d}{dt} \frac{\partial \Delta}{\partial \dot{\beta}} + \frac{\partial \Delta}{\partial \beta} \right] \delta \beta dv dt = 0, \end{aligned} \quad (4.237)$$

where

$$\mathbf{q}_{\beta} = \frac{\partial \Psi}{\partial \nabla \beta} \cdot \mathbf{n} \quad (4.238)$$

is a driving force of the plastic distortion on the boundary $\partial \Omega$. There are two distinct cases where the integral involving \mathbf{q}_{β} vanishes (and these are the only ones considered in the sequel). Firstly, if the value of β is known on the entire boundary $\partial \Omega$ (as e.g. in a grain whose boundaries do not allow dislocation transmission) then $\delta \beta$ vanishes on the boundary and the integral term drops. Secondly, if β is not generally known on the boundary, but if periodic boundary conditions are enforced (e.g. for homogenization problems), the plastic distortion and hence its variation is periodic on the boundary whereas forces \mathbf{q}_{β} are antiperiodic on the boundary. Therefore, the boundary integral also vanishes. In both cases the above equation reduces to

$$\int_{\Omega} \left(\frac{\delta \Psi}{\delta \beta} + \frac{\partial \Delta}{\partial \dot{\beta}} \right) \delta \beta dv \Big|_{t_n}^{t_{n+1}} + \int_{t_n}^{t_{n+1}} \int_{\Omega} \left[-\frac{d}{dt} \frac{\partial \Delta}{\partial \dot{\beta}} + \frac{\partial \Delta}{\partial \beta} \right] \delta \beta dv dt = 0. \quad (4.239)$$

As this equation must hold for arbitrary variations $\delta \beta$, we see that, in the limit of an infinitesimal time increment $\Delta t = t_{n+1} - t_n$ and with $\delta \beta(t_n) = 0$, the state of the internal variable field β at time $t = t_{n+1}$ is obtained from

$$\frac{\delta \Psi}{\delta \beta} + \frac{\partial \Delta}{\partial \dot{\beta}} = 0. \quad (4.240)$$

This is equivalent to Biot's equation (4.228). The minimizing path $\beta(x, t)$ inside the time interval must satisfy the Euler equation

$$-\frac{d}{dt} \frac{\partial \Delta}{\partial \dot{\beta}} + \frac{\partial \Delta}{\partial \beta} = 0, \quad (4.241)$$

which is identically fulfilled for homogeneous dissipation potentials Δ of degree 1 as those considered here.

For the specific problem considered here, the minimum principle then requires that

$$\int_{\Omega} \left(\dot{\Psi} + \Delta \right) dv \rightarrow \min \quad (4.242)$$

where minimization with respect to the rate of the internal (plastic) variables is implied.

Based on the finite element discretization, we know that the plastic distortion and displacement field are approximated by

$$\mathbf{u}(\mathbf{x}) = \mathbf{N}(\mathbf{x}) \cdot \hat{\mathbf{u}}, \quad \beta(\mathbf{x}) = \widetilde{\mathbf{N}}(\mathbf{x}) \cdot \hat{\mathbf{b}}, \quad (4.243)$$

so that (4.242) transforms into

$$\int_{\Omega} \left(\frac{\delta \Psi}{\delta \hat{\mathbf{b}}} \cdot \dot{\hat{\mathbf{b}}} + \tau_{\text{crit}} |\widetilde{\mathbf{N}} \cdot \dot{\hat{\mathbf{b}}}| \right) dv \rightarrow \min. \quad (4.244)$$

Furthermore, in a time-discrete setting we approximate the rate for a small incremental time step Δt in an explicit manner by

$$\dot{\hat{\mathbf{b}}} \approx \frac{1}{\Delta t} (\hat{\mathbf{b}}_{n+1} - \hat{\mathbf{b}}_n), \quad (4.245)$$

which allows for the formulation

$$\int_{\Omega} \left(\frac{\delta \Psi}{\delta \hat{\mathbf{b}}} \cdot (\hat{\mathbf{b}}_{n+1} - \hat{\mathbf{b}}_n) + \tau_{\text{crit}} |\widetilde{\mathbf{N}} \cdot (\hat{\mathbf{b}}_{n+1} - \hat{\mathbf{b}}_n)| \right) dv \rightarrow \min. \quad (4.246)$$

Variation with respect to the unknown vector $\hat{\mathbf{b}}_{n+1}$ yields

$$\int_{\Omega} \left(\frac{\delta \Psi}{\delta \hat{\mathbf{b}}} + \tau_{\text{crit}} \text{sign} \left[\widetilde{\mathbf{N}} \cdot (\hat{\mathbf{b}}_{n+1} - \hat{\mathbf{b}}_n) \right] \widetilde{\mathbf{N}} \right) dv \cdot \delta \hat{\mathbf{b}}_{n+1} = 0. \quad (4.247)$$

By including the elastic variables also (displacements discretized at nodes), the total variational problem reduces to a set of two equilibrium conditions, one macroscopic condition from minimizing the total energy potential with respect to the elastic variables and one microstructural equilibrium condition for the evolution of the internal variables:

$$\int_{\Omega} \frac{\delta \Psi}{\delta \mathbf{d}} dv = 0, \quad (4.248)$$

$$\int_{\Omega} \left[\frac{\delta \Psi}{\delta \hat{\mathbf{b}}} + \tau_{\text{crit}} \text{sign} \left[\widetilde{\mathbf{N}} \cdot (\hat{\mathbf{b}}_{n+1} - \hat{\mathbf{b}}_n) \right] \right] dv = 0, \quad (4.249)$$

where the last term in the latter condition is different from the formulation at zero dissipation. The first macroscopic equilibrium condition is the same as in (4.197). Replacing the microstructural equilibrium condition (4.198) by (4.249), one can again solve the minimization problem numerically by employing Algorithm 3.

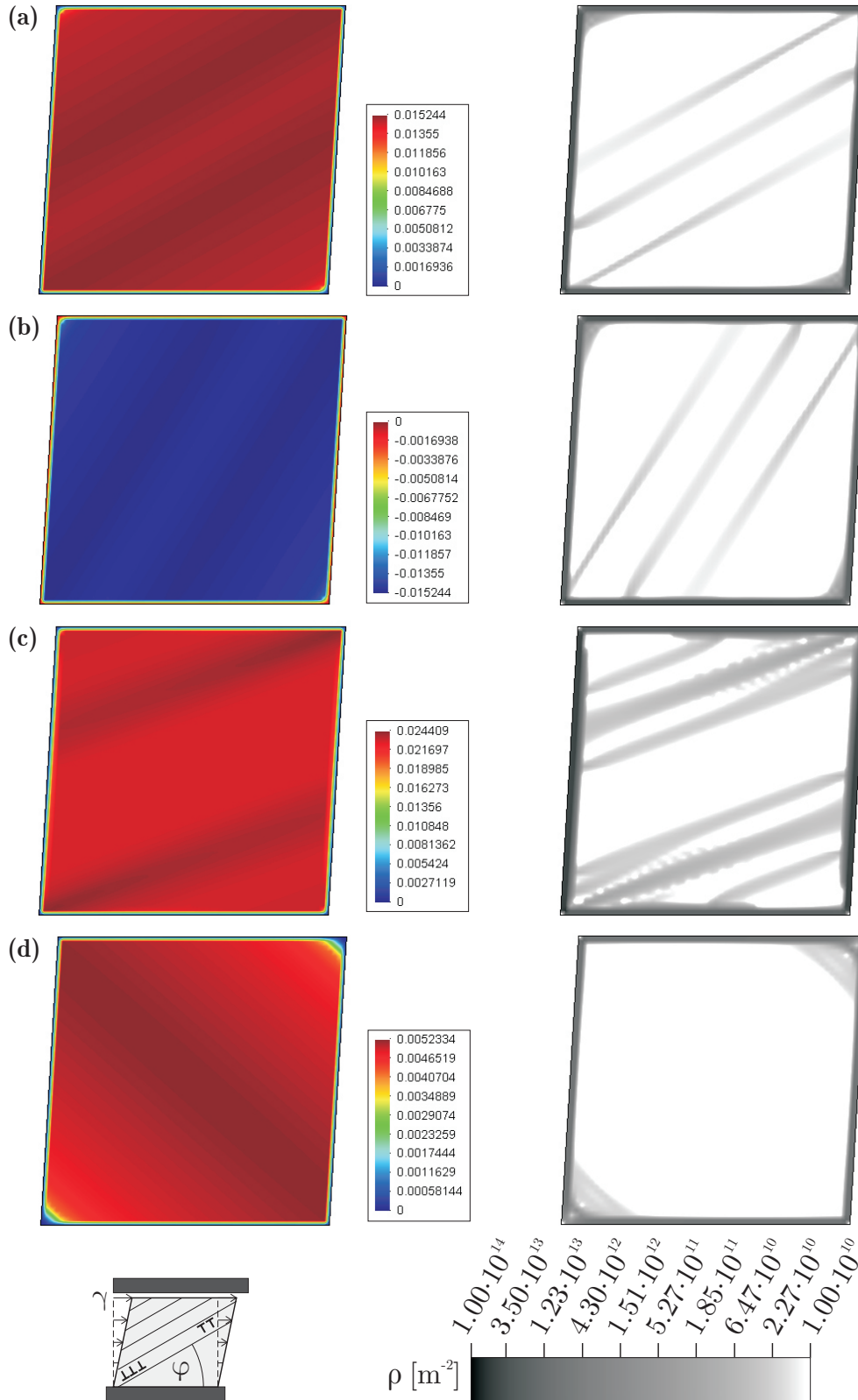


Figure 4.36: Equilibrium configuration of the plastic distortion and the dislocation density in a plane-constrained simple shear test of a square single crystal (side length $200 \mu\text{m}$) at $\gamma = 3\%$ with a single active slip system under (a) $\varphi = 30^\circ$, (b) $\varphi = 60^\circ$, (c) $\varphi = 20^\circ$, (d) $\varphi = 140^\circ$.

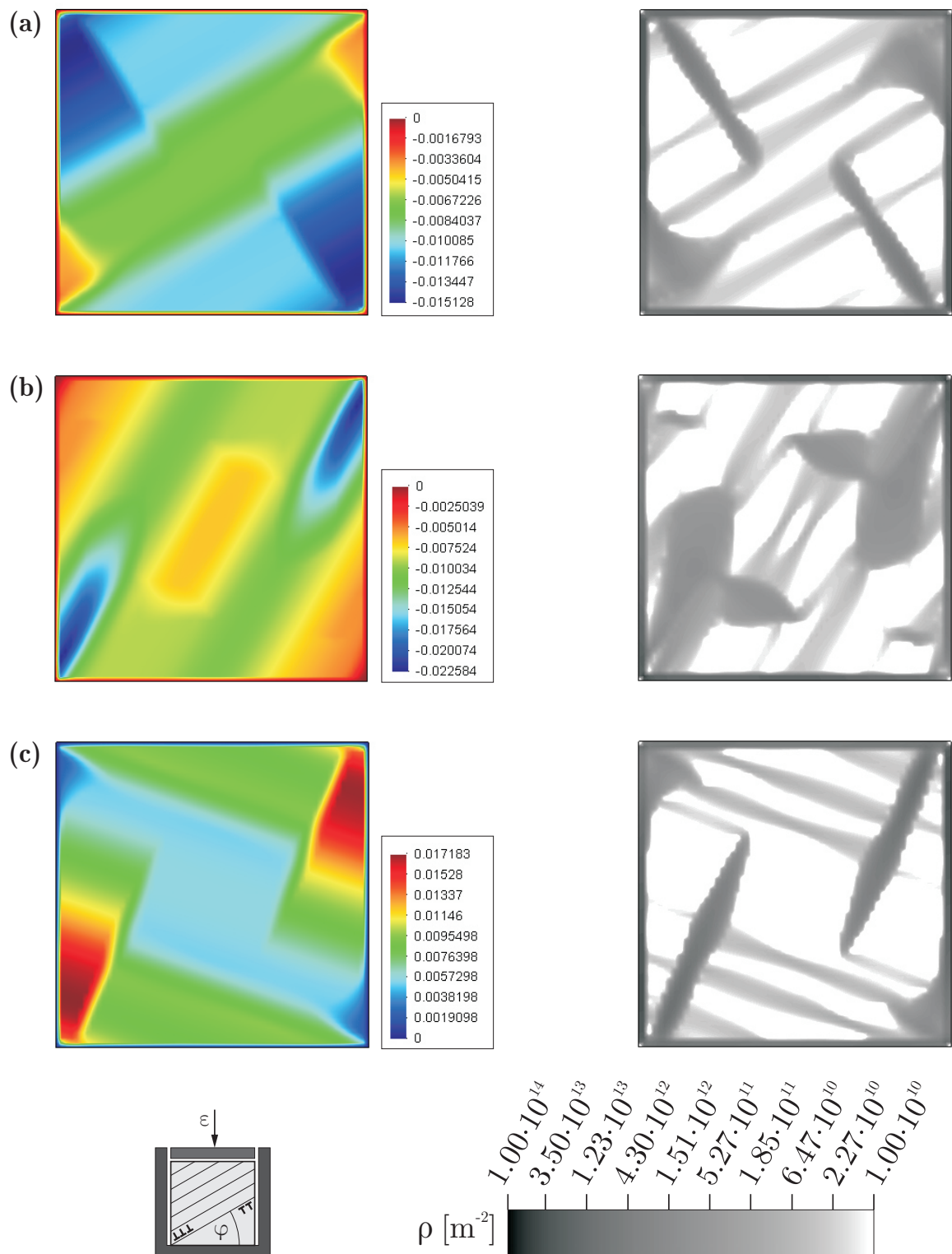


Figure 4.37: Equilibrium configuration of the plastic distortion and the dislocation density in a plane-constrained compression test of a square single crystal (side length $200\ \mu\text{m}$) at $\gamma = 1\%$ with a single active slip system under (a) $\varphi = 30^\circ$, (b) $\varphi = 60^\circ$, (c) $\varphi = 160^\circ$.

4.9 Numerical Examples

All computations in this Section are for aluminum with the material parameters summarized in Table 4.2. For better visibility of the deformed shape, deformations in all graphics are magnified by a factor of 2. Graphics illustrate the plastic distortion β , the stress distribution and the dislocation density ρ (usually on a logarithmic scale to display the dislocation density over a wider range). All computations were carried out using the finite element code FEAP (Zienkiewicz and Taylor, 2005).

Figure 4.36 illustrates the plastic distortion β and the dislocation density ρ in a single crystal of square shape during a plane-constrained simple shear test (shear strain $\gamma = 3\%$). Figure 4.37 shows analogous images for a constrained compression test of a square single crystal. In both Figures the crystal is assumed to be rigidly constrained, i.e. the plastic distortion must vanish on the boundary ($\beta = 0$ on the entire boundary) and displacements on all boundaries are prescribed as well (with L the width and h the height of the crystal): $u(x, y = 0) = v(x, y = 0) = 0$, $u(x, y = h) = \gamma h$, $v(x, y = h) = \varepsilon h$, and $v(x = 0, y) = v(x = L, y) = 0$, $u(x = 0, y) = u(x = L, y) = \gamma y$. Graphics demonstrate results for different slip system orientations (defined by the in-plane angle φ of the slip direction s with the x-axis). Dislocations pile up at the impenetrable boundaries but, as an interesting issue, do not leave the central part of the crystal completely dislocation-free: In the interior of the crystal dislocations arrange in specific patterns depending on the slip system orientation and on the crystal geometry, giving rise to substructures of dislocations within grains. The formation of such substructures can also be interpreted as the formation of subgrain boundaries as has been observed in polycrystalline aluminum and iron, see e.g. (Liu et al., 2002; Hansen et al., 2001, 2008). It has been argued (Liu et al., 2002) that such subgrains can – under continued plastic deformation – transform into smaller grains yielding a collective grain refinement. Severe plastic deformation as e.g. during equal channel angular pressing (Le and Kochmann, 2009) can hence be utilized to produce smaller grains which, in turn, give rise to excellent yield strength. Here, dislocations arrange within the grain to accommodate a state of lowest energy and yield subgrain structures. Note that the specific form of the substructure considerably depends on the choice of material parameters, the active slip system and the particular type of the chosen defect energy. It becomes apparent from these examples here and many other numerical experiments on single- and polycrystals that the orientation of these subgrain dislocation walls almost always coincides with the directions s and m of the active slip system.

As the dislocation density requires spatial derivatives of discretized field variables, it is important to check the mesh-independence of solutions. Figure 4.38 compares the plastic distortion in a square single crystal during a simple shear test as obtained from the present approach with meshes of 900, 3600 and 6400 elements. The results indicate that, of course, the mesh refinement affects the correct resolution of β (in particular at the boundaries where dislocations pile up in thin boundaries whose resolution is constrained by the element size), but the qualitative solution remains almost unaltered and appears mesh-independent.

material	E (GPa)	ν	b (Å)	ρ_s (m ⁻²)	k
aluminum	70.0	0.3	2.5	$4 \cdot 10^{14}$	$4 \cdot 10^{-4}$

Table 4.2: Material characteristics

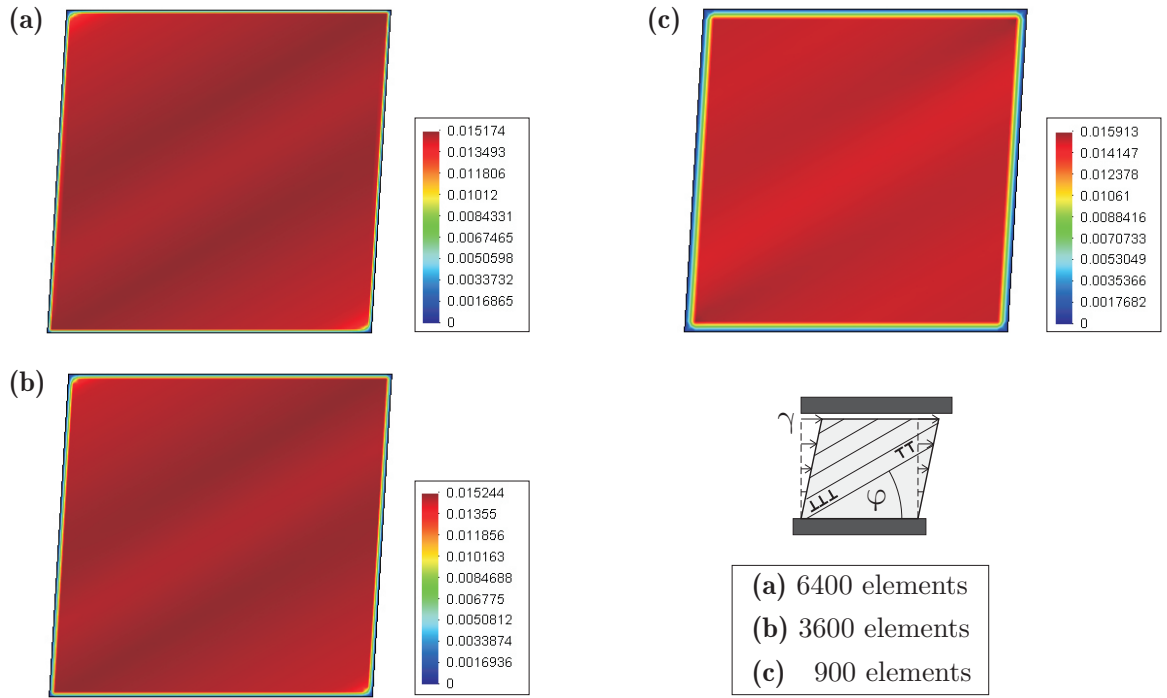


Figure 4.38: Comparison of β obtained from different meshes (900, 3600 and 6400 bilinear elements) for a square single crystal (side length $200 \mu\text{m}$) with a single active slip system ($\varphi = 30^\circ$) at overall strain $\gamma = 3\%$.

Having outlined the numerical method for general two-dimensional problems, we can check the accuracy of the analytical solutions for the one-dimensional bicrystal problems presented in Sections 4.1-4.6 as well as in the literature (Le and Sembriring, 2008a) for single crystals. Figure 4.39 illustrates numerical results for the plastic distortion in a single crystal deformed in shear (shear strain γ) and extension (tensile strain ε) for various slip system orientations. The crystal's horizontal in-plane extension is assumed very large such that periodic boundary conditions are enforced on the side boundaries: $\mathbf{u}(x = 0, y) = \mathbf{u}(L, y)$ and $\beta(x = 0, y) = \beta(x = L, y)$ where L is the horizontal width of the body under investigation. The top and bottom boundaries rigidly prescribe displacements and are impenetrable for dislocations: $\mathbf{u}(x, y = 0) = \mathbf{0}$, $\beta(x, y = 0) = 0$, $u(x, y = h) = \gamma h$, $v(x, y = h) = \varepsilon h$, $\beta(x, y = h) = 0$, with h the height of the crystal. The corresponding curves compare the plastic distortion in the central cross-section of the displayed crystal to the analytical solution (Le and Sembriring, 2008a). Figure 4.40 displays the analogous results for a deformed bicrystal with symmetric active slip systems in comparison with the results from Sections 4.1-4.6. Both the plastic distortion and the boundary layer thickness show a high degree of coincidence in all examples.

Having outlined the accuracy of the numerical results and the mesh-independence of the present method, we can investigate several examples to illustrate the specific effects of the continuum-dislocation approach chosen here. One of the crucial differences from classical plasticity theories is the model-inherent length scale which is characterized in particular by the saturated dislocation density and which gives rise to observable size effects typical of problems of crystal plasticity. Figure 4.42 illustrates the plastic distortion and the distribution of the shear stress σ_{12} in a square single crystal during a plane-constrained simple shear test (as before, fixed strain $\gamma = 1\%$) for a given active slip system and with varying crystal

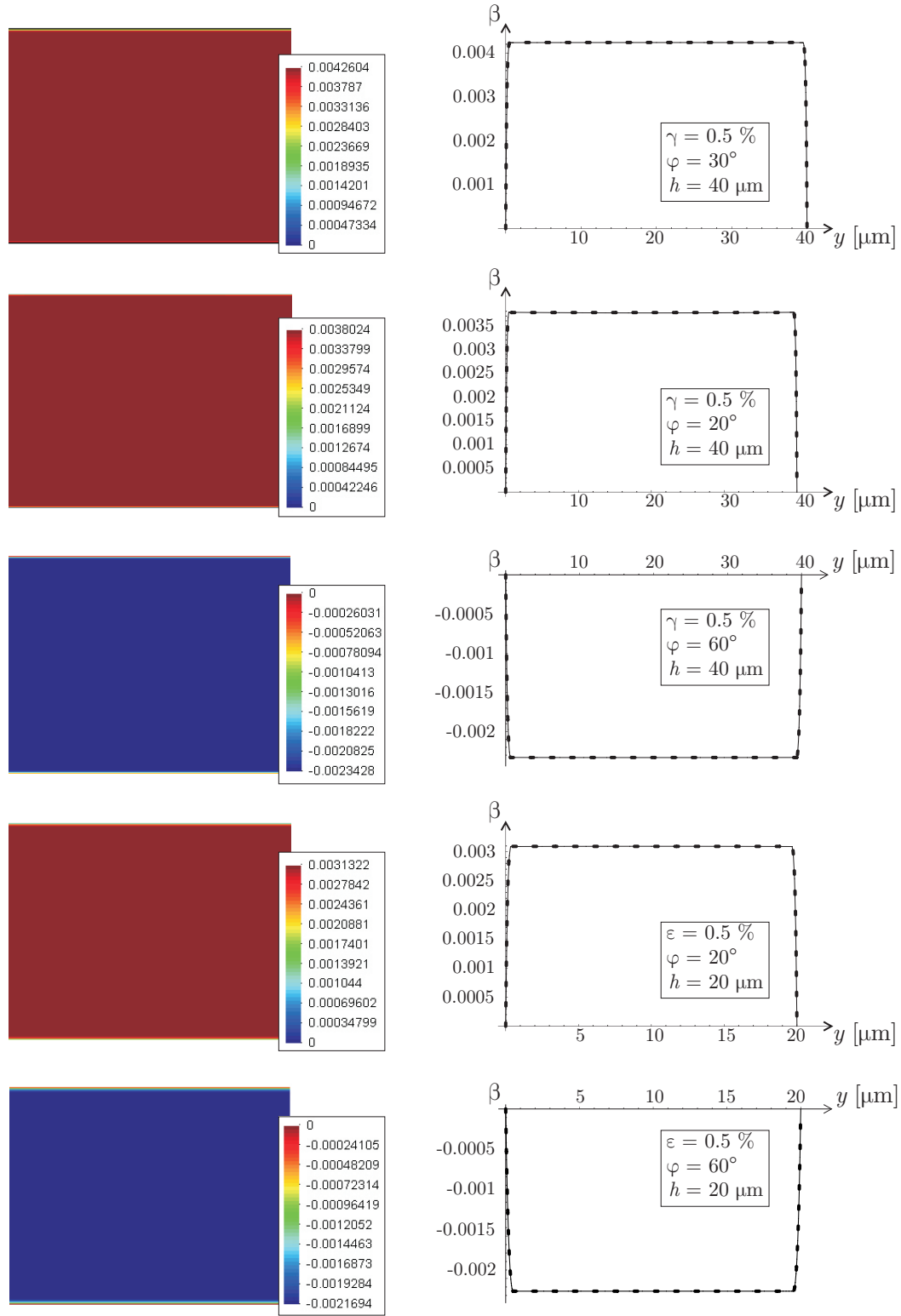


Figure 4.39: Equilibrium configuration of the plastic distortion in a long thin strip (height $40\mu\text{m}$) under uniaxial extension ($\varepsilon = 0.5\%$) or simple shear ($\gamma = 0.5\%$) with different active slip systems; comparison of β in the middle cross-section from numerics (dotted line) and from Chapter 4.1 (solid line).

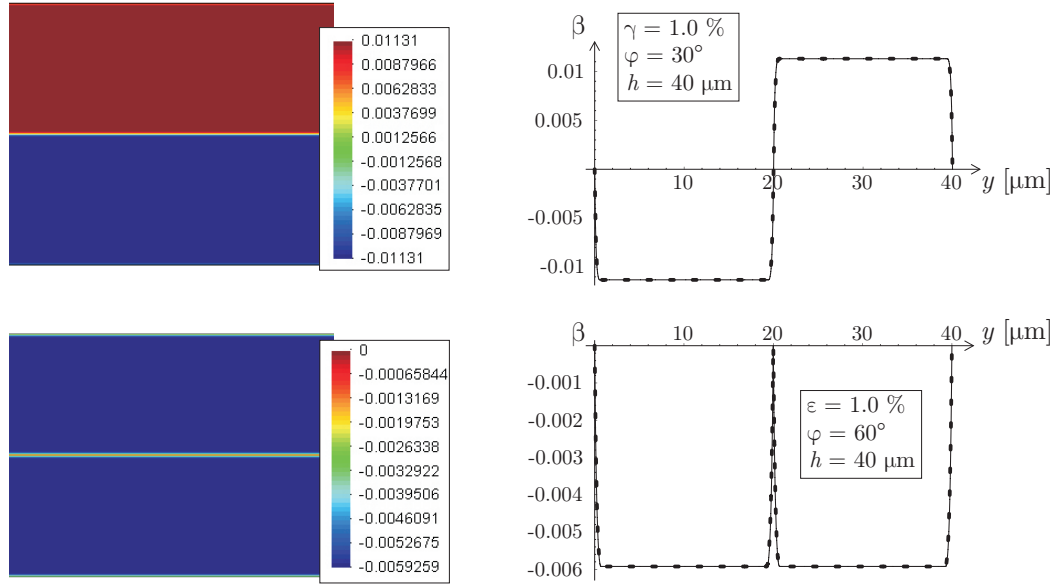


Figure 4.40: Equilibrium configuration of the plastic distortion in a long thin strip (height $40\mu\text{m}$) under uniaxial extension ($\varepsilon = 1.0\%$) or simple shear ($\gamma = 1.0\%$) with different active slip systems; comparison of β in the middle cross-section from numerics (dotted line) and from Chapter 4.1 (solid line).

size (for comparison all crystals are magnified to appear of the same final size). Except for the crystal size all other parameters remain unaltered. As the side length a of the crystal decreases from 2 cm to $30\mu\text{m}$, dislocations are forced to concentrate in a smaller volume and hence more rapidly reach the saturation state. With decreasing crystal size, the relative size of the boundary layers of dislocations increases, the plastic distortion is more severely constrained and, as a consequence, the shear stress increases due to dislocation back-stresses.

Recording the shear stress in the center of the crystal at different crystal sizes (represented by the side length a) results in Figure 4.41, which clearly indicates a size-dependence of the shear stress of the type

$$\sigma_{12} = \sigma_0 + \frac{c_\sigma}{a}, \quad (4.250)$$

where σ_0 and c_σ are constant parameters. Curve-fitting reveals that σ_0 agrees well with the solution of an unconstrained (infinitely extended) single crystal with the given material properties. For large dimensions the second term in (4.250) is negligible: the difference of the shear stress e.g. for $a = 2\text{ mm}$ and for $a = 2\text{ cm}$ vanishes. With decreasing size the second term in (4.250) dominates giving rise to the size effect.

The size effect is not only observed for completely constrained single crystals. In the following we investigate results from models for infinitely extended thin strips as well as for (simple) polycrystals. Figure 4.43 illustrates the model of an infinitely extended thin film of homogeneous material. Periodic boundary conditions are enforced as $\mathbf{u}(x = 0, y) = \mathbf{u}(x = a, y)$ and $\beta(x = 0, y) = \beta(x = a, y)$. The top and bottom displacement boundary conditions are rigidly enforced. First, we investigate the thin strip subject to a simple shear deformation ($\mathbf{u}(x, y = 0) = 0$, $u(x, y = h) = \gamma h$, $v(x, y = h) = 0$). For a total strain of $\gamma = 2\%$ we measure the shear force F at the top boundary and normalize F with respect to the out-of-plane thickness t of the strip and the width a of the part under investigation. F/ta can also be interpreted as the mean shear stress σ_{xy} in the crystal. Then we analyze the compressive

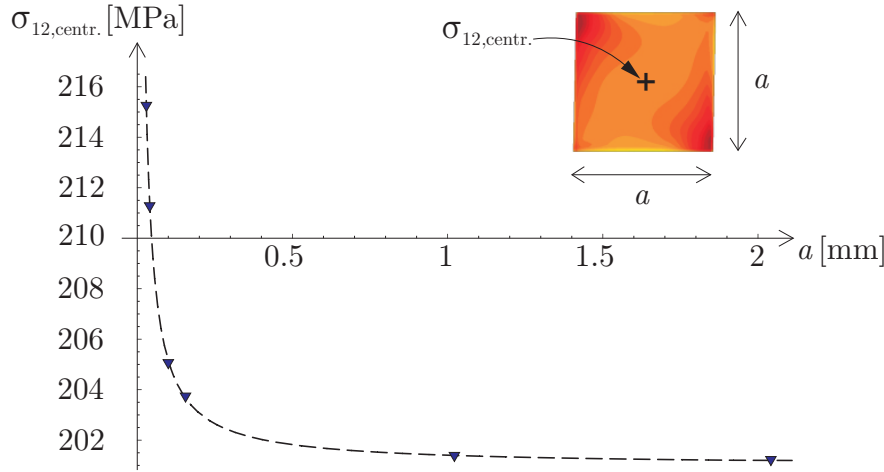


Figure 4.41: Relation between the size of a constrained single crystal under simple shear and the shear stress in the central part of the crystal (for $\varphi = 30^\circ$ and $\gamma = 1\%$). Triangles result from FE results of specimens with varying dimensions; the fitted curve (dashed line) is $(200.9878 \text{ MPa} + 0.4160 \text{ MPa/mm} \cdot a^{-1})$. The analytical solution of the shear stress for an unconstrained single-slip crystal is 201.92 MPa.

behavior of the thin strip by prescribing $u(x, y = 0) = 0$, $v(x, y = h) = 0$, $v(x, y = h) = \varepsilon h$. For a total strain of $\varepsilon = -2\%$, the compressive force F at the top boundary is normalized as before so that F/ta represents the average compressive strain σ_{yy} in the crystal. Results for the mean stresses vs. the film height are summarized in Figures 4.47. To illustrate the behavior of Eq. (4.250), the normalized force is plotted versus the inverse crystal height in all plots in Figures 4.47 and 4.48.

Figure 4.44 exemplarily explains the microstructural differences giving rise to the increased stresses on smaller scales. As the size decreases, the gradient of the plastic distortion, hence the dislocation density and as a consequence the microstructure energy rapidly increase. Consequently, dislocations can no longer be confined to relatively thin boundary layers at the crystal boundaries but pile up, extending more and more into the crystal interior. Figure 4.44 illustrates the distribution of the dislocation density in the thin film of Figure 4.43 with changing crystal height. As the crystal height decreases, the (relative) boundary layer thickness as well as the dislocation density in the crystal interior increase.

Figure 4.45 illustrates another example of a thin strip but with non-uniform slip systems. The (periodically continued) strip consists of three grains with equal dimensions ($d = h$ and $a = 3h$) but different active slip systems characterized by the angles φ_i . Grain boundaries are again assumed mobile but impenetrable for dislocations. The strip is subjected to a simple shear deformation ($\gamma = 1\%$) and the mean shear force F/ta is recorded. Figure 4.48a shows the curve of F/ta vs. the inverse crystal height h .

Finally, Figure 4.46 sketches a rough model of a polycrystal. We assume grains of a symmetric hexagonal shape which are arranged in a periodic manner. Considering a thin strip, we now enforce periodic boundary conditions of the type $u(x, y = 0) = 0$, $u(x, y = h) = \gamma h$, $v(x, y = 0) = v(x, y = h) = 0$, $\beta(x, y = 0) = \beta(x, y = h) = 0$, $\mathbf{u}(0, y) = \mathbf{u}(a, y)$, $\beta(0, y) = \beta(a, y)$. The model consists of four different grains with different orientations of the active slip systems as indicated in Figure 4.46. We record the total shear force F at the

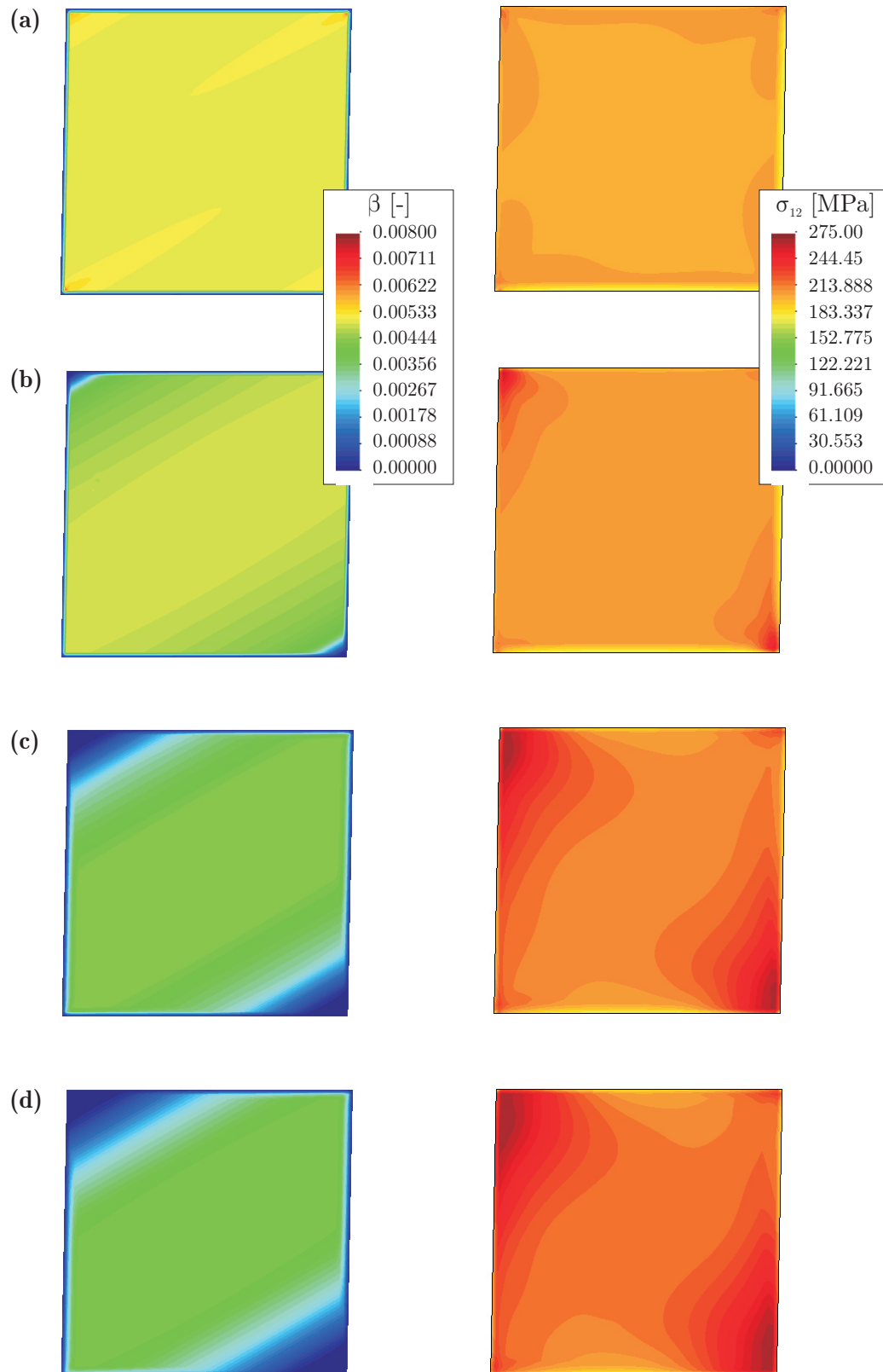


Figure 4.42: Equilibrium configuration of the plastic distortion and corresponding shear stress distribution under simple shear ($\gamma = 1\%$) in a square crystal with $\varphi = 30^\circ$ and different crystal sizes (side length a): (a) $a = 2$ cm, (b) $a = 0.15$ mm, (c) $a = 40$ μm , (d) $a = 30$ μm .

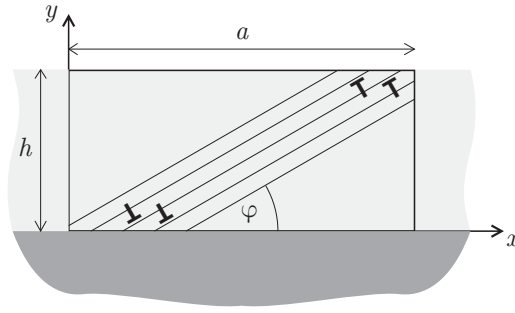


Figure 4.43: Model of a single-crystal thin strip with one active slip system. Periodic boundary conditions are enforced as $\mathbf{u}(x=0, y) = \mathbf{u}(x=a, y)$ and $\beta(x=0, y) = \beta(x=a, y)$.

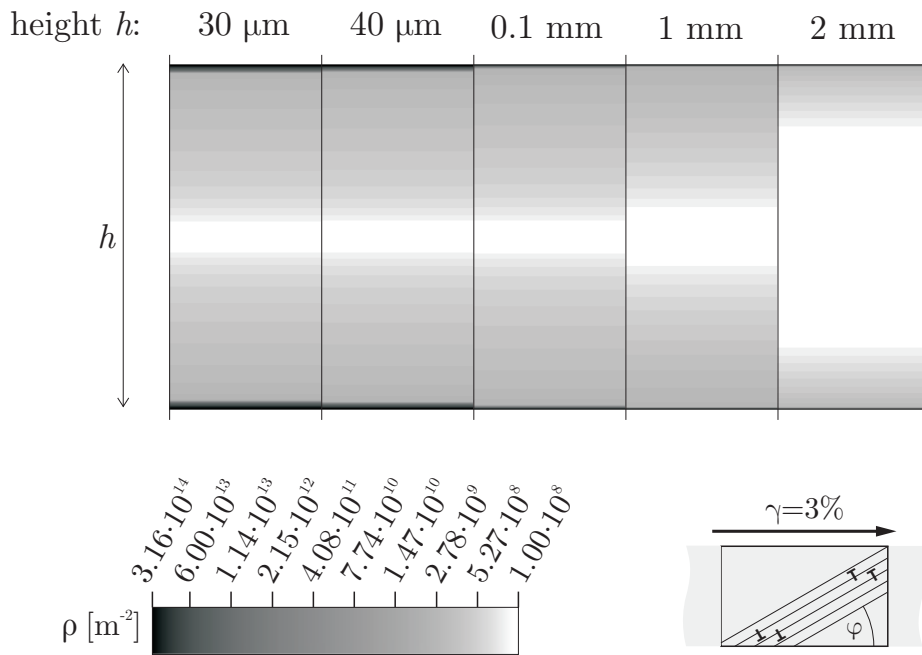


Figure 4.44: Dislocation distribution in a sheared thin strip (periodic boundary conditions) at strain $\gamma = 3\%$ with $\varphi = 35^\circ$ for various heights of the crystal.

top boundary and normalize F with respect to the thickness t and the height $h = a$. The resulting curve F/ta versus the side length h is plotted in Figure 4.48b.

The summary of all results obtained from the infinitely extended thin films and the hexagonal-grain polycrystal model are compared in Figures 4.47 and 4.48. Curves are fitted to a law of the type $f(\sigma) = \sigma_0 + c_\sigma/h^n$. Table 4.3 provides the fitted values of constants σ_0 , c_σ and n for all four examples. Interestingly, both thin film curves (Figures 4.47a and b) as well as the three-grain thin film curve (Figure 4.48a) display an approximately linear behavior with $0.998 \leq n \leq 1.083$. This inverse relation has already been observed in Section 4.2-4.6.2 (see the brief summary in Section 4.7). The curve of results from the polycrystal model with hexagonal grains follows – to a very high accuracy – a law with $n = 0.639$, which considerably deviates from the typical inverse law observed before. This result is of particular interest as the well-known Hall-Petch relation (for not too small grain sizes) predicts $n = 0.5$. The change from the single to a polycrystal with a large number of grains and ran-

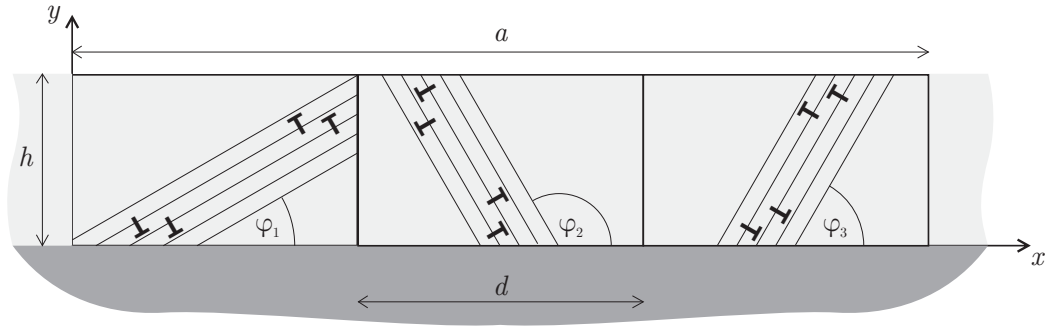
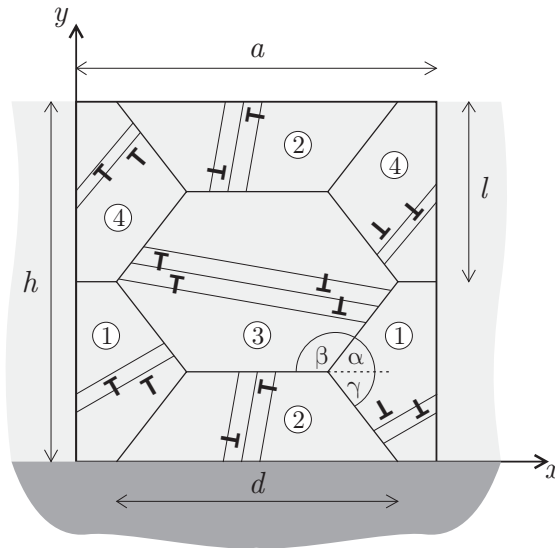


Figure 4.45: Model of a simple polycrystalline thin strip with one active slip system within each of the three grains. Periodic boundary conditions are enforced as $\mathbf{u}(x = 0, y) = \mathbf{u}(x = a, y)$ and $\beta(x = 0, y) = \beta(x = a, y)$. Results are computed with $\varphi_1 = 30^\circ$, $\varphi_2 = 120^\circ$, $\varphi_3 = 60^\circ$.



geometry	value
h	0.04 mm...2 mm
a	h
l	$0.5 h$
d	$0.789 a$
α	60°
β	120°
γ	60°

Figure 4.46: Model of a polycrystalline thin strip consisting of hexagonal grains with one active slip system within each grain. Periodic boundary conditions require that $\mathbf{u}(x = 0, y) = \mathbf{u}(x = a, y)$ and $\beta(x = 0, y) = \beta(x = a, y)$.

domly distributed slip system orientations might be responsible for the decreasing value of n . Present research investigates values of n as the number of grains and hence of represented slip system orientations in the representative unit cell is increased.

4.10 Discussion and Conclusions

In this Chapter a continuum dislocation theory was applied in order to model the plastic deformation of crystalline solids and to determine the dislocation distribution in strained crystals. We adopted the formulation proposed by Berdichevsky (2006a,b) for the energy of the microstructure, which exhibits a saturation behavior by penalizing dislocation densities higher than a material constant (the saturated dislocation density ρ_s). This particular form of the dislocation energy gives rise to size effects which became obvious throughout all analyses presented in the present Chapter.

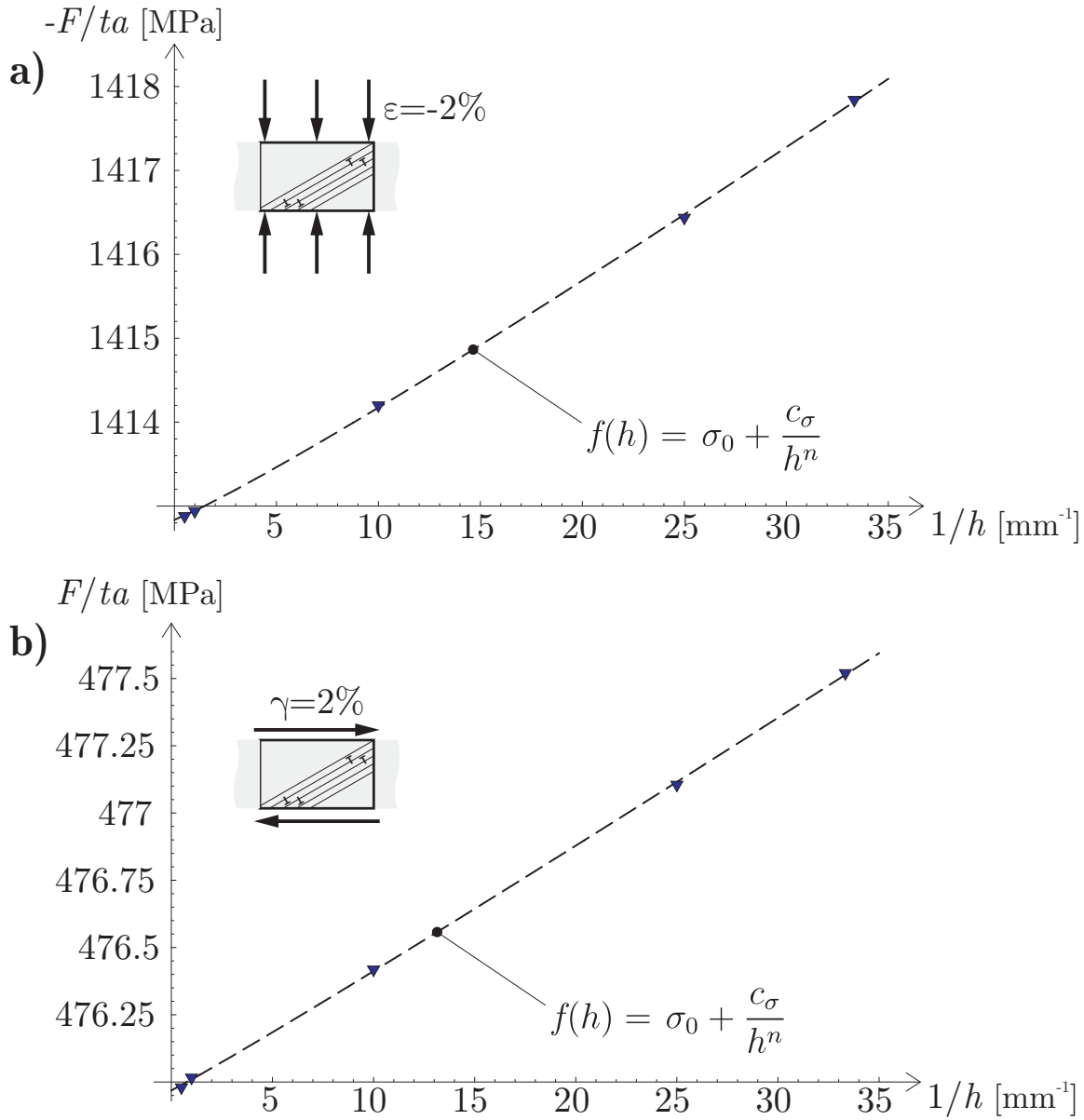


Figure 4.47: Normalized force per thickness and unit length versus inverse size of the body under investigation ($\varphi = 35^\circ$). Corresponding values for the fitted curves are summarized in Table 4.3. The analytical solution for an unconstrained crystal for F/ta yields a) -1409.14 MPa, b) 475.47 MPa.

First, the simple model of a thin-strip bicrystal consisting of two perfectly bonded single crystals was investigated with both crystals deforming in single-slip with different slip system orientations. Analytical solutions for the cases of plane-constrained shear and uniaxial extension were presented both for zero and for non-zero dissipation, assuming symmetric active slip systems. A combination of shear and extension at non-zero dissipation was shown to result in a linear superposition of results from independent loading cases. The general case of unsymmetric slip systems as well as of mixed shear and extension at zero and non-zero dissipation was studied by employing a numerical approach. For all examples, solutions comprised the evolution of the plastic distortion, the dislocation density and the stress-strain curve. In particular, we quantitatively described the pile-up of dislocations

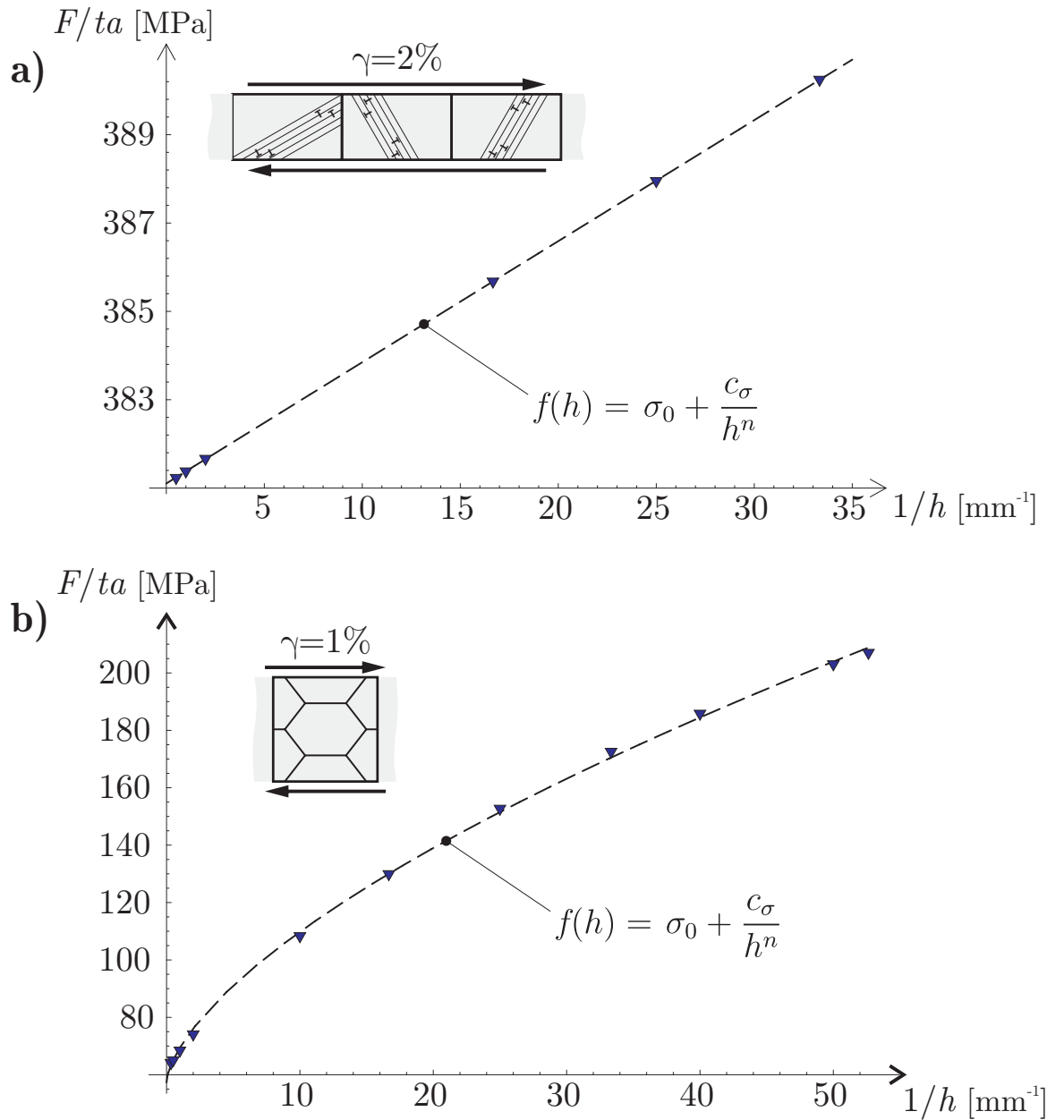


Figure 4.48: Normalized force per thickness and unit length versus inverse size of polycrystalline models. Corresponding values for the fitted curves are summarized in Table 4.3.

at the boundaries and interfaces of the crystals and the resulting stress-strain behavior. Of course, these analytical examples presented here are simplistic and only take into account a few characteristics of actual material behavior. However, an analytical solution is a rare find in the field of highly non-linear dislocation mechanics and the present model allows for neat closed-form analytical solutions in all of the fundamental problems investigated (despite its high degree of non-linearity and its complex formulation). Therefore, these basic problems were reported first, where many characteristics could be discussed.

These analytical examples indicate that there exists an energetic threshold for the nucleation of dislocations, which depends on the orientation of the slip system and is inversely proportional to the height of the bicrystal. Thus, a size effect becomes apparent as the yield

example	Figure	σ_0 (MPa)	c_σ (MPa/mm)	n
compression	Fig. 4.47a	1412.84	0.10817	1.08228
shear	Fig. 4.47b	475.97	0.04078	1.03664
shear (3 grains)	Fig. 4.48a	381.75	0.22939	0.99884
shear (polycrystal)	Fig. 4.48b	57.35	12.04603	0.63879

Table 4.3: Curve-fitting parameters from Figures 4.47 and 4.47.

stress of the bicrystal (in tension, shear, and a combination of both) shows an inverse proportionality to the height of the bicrystal. Above this threshold stress dislocations are nucleated and pile up at the crystal boundaries, forming thin layers of concentrated dislocations at the boundaries and leaving the central part of the single crystals dislocation free. This behavior has also been reported from discrete dislocation dynamics. Indeed, a comparison of results from this approach with those from discrete dislocation dynamics for a single crystal strip – both qualitatively and quantitatively – shows good agreement (Le and Sembringer, 2008a,b). With decreasing crystal size dislocation boundary layers grow into the crystal, thus resulting in higher stresses as well. Furthermore, we observed a work-hardening section of the stress-strain curve which also depends on the orientation of the slip system and the height of the bicrystal. At non-zero dissipation the stress-strain curve turns into a classical hysteresis loop exhibiting the Bauschinger effect.

Then, the simple model was enhanced by deriving a variational formulation to be solved by a finite element approach. At zero dissipation this method numerically minimizes the total stored energy with respect to the unknown displacement field as well as the field of the plastic distortion. At non-zero dissipation the variational formulation originally proposed by Ortiz and Repetto (1999) was extended to allow for an analogous description for strain-gradient models. As a consequence, we can analyze the distribution of dislocations, of the plastic distortion and of the stresses in plane-strain crystals with one active slip system with arbitrary two-dimensional loading at zero and non-zero dissipation. A comparison of numerical results with the analytical solution for infinitely extended single crystals and bicrystals shows a very good agreement of the solutions. Interesting features of the numerical results predominantly comprise two important observations:

As a first important result, we again observe underlying size effects of solutions. With decreasing crystal size dislocation pile-ups at the grain boundaries extend more into the crystal interior, resulting in higher stresses. For single crystals the same inverse proportionality as before was observed. The well-known Hall-Petch relation predicts a dependence of the type $\sigma \propto 1/d^{0.5}$ where d is the grain diameter. Results presented here deviate from this law. This difference might be overcome by admitting the penetration of grain boundaries by dislocations at sufficiently high stress concentrations. Also, size effects of the present inverse type have been reported for various problems involving thin metal strips, see e.g. (Nicola et al., 2003). Interestingly, simple models of a polycrystal (consisting of periodically repeated hexagonal grains) show a dependence of $\sigma \propto 1/d^n$ where n ranges between 0.5 and 1, i.e. between the Hall-Petch law and the inverse proportionality observed for single crystals. It is theorized that with increasing number of grains considered (and hence with increasing number of slip system orientations represented in the polycrystal) the size effect may tend towards the Hall-Petch law.

The second interesting observation from numerical simulations is the formation of dislocation subgrain structures as energy minimizers. Depending on the grain geometry, the ap-

plied loads, the slip system orientation and the material properties, dislocations do not only pile up at grain boundaries (where the plastic distortion is forced to vanish) but may also form particular structures within single crystals. In most examples dislocations concentrate along bands of higher plastic slip within crystals. Note that the formation of such dislocation substructures is not the result of a loss of convexity (as in this case the energy clearly is convex) and would not occur as a homogeneous laminate pattern in an infinitely extended or periodically repeated crystal. Instead, these dislocation substructures form heterogeneously as a consequence of the given boundary conditions of vanishing plastic distortion on the grain boundaries. Therefore, the observed subgrain structures highly depend on the grain geometry and also the size of the grain. Hansen et al. (2001, 2008) argued that the formation of such subgrain dislocation structures is an important mechanism for grain refinement during severe plastic deformation. The subgrains can – under continued plastic deformation – transform into independent smaller grains with commonly low-angle boundaries. Interestingly, substructures tend to form in grains of medium size whereas small grains highly prohibit the formation of such subgrain boundaries. This is in good qualitative agreement with experimental results, which indicate the formation of such subgrain cell structures to achieve fine-grained materials where, in turn, fine grain interiors are almost dislocation-free. The present investigation hints at a possible mechanism for the initiation of such subgrain structures.

Of course, the present model is subject to several limitations to be addressed in the future. In particular, the numerical procedure can easily be generalized to three-dimensional problems, and it can be modified to account for two active slip systems. In the latter case it is important to specify the interaction of dislocations on different slip systems (Le and Sembriring, 2008b; Kochmann and Le, 2009b). Furthermore, the examples considered here accounted for impenetrable grain boundaries. As a next step, dislocations can be allowed to travel through grain boundaries if the stress concentration at the boundary due to the dislocation pile-up reaches a critical value. Alternatively, grain boundaries can be understood as low-angle boundaries whose energy can be accounted for e.g. in terms of a Read-Shockley formulation. This way the defect energy must be expanded by the energy of the grain boundaries while the plastic distortion is no longer restricted on the grain boundaries. In this context, it is also important to analyze the influence of free surfaces where the surface energy should limit the number of dislocations leaving the crystal. Finally, the present model is restricted to small strains. An extension to finite strains would allow for the computation of practical examples with higher strains, e.g. indentation experiments which exhibit a size effect as well, or equal channel angular extrusion processes which result in ultrafine-grained materials. As the free energy in finite elasto-plasticity can no longer be presumed to be convex (see Section 3), minimizers can be modeled as laminate microstructures where the influence of dislocations (in particular at the laminate phase boundaries) is of major importance and can now, at least in principle, be modeled.

5 A Continuum Model for the Initiation and Evolution of Deformation Twins

5.1 Introduction

Slip and twinning are the major deformation modes which accommodate a change of shape under the action of applied tractions or displacements. Deformation twins have been reported to occur especially in b.c.c., h.c.p. and lower symmetry metals and alloys but also in many f.c.c. metals and alloys with low stacking-fault energy, or other intermetallic compounds as well as in geological materials such as calcite or quartz. Twinning becomes particularly important in metals with only a limited number of slip systems, as it can operate to provide the five slip systems required to satisfy the criterion for a general slip deformation. Deformation twinning basically divides the originally uniform single crystal into two volumetric parts – a parent phase (with unaltered crystal lattice) and a twin phase (with a different crystal lattice orientation). Both phases normally occur in the form of lamellar structures where a bicrystal consisting of neighboring parent and twin phase is commonly referred to as a *twin*. The twin lattice can be generated either by a rotation of the original crystal lattice by 180° about some axis (mode I) or by reflection in some plane (mode II) so that in both cases – when joint with the undistorted parent phase – an unfaulted single crystal is formed, which exhibits a twin boundary with coincident lattice positions at the interface. This topic is closely related to martensitic phase transformations and the observed effect of transformation induced plasticity (TRIP). In this Chapter, however, we will limit our analysis to the effects of twinning induced plasticity (TWIP).

The formation of deformation twins has a significant impact on the macroscopic stress-strain response. The evolution of twins provides TWIP alloys with excellent hardening behavior (Allain et al., 2004), allowing for higher stresses and larger strains than in common f.c.c. or b.c.c. metals. As a special characteristic, the onset of twinning, i.e. the rapid nucleation of deformation twins, often gives rise to a load drop in the stress-strain behavior (Christian and Mahajan, 1995). The increase of strength and work hardening during microstructure refinement by twinning in manganese steels or other TWIP-alloys is theorized to result from the dislocation pile-ups near the twin boundaries (raising the boundary energy) and the related size-effects. Experiments on single crystals have shown that particularly f.c.c. metals normally do not twin before appreciable plastic deformation by dislocation slip has occurred, while e.g. b.c.c. metals often exhibit deformation twinning even in the elastic region before the onset of macroscopic yielding. It is, however, well accepted that twinning in metals is often accompanied or preceded by microslip and that the formation of deformation twins is initiated by pre-existing dislocation configurations which dissociate into twin boundary structures. Furthermore, it is believed that the finite boundary energies accompanying the pile-up of dislocations limit the refinement of microstructure and hence are responsible for the formation of discrete twin patterns.

In this Chapter we develop a micro-mechanical model to describe the initiation and evolution of deformation twins in metals and alloys by employing a continuum dislocation

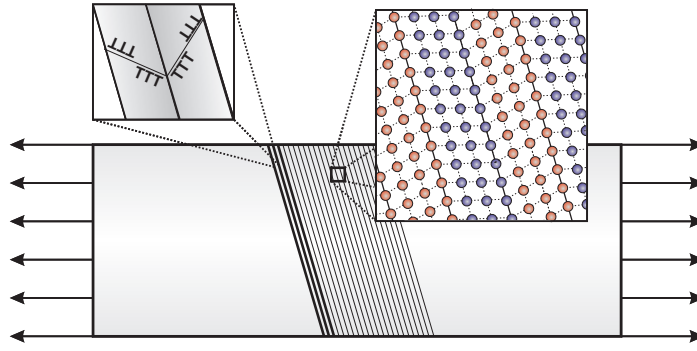


Figure 5.1: Microstructural twin patterns form under applied loads.

approach. We follow the strategy presented in the preceding Chapter, and we adopt the logarithmic energy formulation for the continuum dislocation theory, as proposed by Berdichevsky (2006b). A new ingredient of this theory compared to the previous Chapter is the so-called twinning shear produced by the existing dislocations in the already active slip system, which plays a similar role as Bain's strain in the theory of martensitic phase transformations, see e.g. (Bhattacharya, 2003). This twinning shear followed by a rotation enables the initially homogeneous crystal to form the twin phase from the parent phase. The underlying mechanism of twin formation is closely related to that of Bullough (1957), who employed a decomposition of the deformation into shear and rotation. The introduction of the twinning shear into the energy of the twin renders the energy multi-welled and non-convex. It can be shown by standard variational calculus that, in a certain range of straining, a mixing of parent and twin phase is energetically more preferable and the volume fraction of the twin phase has a finite value at the onset of deformation twinning. This finite jump provides space (or mean free path) for the subsequent dislocation pile-up within the twin phase. In spite of the dislocation pile-up in the twin phase and in the parent phase, the formation of the twin phase does not lead to hardening of the material but rather to a load drop in the stress-strain curve, until the transition from parent to twin phase is completed and the material hardens again. The load-drop can be explained by the spontaneous formation and subsequent increase of the volume fraction of the twin phase near the second minimum of the energy which considerably lowers the total energy of the material. We also consider the evolution of deformation twins when dissipation cannot be neglected. In this case the dissipation potential should also include the dissipation due to the motion of twin boundaries. The stress-strain curve is shown to be irreversible and exhibits the hysteresis behavior typically characterizing dissipative systems. The influence of temperature, strain-rate or microstructural characteristics such as grain size or stacking fault energy on the onset of twinning were investigated e.g. by Meyers et al. (1995). In this Chapter, however, we limit ourselves to a rate-independent, isothermal, dislocation-based description of the origin and evolution of deformation twins.

5.2 Plane-Constrained Shear of Twins

Without going into detail about the lamellar twin structure, let us first consider a single crystal under plane-constrained shear. This problem is closely related to that presented in Section 4.4 where the plane-constrained shear problem of a bicrystal was investigated. In contrast to that analysis, we here assume varying volume fractions of twin and parent phase,

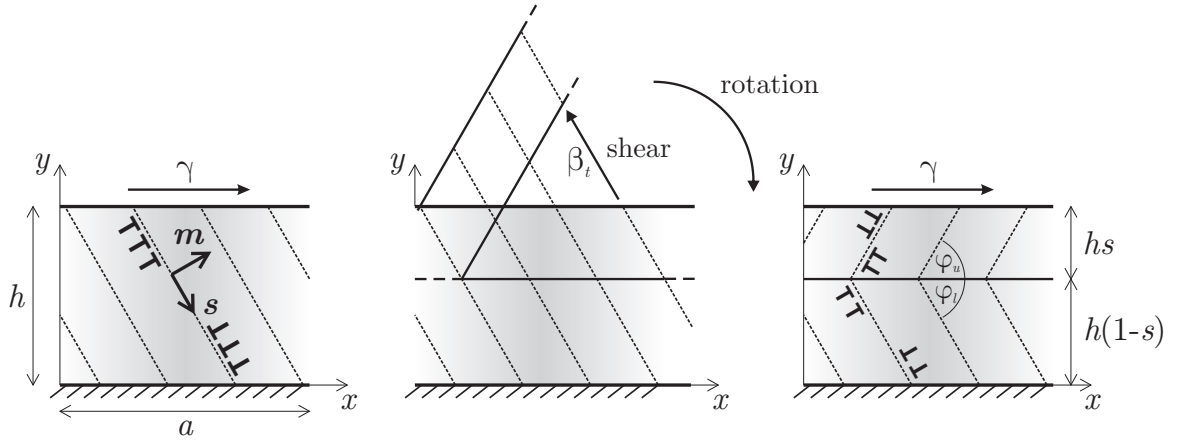


Figure 5.2: Schematic of the model crystal with one active slip system (\mathbf{s}, \mathbf{m}) and the formation of deformation twin by a twinning shear through movement of dislocations to the twin boundary followed by a rigid rotation.

which is modeled as a varying height ratio of the two perfectly-bonded single crystals. The analysis will hence follow the same line of reasoning outlined in Section 4.4.

Our model in this Chapter consists of a homogeneous crystal in form of a thin strip. Let the cross-section of the strip be the same as before, i.e. a rectangle of width a and height h , $0 \leq x \leq a$, $0 \leq y \leq h$. The crystal is subject to a plane-constrained shear deformation in a hard device enforcing on its upper and lower sides the displacements

$$u(0) = 0, \quad v(0) = 0, \quad u(h) = \gamma h, \quad v(h) = 0, \quad (5.1)$$

where $u(y)$ and $v(y)$ are the longitudinal and transverse displacements, respectively, with γ being the overall shear strain. First, we assume that the thickness of the strip in the z -direction L is large and the width a is much greater than the height h ($L \gg a \gg h$) to neglect end effects and to have the stresses and strains depending only on one variable y in the central part of the strip.

For the plane-strain state, the in-plane components of the strain tensor read

$$\varepsilon_{xx} = 0, \quad \varepsilon_{xy} = \varepsilon_{yx} = \frac{1}{2}u_{,y}, \quad \varepsilon_{yy} = v_{,y}. \quad (5.2)$$

If the overall shear strain γ is sufficiently small, then the crystal deforms elastically and $u = \gamma y$, $v = 0$ everywhere in the strip.

If γ exceeds some critical threshold, then edge dislocations may appear to reduce the crystal's energy. We assume that the crystal is initially uniform with only one active slip system, with the slip direction (or the direction of the Burgers vector) $\mathbf{s} = (\cos \varphi, \sin \varphi, 0)^T$ perpendicular to the z -axis and inclined at an angle φ with the x -axis, and the dislocation lines parallel to the z -axis. The normal vector to the slip plane is given by $\mathbf{m} = (-\sin \varphi, \cos \varphi, 0)^T$. Of course, one may wish to account for at least two independent slip systems to model the physical reality, especially as twinning and cross-slip are very well-known to be interacting mechanisms. However, to further simplify the analysis we shall limit our consideration to only one active slip system. Therefore, we have for the plastic distortion $\beta_{ij} = \beta s_i m_j$, and we may assume that β also depends on y only: $\beta = \beta(y)$ (translational invariance).

When loading the initially uniform single crystal, edge dislocations are nucleated along the given slip lines and accumulate upon further straining. As γ increases further, it might be energetically more preferable to form the twin phase by a twinning shear followed by a rigid rotation as depicted in Figure 5.2. Let the volume fraction of the twin phase be s , while the volume fraction of the parent phase be $1 - s$. For simplicity, we first limit our analysis to only one twin with the parent phase in the lower portion and the twin phase in the upper portion of the crystal (the order of phases does not qualitatively change results). The twinning shear is realized by the motion of already existing edge dislocations along slip lines to the twin boundary leaving the crystal again dislocation- and stress-free. The subsequent rigid rotation of the twin phase does not change the energy of the crystal but changes the existing slip system of the parent phase (s_l, m_l) with angle φ_l into the new slip system (s_u, m_u) of the twin phase with angle φ_u . From symmetry it follows that $\varphi_u = -\varphi_l = \varphi$.

Upon further straining the plastic distortion can be additively decomposed into

$$\beta_{ij}(y) = \begin{cases} \beta s_i^l m_j^l & \text{for } 0 < y < h(1 - s), \\ \beta s_i^u m_j^u + \beta_t s_i^l m_j^l + \omega_{ij} & \text{for } h(1 - s) < y < h, \end{cases} \quad (5.3)$$

with β_t denoting the constant twinning shear and ω_{ij} being the constant skew-symmetric rotation tensor. This additive split of the plastic distortion is a good approximation for small twinning shear and small rotation.

Because of the prescribed displacements (5.1) dislocations cannot penetrate the boundaries $y = 0$ and $y = h$, therefore

$$\beta(0) = \beta(h) = 0. \quad (5.4)$$

Furthermore, dislocations cannot penetrate the twin boundary either because the neighboring crystal does not admit the same slip system, so

$$\beta(h(1 - s)) = 0. \quad (5.5)$$

This assumption, again, is a simplification as effects such as dislocation emission, boundary sliding or boundary diffusion are not accounted for.

The in-plane components of the plastic strain tensor $\varepsilon_{ij}^p = \frac{1}{2}(\beta_{ij} + \beta_{ji})$ read

$$\begin{aligned} \varepsilon_{xx}^p &= -\frac{1}{2}\beta \sin 2\varphi - \frac{1}{2}\beta_t \sin 2\varphi_l, & \varepsilon_{xy}^p &= \frac{1}{2}\beta \cos 2\varphi + \frac{1}{2}\beta_t \cos 2\varphi_l, \\ \varepsilon_{yy}^p &= \frac{1}{2}\beta \sin 2\varphi + \frac{1}{2}\beta_t \sin 2\varphi_l, \end{aligned} \quad (5.6)$$

with the following piecewise-defined functions defined in the upper and lower part of the crystal:

$$[\beta(y), \varphi, \beta_t] = \begin{cases} [\beta_u(y), \varphi_u, \beta_t], & \text{for } h(1 - s) < y < h, \\ [\beta_l(y), \varphi_l, 0], & \text{for } 0 < y < h(1 - s). \end{cases} \quad (5.7)$$

As we intend to investigate deformation twinning, we assume the rotation of the upper part such that the active slip systems after rotation are symmetric with respect to the interface ($\varphi_u = -\varphi_l = \varphi$). A rather simple geometric analysis shows that in this case the twinning shear is given by

$$\beta_t = -2 \cot \varphi. \quad (5.8)$$

The described mechanism of twin formation is closely related to that of Bullough (1957), who proposed to accommodate deformation twinning by the same mechanism but with the restriction that β_t produces a shear of the parent crystal lattice by multiples of the Burgers' vector in each slip plane onto a stress-free reflected twin lattice. This description was argued to have only little physical significance due to the rather unrealistically high amount of dislocations required to form the high-angle tilt boundary. Here, we adopt Bullough's formal decomposition but assume only a minor rotation by a few degrees to create a low-angle phase boundary and to produce twin structures with alternating slip orientations deviating only by a small angle. This leads to a small twinning shear as observed e.g. by Reed-Hill and Abbashian (1994).

With (5.2) and (5.6) we obtain the in-plane components of the elastic strain tensor which follows from $\varepsilon_{ij}^e = \varepsilon_{ij} - \varepsilon_{ij}^p$,

$$\begin{aligned}\varepsilon_{xx}^e &= \frac{1}{2}(\beta \sin 2\varphi + \beta_T \sin 2\varphi_l), & \varepsilon_{xy}^e &= \frac{1}{2}(u_{,y} - \beta \cos 2\varphi - \beta_T \cos 2\varphi_l), \\ \varepsilon_{yy}^e &= v_{,y} - \frac{1}{2}(\beta \sin 2\varphi + \beta_T \sin 2\varphi_l).\end{aligned}\quad (5.9)$$

As β depends only on y , there are two non-zero components of Nye's dislocation density tensor $\alpha_{ij} = \epsilon_{jkl}\beta_{il,k}$ (Nye, 1953), with ϵ_{jkl} the permutation symbol, namely, $\alpha_{xz} = \beta_{,y} \sin \varphi \cos \varphi$ and $\alpha_{yz} = \beta_{,y} \sin^2 \varphi$ (see also the previous Chapter). Thus, the resultant Burgers' vector of all dislocations, whose lines cut the area perpendicular to the z -axis, is parallel to the slip direction \mathbf{s} . The scalar dislocation density equals

$$\rho = \frac{1}{b} |\beta_{,y} \sin \varphi|, \quad (5.10)$$

where b is the magnitude of the Burgers' vector. Note that we do not include a contribution to the dislocation density from the twinning shear β_t as well as from the rigid rotation due to the following reason. The gradient of piecewise constant β_T and the piecewise constant rotation do not produce a non-zero dislocation density within each part of the crystal but may produce a surface dislocation density arising from their jumps at the twin boundary, which would enter a surface energy. However, we consider metals and alloys exhibiting a low stacking fault energy (hence favoring deformation twinning) so that we may neglect this surface energy contribution.

Assuming that the crystal is elastically isotropic with equal elastic moduli, we write for the energy per unit volume (Berdichevsky, 2006a,b)

$$\Psi(\varepsilon_{ij}^e, \alpha_{ij}) = \frac{1}{2}\lambda (\varepsilon_{ii}^e)^2 + \mu \varepsilon_{ij}^e \varepsilon_{ij}^e + \mu k \ln \frac{1}{1 - \frac{|\beta_{,y} \sin \varphi|}{b\rho_s}}, \quad (5.11)$$

where μ and λ are the Lamé elastic moduli, ρ_s is the saturated dislocation density and k a material constant. The logarithmic nature of the energy of the dislocation network was extensively discussed in Section 4.1.3. Note that the constant rigid rotation ω_{ij} does not influence the bulk energy of the lattice with dislocations.

The first and second term of (5.11) describe the elastic energy, the last term represents the energy of the dislocation network. With (5.7), (5.9) and (5.11) the total energy functional

becomes

$$\begin{aligned} \mathcal{I}(u, v, \beta, s) = aL \int_0^h & \left[\frac{1}{2} \lambda v_{,y}^2 + \frac{1}{2} \mu (u_{,y} - \beta \cos 2\varphi - \beta_T \cos 2\varphi_l)^2 \right. \\ & + \frac{1}{4} \mu (\beta \sin 2\varphi + \beta_T \sin 2\varphi_l)^2 + \mu (v_{,y} - \frac{1}{2} \beta \sin 2\varphi - \frac{1}{2} \beta_T \sin 2\varphi_l)^2 \\ & \left. + \mu k \ln \frac{1}{1 - \frac{|\beta_{,y} \sin \varphi|}{b\rho_s}} \right] dy. \end{aligned} \quad (5.12)$$

As already mentioned, TWIP-alloys have rather low stacking fault energies, so the contribution of surface energy to this functional can be neglected.

With this total stored energy at hand, we can apply those thermodynamic principles outlined in Section 2.5.1 in order to model the evolution of all variables involved for a given deformation path. First, functional (5.12) can be reduced to a functional depending on $\beta(y)$ and s only by application of the principle of minimum potential energy. Indeed, by first fixing $\beta(y)$ and s and taking the variation of (5.12) with respect to u and v (i.e. by minimization with respect to the displacement field), we derive the equilibrium equations

$$\begin{aligned} \mu (u_{,y} - \beta \cos 2\varphi - \beta_T \cos 2\varphi_l)_{,y} &= 0, \\ [(\lambda + 2\mu) v_{,y} - \mu (\beta \sin 2\varphi + \beta_T \sin 2\varphi_l)]_{,y} &= 0. \end{aligned} \quad (5.13)$$

Integrating these equations and applying boundary conditions (5.1) as well as continuity of displacements and tractions at the twin boundary $y = h(1 - s)$, we obtain

$$\begin{aligned} u_{,y} &= \gamma + \beta \cos 2\varphi - \langle \beta \cos 2\varphi \rangle + \beta_T \cos 2\varphi_l - s\beta_t \cos 2\varphi_l, \\ v_{,y} &= \bar{\kappa} (\beta \sin 2\varphi - \langle \beta \sin 2\varphi \rangle + \beta_T \sin 2\varphi_l - s\beta_t \sin 2\varphi_l), \end{aligned} \quad (5.14)$$

where, as before, $\bar{\kappa} = \frac{\mu}{\lambda + 2\mu}$ and $\langle \cdot \rangle = \frac{1}{h} \int_0^h \cdot dy$.

Substitution of (5.14) into (5.12) leads to the energy functional in terms of β and s

$$\begin{aligned} \mathcal{I}(\beta, s) = aL\mu \int_0^h & \left[\frac{1}{2} (1 - \bar{\kappa}) (\beta \sin 2\varphi + \beta_T \sin 2\varphi_l)^2 + \frac{1}{2} \bar{\kappa} (\langle \beta \sin 2\varphi \rangle + s\beta_t \sin 2\varphi_l)^2 \right. \\ & \left. + \frac{1}{2} (\gamma - \langle \beta \cos 2\varphi \rangle - s\beta_t \cos 2\varphi_l)^2 + k \ln \frac{1}{1 - \frac{|\beta_{,y} \sin \varphi|}{b\rho_s}} \right] dy. \end{aligned} \quad (5.15)$$

For small up to moderate dislocation densities the logarithmic term in (5.15) may be approximated by keeping the leading two terms of a Taylor expansion only, i.e.

$$\ln \frac{1}{1 - \frac{|\beta_{,y} \sin \varphi|}{b\rho_s}} \cong \frac{|\beta_{,y} \sin \varphi|}{b\rho_s} + \frac{1}{2} \frac{\beta_{,y}^2 \sin^2 \varphi}{(b\rho_s)^2}, \quad (5.16)$$

so that

$$\begin{aligned} \mathcal{I}(\beta, s) = aL\mu \int_0^h & \left[\frac{1}{2} (1 - \bar{\kappa}) (\beta \sin 2\varphi + \beta_T \sin 2\varphi_l)^2 + \frac{1}{2} \bar{\kappa} (\langle \beta \sin 2\varphi \rangle + s\beta_t \sin 2\varphi_l)^2 \right. \\ & \left. + \frac{1}{2} (\gamma - \langle \beta \cos 2\varphi \rangle - s\beta_t \cos 2\varphi_l)^2 + k \left(\frac{|\beta_{,y} \sin \varphi|}{b\rho_s} + \frac{1}{2} \frac{\beta_{,y}^2 \sin^2 \varphi}{(b\rho_s)^2} \right) \right] dy. \end{aligned} \quad (5.17)$$

We shall further deal with this functional only.

Next, we need to provide a framework for the determination of the internal (plastic variables), i.e. the plastic distortion β . If dissipation is negligible, then, following the principle of minimum potential energy (2.222), the plastic distortion β and the volume fraction s minimize (5.17) under the constraints (5.4) and (5.5) as well as $0 \leq s \leq 1$. As before, the overall shear strain γ is regarded as a given function of time (control parameter), so one can study the evolution of the dislocation network and also of volume fractions, which accompany the change of γ .

If the resistance to dislocation and twin boundary motion cannot be neglected, then the energy minimization must be replaced by the Biot equation (2.246), modified for the particular situation here, viz. dissipation does not only occur due to changes of the plastic slips ($\dot{\gamma} \neq 0$) but also as a consequence of twin boundary motion ($\dot{s} \neq 0$). Thus, we arrive at the variational equation (Sedov, 1968; Carstensen et al., 2002)

$$\delta \mathcal{I} + aL \int_0^h \frac{\partial \Delta_p}{\partial \dot{\beta}} \delta \beta \, dy + aL \frac{\partial \Delta_t}{\partial \dot{s}} \delta s = 0, \quad (5.18)$$

where in case of rate-independent plasticity

$$\Delta_p = \tau_{\text{crit}} |\dot{\beta}|, \quad \Delta_t = \mu \varepsilon_t |\dot{s}|. \quad (5.19)$$

These functions are the dissipation potentials due to plastic slip and motion of the twin boundary, respectively, with τ_{crit} denoting the critical resolved shear stress, ε_t a material constant related to motion of the twin boundary, and the dot above a scalar function denoting its time derivative. Note that unlike for the energy minimization, where we neglected the surface energy of the twin boundary due to a low stacking fault energy, we here account for dissipation due to twin boundary motion because every such motion is accompanied by the collective motion of accumulated dislocations giving rise to dissipation.

Thus, from Eq. (5.18) we derive the evolution equations for $\dot{\beta} \neq 0$ and $\dot{s} \neq 0$

$$\frac{\partial \Delta_p}{\partial \dot{\beta}} = -\frac{\delta_\gamma \Psi}{\delta \beta}, \quad \frac{\partial \Delta_t}{\partial \dot{s}} = -\frac{\delta_\gamma \Psi}{\delta s}. \quad (5.20)$$

Note that the first equation corresponds exactly to (2.246) while the second is the corresponding counterpart for twin boundary motion. The right hand side of the flow rule (5.20)₁ is the negative variational derivative of the energy with respect to β

$$\varkappa = -\frac{\delta_\gamma \Psi}{\delta \beta} = -\frac{\partial \Psi}{\partial \beta} - \frac{\partial}{\partial y} \frac{\partial \Psi}{\partial \beta_{,y}}. \quad (5.21)$$

Similarly, the right hand side of (5.20)₂ is the negative variational derivative of the energy with respect to s , which we denote by \varkappa_s . Its computation will be presented in subsequent Sections. For $\dot{\beta} = 0$, the flow rule (5.20)₁ does not have to be satisfied: It is replaced by the equation $\dot{\beta} = 0$. Analogously, for $\dot{s} = 0$ we have instead of (5.20)₂ the evolution equation $\dot{s} = 0$. This exception is often formulated in terms of differential inclusions, see e.g. Section 2.5.1.

5.3 Energy Minimizers and the Initiation of Slip and Twinning

5.3.1 Deformation of the Crystal at Zero Dissipation

First, we investigate the plastic deformation of the model twin at zero dissipation and thereby estimate the onset of plastic flow and of twinning. The crystal is initially uniform and beha-

ves elastically. From experimental evidence and also from the problem formulation above we conclude two competing mechanisms of the microstructure to reduce the crystal's energy upon further straining. On the one hand, macroscopic plastic slip may occur throughout the entire crystal along the principal slip system (s, m) and we should find a distinct threshold for the first occurrence of $\beta \neq 0$ (onset of plastic flow). On the other hand, we can expect a twinning threshold where deformation twins begin to grow into the material, characterized by $s > 0$. Both thresholds will be determined from energy minimization.

If the resistance to dislocation and twin boundary motion can be neglected (and hence the energy dissipation is zero), the determination of $\beta(y)$ and s reduces to the minimization of the total energy (5.17). Let us make use of the same dimensionless quantities introduced in the previous Chapter, i.e.

$$E = \frac{b\rho_s}{aL\mu}\mathcal{I}, \quad \xi = b\rho_s y. \quad (5.22)$$

The dimensionless variable ξ changes on the interval $(0, H)$ where $H = b\rho_s h$. Functional (5.17) reduces to

$$E(\beta, s) = \int_0^H \left[\frac{1}{2}(1 - \bar{\kappa}) (\beta \sin 2\varphi + \beta_t \sin 2\varphi_l)^2 + \frac{1}{2}\bar{\kappa} (\langle \beta \sin 2\varphi \rangle + s\beta_t \sin 2\varphi_l)^2 \right. \\ \left. + \frac{1}{2} (\gamma - \langle \beta \cos 2\varphi \rangle - s\beta_t \cos 2\varphi_l)^2 + k(|\beta'| \sin \varphi| + \frac{1}{2}\beta'^2 \sin^2 \varphi) \right] d\xi, \quad (5.23)$$

where the prime denotes differentiation with respect to ξ . We minimize functional (5.23) among functions satisfying the boundary conditions

$$\beta(0) = \beta(h(1 - s)) = \beta(h) = 0. \quad (5.24)$$

The results obtained in (Berdichevsky and Le, 2007; Le and Sembriring, 2008a,b) and in the previous Chapter, as well as from discrete dislocation simulations (Needleman and Van der Giessen, 2001; Shu et al., 2001), suggest to seek the minimizer in the form of thin boundary layers of concentrated dislocations, leaving the central part of each crystal dislocation-free. Thus, we write

$$\beta(\xi) = \begin{cases} \beta_l(\xi), & \text{for } \xi \in (0, l_l), \\ \beta_{lm}, & \text{for } \xi \in (l_l, H(1 - s) - l_l), \\ \beta_l(H(1 - s) - \xi), & \text{for } \xi \in (H(1 - s) - l_l, H(1 - s)), \\ \beta_u(\xi), & \text{for } \xi \in (H(1 - s), H(1 - s) + l_u), \\ \beta_{um}, & \text{for } \xi \in (H(1 - s) + l_u, H - l_u), \\ \beta_u(H(2 - s) - \xi), & \text{for } \xi \in (H - l_u, H), \end{cases} \quad (5.25)$$

where β_{lm} and β_{um} are constants, l_l and l_u are unknown constant boundary layer thicknesses with $0 \leq l_l \leq \frac{1}{2}H(1 - s)$ and $0 \leq l_u \leq \frac{1}{2}Hs$, and $\beta_l(l_l) = \beta_{lm}$ and accordingly $\beta_u(H(1 - s) + l_u) = \beta_{um}$. We must find functions $\beta_l(\xi)$, $\beta_u(\xi)$ and constants β_{lm} , β_{um} , l_l and l_u .

Varying the above energy functional (5.23) with respect to β_l and β_u from (5.25), we arrive at the following set of differential equations:

$$(1 - \bar{\kappa})\beta_l \sin^2 2\varphi_l + \bar{\kappa} (\langle \beta \sin 2\varphi \rangle + s\beta_t \sin 2\varphi_l) \sin 2\varphi_l \\ - (\gamma - \langle \beta \cos 2\varphi \rangle - s\beta_t \cos 2\varphi_l) \cos 2\varphi_l - k\beta_l'' \sin^2 \varphi_l = 0, \quad (5.26)$$

$$(1 - \bar{\kappa}) (\beta_u \sin 2\varphi_u + \beta_t \sin 2\varphi_l) \sin 2\varphi_u + \bar{\kappa} (\langle \beta \sin 2\varphi \rangle + s\beta_t \sin 2\varphi_l) \sin 2\varphi_u \\ - (\gamma - \langle \beta \cos 2\varphi \rangle - s\beta_t \cos 2\varphi_l) \cos 2\varphi_u - k\beta_u'' \sin^2 \varphi_u = 0. \quad (5.27)$$

on $(0, l_l)$ and $(H(1-s), H(1-s) + l_u)$, respectively, where $\beta_l(\xi)$ and $\beta_u(\xi)$ are subject to the boundary conditions

$$\beta_l(0) = 0, \quad \beta_l(l_l) = \beta_{lm}, \quad \beta_u(H(1-s)) = 0, \quad \beta_u(H(1-s) + l_u) = \beta_{um}. \quad (5.28)$$

Variation of (5.23) with respect to l_l and l_u from (5.25) gives two additional boundary conditions at $\xi = l_l$ and $\xi = H(1-s) + l_u$, respectively,

$$\beta'_l(l_l) = 0, \quad \beta'_u(H(1-s) + l_u) = 0, \quad (5.29)$$

which means that the dislocation density must be continuous. Varying the energy functional with respect to β_{lm} and β_{um} from (5.25) and applying $\varphi_u = -\varphi_l = \varphi$, we obtain conditions for β_{lm} at $\xi = l_l$ and β_{um} at $\xi = H(1-s) + l_u$,

$$2k |\sin \varphi| \operatorname{sign}(\beta_l) + (H(1-s) - 2l_l) [-\gamma \cos 2\varphi + (1 - \bar{\kappa})\beta_{lm} \sin^2 2\varphi - \bar{\kappa} \sin 2\varphi (\langle \beta \sin 2\varphi \rangle - s\beta_t \sin 2\varphi) + \cos 2\varphi (\langle \beta \cos 2\varphi \rangle + s\beta_t \cos 2\varphi)] = 0 \quad (5.30)$$

and

$$2k |\sin \varphi| \operatorname{sign}(\beta_u) + (Hs - 2l_u) [-\gamma \cos 2\varphi + (1 - \bar{\kappa}) \sin^2 2\varphi (\beta_{um} - \beta_t) + \bar{\kappa} \sin 2\varphi (\langle \beta \sin 2\varphi \rangle - s\beta_t \sin 2\varphi) + \cos 2\varphi (\langle \beta \cos 2\varphi \rangle + s\beta_t \cos 2\varphi)] = 0, \quad (5.31)$$

respectively. Finally, variation of (5.23) with respect to s yields the following additional condition to determine s

$$\beta_t [\cos 2\varphi (\langle \beta \cos 2\varphi \rangle - \gamma) - \bar{\kappa} \sin 2\varphi \langle \beta \sin 2\varphi \rangle] + \frac{1}{2}(1 - \bar{\kappa})\beta_t^2 \sin^2 2\varphi + s\beta_t^2 (\cos^2 2\varphi + \bar{\kappa} \sin^2 2\varphi) - \frac{1}{2}k \sin^2 \varphi [\beta_u'^2(H(1-s)) - \beta_l'^2(H(1-s))] = 0, \quad (5.32)$$

where the latter term stems from the Weierstrass-Erdmann corner condition (Gelfand and Fomin, 2000) and characterizes the jump of the dislocation density at the moving interface.

Eqs. (5.26), (5.28) and (5.29) yield the solution

$$\beta_l(\xi) = \beta_{lp} [1 - \cosh \eta \xi + \tanh \eta l_l \sinh \eta \xi], \quad (5.33)$$

$$\beta_u(\xi) = \beta_{up} [1 - \cosh \eta (\xi - H(1-s)) + \tanh \eta l_u \sinh \eta (\xi - H(1-s))], \quad (5.34)$$

with

$$\eta = 2\sqrt{\frac{1 - \bar{\kappa}}{k}} |\cos \varphi| \quad (5.35)$$

and

$$\begin{aligned} \beta_{lp} &= \frac{\cos 2\varphi (\gamma - \langle \beta \cos 2\varphi \rangle) + \bar{\kappa} \sin 2\varphi \langle \beta \sin 2\varphi \rangle - s\beta_t (\cos^2 2\varphi + \bar{\kappa} \sin^2 2\varphi)}{(1 - \bar{\kappa}) \sin^2 2\varphi}, \\ \beta_{up} &= \frac{\cos 2\varphi (\gamma - \langle \beta \cos 2\varphi \rangle) - \bar{\kappa} \sin 2\varphi \langle \beta \sin 2\varphi \rangle - s\beta_t (\cos^2 2\varphi - \bar{\kappa} \sin^2 2\varphi)}{(1 - \bar{\kappa}) \sin^2 2\varphi} + \beta_t \end{aligned} \quad (5.36)$$

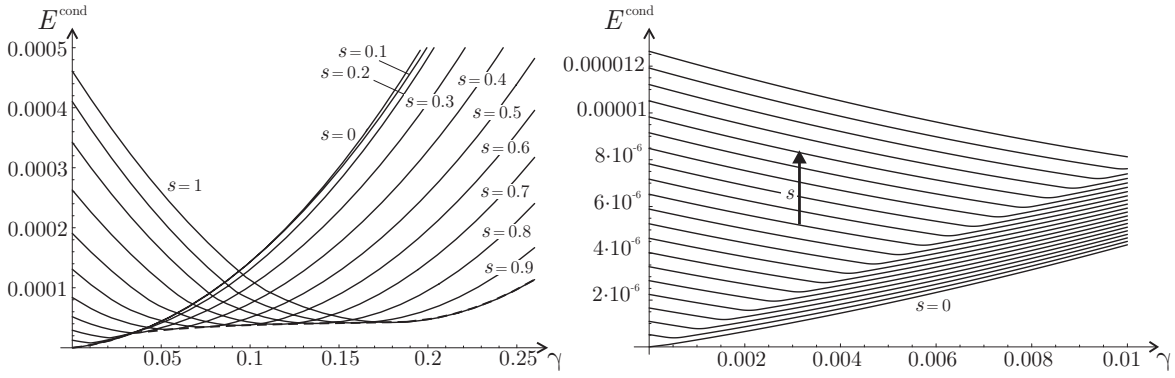


Figure 5.3: Condensed energy $E^{\text{cond}}(s, \gamma) = \min E(\beta_l, \beta_u, l_l, l_u)$ versus overall shear strain γ for various volume fractions s (left) with a magnification (right) for small values of s and small strains (clearly indicating that $s = 0$ minimizes the energy in that region). The actual energy with evolving s follows the path of least energy; computed with $\varphi = 87^\circ$, $h = 100\mu\text{m}$ and material parameters from Table 5.1.

along with $\beta_{im} = \beta_{ip}(1 - 1/\cosh \eta l_i)$, $i = l, u$. The average quantities can be obtained as

$$\langle \beta \sin 2\varphi \rangle = \frac{\sin 2\varphi}{H} [-2\beta_{lp}(l_l - \tanh(\eta l_l)/\eta) - \beta_{lm}(H(1-s) - 2l_l) + 2\beta_{up}(l_u - \tanh(\eta l_u)/\eta) + \beta_{um}(Hs - 2l_l)], \quad (5.37)$$

$$\langle \beta \cos 2\varphi \rangle = \frac{\cos 2\varphi}{H} [2\beta_{lp}(l_l - \tanh(\eta l_l)/\eta) + \beta_{lm}(H(1-s) - 2l_l) + 2\beta_{up}(l_u - \tanh(\eta l_u)/\eta) + \beta_{um}(Hs - 2l_l)]. \quad (5.38)$$

Applying solutions (5.33) and (5.34) together with (5.36) and (5.37) to the energy functional (5.23), we can write the total energy of the crystal as (not written out here for brevity)

$$E = E(\beta_{lp}, \beta_{up}, l_l, l_u, s). \quad (5.39)$$

To find the solution, we must find the global minimum of the total energy with respect to these quantities with additional constraints

$$0 \leq s \leq 1, \quad 0 \leq l_l \leq \frac{1}{2}H(1-s), \quad 0 \leq l_u \leq \frac{1}{2}Hs. \quad (5.40)$$

5.3.2 Onset of Twinning and Number of Twins

As we intend to model the origin of twinning and the evolution of deformation twins, one of the key objectives is to find the onset and the evolution of the volume fraction $s > 0$ in the present model. Figure 5.3 illustrates the total energy as a function of the shear strain γ for fixed values of $0 \leq s \leq 1$ and the minimizing path, along which s changes from

Material	μ (GPa)	ν	b (Å)	ρ_s (m ⁻²)	k
Aluminum	26.3	0.33	2.5	$1.834 \cdot 10^{15}$	0.000156

Table 5.1: Material characteristics

0 to 1. Note that s does not increase continuously from 0 but eventually jumps from 0 to some finite value as soon as the twinning threshold is reached. The right image shows a magnification for small strains, which clearly indicates that $s = 0$ (untwinned parent phase) exhibits minimal energy for considerable strains.

Figure 5.4 shows the evolution of all model parameters obtained from numerical minimization of (5.39) as functions of the shear strain γ . Results show that plastic slip occurs first at a rather small strain (in this example $\gamma_{en} \approx 6.83 \cdot 10^{-5}$) and dislocations are nucleated and accumulate in the uniform crystal. Since this threshold occurs before the onset of twinning, the threshold value is the same as for a single crystal, which was presented by Le and Sembriring (2008a):

$$\gamma_{en} = \frac{2k \sin \varphi}{hb\rho_s |\cos 2\varphi|}. \quad (5.41)$$

Upon further straining twinning becomes energetically favorable and s jumps to some finite value (here at $\gamma_{tw} \approx 0.030$). From this point on, all existing dislocations are consumed by the newly created twin phase, the parent part of the crystal remains elastic whereas the twin crystal starts to nucleate and accumulate dislocations. Note that these results are only valid if no dissipation due to dislocation motion occurs. In physical reality, dislocation motion is required to nucleate and arrange the twin boundary such that not all dislocations are consumed by the newly created twin phase, but both phases exhibit plastic deformation. This behavior can be observed in Section 5.4 where the dissipation is no longer neglected. Thanks to the finite jump of s , free space (or mean free path) is provided for the immediate dislocation pile-up in the twin phase. Further straining results in a steady increase of s , until finally $s = 1$, i.e. the parent phase vanishes, and the whole crystal exhibits dislocation pile-up along the twin slip system.

So far, we have only considered the volume fractions of parent and twin phases but never specified the number of twins in the crystal. Now, let us qualitatively estimate the number of twins that arise during deformation twinning in the present model. Assuming n twins of equal height and volume ratio within each crystal, a rather simple analysis shows that, with the constraints

$$\beta(0) = \beta(H(i-s)/n) = \beta(Hi/n) = 0, \quad i = 1, \dots, n, \quad (5.42)$$

and the ansatz

$$\beta(\xi) = \beta(\xi - H(i-1)/n), \quad \text{for } H(i-1)/n \leq \xi \leq Hi/n, \quad i = 1, \dots, n, \quad (5.43)$$

we arrive at the very same solution for β given in (5.33), (5.34) if we replace H by H/n , i.e. we obtain a periodic deformation of the crystal where each single twin exhibits the same deformation computed above.

To estimate the number of twins, we extend the total energy of the crystal by also taking into account the energy stored at the side surfaces of the crystal (i.e. at $x = 0$ and $x = a$), where the following (rigid) boundary conditions are assumed

$$u(0, \xi) = u(a, \xi) = \gamma\xi, \quad v(0, \xi) = v(a, \xi) = 0. \quad (5.44)$$

Prescribing displacements on these surfaces in a hard device is equivalent to placing the model crystal between ideally rigid neighboring grains of a polycrystal. Thus, these surfaces

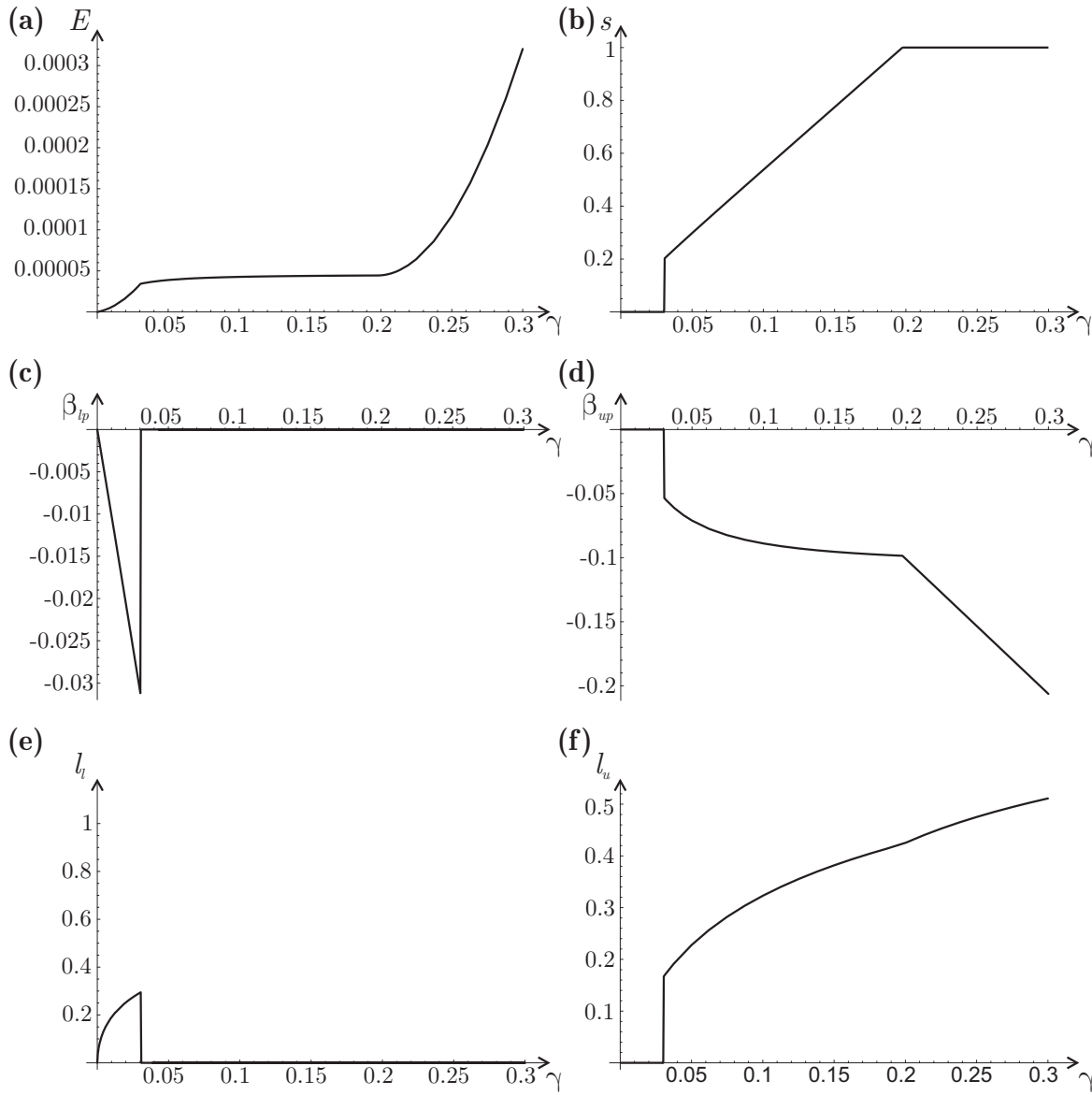


Figure 5.4: Results from minimizing the total energy functional: (a) total energy, (b) volume fraction s , (c) β_{lp} , (d) β_{up} , (e) l_l and (f) l_u , as functions of the overall shear strain γ . Computed with $\varphi = 87^\circ$, $h = 100\mu\text{m}$ and material properties from Table 5.1.

cannot deform in the twin-like zig-zag pattern resulting from the above model. At each of the two surfaces a thin boundary layer of thickness d is deformed elastically to accommodate the rigid boundaries (see Figure 5.5). Furthermore, we can divide the inner energy of the crystal into energy of the strained layers $E_{lay} = \mu(a - 2d)L E/b\rho_s$ (with E the dimensionless energy calculated above) and surface energy of the twin boundaries E_{sf} . Before, we did not account for this surface energy due to the low stacking fault energy. Here, however, as the number of twins and hence the number of twin boundaries may become quite high, we include this surface energy simply as $E_{sf} = 2n\Gamma(a - 2d)L$ with Γ as the constant surface energy of the twin boundaries. Now, we have two competing contributions to the total crystal energy which consists of inner energy $E_{in} = E_{sf} + E_{lay}$ stored in the central part of the crystal, as described above, and the total elastic energy of the side boundary layers E_{bd} (grey boundary regions in Figure 5.5).

As the number of twins n increases, E_{in} increases due to the rising number of twin boun-

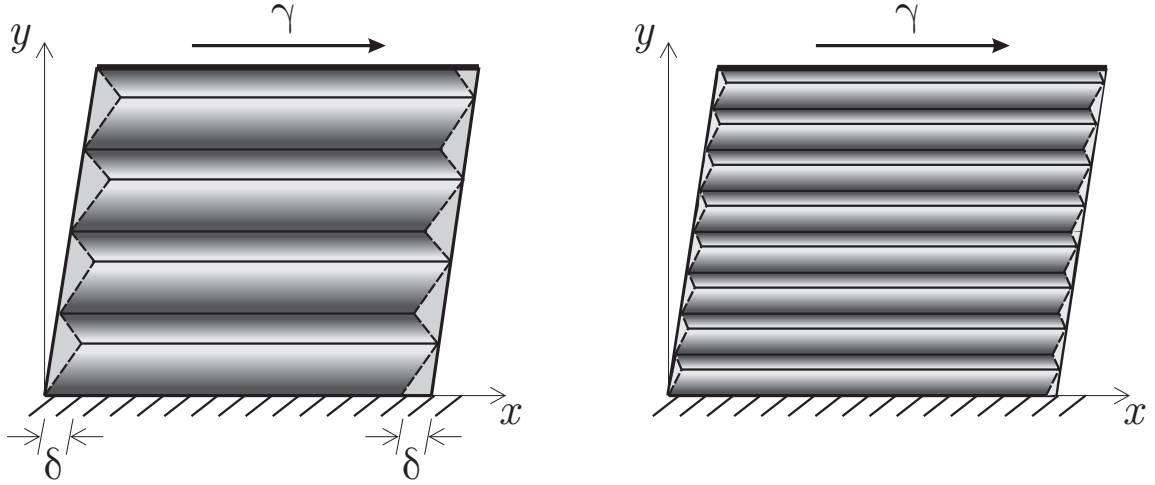


Figure 5.5: Schematic illustrating the boundary regions (thickness δ) with stored elastic energy to accommodate rigid side boundaries (for $n = 4$ and $n = 8$).

daries with stress concentrations, and simultaneously E_{bd} decreases with decreasing zig-zagging of the boundary. For a rather qualitative picture, let us take the evolution of volume ratio s as from Figure 5.4, obtain the boundary zig-zag patterns as a function of n and finally minimize the normalized total energy $E_{tot} = E_{in} + E_{bd}$ with respect to the number of twins n . We thereby need to make an assumption about the boundary layer thickness d , which we assume to be of the same order of magnitude as the depth of the zig-zag structure; the exact value is unimportant for a qualitative estimate. Numerical results for evolving n as a function of γ via the outlined method are shown in Figure 5.6 with $\Gamma = 0.044 \text{ J/m}^2$ which is the coherent twin boundaries energy of copper (Hirth and Lothe, 1982). At the onset of twinning the number of twins to minimize the total energy exhibits a rather high value (here, $n \approx 100$), then decreases and increases again to a local maximum towards the middle of twin formation, and finally moderately decreasing until n approaches 1 as the crystal detwins and s approaches 1. Note, however, that this result is sensitive to changes of the surface energy of the twin boundary and other parameters.

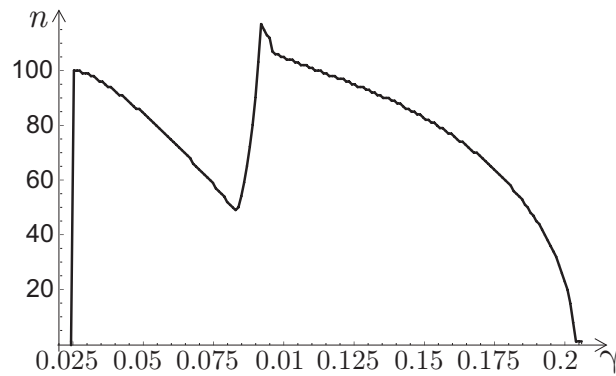


Figure 5.6: Evolution of the number of twins n with increasing overall shear strain γ . For computations we used $\varphi = 87^\circ$, $h = 100 \mu\text{m}$, $a = h$, $\Gamma = 0.044 \text{ J/m}^2$ and material properties from Table 5.1; d is the triangle thickness of the side boundaries.

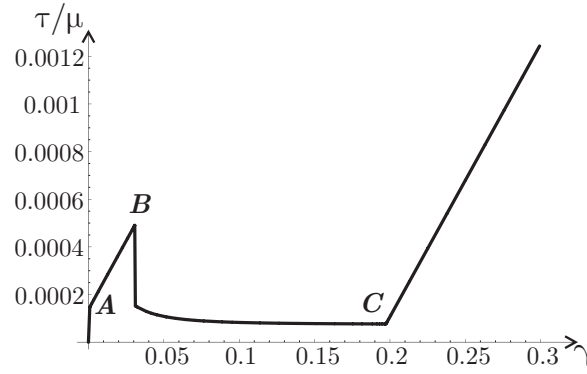


Figure 5.7: Normalized shear stress versus shear strain curve (computed with the same numerical values as above). Note the change of slope upon the onset of plastic flow (point A) and the sharp load drop at the initiation of deformation twins (point B). At point C the entire crystal has adopted the twin lattice and the again uniform single crystal exhibits further hardening.

5.3.3 Stress-Strain Behavior at Zero Dissipation

To complete this Section, let us calculate the shear stress τ which is a measurable quantity. The normalized shear stress becomes (with γ_{en} from (5.41))

$$\frac{\tau}{\mu} = \begin{cases} \gamma, & \gamma \leq \gamma_{en}, \\ \gamma - (\langle \beta \rangle + s\beta_t) \cos 2\varphi, & \gamma > \gamma_{en}. \end{cases} \quad (5.45)$$

Below the energetic threshold for the onset of plastic slip, the crystal behaves elastically. Above this yield stress (point A in Figure 5.7) the crystal exhibits plastic flow. The second term of (5.45) for $\gamma > \gamma_{en}$ causes hardening due to dislocation pile-up. The same term is also responsible for a load drop upon the initiation of deformation twinning at point B, and a subsequent softening during the evolution of phases up to point C, as can clearly be seen in Figure 5.7. The load drop and the subsequent softening behavior can be explained by the spontaneous formation and subsequent increase of the volume fraction of the twin phase near the second minimum of the energy, which considerably lowers the total energy of the crystal. Since the stress is derivable from the energy of the crystal, the load drop and the softening behavior become obvious. Note that upon unloading the crystal recovers reversibly along the same stress-strain path, and all nucleated dislocation annihilate and deformation twins vanish due to the absence of dissipation.

5.4 Plastic Deformation at Non-Zero Dissipation

5.4.1 Evolution of Plastic Distortion and Volume Fractions

Now that we have shown the existence of energetic thresholds for both plastic flow and deformation twinning, we analyze the deformation of the model crystal at non-zero dissipation which gives a more realistic picture. If the resistance to dislocation motion (and hence the dissipation of energy) cannot be neglected, the plastic distortion may evolve only if the yield condition $|\mathcal{K}| = \tau_{crit}$ is satisfied, the volume ratio s may only change if the condition

$|\varkappa_s| = \varepsilon_s \mu$ holds. If $|\varkappa| < \tau_{\text{crit}}$ or $|\varkappa_s| < \varepsilon_s \mu$, then β or s , respectively, is frozen and remains unaltered.

Computing the variational derivative of (5.23), we derive from (5.20) the dimensionless yield conditions for β in the parent and twin part of the crystal

$$|\Xi_l(\gamma)| = |(1 - \bar{\kappa})\beta_l \sin^2 2\varphi - \cos 2\varphi(\gamma - \langle \beta \cos 2\varphi \rangle)| \quad (5.46)$$

$$\begin{aligned} & -\bar{\kappa} \sin 2\varphi \langle \beta \sin 2\varphi \rangle + s\beta_t(\cos^2 2\varphi + \bar{\kappa} \sin^2 2\varphi) - k\beta_l'' \sin^2 \varphi = \tau_{\text{crit},l}/\mu, \\ |\Xi_u(\gamma)| &= |(1 - \bar{\kappa})(\beta_u - \beta_t) \sin^2 2\varphi - \cos 2\varphi(\gamma - \langle \beta \cos 2\varphi \rangle)| \quad (5.47) \\ & + \bar{\kappa} \sin 2\varphi \langle \beta \sin 2\varphi \rangle + s\beta_t(\cos^2 2\varphi - \bar{\kappa} \sin^2 2\varphi) - k\beta_u'' \sin^2 \varphi = \tau_{\text{crit},u}/\mu, \end{aligned}$$

and the evolution equation for s

$$\begin{aligned} |\Xi_\varepsilon(\gamma)| &= |\beta_t(\cos 2\varphi(\langle \beta \cos 2\varphi \rangle - \gamma) - \bar{\kappa} \langle \beta \sin 2\varphi \rangle \sin 2\varphi) + \frac{1}{2}(1 - \bar{\kappa})\beta_t^2 \sin^2 2\varphi \\ & + s\beta_t^2(\cos^2 2\varphi + \bar{\kappa} \sin^2 2\varphi) - \frac{1}{2}k \sin^2 \varphi (\beta_u^2(H(1 - s)) - \beta_l^2(H(1 - s)))| = \varepsilon_t. \end{aligned} \quad (5.48)$$

We first analyze the behavior upon loading: Thanks to the symmetry of the slip systems we may assume that $\tau_{\text{crit},l} = \tau_{\text{crit},u} = \tau_{\text{crit}}$. Let us introduce the critical shear strain for the onset of plastic flow

$$\gamma_{cr} = \tau_{\text{crit}}/\mu \cos 2\varphi \quad (5.49)$$

and the deviation of $\gamma(t)$ from the critical strain,

$$\gamma_r = \gamma - \gamma_{cr} \quad (5.50)$$

Furthermore, we must have $\dot{s} \geq 0$, and $\beta \approx 0$ at the beginning of loading. We hence simplify (5.46), (5.47) and (5.48) to the set of evolution equations

$$\Xi_l(\gamma_r) = 0, \quad \Xi_u(\gamma_r) = 0, \quad \Xi_\varepsilon(\gamma) = \varepsilon_t. \quad (5.51)$$

The analogous problems solved in Chapter 4 suggest that the solution for β_l and β_u is symmetric within each part, i.e.

$$\begin{aligned} \beta_l(\xi) &= \beta_l(H(1 - s) - \xi) & \text{for } \xi \in (\tfrac{1}{2}H(1 - s), H(1 - s)), \\ \beta_u(\xi) &= \beta_u(H(2 - s) - \xi) & \text{for } \xi \in (H - \tfrac{1}{2}Hs, H). \end{aligned} \quad (5.52)$$

Functions $\beta_l(\xi)$ and $\beta_u(\xi)$ are determined from Eqs. (5.51)_{1,2} and the boundary conditions

$$\beta_l(0) = 0, \quad \beta_u(H(1 - s)) = 0, \quad \beta_l'(\tfrac{1}{2}H(1 - s)) = 0, \quad \beta_u'(H - \tfrac{1}{2}Hs) = 0. \quad (5.53)$$

The first and second conditions mean that dislocations cannot reach the boundary of the regions because of the prescribed displacements. The third and fourth conditions follow from the continuity of plastic distortion and the symmetry properties (5.52).

Eqs. (5.51) and (5.53) admit the solution

$$\begin{aligned} \beta_l(\xi) &= \beta_{lp} \left[1 - \cosh \eta \xi + \tanh(\tfrac{1}{2}\eta H(1 - s)) \sinh \eta \xi \right], \\ \beta_u(\xi) &= \beta_{up} \left[1 - \cosh \eta (\xi - H(1 - s)) + \tanh(\tfrac{1}{2}\eta Hs) \sinh \eta (\xi - H(1 - s)) \right], \end{aligned} \quad (5.54)$$

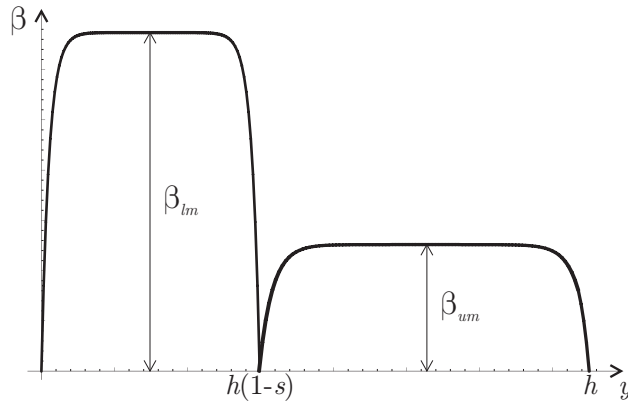


Figure 5.8: Qualitative solution for the plastic distortion β throughout the crystal.

with

$$\eta = 2\sqrt{\frac{1-\bar{\kappa}}{k}} |\cos \varphi| \quad (5.55)$$

and

$$\begin{aligned} \beta_{lp} &= \frac{\cos 2\varphi (\gamma_r - \langle \beta \cos 2\varphi \rangle) + \bar{\kappa} \sin 2\varphi \langle \beta \sin 2\varphi \rangle - s\beta_t(\cos^2 2\varphi + \bar{\kappa} \sin^2 2\varphi)}{(1 - \bar{\kappa}) \sin^2 2\varphi}, \\ \beta_{up} &= \frac{\cos 2\varphi (\gamma_r - \langle \beta \cos 2\varphi \rangle) - \bar{\kappa} \sin 2\varphi \langle \beta \sin 2\varphi \rangle - s\beta_t(\cos^2 2\varphi - \bar{\kappa} \sin^2 2\varphi)}{(1 - \bar{\kappa}) \sin^2 2\varphi} + \beta_t. \end{aligned} \quad (5.56)$$

The average quantities read

$$\begin{aligned} \langle \beta \sin 2\varphi \rangle &= \frac{2 \sin 2\varphi}{H} \left[-\beta_{lp} \left(\frac{1}{2} H (1-s) - \tanh \left(\frac{1}{2} \eta H (1-s) \right) / \eta \right) \right. \\ &\quad \left. + \beta_{up} \left(\frac{1}{2} H s - \tanh \left(\frac{1}{2} \eta H s \right) / \eta \right) \right], \end{aligned} \quad (5.57)$$

$$\begin{aligned} \langle \beta \cos 2\varphi \rangle &= \frac{2 \cos 2\varphi}{H} \left[\beta_{lp} \left(\frac{1}{2} H (1-s) - \tanh \left(\frac{1}{2} \eta H (1-s) \right) / \eta \right) \right. \\ &\quad \left. + \beta_{up} \left(\frac{1}{2} H s - \tanh \left(\frac{1}{2} \eta H s \right) / \eta \right) \right]. \end{aligned} \quad (5.58)$$

Figure 5.8 qualitatively sketches the plastic distortion within each part of the crystal, which is of the same type as the solutions presented in Section 4.

Solving the above evolution equations is numerically cumbersome. Instead, we transform the problem into a minimization problem, which can easily be solved by using standard energy minimization techniques. Therefore, we modify the total energy functional by removing the linear term in β' and adding an artificial term to obtain

$$\begin{aligned} E^*(\beta, s) &= \int_0^H \left[\frac{1}{2} (1 - \bar{\kappa}) (\beta \sin 2\varphi + \beta_T \sin 2\varphi_l)^2 + \frac{1}{2} \bar{\kappa} (\langle \beta \sin 2\varphi \rangle + s\beta_t \sin 2\varphi_l)^2 \right. \\ &\quad \left. + \frac{1}{2} (\gamma_r - \langle \beta \cos 2\varphi \rangle - s\beta_t \cos 2\varphi_l)^2 + \frac{1}{2} k \beta'^2 \sin^2 \varphi + s\epsilon_t \right] d\xi. \end{aligned} \quad (5.59)$$

$E^*(\beta, s)$ can be regarded as an accumulated energy functional for standard dissipative solids, and it is simple to verify that the minimizer of E^* automatically satisfies the evolution equations, as they are the exact Euler equations thereof.

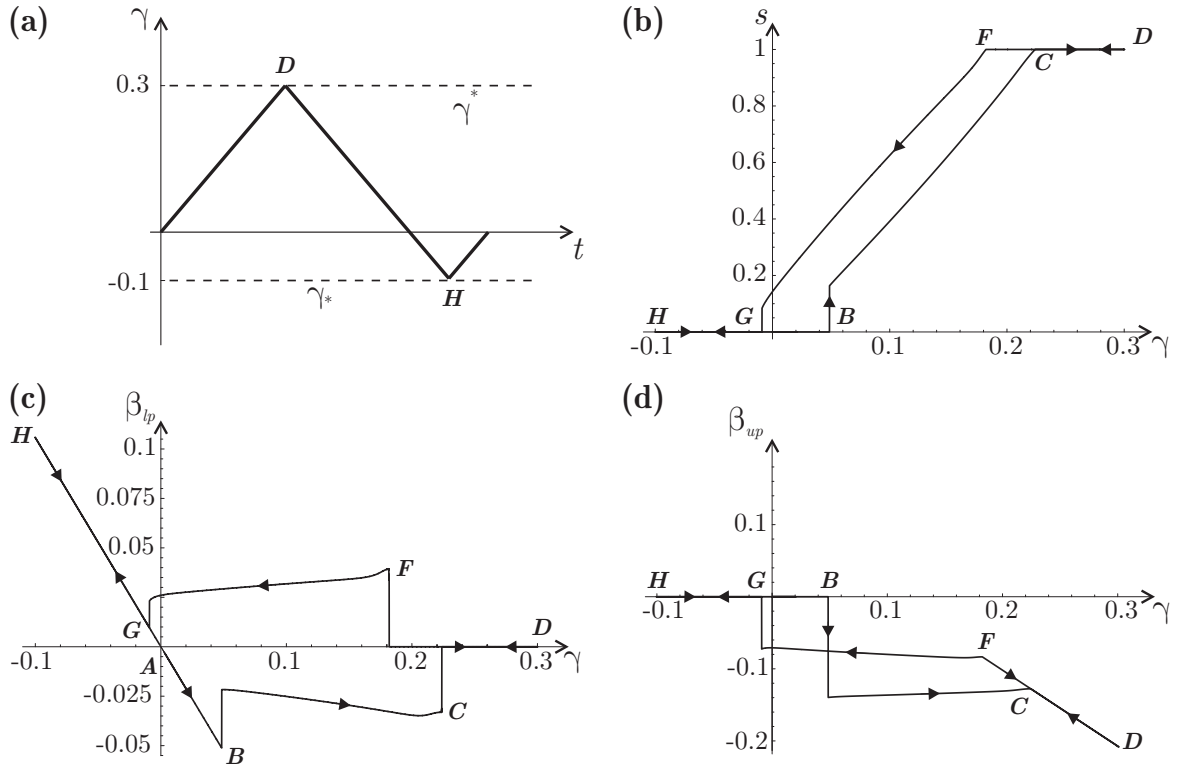


Figure 5.9: Results from minimizing the total energy functional: (a) loading path $\gamma(t)$, (b) volume fraction s , (c) β_{lp} , (d) β_{up} as functions of the overall shear strain γ . Computed with $\varphi = 87^\circ$, $h = 100\mu\text{m}$, $\varepsilon_t = 5 \cdot 10^{-5}$ and remaining material properties from Table 5.1.

Applying solution (5.54) together with (5.56) and (5.57) to the energy functional (5.59), we may write the total energy of the crystal as (again not written out here for brevity)

$$E^* = E^*(\beta_{lp}, \beta_{up}, s). \quad (5.60)$$

To find the solution, we must minimize the modified energy (5.60) with respect to these quantities with the additional constraint $0 \leq s \leq 1$.

After reaching $\gamma^* > \gamma_{cr}$, we unload the crystal by decreasing γ . Since \varkappa becomes smaller than τ_{crit} , β_{lp} and β_{up} do not change until, respectively,

$$-\Xi_l(\gamma) = \gamma_{cr} \cos 2\varphi, \quad -\Xi_u(\gamma) = \gamma_{cr} \cos 2\varphi \quad (5.61)$$

Analogously, the volume fraction s is frozen until

$$\Xi_\varepsilon(\gamma) = -\varepsilon_t. \quad (5.62)$$

From (5.61) we can see that plastic slip in both parts of the crystal begins when $\gamma - (\gamma^* - \gamma_{cr}) = -\gamma_{cr}$, i.e. for $\gamma = \gamma^* - 2\gamma_{cr}$. From that value of γ , the yield condition for β reads $\varkappa = -\tau_{crit}$ (and accordingly for s) leading to the set of evolution equations

$$\Xi_l(\gamma_l) = 0, \quad \Xi_u(\gamma_l) = 0, \quad \Xi_\varepsilon(\gamma) = -\varepsilon_t, \quad (5.63)$$

where we use

$$\gamma_l = \gamma + \gamma_{cr}. \quad (5.64)$$

Comparing Eqs. (5.51) to (5.63), it becomes apparent that the solution during unloading can be obtained in exactly the same manner as before, i.e. by minimizing (5.60) if we replace γ_r by γ_l and ε_t by $-\varepsilon_t$ in (5.59).

Figure 5.9 illustrates the results from numerical minimization. Graphs illustrate the evolution of β_{lp} and β_{up} as well as s as functions of the overall shear strain γ for the closed loading path shown (with $\gamma_{cr} = \gamma_{en}$ from energy minimization, $\gamma^* = 0.3$ and $\gamma_* = -0.1$). As for zero dissipation, the onset of twinning (point B) appears at higher strains than the onset of plastic flow A, and it comes along with a finite jump of the twin phase volume fraction. Note that here, in contrast to the case of zero dissipation, a large amount of existing dislocations is consumed by the newly created twin phase (the plastic distortion β_{lp} in the parent phase exhibits an abrupt decrease at point B) but there are dislocations remaining in the parent phase such that both parent and twin phase deform plastically. Eventually, the plastic distortion and hence the dislocation density in the parent phase decrease to zero (point C) as the parent phase vanishes. During unloading of the crystal we observe a similar behavior: After initial elastic loading (section D-E) the crystal exhibits plastic flow until at point F the crystal starts to detwin. Detwinning has completed at point G, which is followed by further plastic flow of the now uniform parent phase. Finally, re-loading the crystal closes the loading path.

5.4.2 Stress-Strain Behavior

It is interesting to calculate the shear stress τ which is a measurable quantity. During positive loading beyond the critical shear strain we have for the normalized shear stress

$$\frac{\tau}{\mu} = \gamma_{cr} + \gamma_r - (\langle\beta\rangle + s\beta_t) \cos 2\varphi. \quad (5.65)$$

The second term of (5.65) causes hardening due to dislocation pile-up and a load drop at the initiation of deformation twinning. Note that this stress-strain behavior also highly depends on the number of twins n and the choice of ε_t .

During inverse loading when the yield conditions $\varkappa = -\tau_{crit}$ and $\varkappa_s = -K_s$ hold true, Eq. (5.65) changes into

$$\frac{\tau}{\mu} = -\gamma_{cr} + \gamma_l - (\langle\beta\rangle + s\beta_t) \cos 2\varphi, \quad (5.66)$$

with the deviation $\gamma_l = \gamma + \gamma_{cr}$ used instead of $\gamma_r = \gamma - \gamma_{cr}$.

Figure 5.10 shows the normalized shear stress versus shear strain curve for the given straining path of Figure 5.9. The straight line O – A corresponds to purely elastic loading with γ increasing from zero to γ_{cr} . Section A – B corresponds to plastic flow without deformation twinning with $\varkappa = \tau_{crit}$. Yielding begins at point A with the yield stress $\sigma_y = \tau_{crit}$, and we can observe a work hardening section due to dislocation pile-up. The initiation of twinning at point B is indicated by the characteristic sharp load drop (Christian and Mahajan, 1995). During further straining volume fractions of parent and twin phases evolve and the load remains almost constant (see the plateau in section B – C). Finally, at point C we again observe a uniform crystal with $s = 1$, i.e. deformation twinning has ended and the common hardening by dislocation pile-up occurs in the single crystal which has now completely adopted the twin lattice. During unloading as γ decreases from γ^* to $\gamma^* - 2\gamma_{cr}$ (line D – E), the plastic distortion β and volume fraction s are frozen. As γ decreases

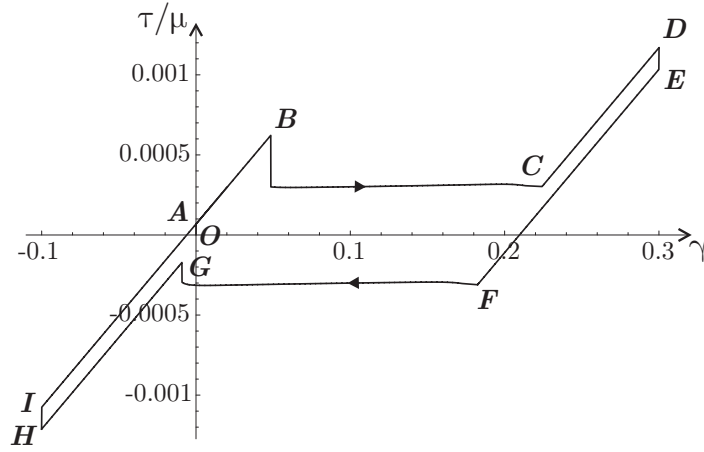


Figure 5.10: Normalized shear stress versus shear strain curve for the loading path of Figure 5.9. The onset of twinning upon loading is at point **B** and during unloading at point **F**. Computed with $\varphi = 87^\circ$, $h = 100\mu m$, $\varepsilon_t = 5 \cdot 10^{-5}$ and remaining material properties from Table 5.1.

further to γ_* , plastic yielding occurs with $\kappa = -\tau_{\text{crit}}$ (section **E – F**) and further on with $\kappa_s = -K_s$. The onset of detwinning during inverse loading is clearly indicated in the cycle by the beginning stress plateau at point **F**, and detwinning ends at point **G**, where we observe another minor load drop as soon as the twin phase vanishes. This stress plateau during unloading is followed by hardening of the now uniform single crystal (section **G – H**). Re-loading the uniform crystal closes the hysteresis loop.

5.5 Discussion and Conclusions

In this Chapter, we present a micro-mechanical model for the initiation and evolution of deformation twins, which exhibits several interesting features that need discussion in the context of physical reality. The model is based on the accommodation of deformation twinning by a combined mechanism of rotation and plastic twinning shear, comparable to Bullough's formal theory. Bullough introduced the idea of combining shear and rotation to form twins, and he proposed to shear the parent lattice such that each slip system is rotated onto another existing slip system, hence normally requiring a rather large rotation in f.c.c. and b.c.c. metals. This large rotation can only be accommodated by very high dislocation concentrations at the twin boundary, whose occurrence is physically doubtful. The twin boundary in our model (where we adopt Bullough's formal decomposition) is low-angle such that a few dislocations along the boundary are sufficient to accommodate the rotation. Experimental observations have shown that deformation twins (and also dislocation laminate structures) indeed often arise with low boundary tilt angles (Baihe et al., 1990; Skaland et al., 1993), which justifies the present approach.

Of course, the present model is simplistic in some sense and can be generalized in several directions, most of which are rather technical issues to be addressed at present and in the future. First, multiple slip systems can be accounted for (Le and Sembriring, 2008a) since cross-slip and dislocation pinning are important mechanisms in the context of twin initiation. Then, the present model is limited to small rotation and small twinning shear β_t . A more general approach should formulate the problem using finite deformations and

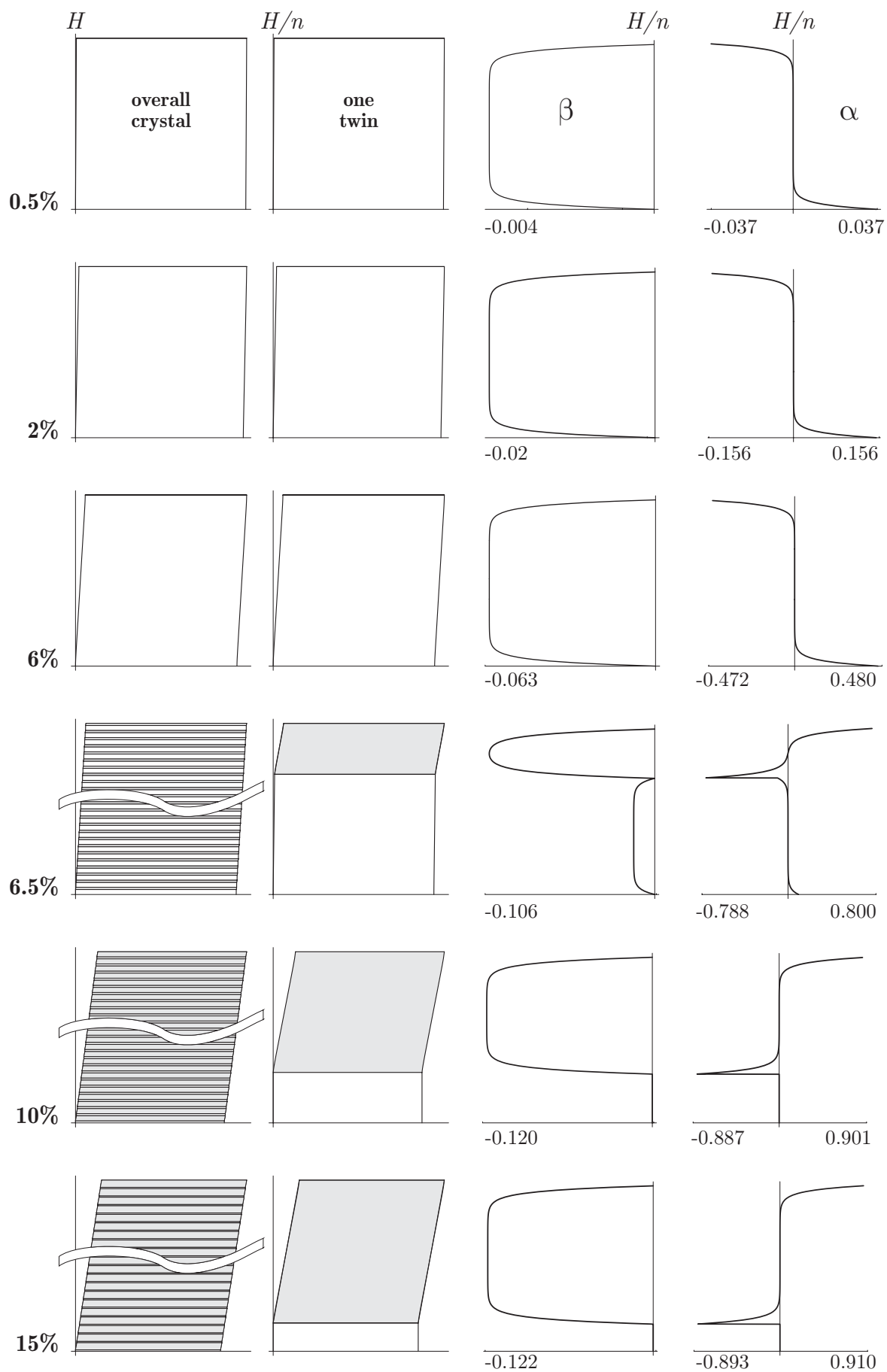


Figure 5.11: Twin formation during a closed loading cycle (part 1).

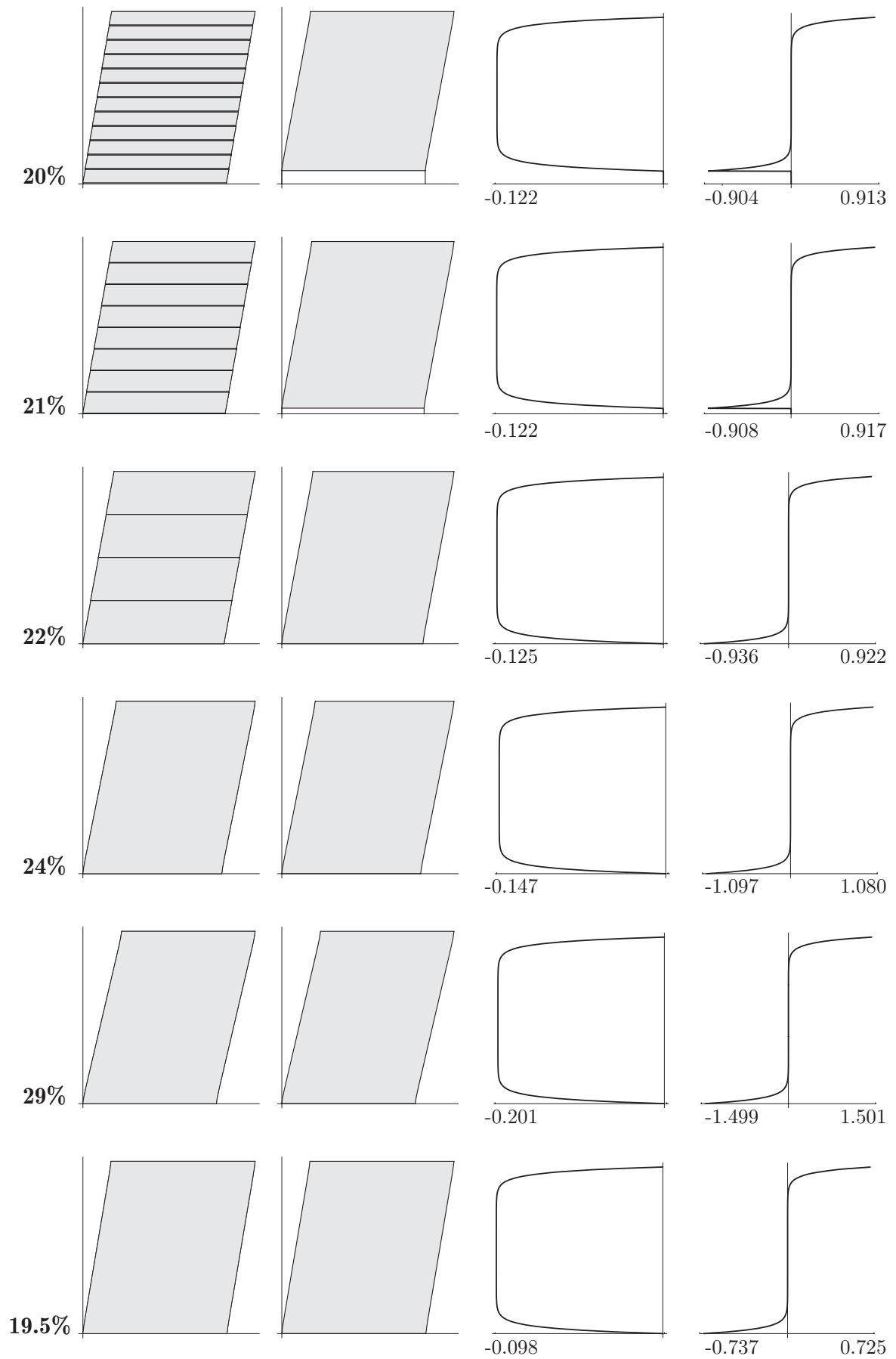


Figure 5.12: Twin formation during a closed loading cycle (part 2).

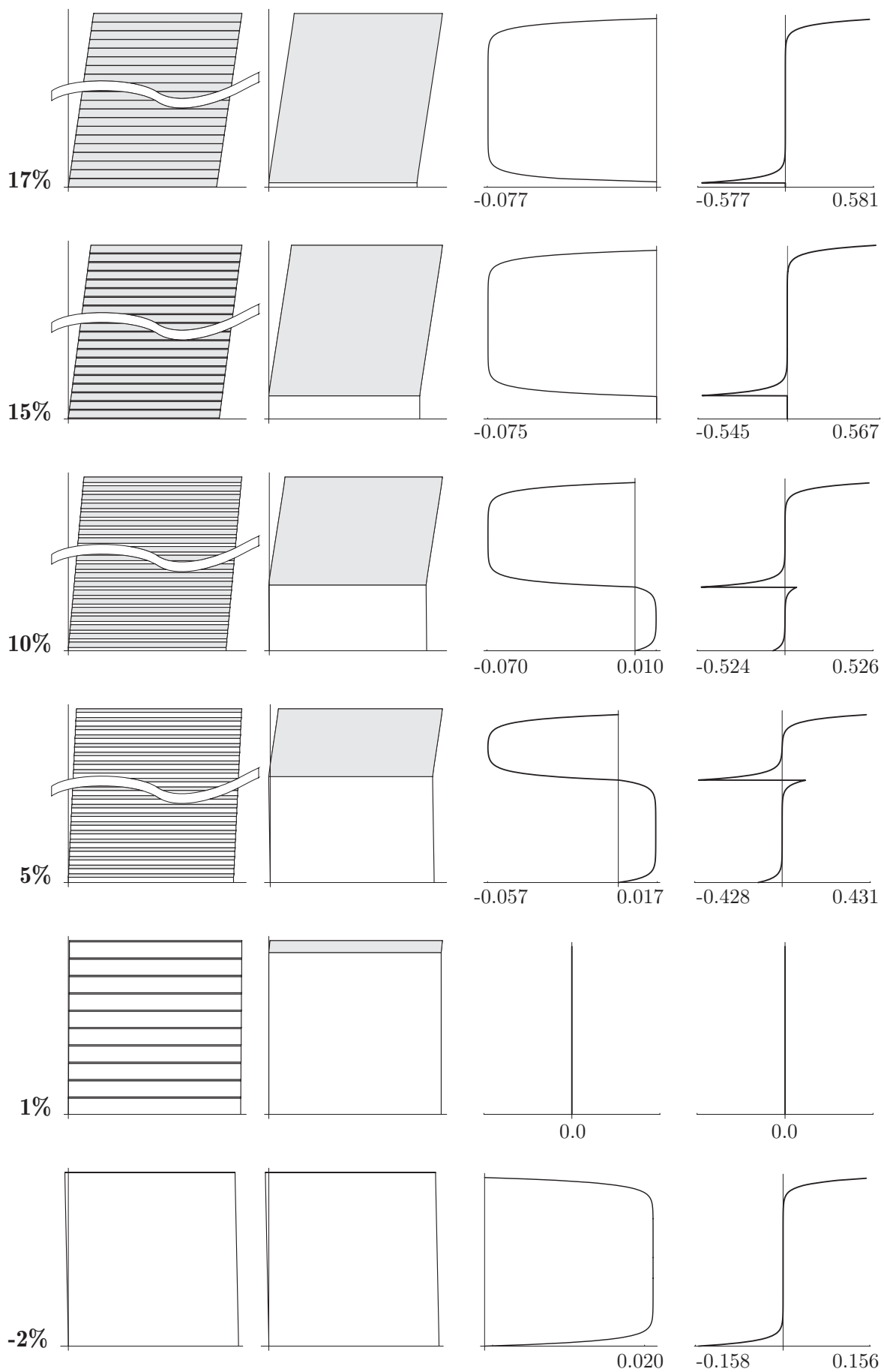


Figure 5.13: Twin formation during a closed loading cycle (part 3).

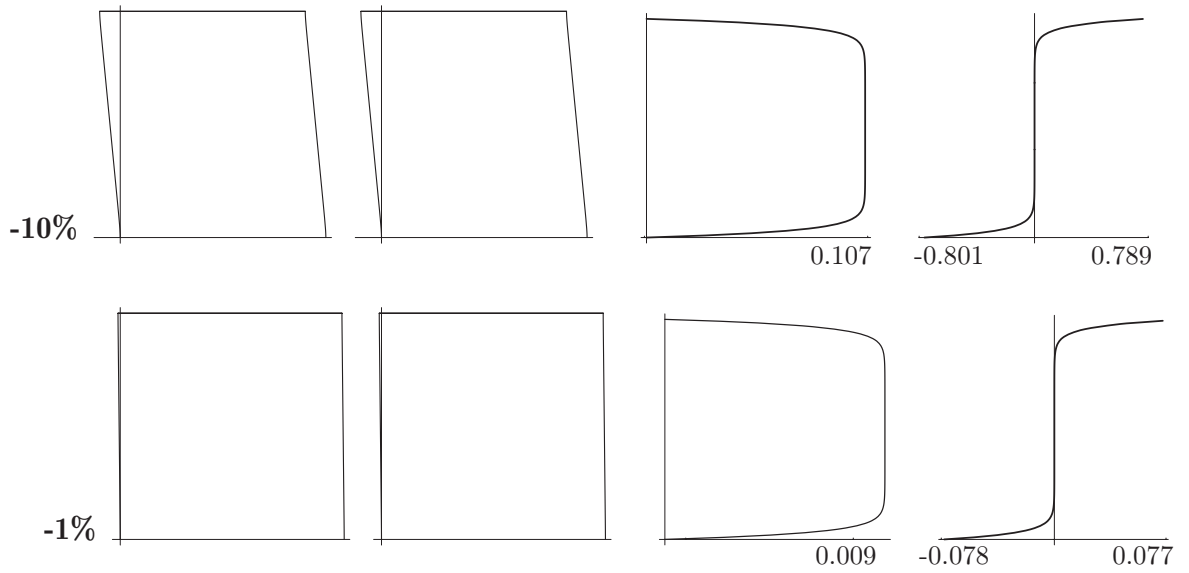


Figure 5.14: Twin formation during a closed loading cycle (part 4). Graphics illustrate the deformation of the overall crystal (with a rough sketch of the number of twins; in some cases the number of twins is too high to be shown accurately), the deformation of a single twin (parent phase below twin phase), the plastic distortion β and the normalized dislocation density α throughout the height of the twin.

hence employing the usual multiplicative split of the deformation gradient as $\mathbf{F} = \mathbf{F}_e \mathbf{F}_p$ and $\mathbf{F}_p = \mathbf{F}_\beta \mathbf{R} \mathbf{F}_{\beta_t}$ in the twin phase where $\mathbf{F}_\beta = \mathbf{I} + \beta \mathbf{s} \otimes \mathbf{m}$ and $\mathbf{F}_{\beta_t} = \mathbf{I} + \beta_t \mathbf{s}_t \otimes \mathbf{m}_t$ contain finite β and β_t (which may be of the order of magnitude 1) and \mathbf{R} performs the rigid rotation. First results from this approach show a qualitatively good agreement of those results presented here for small rotation φ (Homayonifar and Mosler, 2009). Finally, the present model needs generalization to loading in three dimensions and can then be implemented in modeling polycrystals. However, any such addition to this model will render the solution very cumbersome and no longer allow for an analytical treatment like in the present analysis.

Despite these shortcomings the present model exhibits several interesting qualitative features to review in the following. We showed that there exist distinct energetic thresholds for the onset of plastic flow and for the origin of deformation twinning (the so-called twinning stress). The present analysis showed that (for those material properties chosen) plastic flow can be expected to occur at rather low strains far before deformation twins arise (dependent on the choice of φ and β_t , among others). This is in good agreement with experimental evidence showing that dislocations have to be nucleated first (see Mahajan (1972, 1975) and Christian and Mahajan (1995)). Furthermore, we presented the evolution of the twin phase volume fraction, which arises from a uniform single crystal and increases until finally the entire crystal exhibits the twin lattice structure (i.e. the original slip system has been rotated by a small angle $2(90^\circ - \varphi)$). Then, we investigated the stress-strain behavior of the model crystal during twinning and observed, after an initial plastic hardening section, a large load drop in the stress-strain curve as soon as the twin phase originates from the parent crystal. Such load drops (followed by a stress plateau) have quite often been observed in experiments in particular on single crystals and have been reported e.g. by Botta et al. (1988) or Farrell and Evans (1965). In polycrystals such strong load drops are rather uncommon,

which can be explained by the different grain orientations causing different twinning stresses and hence resulting in a stress-strain behavior which is based on a homogenization of the single crystal responses. The resultant stress-strain response can be considered to show multiple small load drops during general hardening, as observed e.g. by Siedersleben and Taylor (1989). Note that the changing number of twins n (as sketched in Section 5.3) will also show an impact on the stress-strain behavior. We also showed a basic estimate of the actual number of twins during deformation twinning. These results are only of qualitative nature (in particular as they depend on many unknown parameters such as the twin boundary surface energy or the thickness of the elastic side boundaries) but sketch a reasonable picture of a large number of small twins upon the onset of deformation twinning, which then coalesce to gradually decrease the number of twins. Finally, we presented the evolution of deformation twins at non-zero dissipation clearly showing similar effects and in particular a broad stress-strain hysteresis with sharp load drops at the onset of twinning and at the end of detwinning. Note that the present model is based on ideal assumptions which allow the crystal to form deformation twins during loading and to detwin upon unloading. This, however, cannot always be observed experimentally.

Although most results show a very good qualitative agreement with experimental evidence, a quantitative comparison cannot be presented at the present stage since many material parameters in this model are still unknown. In the future, we will attack the problem of generalizing this model to a more complex formulation and compare results to experimental findings. However, the qualitative results presented above justify the formulation of the micro-mechanical model which is not based on phenomenological but on energetic considerations.

6 Conclusions and Outlook

In this thesis we investigated the origin and evolution of microstructures in crystalline solids during elasto-plastic deformation. A review of the thermo-mechanical fundamentals revealed the underlying thermodynamic principles which have been applied to predict the formation and subsequent evolution of material microstructures and to model the resulting mechanical behavior. Based upon these principles, we analyzed two major aspects of microstructure modeling, for each of which we then presented novel modeling techniques and thereby determined microstructures which can indeed be observed experimentally.

Before leaving the field of classical plasticity theory, we investigated the origin of microstructures in finite elasto-plasticity. For a Neo-Hookean material we showed that the non-(quasi)convexity of the free energy gives rise to small-scale fluctuations as minimizers of the variational problem of minimum potential energy. Relaxing the energy and replacing the energy density by an approximation of its rank-one-convex hull, we outlined an incremental approach and a corresponding numerical algorithm to solve the variational problem. As a result we observed the formation of laminate microstructures of first order, whose characteristics depend on the choice of the active slip system and the material parameters chosen. We investigated the influence of material hardening, of the slip system orientation, of cyclic loading and of a second active slip system. In particular, we stressed the importance of an incremental strategy which captures the already existing microstructure at the beginning of each time step and the exact resultant amount of dissipation, as compared to the solution obtained from the condensed energy for a single time step as often employed in the scientific literature. Results comprised an extensive overview of the characteristics of the resulting laminate microstructures in homogeneously deformed crystals.

Another important aspect of microstructure modeling arises from the necessity to account for lattice defects in the constitutive framework since these defects, and here predominantly dislocations, accommodate plastic deformation of the crystalline solid. Therefore, we left the terrain of classical plasticity theory and outlined a formulation of a continuum dislocation theory. The free energy density was extended by a term capturing the microstructural defect energy where we adopted a logarithmic formulation: this form ensures a saturation effect of dislocations, i.e. dislocations cannot appear at arbitrarily high local concentration in the crystal, but the material exhibits a saturation density which must not be overcome. Based on the continuum dislocation approach, we investigated several benchmark problems, now employing a small-strain formulation to allow for analytical solutions for some of the highly non-linear problems. First, we presented closed-form analytical solutions for the problems of shear, extension and a combination of shear and extension at the example of thin film bicrystals with one active slip system in each single crystal. The assumption of impenetrable grain boundaries results in the pile-up of dislocations at the barriers and leads to related stress concentrations. In particular, a size effect became apparent due to the limitations of dislocation storage in the material, i.e. the yield stress and the hardening rate exhibit an inverse proportionality to the height of the bicrystal.

We then demonstrated a variational formulation for the continuum dislocation model, which allows for a numerical solution based on finite element techniques. Results from this

approach comprised dislocation structures and related effects in single- and polycrystals. First, numerical results confirmed the analytical solutions derived. Next, the inspection of simple grain geometries with fully constrained grain boundaries revealed the origin of dislocation substructures within single-crystal grains (depending on the grain size and forming heterogeneously due to stress concentrations e.g. at boundaries). The formation of such substructures during plastic deformation has often been argued to be responsible for the experimentally observed refinement of grains. Besides, we again reported obvious size effects since stresses and other characteristics highly depend on the grain geometry. In particular, we observed an inverse proportionality of the stresses to the characteristic grain side length. For simple models of polycrystals, results deviated from the aforementioned inverse proportionality and showed a dependence closer to the well-known Hall-Petch relation.

Finally, the continuum dislocation approach was modified to model the mechanism of deformation twinning in a simple setting. The energy minimum of a strained single-crystal is achieved by forming a lamellar structure with alternating symmetric lattice rotations. In contrast to earlier analytical approaches to model deformation twinning, we enhanced the theory by accounting for the dislocation structures within the lamellae: dislocations pile up first in the untwinned single crystal, are then consumed to a major part by the forming twin boundary and finally pile up within each parent- and twin-phase single crystal. The pile-up at twin boundaries exhibits a typical size effect and hence limits the refinement of twins, i.e. the actual number of twins is bounded. We determined energetic thresholds both for plastic flow and for the onset of deformation twinning. Partially analytical solutions both for zero and non-zero dissipation elucidated the typical mechanical behavior of TWIP crystals and gave insight into some of the experimentally observed specifics. In particular, the stress-strain hysteresis shows a characteristic sharp load drop at the onset of twinning, followed by a stress plateau, during which the crystal gradually transforms from the original parent lattice into the twin phase.

The models presented, of course, bear room for improvement. In particular, we would like to draw the attention to the following issues which will be addressed in the future or are subject of present research already. The incremental approach to model first-order laminates at finite strains can be modified to include second-order laminates. The analytical set-up is analogous and unproblematic. Unfortunately, the relaxation can no longer be performed analytically such that the numerical effort will rise considerably. Further generalizations include multiple general slip systems and compressible material behavior. Also, the outlined method at the material point will be implemented into a finite element code to model actual macroscopic problems and hence to allow for a comparison with experimental results.

The continuum dislocation approach is limited in terms of its modeling assumptions (most of them made to allow for neat solutions since this is, to our knowledge, the first attempt to make use of this type of energy formulation in modeling these specific dislocation structures). A refined model will consider multiple active slip systems to accommodate plastic flow. Furthermore, we assumed the interfaces and boundaries of the crystals to be impenetrable for dislocations, which is a strong assumption. The transmission of dislocations through grain and twin boundaries or the absorption of dislocations into the boundaries occur if the applied stress is sufficient to overcome the imposed energetic barrier. In a next step, we will weaken the condition at the grain boundaries but not imposing any constraints on the plastic slip but incorporating the energy of the low-angle grain boundaries into the energetic framework. Our analysis was furthermore limited to plane problems. The outlined variational formulation can easily be modified to three-dimensional problems. Also, this approach can be extended to finite deformations, a rather technical issue to be addressed in the

future as well. As it is based on the same formulation, the same issues apply to the model for deformation twinning. There, it would furthermore be beneficial to develop a variational formulation to treat general macroscopic problems by employing a finite element approach.

Finally, the most auspicious possible generalization of those methods presented here consists of a combination of both approaches. The extension of the continuum dislocation model to finite strains will inevitably encounter a non-convex free energy, which can be relaxed so that the energy minimum is accommodated by e.g. lamellar microstructures. The outlined incremental formulation for the description of these microstructures can be employed but must now be coupled to the continuum dislocation approach to account for the pile-up of dislocations at interfaces of the lamellar structure. As a first step, the relaxation-based model presented here can be modified to account for dislocation energies at the boundaries (as a function of the plastic slip at the boundary), which results in anisotropic hardening. Research in this direction is already under way.

In conclusion, this thesis presented progress in several research directions of modeling microstructures in solid mechanics. Unlike in many phenomenological plasticity theories, the formation of lamellar patterns, of dislocation substructures and of deformation twins was investigated based on thermo-mechanical considerations and micro-mechanical energetic principles. Results comprise the prediction of microstructures and of the resulting mechanical behavior, which qualitatively match experimental observations very well.

References

- Acerbi, E., Fusco, N., 1984. Semicontinuity Problems in the Calculus of Variations. *Arch. Rat. Mech. Anal.* 86, 125–145.
- Acharya, A., Bassani, J. L., 2001. Lattice incompatibility and a gradient theory of crystal plasticity. *J. Mech. Phys. Solids* 48, 1565–1595.
- Acharya, A., 2003. Driving forces and boundary conditions in continuum dislocation mechanics. *Proc. R. Soc. Lond. A* 459, 1343–1363.
- Aifantis, E. C., 1987. The physics of plastic deformation. *Int. J. Plasticity* 3, 211–247.
- Aifantis, K. E., Soer, W. A., De Hosson, J. T. M., Willis, J. R., 2006. Interfaces within strain-gradient plasticity: theory and experiments. *Acta Mater.* 54, 5077–5085.
- Aifantis, K. E., Willis, J. R., 2005. The role of interfaces in enhancing the yield strength of composites and polycrystals. *J. Mech. Phys. Solids* 53, 1047–1070.
- Allain, K. E., Chateau, J. P., Bouaziz, O., 2004. A physical model of the twinning-induced plasticity effect in a high manganese austenitic steel. *Mater. Sci. Eng. A* 387, 143–147.
- Ashby, M. F., 1970. The deformation of plastically non-homogeneous materials. *Philos. Mag.* 21, 399–424.
- Baihe, M., Keming, F., Weimin, B., 1990. On the microstructure of graphite spherulites in cast irons by TEM and HREM. *Acta Metall. Mater.* 38, 2167–2174.
- Ball, J. M., 1977. Convexity Conditions and Existence Theorems in Nonlinear Elasticity. *Arch. Rat. Mech. Anal.* 63, 337–403.
- Ball, J. M., 2002. Some Open Problems in Elasticity. In: Newton, P., Holmes, P., Weinstein, A. (eds.), *Geometry, Mechanics, and Dynamics*, pp. 3–59, Springer, New York.
- Ball, J. M., James, R. D., 1987. Fine phase mixtures as minimizers of energy. *Arch. Rat. Mech. Anal.* 100, 13–52.
- Ball, J., James, R., 1992. Proposed experimental tests of a theory of fine microstructures and the two-well problem. *Philos. Trans. Royal Soc. A* 338, 389–450.
- Bartel, T., 2009. Multiskalenmodellierung martensitischer Phasentransformationen in Formgedächtnislegierungen unter Verwendung relaxierter Energiepotenziale. Dissertation. Ruhr-Universität Bochum, Germany.
- Bartels, S., Carstensen, C., Hackl, K., Hoppe, U., 2004. Effective Relaxation for Microstructure Simulations: Algorithms and Applications. *Comp. Meth. Appl. Mech. Eng.* 193, 5143–5175.
- Berdichevsky, V. L., 2005. Homogenization in micro-plasticity. *J. Mech. Phys. Solids* 53, 2457–2469.

- Berdichevsky, V. L., 2006a. On thermodynamics of crystal plasticity. *Scripta Mater.* 54, 711-716.
- Berdichevsky, V. L., 2006b. Continuum theory of dislocations revisited. *Continuum Mech. Thermodyn.* 18, 195-222.
- Berdichevsky, V. L., Le, K. C., 2007. Dislocation nucleation and work hardening in anti-plane constrained shear. *Continuum Mech. Thermodyn.* 18, 455-467.
- Berdichevsky, V. L., Sedov, L. I., 1967. Dynamic theory of continuously distributed dislocations. Its relation to plasticity theory. *J. Appl. Math. Mech. (PMM)* 31, 989-1006.
- Betten, J., 1987. *Tensorrechnung für Ingenieure*, Teubner, Stuttgart.
- Bhattacharya, K., 2003. *Microstructure of martensite. Why it forms and how it gives rise to the shape-memory effect*. Oxford University Press, Oxford.
- Bilby, B. A., 1955, in *Report of the Conference on Defects in Crystalline Solids*, Physical Society, London, 124.
- Bilby, B. A., Bullough, R., Smith, E., 1955. Continuous distributions of dislocations: a new application of the methods of non-Riemannian geometry. *Proc. Roy. Soc. A* 231, 263-273.
- Biot, M. A., 1965. *Mechanics of Incremental Deformations*. John Wiley & Sons Inc., New York.
- Botta, W. J., Christian, J. W., Taylor, G., 1988. Solution hardening and softening of Nb-Zr single-crystals. *Philos. Mag.* 57, 703-716.
- Boyde, A., 2003. Improved digital SEM of cancellous bone: scanning direction of detection, through focus for in-focus and sample orientation. *J. Anat.* 202, 183-194.
- Bullough, R., 1957. Deformation twinning in the diamond structure. *Proc. Roy. Soc. London A* 241, 568-577.
- Bullough, R., 1964. *Dislocations*, A.E.R.E., Harwell.
- Cahn, R. W., 1954. Twinned Crystals. *Adv. Phys.* 3, 363-445.
- Canadinc, D., Sehitoglu, H., Maier, H. J., Chumlyakov, Y. I., 2005. Strain hardening behavior of aluminum alloyed Hadfield steel single crystals. *Acta Mater.* 53, 1831-1842.
- Capolungo, L., Spearot, D. E., Cherkaoui, M., et al., 2007. Dislocation nucleation from bi-crystal interfaces and grain boundary ledges: Relationship to nanocrystalline deformation. *J. Mech. Phys. Solids* 55, 2300-2327.
- Carstensen, C., Hackl, K., Mielke, A., 2002. Non-convex potentials and microstructures in finite-strain plasticity. *Proc. Royal Soc. London A* 458, 299-317.
- Carstensen, C., Conti, S., Orlando, A., 2008. Mixed analytical-numerical relaxation in finite single-slip crystal plasticity. *Continuum Mech. Thermodyn.* 20, 275-301.
- Charsley, P., 1981. Dislocation arrangements in polycrystalline copper alloys fatigued to saturation. *Mat. Sci. Eng. A* 47, 181-185.
- Christian, J. W., Mahajan, S., 1995. Deformation twinning. *Progr. Mater. Sci.* 39, 1-157.

- Chu, C., James, R. D., 1995. Analysis of microstructures in Cu-14.0%Al-3.9%Ni by energy minimization. *Journal de Physique IV, Colloque C8*, vol. 5, 143-149. Image reprinted from journaldephysique.org by kind permission.
- Cohen, J. B., Weertman, J., 1963. A dislocation model for twinning in f.c.c. metals. *Acta Metall.* 11, 996.
- Conti, S., Ortiz, M., 2008. Minimum principles for the trajectories of systems governed by rate problems. *J. Mech. Phys. Solids* 56, 1885-1904.
- Conti, S., Theil, F., 2005. Single-slip elastoplastic microstructures. *Arch. Rat. Mech. Anal.* 178, 125-148.
- Cook, R. D., Malkus, D. S., Plesha, M. E., Witt, R. J., 2002. *Concepts and Applications of Finite Element Analysis*. Wiley, New York.
- Cosserat, E., Cosserat, F., 1909. *Théorie Des Corps Déformables*. Hermann, Paris.
- Dacorogna, B., 1989. *Direct Methods in the Calculus of Variations*. Springer, New York.
- DeSimone, A., Dolzmann, G., 2000. Material Instabilities in Nematic Elastomers. *Physica D* 136: 175–191.
- Dillon, O. W., Perzyna, P., 1972. A gradient theory of materials with memory and internal changes. *Arch. Mech.* 24, 727-747.
- Dimitrijevic, B. J., Hackl, K., 2008. A method for gradient enhancement of continuum damage models. *Technische Mechanik* 28, 43-52.
- Dmitrieva, O., Dondl, P., Müller, S., Raabe, D., 2009. Lamination microstructure in shear deformed copper single crystals. *Acta Mater.*, in press.
- Dolzmann, G., 1999. Numerical Computation of Rank-One Convex Envelopes. *SIAM J. Num. Anal.* 36, 1621–1635.
- Dolzmann, G., 2003. *Variational Methods for Crystalline Microstructure – Analysis and Computation*. Springer-Verlag, Berlin.
- Ericksen, J. L., 1975. Equilibrium of bars. *J. Elasticity* 5, 191-201.
- Eringen, A. C., 1972. Nonlocal polar elastic continua. *Int. J. Eng. Sci.* 10, 1-16.
- Eshelby, J. D., Frank, F. C., Nabarro, F. R. N., 1951. The equilibrium of linear arrays of dislocations. *Philos. Mag.* 42, 351-364.
- Evers, L. P., Parks, D. M., Brekelmans, W. A. M., Geers, M. G. D., 2002. Crystal plasticity model with enhanced hardening by geometrically necessary dislocation accumulation. *J. Mech. Phys. Solids* 50, 2403-2424.
- Ewing, A., Rosenhain, W., 1899. The Crystalline Structure of Metals. *Philos. Trans. Roy. Soc. A* 193, 353-375.
- Farrell, K., Evans, P. R. V., 1965. Some observations of mechanical twinning in polycrystalline Niobium. *J. Less Common Metals* 8, 222.

- Fleck, N. A., Hutchinson, J. W., 2001. A reformulation of strain-gradient plasticity. *J. Mech. Phys. Solids* 49, 2245-2271.
- Flügge, W., 1972. *Tensor analysis*. Springer, New-York.
- Fox, N., 1968. On the continuum theory of dislocations and plasticity. *Quart. J. Mech. Appl. Math.* 21, 67-75.
- Frank, F. C., Read, W. T., 1950. Multiplication process for slow moving dislocations. *Phys. Rev.* 79, 722-723.
- Frenkel, J., 1926. Zur Theorie der Elastizitätsgrenze und der Festigkeit kristallinischer Körper. *Z. Phys.* 37, 572-609.
- Frenkel, J., Kontorova, T., 1939. On the theory of plastic deformation and twinning. *Acad. Sci. USSR J. Phys.* 1, 137-149.
- Freund, L. B., 1987. The stability of dislocations threading a strained layer on a substrate. *J. Appl. Mech.* 43, 553-557.
- Fu, R. D., Qiu, L., Wang, T. S., et al., 2005. Cryogenic deformation microstructures of 32Mn–7Cr–1Mo–0.3N austenitic steels. *Materials Characterization* 55, 355–361.
- Gao, H., Huang, Y., Nix, W. D., Hutchinson, J. W., 1999. Mechanism-based strain gradient plasticity - I. Theory. *J. Mech. Phys. Solids* 47, 1239-1263.
- Gelfand, I. M., Fomin, S. V., 2000. *Calculus of variations*. Dover Publications, New York.
- Germain, P., 1973. *Cours de Mécanique des Milieux Continus*. Masson et Cie, Paris.
- Govindjee, S., Mielke, A., Hall, G. J., 2003. The free energy of mixing for n-variant martensitic phase transformations using quasi-convex analysis. *J. Mech. Phys. Solids* 51, 1-26.
- Green, A. E., Rivlin, R. S., 1964. Simple forces and stress multipoles. *Arch. Rat. Mech. Anal.* 16, 325-353.
- Groma, I., Csikor, F. E., Zaiser, M., 2003. Spatial correlations and higher-order gradient terms in a continuum description of dislocation dynamics. *Acta Mater.* 51, 1271-1281.
- Groma, I., Györgyi, G., Kocsis, B., 2007. Dynamics of coarse grained dislocation densities from an effective free energy. *Philos. Mag.* 87, 1185-1199.
- Gürses, E., 2007. *Aspects of Energy Minimization in Solid Mechanics: Evolution of Inelastic Microstructures and Crack Propagation*. Dissertation. Universität Stuttgart, Germany.
- Gurtin, M. E., 1972. The Linear Theory of Elasticity. In: Flügge, S. (ed.), *Encyclopedia of Physics* VIa/2, Springer, Berlin.
- Gurtin, M. E., 2003. On a framework for small-deformation viscoplasticity: free energy, microforces, strain gradients. *Int. J. Plasticity* 19, 47-90.
- Gurtin, M. E., Anand, L., 2005. A theory of strain-gradient plasticity for isotropic, plastically irrotational materials. Part II: Finite deformations. *Int. J. Plasticity* 21, 2297-2318.
- Gurtin, M. E., Anand, L., Suvrat, P. L., 2007. Gradient single-crystal plasticity with free energy dependent on dislocation densities. *J. Mech. Phys. Solids* 55, 1853-1878.

- Hackl, K., 2005. Relaxation and evolution of microstructures – some conceptual ideas. Oberwohlfach Report 52, p. 2988-2990.
- Hackl, K., 2006. Relaxed potentials and evolution equations. In: Gumbsch, P. (ed.), Third International Conference on Multiscale Materials Modeling. Fraunhofer IRB Verlag.
- Hackl, K., Fischer, F. D., 2007. On the relation between the principle of maximum dissipation and inelastic evolution given by dissipation potentials. Proc. Royal Soc. London A 464, 117–132.
- Hackl, K., Heinen, R., 2008. A micromechanical model for pretextured polycrystalline shape-memory alloys including elastic anisotropy. Continuum Mech. Thermodyn. 19, 499-510.
- Hackl, K., Kochmann, D. M., 2008. Relaxed potentials and evolution equations for inelastic microstructures. In: Daya Reddy, B. (ed.), IUTAM Symposium on Theoretical, Computational and Modelling Aspects of Inelastic Media. Springer, Berlin, pp. 27-39.
- Hackl, K., Mielke, A., Mittenhuber, D., 2003. Dissipation distances in multiplicative elastoplasticity. In: Wendlang, W. L., Efendiev, M. (eds.), Analysis and Simulation of Multifield Problems. Springer, New York.
- Hackl, K., Schmidt-Baldassari, M., Zhang, W., 2003. A micromechanical model for polycrystalline shape-memory alloys. Mater. Sci. Eng. A 378, 503-506.
- Hadamard, J., 1903. Leçons sur la propagation des ondes et les équations de l'hydrodynamique, Hermann, Paris.
- Hall, E. O., 1951. The deformation and ageing of mild steel. Proc. Phys. Soc. B 64, 742-753.
- Hall, E. O., 1954. Twinning. Butterworths, London.
- Han, C. S., Gao, H. J., Huang, Y. G., Nix, W. D., 2005a. Mechanism-based strain gradient crystal plasticity – I. Theory. J. Mech. Phys. Solids 53, 1188-1203.
- Han, C. S., Gao, H. J., Huang, Y. G., Nix, W. D., 2005b. Mechanism-based strain gradient crystal plasticity – II. Analysis. J. Mech. Phys. Solids 53, 1204-1222.
- Hanamura, T., Tanino, M., 1989. A new type of twinning in TiAl-2wt% Mn intermetallic compound. J. Mat. Sci. Lett. 8, 24-28.
- Hansen, N., Huang, X., Hughes, D. A., 2001. Microstructural evolution and hardening parameters. Mat. Sci. Eng. A 317, 3-11.
- Hansen, N., Huang, X., Winterh, G., 2008. Grain orientation, deformation microstructure and flow stress. Mat. Sci. Eng. A 494, 61–67.
- Hartmaier, A., Fivel, M. C., Canova, G. R., Gumbsch, P., 1998. 3D discrete dislocation models of thin-film plasticity, in Cammarata, R. C., Busso, E. P., Nastasi, M., Oliver, W. C. (eds.), Thin-Films-Stresses and Mechanical Properties VII, Mat. Res. Soc. Symp. Proc. 505, 539-544.
- Hirth, J.P., Lothe, J., 1982. Theory of Dislocations. Krieger Publishing Company, Malabar, Florida, 2nd edition.

- Hochrainer, T., Zaiser, M., 2005. Fundamentals of a continuum theory of dislocations. SM-PRI 2005.
- Homayonifar, M., Mosler, J., GKSS Forschungszentrum, private communication.
- Huang Y., Gao H., Nix W. D., Hutchinson, J. W., 2000. Mechanism-based strain gradient plasticity – II. Analysis. *J. Mech. Phys. Solids* 48, 99-128.
- Huang, Y., Hwang, Q. S., Li, K. C., Gao, H., 2004. A conventional theory of mechanism-based strain gradient plasticity. *J. Mech. Phys. Solids* 20, 753-782.
- Hughes, T. J. R., 1987. *The Finite Element Method*. Prentice-Hall, Englewood Cliffs, New Jersey.
- Ilic, S., 2008. Multi-scale modeling of the composite materials. Dissertation, Ruhr-Universität Bochum, Germany.
- Iwahashi, Y., Wang, J., Horita, Z., Nemoto, M., Langdon, T. G., 1996. Principle of equal channel angular pressing for the processing of ultra-fine grained materials. *Scripta Mater.* 35, 143-146.
- Jin, N. Y., Winter, A. T., 1984. Dislocation structures in cyclically deformed [001] copper crystals. *Acta Met.* 32, 1173-1176.
- Kaschner, G. C., Tomé, C. N., Beyerlein, I. J., et al., 2006. Role of twinning in the hardening response of zirconium during temperature reloads. *Acta Mater.* 54, 2887-2896.
- Kaschner, G. C., Tomé, C. N., McCabe, R. J., et al., 2007. Exploring the dislocation/twin interactions in zirconium. *Mat. Sci. Eng. A* 463, 122-127.
- Khan, A. S., Huang, S., 1995. *Continuum theory of plasticity*. Wiley, New York.
- Kochmann, D. M., Hackl, K., 2009. Time-continuous evolution of microstructures in finite plasticity. In: Hackl, K. (ed.), *Proceedings of the IUTAM Symposium on Variational Concepts with Applications to the Mechanics of Materials*. Springer, Berlin, in press.
- Kochmann, D. M., Le, K. C., 2008. Plastic deformation of bicrystals within continuum dislocation theory. *J. Math. Mech. Solids*, pre-published online 11 March 2008 (doi: 10.1177/1081286507087322).
- Kochmann, D. M., Le, K. C., 2008. Dislocation pile-ups in bicrystals within continuum dislocation theory. *Int. J. Plasticity* 24, 2125-2147.
- Kochmann, D. M., Le, K. C., 2009. A continuum model for the initiation and evolution of deformation twins. *J. Mech. Phys. Solids* 57, 987-1002.
- Kochmann, D. M., Le, K. C., 2009. Continuum dislocation theory and related size effects in crystal plasticity. In: Columbus, F. (ed.), title to be announced, Nova Science Publishers, Hauppauge, New York.
- Kohn, R., 1991. The relaxation of a double-well problem. *Continuum Mech. Thermodyn.* 3, 193-236.
- Kohn, R. V., Strang, G., 1986. Optimal Design and Relaxation of Variational Problems I, II, III. *Commun. Pure Appl. Math.* 39, 113–137, 139–182, 353–377.

- Kondo, K., 1952. On the geometrical and physical foundations of the theory of yielding. Proc. 2. Japan Congr. Appl. Mech., pp. 41-47.
- Kröner, E., 1958. *Kontinuumstheorie der Versetzungen und Eigenspannungen*. Springer, Berlin.
- Kunin, I. A., 1983. *Elastic Media with Microstructure*, vol. 2. Springer, Berlin.
- Lambrecht, M., Miehe, C., Dettmar, J., 2003. Energy relaxation of non-convex incremental stress potentials in a strain-softening elastic-plastic bar. *Int. J. Solids Struct.* 40, 1369-1391.
- Lardner, R. W., 1969. Dislocation dynamics and the theory of the plasticity of single crystals. *Z. Angew. Math. Phys.* 20, 514-529.
- Le, K. C., Berdichevsky, V. L., 2001. Energy distribution in a neutral gas of point vortices. *J. Stat. Phys.* 104, 883-894.
- Le, K. C., Kochmann, D. M., 2009. A simple model for dynamic recrystallization during severe plastic deformation. *Arch. Appl. Mech.* 79, 579-586.
- Le, K. C., Sembiring, P., 2008a. Plane constrained shear of single crystals within continuum dislocation theory. *Arch. Appl. Mech.* 78, 587-597.
- Le, K. C., Sembiring, P., 2008b. Plane-constrained shear of a single crystal strip with two active slip-systems. *J. Mech. Phys. Solids* 56, 2541-2554.
- Le, K. C., Stumpf, H., 1996a. On the determination of the crystal reference in nonlinear continuum theory of dislocations. *Proc. Roy. Soc. London A* 452, 359-371.
- Le, K. C., Stumpf, H., 1996b. Nonlinear continuum theory of dislocations. *Int. J. Eng. Sci.* 34, 339-358.
- Le, K. C., Stumpf, H., 1996c. A model of elastoplastic bodies with continuously distributed dislocations. *Int. J. Plasticity* 12, 611-627.
- Lee, E. H., Lin, D. T., 1967. Finite-strain elastic-plastic theory particularly for plane wave analysis. *J. Appl. Phys.* 38, 19.
- Leibfried G., 1951. Verteilung von Versetzungen im statischen Gleichgewicht. *Z. Phys.* 130, 214-226.
- Li, Z. J., Winther, G., Hansen, N., 2006. Anisotropy in rolled metals induced by dislocation structure. *Acta Mater.* 54, 401-410.
- Libbrecht, K. G., 2009. Image reprinted from snowcrystals.com by kind permission.
- Liu, Q., Huang, X., Lloyd, D. J., Hansen, N., 2002. Microstructure and strength of commercial purity aluminium (AA 1200) cold-rolled to large strains. *Acta Mater.* 50, 3789-3802.
- Louchet, F., Weiss, J., Richeton, T., 2006. Hall-Petch law revisited in terms of collective dislocation dynamics. *Phys. Rev. Lett.* 97(7), no. 075504.
- Lukáš, P., Kunz, L., Svoboda, M., 1999. Stress-strain response and fatigue life of copper single crystals cyclically loaded with a positive mean stress. *Mat. Sci. Eng. A* 272, 31-37.

- Mahajan, S., 1972. Nucleation and growth of deformation twins in Mo-35 at-percent Re alloy. *Phil. Mag.* 26, 161.
- Mahajan, S., 1975. Interrelationship between slip and twinning in bcc crystals. *Acta Met.* 23, 671-684.
- Marsden, J. E., Hughes, T. J. R., 1994. *Mathematical Foundations of Elasticity*. Dover Publications Inc., New York.
- Meng, L., et al., 2007. Dependence of deformation twinning on grain orientation in compressed high manganese steels. *Scripta Mater.* 56, 931-934.
- Meyers, M. A., et al., 1995. High-strain, high-strain-rate behavior of tantalum. *Metall. Mater. Trans.* 26, 2493-2501.
- Miehe, C., 2000. Strain-driven homogenization of inelastic microstructures and composites based on an incremental variational formulation. *Int. J. Numer. Meth. Eng.* 55, 1285-1322.
- Miehe, C., Schotte, J., Lambrecht, M., 2002. Homogenization of inelastic solid materials at finite strains based on incremental minimization principles. Application to the texture analysis of polycrystals. *J. Mech. Phys. Solids* 50, 2123-2167.
- Miehe, C., Lambrecht, M., Gürses, E., 2004. Analysis of material instabilities in inelastic solids by incremental energy minimization and relaxation methods: evolving deformation microstructures in finite plasticity. *J. Mech. Phys. Solids* 52, 2725-2769.
- Mielke, A., 2002. Finite elastoplasticity, Lie groups and geodesics on $SL(d)$. In: Newton, P., Weinstein, A., Holmes, P. (eds.), *Geometry, Dynamics, and Mechanics*. Springer, Berlin.
- Mielke, A., 2004. Deriving new evolution equations for microstructures via relaxation of variational incremental problems. *Comp. Meth. Appl. Mech. Eng.* 193, 5095-5127.
- Mielke, A., Ortiz, M., 2007. A class of minimum principles for characterizing the trajectories and the relaxation of dissipative systems. *ESAIM: Control, Optimization and Calculus of Variations* 14 (3), 494-516.
- Mooney, M., Wolstenholme, W. E., 1952. Modulus and relaxation of elastomers in torsion at low temperatures. *Ind. Eng. Chem.* 44, 335-342.
- Morrey, C. B., 1952. Quasi-Convexity and the Lower Semicontinuity of Multiple Integrals. *Pacific J. Math.* 2, 25-53.
- Narita, N., Takamura, J.-I., 1992. Deformation twinning in f.c.c. and b.c.c. metals, in: Nabarro, F. R. N. (ed.), *Dislocations in Solids*, Vol. 9. North-Holland, Amsterdam, pp. 135-190.
- Needleman, A., Van der Giessen, E., 2001. Discrete dislocation and continuum descriptions of plastic flow. *Mater. Sci. Eng. A* 309-310, 1-13.
- Nguyen, Q. S., 2000. *Stability and Nonlinear Solid Mechanics*. John Wiley & Sons, New York.
- Nicola, L., Van der Giessen, E., Needleman, A., 2003. Discrete dislocation analysis of size effects in thin films. *J. Appl. Phys.* 93, 5920-5928.
- Nix, W. D., 1998. Yielding and strain hardening of thin metal films on substrates. *Scripta Mater.* 39, 545-554.

- Noll, W., 1954. Ph.D. Thesis, Indiana University.
- Nye, J. F., 1953. Some geometrical relations in dislocated crystals. *Acta Metall.* 1, 153-162.
- Orowan, E., 1934. Zur Kristallplastizität. III Über den Mechanismus des Gleitvorganges. *Z. Phys.* 89, 634-659.
- Ortiz, M., Repetto, E. A., 1999. Nonconvex energy minimization and dislocation structures in ductile single crystals. *J. Mech. Phys. Solids* 47, 397-462.
- Ortiz, M., Repetto, E. A., Stainier, L., 2000. A theory of subgrain dislocation structures. *J. Mech. Phys. of Solids* 48, 2077-2114.
- Peach, M. O., Köhler, J. S., 1950. The forces exerted on dislocations and the stress fields produced by them. *Phys. Rev.* 80, 436-439.
- Pedregal, P., 1993. Laminates and Microstructure. *European J. Appl. Math.* 4, 121-149.
- Petch, N. J., 1953. The cleavage strength of polycrystals, *J. Iron Steel Inst.* 174, 25-28.
- Polanyi, M., 1934. Über eine Art Gitterstörung, die einen Kristall plastisch machen könnte. *Z. Phys.* 89, 660-664.
- Proust, G., Tomé, C. N., Jain, A., Agnew, S. R., 2009. Modeling the effect of twinning and detwinning during strain-path changes of magnesium alloy AZ31. *Int. J. Plasticity* 25, 861-880.
- Rasmussen, K., Pedersen, O., 1980. Fatigue of copper polycrystals at low plastic strain amplitudes. *Acta Metall.* 28, 1467-1478.
- Reed-Hill, R. E., 1973. *Physical Metallurgy Principles*, 2nd edition. D. Van Nostrand Company, New York.
- Reed-Hill, R. E., Abbashian R., 1994. *Physical Metallurgy Principles*, 3rd edition. PWS Publishing Company, Boston.
- Rivlin, R. S., Saunders, D. W., 1952. The free energy of deformation for vulcanized rubber. *Trans. Faraday Soc.* 48, 200-206.
- Rockafellar, R. T., 1970. *Convex Analysis*. Princeton University Press, Princeton.
- Scipio, L. A., 1967. *Principles of continua with applications*. Wiley, New York.
- Sedov, L. I., 1965. Mathematical methods of constructing models of continuum media. *Usp. Matem. Nauk.* 20, 123-182.
- Sedov, L. I., 1968. Variational methods of constructing models of continuous media. In: Parkus, H., Sedov, L. I. (eds.), *Irreversible aspects of continuum mechanics and Transfer of Physical Characteristics in Moving Fluids*. Springer Verlag, Wien and New York, 1968.
- Segal, V.M., 1995. Material processing by simple shear. *Mater. Sci. Eng. A* 197, 157-164.
- Šilhavý, M., 1997. *The Mechanics and Thermodynamics of Continuous Media*. Springer-Verlag, Berlin.
- Shu, J. Y., Fleck, N. A., 1999. Strain gradient crystal plasticity: size-dependent deformation of bicrystals. *J. Mech. Phys. Solids* 47, 297-324.

- Shu, J. Y., Fleck, N. A., Van der Giessen, E., Needleman, A., 2001. Boundary layers in constrained plastic flow: comparison of nonlocal and discrete dislocation plasticity. *J. Mech. Phys. Solids* 49, 1361-1395.
- Siedersleben, M. E., Taylor, G., 1989. Slip systems in bcc Li-Mg alloys. *Philos. Mag.* 60, 631-647.
- Simo, J. C., 1988. A framework for finite strain elastoplasticity based on maximum plastic dissipation and the multiplicative decomposition. I. Continuum formulation. *Comput. Meth. Appl. Mech. Eng.* 66, 199-219.
- Simo, J. C., 1988. A framework for finite strain elastoplasticity based on maximum plastic dissipation and the multiplicative decomposition. II. Computational Aspects. *Comput. Meth. Appl. Mech. Eng.* 68, 1-31.
- Skaland, T., Grong, O., Grong, T., 1993. A model for the graphite formation in ductile cast-iron solid state transformation reactions. *Metall. Trans. A* 24, 2347-2353.
- Spearot, D. E., Jacob, K. I., McDowell, D. L., 2007. Dislocation nucleation from bicrystal interfaces with dissociated structure. *Int. J. Plasticity* 23, 143-160.
- Spearot, D. E., Tschopp, M. A., Jacob, K. I., McDowell, D. L., 2007. Tensile strength of $\langle 100 \rangle$ and $\langle 110 \rangle$ tilt bicrystal copper interfaces. *Acta Mater.* 55, 705-714.
- Šverák, V., 1992. Rank-one convexity does not imply quasiconvexity, *Proc. Roy. Soc. Edinburgh* 120 A, 185-189.
- Taylor, G. I., 1934. The mechanism of plastic deformation of crystals. Part I. Theoretical. *Proc. Roy. Soc. London A* 145, 362-387.
- Teodosiu, C., 1969. A dynamic theory of dislocations and its application to the theory of elastic-plastic continuum. *Fundamental Aspects of Dislocation Theory*. NBS Special Publication 317, U.S. Government Printing Office, Gaithersburg, 837-876.
- Truesdell, C., Noll, W., 1965. The nonlinear field theories of mechanics. In: Flügge, S. (ed.), *Encyclopedia of Physics* III/3, Springer, Berlin.
- Truesdell, C., Toupin, R. A., 1960. The classical field theories. *Handbuch der Physik*, Band III/I. Springer, Berlin.
- Tschopp, M. A., Tucker, G. J., McDowell, D. L., 2007. Structure and free volume of $\langle 110 \rangle$ symmetric tilt grain boundaries with the E structural unit. *Acta Mater.* 55, 3959-3969.
- Venables, J. A., 1964. In: Reed-Hill, R. E., Hirth, J. P., Rogers, H. C. (eds.), *Deformation twinning*. Gordon & Breach, New York.
- Volokh, K. Y., Trapper, P., 2007. A simple theory of strain gradient plasticity based on stress-induced anisotropy of defect diffusion. *Int. J. Plasticity* 23, 2085-2114.
- Volterra, V., 1905. *Ann. Ec. Norm.* 24, 401.
- Weertman, J., 1965. The Peach-Koehler equation for the force on a dislocation modified for hydrostatic pressure. *Philos. Mag.* 11, 1217-1223.
- Young, L. C., 1969. *Lectures on the Calculus of Variations and Optimal Control Theory*. Saunders, London.

- Yumen, L., 1989. Low-energy dislocation structure in cyclically deformed quench-tempered steel. *Mat. Sci. Eng. A* 113, 237-244.
- Ziegler, H., Wehrli, C., 1987. The Derivation of Constitutive Relations from the Free Energy and the Dissipation Function. In Wu, Th. Y., Hutchinson, J. W. (eds.), *Advances in Applied Mechanics*, vol. IV. Academic Press Inc.
- Zienkiewicz, O. C., Taylor, R. L., 2005. *The Finite Element Method*, 6th edition, vol. 1-2. Elsevier, Oxford.

Reference to Pre-Publications

In accordance with §7(1) parts of this dissertation have been published in international scientific journals and conference proceedings in consultation with the supervisors, Professors Klaus Hackl and Khanh Chau Le. Where appropriate, references in this thesis note the following pre-publications:

- Hackl, K., Kochmann, D. M., 2008. Relaxed potentials and evolution equations for inelastic microstructures. In: Daya Reddy, B. (Ed.), IUTAM Symposium on Theoretical, Computational and Modelling Aspects of Inelastic Media. Springer, Berlin, pp. 27-39.
- Kochmann, D. M., Hackl, K., 2009. Time-continuous modeling of microstructures in single-slip finite elastoplasticity based on energy relaxation. *Proc. Appl. Math. Mech.* 9, in press.
- Kochmann, D. M., Hackl, K., 2009. Time-continuous evolution of microstructures in finite plasticity. In: Hackl, K. (Ed.), *Proceedings of the IUTAM Symposium on Variational Concepts with Applications to the Mechanics of Materials*. Springer, Berlin, in press.
- Kochmann, D. M., Le, K. C., 2008. Dislocation pile-ups in bicrystals within continuum dislocation theory. *Int. J. Plasticity* 24, 2125-2147.
- Kochmann, D. M., Le, K. C., 2008. Plastic deformation of bicrystals within continuum dislocation theory. *J. Math. Mech. Solids*, pre-published online, 11 March 2008 (doi: 10.1177/1081286507087322).
- Le, K. C., Kochmann, D. M., 2009. A simple model for dynamic recrystallization during severe plastic deformation. *Arch. Appl. Mech.* 79, 579-586.
- Kochmann, D. M., Le, K. C., 2008. Plastic deformation of bicrystals within continuum dislocation theory. *Proc. Appl. Math. Mech.* 8, pp. 10435–36.
- Kochmann, D. M., Le, K. C., 2009. A continuum model for the initiation and evolution of deformation twins. *J. Mech. Phys. Solids* 57, 987-1002.
- Kochmann, D. M., Le, K. C., 2009. Continuum dislocation theory and related size effects in crystal plasticity. In: Columbus, F. (ed.), book title to be announced, Nova Science Publishers, Hauppauge, New York, in press.
- Le, K. C., Kochmann, D. M., 2009. An energetic approach to deformation twinning. In: Hackl, K. (Ed.), *Proceedings of the IUTAM Symposium on Variational Concepts with Applications to the Mechanics of Materials*. Springer, Berlin, in press.

Curriculum Vitae

Personal Data

Name	Dennis Michael Kochmann
Date of Birth	February 19, 1982
Place of Birth	Bottrop, Germany
Nationality	German
Marital Status	single

School Education

08/1988 – 10/1989	Annette-von-Droste-Hülshoff-Grundschule Bottrop
10/1989 – 07/1992	Agatha-Grundschule Bottrop
08/1992 – 06/2001	Heinrich-Heine-Gymnasium Bottrop, Abitur in June 2001

Civil Service

07/2001 – 05/2002	Knappschafts Krankenhaus Bottrop
-------------------	----------------------------------

University Education

10/2002 – 09/2006	Mechanical Engineering, Ruhr-Universität Bochum, Germany, Diploma (Dipl.-Ing.) in September 2006
09/2005 – 06/2006	Engineering Mechanics, University of Wisconsin – Madison, U.S.A., Master of Science (M.Sc.) in May 2006

Professional Occupation

11/2003 – 08/2005	Student assistant, Lehrstuhl für Allgemeine Mechanik, Ruhr-Universität Bochum, Germany
09/2005 – 06/2006	Research assistant, Micromechanics Laboratory, Department of Engineering Physics, University of Wisconsin – Madison, U.S.A.
10/2006 – present	Research associate, Lehrstuhl für Allgemeine Mechanik, Ruhr-Universität Bochum, Germany

**Mitteilungen aus dem Institut für Mechanik
RUHR-UNIVERSITÄT BOCHUM
Nr. 152**

ISBN 978-3-935892-30-8